Scattering a Bose-Einstein Condensate off a Modulated Barrier

Andrew J. Pyle

Lenhartsville, PA

Master of Science, College of William & Mary, 2012
Bachelor of Science, Kutztown University of Pennsylvania, 2011

A Dissertation presented to the Graduate Faculty
of The College of William & Mary in Candidacy for the Degree of
Doctor of Philosophy

Department of Physics

College of William & Mary
May 2019

APPROVAL PAGE

This Dissertation is submitted in partial fulfillment of
the requirements for the degree of

Doctor of Philosophy

Andrew J. Pyle

Approved by the Committee, February 2019

Committee Chair
Associate Professor Seth Aubin, Physics
College of William & Mary

Professor John Delos, Physics
College of William & Mary

Professor William Cooke, Physics
College of William & Mary

Professor Irina Novikova, Physics
College of William & Mary

[illegible] for Kunal Das

Professor Kunal Das, Physics
Kutztown University of Pennsylvania

ABSTRACT

This thesis presents an experiment to study 1D quantum mechanical scattering by an amplitude-modulated barrier. This experiment represents a first step toward implementing a quantum pump for ultracold atoms based on two such barriers modulated out of phase with one another. A single oscillating barrier imparts or subtracts kinetic energy in discrete amounts from the scattered atoms. In this manner, the energy spectrum of the scattered atoms resembles a comb with a tooth spacing of $\hbar\omega$ where ω is the oscillation frequency of the barrier. This effect is analogous to the frequency modulation of a radio wave to add sidebands to a carrier frequency, where the carrier is the kinetic energy of ultracold atoms and the oscillating barrier provides the modulating signal. Numerical simulations of the scattering process confirm this basic scattering picture. The experiment uses a Bose-Einstein condensate (BEC) of ^{87}Rb. The BEC is released from a relaxed magnetic chip trap and directed horizontally towards a tightly focused laser beam that serves as an oscillating barrier. A magnetic field gradient is used to control the vertical motion of the BEC and to levitate it. Detection is carried out with a time of flight technique with the aim of resolving discrete atomic packet sidebands. This method can be used to study momentum sideband generation with a BEC in the presence of no or very weak interactions. The experiment successfully measured the broadening of the BEC velocity distribution after scattering off the modulated barrier. However, the observation of momentum sidebands remains elusive.

TABLE OF CONTENTS

Acknowledgements vi

Dedication viii

List of Figures ix

List of Tables xiv

CHAPTER

1 Introduction 1

1.1 Motivation 1

1.2 Physics of Single Barrier Scattering 2

1.3 Application to Quantum Pumping 4

1.4 Ultracold Atom Physics 6

1.5 Summary of Thesis Results 7

1.6 Structure of Thesis 8

2 Scattering by an Oscillating Barrier 10

2.1 Introduction 10

2.2 Model 11

2.3 Classical Description 13

2.3.1 The Barrier as an Energy "Elevator" 14

2.3.2 Limiting Cases 14

2.3.3 Generating a Scattered Momentum Spread 16

2.3.4 Incident Distribution 16

2.4 Quantum Description 17

2.4.1 Numerical Propagation Method 18

2.4.2 Quantum vs. Classical: Sidebands 20
2.4.3 Semi-Classical Picture: Sidebands as Multi-Path Interference 21
2.4.4 Atom-Atom Interactions 23
2.5 Experimental Implementation 25
2.5.1 BEC: The Atomic Wavepacket 26
2.5.2 Oscillating Barrier 27
2.5.3 Measuring the Momentum Distribution: Time-of-Flight Imaging 28
2.6 Differential Velocity 28
2.7 Sideband Generation 30
2.8 Experiment Design 32
3 Bose-Einstein Condensate Theory 38
3.1 Harmonic Trap Without Interactions 40
3.2 The Gross-Pitaevskii Equation 42
3.3 The Thomas-Fermi Approximation 47
3.4 Expansion Rate Calculations 50
3.5 Kohn's Theorem 56
4 Apparatus 60
4.1 Magneto-Optical Trap Operation 64
4.1.1 Magneto-Optical Trap 64
4.1.2 MOT Chamber 65
4.1.3 Laser Systems 68
4.1.4 Temperature Measurement 72
4.1.5 Optical Molasses 73
4.1.6 Optical Pumping 77

4.2 Magnetic Trap & Transport 78
4.3 Atom Chip 80
4.3.1 Safety Interlock 85
4.3.2 RF Evaporation to BEC 87
4.3.3 BEC Jitter 91
5 Magnetic Levitation System 99
5.1 Motivation 101
5.2 Design and Theory of Operation 104
5.2.1 Isolation 107
5.2.2 Power Supply 109
5.2.3 MOSFETs 110
5.2.4 Current-Sensing 111
5.2.5 Protection Diodes 111
5.2.6 Snubber 113
5.2.7 Feedback 114
5.2.8 Switchboard 114
5.2.9 MOSFET Selector 118
5.2.10 Gate Driver 118
5.2.11 Safety Interlock 120
5.2.12 Analog Switch 124
5.2.13 Voltage Regulation 125
5.2.14 Terminal Blocks 126
5.2.15 Thermal Concerns 126
5.3 Setup and Control 127
5.3.1 Installation 127
5.3.2 Operation 127

5.4 Levitation Kinematics . . . 129
5.5 Performance . . . 136
5.5.1 Jitter . . . 138
5.5.2 Deformation of the Cloud . . . 141
5.5.3 Horizontal Drift During Levitation . . . 142
6 Experimental Setup . . . 146
6.1 Narrow Momentum Distribution . . . 147
6.2 Initial Momentum Kick . . . 150
6.2.1 Current Pulse Control . . . 151
6.2.2 Performance & Calibration . . . 155
6.3 Oscillating Barrier . . . 158
6.3.1 Focusing & Wavelength . . . 160
6.3.2 Frequency Control . . . 170
6.3.3 Setup & Calibration . . . 172
6.3.4 Optics & Alignment . . . 173
6.4 Detection . . . 181
6.5 Summary of Experimental Sequence . . . 183
7 Results & Discussion . . . 184
7.1 Introduction . . . 184
7.2 Expansion Rate & Mean Velocity . . . 185
7.2.1 Data Collection . . . 185
7.2.2 Preliminary Data . . . 188
7.2.3 Full Spectrum Frequency Data . . . 193
7.2.4 Comparison to Theory . . . 200
7.2.5 Atom Number Dependence . . . 204
7.3 Atomic Cloud Structure . . . 205

7.4 Phase Dependence . . . 211
7.5 Transverse Behavior of Scattered Atoms . . . 216
7.5.1 Transverse Focusing . . . 216
7.5.2 Kapitsa-Dirac Effect . . . 216
7.6 Summary . . . 218
8 Conclusion . . . 222
8.1 Summary of Results . . . 222
8.2 Why No Sidebands? . . . 224
8.3 Experimental Reproducibility . . . 227
8.4 Outlook (And Potential Improvements) . . . 229
APPENDIX A
Additional Expansion Rate Plots . . . 234
APPENDIX B
Additional Overshoot Pulse Tuning Plots . . . 251
APPENDIX C
Push Coil Data . . . 258
APPENDIX D
ADwin Sequencer Panel . . . 263
APPENDIX E
Unit Conversion . . . 265
Bibliography . . . 266
Vita . . . 273

ACKNOWLEDGEMENTS

An extensive amount of effort is required to build and maintain an ultracold atom apparatus. Even more is required to conduct a successful experiment, and yet more while teaching labs with minimal funding. As such, the majority of my time spent conducting research towards my experiment may have been distributed as 95% preparation (planning, simulating, designing, building, troubleshooting, repairing, and maintaining), followed by 5% data collection. This work would not have been possible without the guidance and hard work of my advisor, Seth Aubin, and the contributions put forth by the graduate and many undergraduate students who have passed through the lab. I believe that every student who graduates from our group receives an unparalleled level of experience in optics and electronics under Seth's teaching. I thank Seth for the nutrition provided while working after hours. I would like to thank the committee members for their constructive review over the course of my graduate career. I thank Kunal Das, with whom I conducted research as an undergrad, and who encouraged me to attend graduate school. While in graduate school, he allowed me to continue to use his computers for running simulations. I thank the professors and mentors: Charles Perdrisat, Eugeniy Mikhailov, Mike Kordosky, Bill Cooke, and Todd Averett, with whom I taught undergraduate labs. I am grateful to Todd as a mentor, electronics expert, friend, and fantastic drummer. I acknowledge the theoretical support of the quantum pumping collaboration consisting of myself, Seth Aubin, Megan Ivory, Kunal Das, John Delos, Tommy Byrd, and Kevin Mitchell.

I am grateful to former graduate students Megan Ivory, Austin Ziltz, and Charlie Fancher for the majority of the apparatus build, their teaching, support, and camaraderie. Megan was the pioneering predecessor of the project I presented. Charlie was my consistent, competent colleague and companion in our lab willing to teach and lend moral support. Austin is a local companion, potential future coworker, amazing guitarist, beer brewer, teacher, and electronics expert. I appreciate the contributions Drew Rotunno and Shuangli Du made to the group, especially when their work did not directly benefit their research projects. Drew consistently maintained a positive attitude while organizing the lab and optimizing the apparatus. I thank an undergraduate member of our group, Anuraag Sensharma, for the design and development of the dark-ground imaging system. I thank every studious undergraduate who lightened my grading burden by submitting neat and correct assignments. I thank the physics intramural volleyball team for the fun we had, but I wish them luck in winning a future intramural championship (denial is unhealthy and they will probably need the luck). I wish the PGSA the best and hope that my grilling successor is never without a beer.

I thank the College of William & Mary Physics Department and the Virginia Space Grant Consortium for their support during my research. I would like to thank the physics department secretaries: Carol, Paula, Elle, and Bonnie for their helpfulness, positive attitudes, delightful conversation, and encouragement. I thank Vice-Provost for research, Dennis Mannos, for helping our group acquire a new master laser after our old one, while a long-lived champion, gave out.

I cherish all of my family, my parents Jim & Gale, and my brother Joe for always believing in me. Although, sadly, it is no longer the same, I am grateful for Relevant Church and I treasure the friends I found there.

I thank my former classmate, Riley Howsden, for his friendship and positive career and life advice. I thank Armen Oganesov and Chris Flint for being two of the best friends, classmates, roommates, and groomsmen anyone could ask for. I am forever in debt to Chris's wife, Morgan, for introducing me to the love of my life. Finally, I thank my wife, Jillian, for her love, patience, and support.

I would also like to thank ACEnT Laboratories LLC and Grey Gecko LLC for recruiting me while I was finishing my degree.

To my wife, Jillian, whose patience and support made this work possible, and whose love made it worthwhile.

LIST OF FIGURES

1.1 FM modulation of a wave. 3
1.2 Quantum pumping block diagram. 5

2.1 Kinetic energy shift of an atomic wavepacket by interacting with an oscillating barrier. 12
2.2 Quantum vs. classical comparison of momentum distributions after barrier interaction. 15
2.3 Semiclassical explanation of sidebands through multi-path interference. 22
2.4 Final Momentum Distributions with Different Interaction Strengths. . 24
2.5 Diagram of atoms reflecting after interacting with an oscillating barrier. 26
2.6 Differential Velocity vs. Initial Kinetic Energy 29
2.7 Number of Floquet peaks as a function of parameters. 32
2.8 Number of Floquet peaks as a function of parameters–recolored. . . . 33
2.9 Experiment schematic. 36

3.1 Theoretical condensate expansion rate. 52
3.2 Theoretical condensate density. 53
3.3 Theoretical in-trap condensate radius. 54
3.4 Calculated axial and radial expansion rates. 55

4.1 Apparatus photo. 61
4.2 Apparatus overlay. 62
4.3 Apparatus schematic. 63
4.4 MOT diagram. 66
4.5 MOT photo. 67
4.6 Laser locking diagram. 68
4.7 Laser table layout diagram. 70
4.8 Image of atoms in the MOT. 72
4.9 Optical molasses energy diagram. 74
4.10 MOT, optical molasses/pumping, and magnetic trapping dynamics. . 75
4.11 Image of the magnetic trap. 79

4.12 Transport timing diagram. 81
4.13 Atom chip photo. 82
4.14 Chip trap schematic. 83
4.15 Atom chip trap magnetic field diagram. 84
4.16 Schematic for the Killbox. 86
4.17 RF evaporation diagram. 88
4.18 Evaporation pathway to BEC. 90
4.19 Horizontal location jitter histogram. 92
4.20 Vertical location jitter histogram. 93
4.21 Atom chip trap jitter data. 95
4.22 Optical dipole trap jitter data. 96
4.23 Optical dipole trap heating rate. 97

5.1 Location of levitated atoms after being released from an optical dipole trap. 102
5.2 Atoms falling under suppressed gravity. 103
5.3 Block diagram of levitation system. 104
5.4 Levitiathan current modulator with constituent components. 105
5.5 Full schematic of levitation system. 106
5.6 Schematic of the galvanic isolator circuit. 108
5.7 Schematic of the current-sensing amplifier circuit. 112
5.8 Schematic of the MOSFET snubber circuit. 113
5.9 Schematic of the levitation coil snubber circuit. 114
5.10 Schematic of the error signal circuit. 115
5.11 Schematic of the feedback circuit. 116
5.12 Schematic of the switchboard circuit. 117
5.13 Schematic of the MOSFET selector circuit. 119
5.14 Schematic of the gate driver circuit. 120
5.15 Schematic of the current interlock circuit. 121
5.16 Schematic of the temperature interlock circuit. 122
5.17 Schematic of the external interlock circuit. 122
5.18 Schematic of the interlock latch circuit. 123
5.19 Schematic of the analog switch circuit. 124
5.20 Schematic of the voltage regulators. 125
5.21 Photo of the front panel of the Levitiathan. 128
5.22 Levitation coil current and related kinematics. 133
5.23 Atoms falling with different coil currents and resulting acceleration as a function of current. 134
5.24 Current overshoot pulse tuning data. 135

5.25 Optimal current schemes. . . . 136
5.26 Atomic motion dynamics at different levitation coil currents. . . . 137
5.27 Analysis of magnetic gradient from coil 6. . . . 137
5.28 Current dynamics for levitation. . . . 138
5.29 Vertical levitation jitter. . . . 139
5.30 Horizontal levitation jitter. . . . 140
5.31 Effect on a BEC after being pushed, levitated, and interacting with a barrier. . . . 143
5.32 Effect on the Ioffe field on levitation. . . . 145

6.1 Expansion rates for a BEC released from a relaxed atom chip trap. . . . 149
6.2 Block diagram for the high speed, high current switch called the "Kraken". . . . 152
6.3 Picture and labels for the Kraken. . . . 153
6.4 Kraken schematic. . . . 154
6.5 High current push pulses for generating initial velocity and atomic velocity proportional to charge pumped through the push coil. . . . 156
6.6 Expansion rate of atoms after push coil pulse. . . . 157
6.7 Beam waist measurement setup. . . . 161
6.8 Beam waist measurement setup. . . . 162
6.9 Beam waist measurements along the beam. . . . 164
6.10 Beam waist measurements along the beam, different vertical location. 165
6.11 Beam waist measurements along the beam, third vertical location. . . . 166
6.12 Beam waist vs. axial location. . . . 167
6.13 Beam profile along the vertical direction. . . . 168
6.14 False color plot modeling the barrier beam. . . . 169
6.15 Photo/schematic of the barrier beam optical circuit. . . . 171
6.16 Scope image of non-sinusoidal barrier 172
6.17 Barrier block diagram. . . . 173
6.18 Barrier oscillation monitored via photodiode. . . . 174
6.19 Barrier transmission curves and energy calibration. . . . 175
6.20 Gizmo Photo. . . . 176
6.21 Gizmo Photo. . . . 177
6.22 Gizmo Photo. . . . 178
6.23 Experiment timing diagram. . . . 183

7.1 Gaussian fit to ROI sum. . . . 186
7.2 ROI sum for multiple times of flight, fast velocity, 15 kHz. . . . 187

7.3 ROI sum for multiple times of flight, fast velocity, 11 kHz. 187
7.4 Preliminary axial and vertical expansion rates. 190
7.5 Preliminary cloud size vs. time and axial expansion rate as a function of barrier frequency. 192
7.6 Preliminary axial position over time and velocity as a function of frequency. 194
7.7 Axial cloud size over time and axial expansion rate as a function of barrier frequency, slow velocity. 196
7.8 Axial position over time and axial velocity as a function of barrier drive frequency compared to theory, slow velocity. 197
7.9 Axial cloud size over time and axial expansion rate as a function of barrier drive frequency compared to theory, faster velocity. 198
7.10 Axial position over time and axial velocity as a function of barrier drive frequency compared to theory, faster velocity. 199
7.11 Atom number dependence of expansion rate. 206
7.12 Atom number dependence of expansion rate. 207
7.13 Image of atoms after interacting with an $f = 8$ kHz oscillating barrier and corresponding ROI sum with theoretical comparison. 209
7.14 ROI sum compared to theory for 15 kHz, slow velocity. 210
7.15 ROI sum compared to theory for 10 kHz, slow velocity. 211
7.16 ROI sum compared to theory for 13 kHz, slow velocity. 212
7.17 Quantum and classical expansion rates and velocities for different phases. 214
7.18 Axial cloud size and position with different phases. 215
7.19 Radial focusing of atoms after interacting with a barrier. 217
7.20 Kapitsa-Dirac Effect. 219

A.1 ROI sum for multiple times of flight, slow velocity, 13 kHz. 235
A.2 ROI sum for multiple times of flight, slow velocity, static barrier. . . . 235
A.3 ROI sum for multiple times of flight, slow velocity, 1 kHz. 236
A.4 ROI sum for multiple times of flight, slow velocity, 2 kHz. 236
A.5 ROI sum for multiple times of flight, slow velocity, 4 kHz. 237
A.6 ROI sum for multiple times of flight, slow velocity, 5 kHz. 237
A.7 ROI sum for multiple times of flight, slow velocity, 6 kHz. 238
A.8 ROI sum for multiple times of flight, slow velocity, 7 kHz. 238
A.9 ROI sum for multiple times of flight, slow velocity, 8 kHz. 239
A.10 ROI sum for multiple times of flight, slow velocity, 9 kHz. 239
A.11 ROI sum for multiple times of flight, slow velocity, 10 kHz. 240
A.12 ROI sum for multiple times of flight, slow velocity, 11 kHz. 240

A.13 ROI sum for multiple times of flight, slow velocity, 12 kHz. 241
A.14 ROI sum for multiple times of flight, slow velocity, 13 kHz. 241
A.15 ROI sum for multiple times of flight, slow velocity, 15 kHz. 242
A.16 ROI sum for multiple times of flight, fast velocity, static barrier. . . . 242
A.17 ROI sum for multiple times of flight, fast velocity, 1 kHz. 243
A.18 ROI sum for multiple times of flight, fast velocity, 2 kHz. 244
A.19 ROI sum for multiple times of flight, fast velocity, 3 kHz. 244
A.20 ROI sum for multiple times of flight, fast velocity, 4 kHz. 245
A.21 ROI sum for multiple times of flight, fast velocity, 5 kHz. 245
A.22 ROI sum for multiple times of flight, fast velocity, 6 kHz. 246
A.23 ROI sum for multiple times of flight, fast velocity, 7 kHz. 246
A.24 ROI sum for multiple times of flight, fast velocity, 8 kHz. 247
A.25 ROI sum for multiple times of flight, fast velocity, 9 kHz. 247
A.26 ROI sum for multiple times of flight, fast velocity, 10 kHz. 248
A.27 ROI sum for multiple times of flight, fast velocity, 12 kHz. 248
A.28 ROI sum for multiple times of flight, fast velocity, 13 kHz. 249
A.29 ROI sum for multiple times of flight, fast velocity, 14 kHz. 249
A.30 ROI sum compared to theory for 4 kHz, slow velocity. 250
A.31 ROI sum compared to theory for 5 kHz, slow velocity. 250

B.1 Current overshoot pulse tuning data. 252
B.2 Current overshoot pulse tuning data. 253
B.3 Current overshoot pulse tuning data. 254
B.4 Current overshoot pulse tuning data. 255
B.5 Current overshoot pulse tuning data. 256
B.6 Hold time as a function of pause time. 257
B.7 Pause time for desired drop distance. 257

C.1 Axial push coil data. 259
C.2 Axial push coil analysis. 260
C.3 Radial push coil data. 261
C.4 Radial push coil analysis. 262

D.1 ADwin sequencer panel. 264

LIST OF TABLES

2.1 Quantum split-step operator method parameters. 19
2.2 Optimal scattering parameters. 34

6.1 Push coil parameters. 151
6.2 Barrier beam parameters. 163

7.1 Experimental parameters. 188

CHAPTER 1

Introduction

The objective of the research described in this thesis is to study experimentally the scattering of ultracold atom matter waves from an amplitude modulated potential energy barrier. In addition to observing this type of scattering, the experiment is designed to search for discrete kinetic energy sidebands in the scattering spectrum.

This chapter describes the basic motivation for studying scattering by a time-dependent potential, the basic physics of the scattering process, and the specific application of these barriers to quantum pumps. The chapter also summarizes the basic experimental results of the research and outlines the basic structure of the thesis.

1.1 Motivation

The interaction of particles with periodic time-varying potentials is an essential process in quantum transport physics, laser-electron scattering, and photon assisted tunneling. Motivated by work on photon-assisted tunneling in superconducting diode junction [1], Büttiker and Landauer studied the basic quantum physics of a particle scattering from an amplitude modulated potential in their analysis of electron tunneling time [2]. Since this initial work, a number of theoretical treatments have studied scattering from a time-varying potential in the context of quantum pumping in solid state systems [3], laser-driven electron scattering [4], and photon-assisted tunneling [5, 6, 7]. Furthermore, such periodically-driven systems can feature quantum interference [8], as well as complex behavior such as chaotic scattering and chaos-assisted tunneling [9, 10, 11, 12, 13], as well as dynamical localization [14]. More recently, periodically driven many-body systems have been used to create and study discrete time crystals [15, 16, 17, 18].

The development of ultracold quantum gases [19, 20] and the associated high-precision quantum control of these systems has opened up a flurry of activity in experimentally simulating solid state system with ultracold atoms. This thesis work follows this approach and uses ultracold atom matter waves to study scattering from a periodically modulated laser potential.

1.2 Physics of Single Barrier Scattering

In quantum mechanics, a particle is described by a deBroglie wave. In the case of an electron or an atom, this wave is a matter wave whose oscillation frequency ν depends on the energy E of the particle (kinetic plus potential energy): $E = h\nu$. However, if this matter wave traverses a time-varying potential, then not only is the total energy of the particle modified but so is its deBroglie frequency. In the language of radio frequency electronics, the matter wave “carrier” frequency is “chirped” by the time-varying potential.

If the potential is driven periodically at a frequency ω then the energy of the matter-wave and its deBroglie frequency are modulated. Frequency modulation or FM modulation is a common technique in radio electronics (e.g. FM radio): as

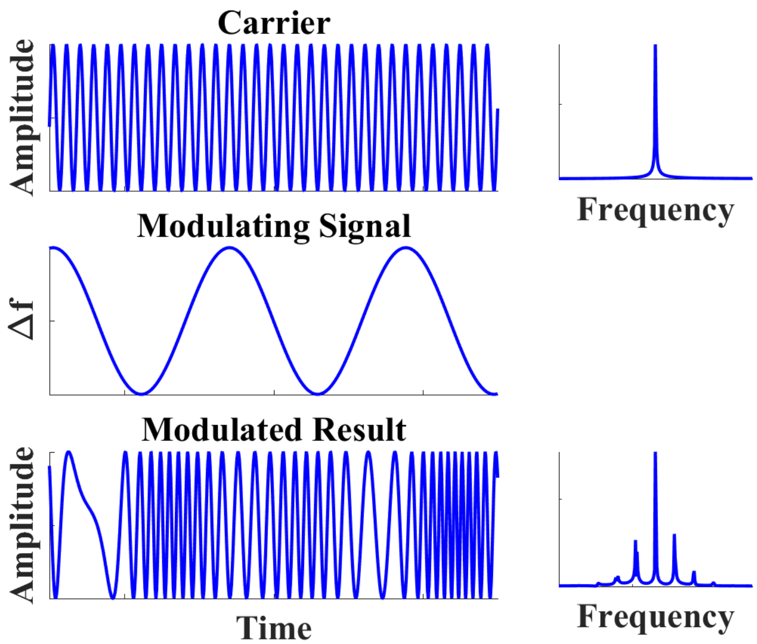

FIG. 1.1: FM modulation of a wave. Top: A single frequency carrier wave shown in the time domain (left) and frequency domain (right). Middle: A signal used to modulate the single frequency carrier wave. Bottom: The result of modulating a single frequency carrier wave shown in the time domain (left) and frequency domain (right).

Figure 1 explains, FM modulation of a wave results in the creation of frequency sidebands that are at discrete intervals of ω from the each other and the carrier wave in frequency space. In the case of a matter wave, the energy separation of the sidebands is $\Delta E = \hbar\omega$. In other words, when a matter wave interacts with a periodically driven potential, then the scattered wave develops energy sidebands that represent increases and decreases in portions of the carrier wave's incident energy. One of the original objective of the thesis research was to observe such sidebands with a matter wave based on an Bose-Einstein condensate (BEC) of ultracold atoms interacting with an amplitude modulated potential energy barrier.

1.3 Application to Quantum Pumping

While a particle scattering from an oscillating barrier potential can develop energy sidebands (or deBroglie wave sidebands), the use of two such barrier potentials modulated out-of-phase from each other offers the prospect of making a pump. Indeed, the original motivation for studying a single modulated barrier was to use it as a building block for multi-barrier pumps [21, 22]. Quantum pumping was first proposed by Thouless in 1983 [23] as a mechanism for generating a well controlled and reversible electrical current in mesoscopic solid state systems via a localized time-varying potential without applying an overall bias potential (i.e. a battery). Furthermore, the quantum pump could potentially generate quantized and coherent transport. While non-adiabatic quantized charge pumps have been successfully implemented in solid state systems [24], ballistic quantum pumps have proven more difficult due to competing capacitive coupling and rectification effects inherent to charge transport [25, 26, 27]. A quantum pump based on ultracold atom carriers (instead of electrons) offers a route around these bottlenecks due the high degree of quantum control of ultracold atom systems, the neutral nature of atoms, and the high degree of coherence achievable in quantum gases, i.e. BEC (see section 1.4 for brief a review of ultracold atom systems).

Figure 1.2 shows the layout of a ballistic atom "turnstile" quantum pump: atoms originating from two reservoirs (i.e. traps) are directed at a localized timevarying double barrier potential located in the center of a 1D channel (i.e. a highly elongated trap) connecting the two sources. The turnstile pump consists of two single potential barriers that are modulated 90° out-of-phase, which results in pumping in a preferential direction (i.e. scattering direction) that depends on the incident speed of the atoms. The atomic motion in such a potential is complicated [22] and shows signs of chaotic behavior, given that atoms can get momentarily trapped be-

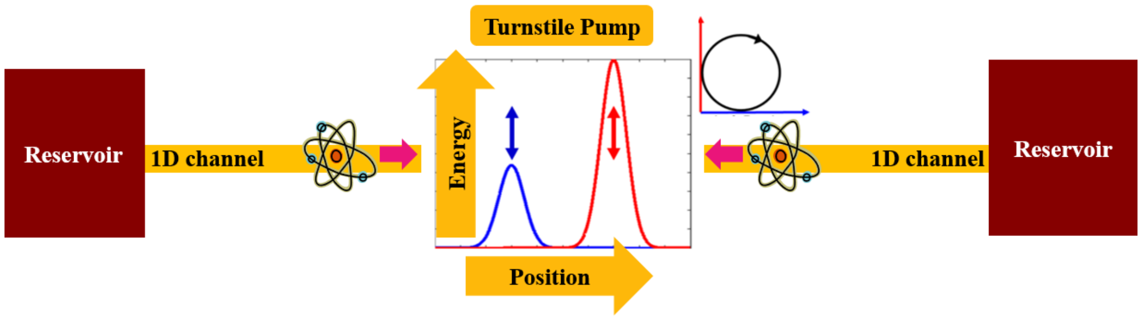

FIG. 1.2: Quantum turnstile pump scheme. Ultracold atoms are directed from two reservoirs via a 1D channel, at the center of which sits a localized turnstile potential. The turnstile consist of two potential barrier oscillating 90° out-of-phase with each other. For a given incident atomic speed the pump preferentially scatters atoms towards one of the reservoirs.

tween the two barriers. Quantum mechanically, the turnstile pump behaves as an interferometer (or Fabry-Perot cavity) since each oscillating barrier acts as a type of beamsplitter. The research in this thesis implements and studies a single oscillating barrier, which can then serve as a building block for constructing a turnstile pump consisting of two oscillating barriers.

An experimental scheme based on ultracold atoms is particularly well suited to implementing such a ballistic turnstile quantum pump. Mono-energetic atomic packets can be directed towards the pump with a laser pulse or a magnetic field gradient pulse. The 1D channel can be implemented with an optical dipole potential via a collimated laser beam red-detuned from an atomic transition, while the barrier potentials can be produced by focusing down blue-detuned laser beams. While an ultracold atom system will not yield a practical solid state device, it can be used to study quantum pumps and test theories of how these should perform. In fact recently, two groups have implemented quantum pumps using ultracold atoms trapped in optical super-lattices [28, 29].

1.4 Ultracold Atom Physics

The field of ultracold atomic physics has developed over the last three decades and offers unparalleled experimental control of both the internal and external degrees of freedom of atoms. The advent of laser cooling and trapping techniques in the late 1980's enabled the cooling of select atomic elements to temperatures in the range of 1-100 μK [30, 31]. These laser cooling techniques are the starting point for further cooling to quantum degeneracy.

The magneto-optical trap or MOT [32] is the standard workhorse of ultracold atomic physics labs. The MOT collects and cools atoms down to the 100 μK scale. The atoms then undergo further optical cooling (e.g. Sysiphus cooling [33, 34], Raman sideband cooling [35], etc.) to the 10 μK scale and are then prepared in a single internal hyperfine spin state. Finally, the atoms are confined by the conservative potential of a magnetic trap [36] or optical dipole laser trap [37]. The final cooling stage uses forced evaporative cooling to reach nK-scale temperatures and generate a quantum degenerate gas, such as a BEC [19, 38, 39] or a degenerate Fermi gas [40]. In the research described in this thesis, the BEC is the starting point for the experiment as it provides a quasi monoenergetic sample of identical atoms that resembles a plane wave with a spatial envelope: the coherence length is on order of the BEC size.

The experimental atomic physics toolbox also provides efficient techniques for precision control of the position, velocity, and potential energy of ultracold atoms. Magnetic traps and optical dipole traps can be used to position atoms in well-controlled locations. Magnetic and optical fields can be used generate specific potential energy distributions (in space) which can then be used to levitate the atoms or accelerate them (or decelerate them) to a specific velocity (e.g. see chapters 5 and 6). Alternatively, Bragg and Raman laser pulses can provide a specific momentum impulse or "kick" to the atoms. Optical lattices formed by counterpropagating laser beams can arrange a sample of atoms in a highly periodic, fixed spatial grid. More recently, spin-specific control over the external degrees of freedom (velocity and position) has become possible with the AC Zeeman potentials produced by microwave near-fields [41].

1.5 Summary of Thesis Results

This thesis summarizes 7 (7.5) years of my research on scattering of a BEC from an oscillating barrier. I have worked on the theory of the scattering, the development of an experiment to observe such scattering, and the experimental observation of such scattering. The theory was developed with Prof. Kunal Das at Kutztown University, Prof. John Delos and Dr. Tommy Byrd at William and Mary, and Prof. Kevin Mitchell, as well as by the Aubin group (myself, Dr. Megan Ivory and Prof. Seth Aubin). I designed the experiment presented in this thesis with the assistance of S. Aubin (advisor): this experiment is a second effort to measure the scattering distribution. Dr. Megan Ivory made a first attempt, which did observe scattering but was hampered by atom-atom interactions (see chapter 2, section 2.4.4). I implemented the experiment and successfully made direct measurements of the scattering. I analyzed most of the data with assistance from S. Aubin.

The main results of my research are the following:

1) Quantum simulations for predicting scattered momentum distribution of matter waves interacting with both a single oscillating barrier and a turnstile quantum pump. This work resulted in two publications:

T. A. Byrd, M. K. Ivory, A. J. Pyle, S. Aubin, K. A. Mitchell, J. B. Delos, and K. K. Das, Scattering by an oscillating barrier: Quantum, classical, and semi-classical comparison, Phys. Rev. A 86, 013622 (2012) [42].

M. K. Ivory, T. A. Byrd, A. J. Pyle, K. K. Das, K. A. Mitchell, S. Aubin, and J. B. Delos, Ballistic atom pumps, Phys. Rev. A 90, 023602 (2014) [22]. This work is not discussed in this thesis.

2) Design and construction of an experiment that can measure the scattered momentum/velocity distribution for a BEC reflecting off an oscillating potential barrier.

3) Direct measurements of the scattered momentum distributions: these measurements show that experiment and theory are in coarse agreement.

4) Experimental access to parameter ranges where sidebands should be observable: While sidebands were not observed, the scattering distributions were more consistent with the quantum prediction than the classical one.

Over the course of my thesis research, I also participated in the following two experimental achievements:

i) Participation in the construction of a dual-species ultracold atom apparatus capable of BEC production:

M. K. Ivory, A. R. Ziltz, C. T. Fancher, A. J. Pyle, A. Sensharma, B. Chase, J. P. Field, A. Garcia, D. Jervis, and S. Aubin, Atom chip apparatus for experiments with ultracold rubidium and potassium gases, Rev. Sci. Instrum. 85, 043102 (2014) [43].

ii) Observation of the AC Zeeman force with a 6.8 GHz microwave near-field on a sample of ultracold ^{87}Rb atoms:

C. T. Fancher, A. J. Pyle, A. P. Rotunno, and S. Aubin, Microwave ac Zeeman force for ultracold atoms, Phys. Rev. A 97, 043430 (2018) [41].

1.6 Structure of Thesis

This thesis is organized by topic under theory, apparatus, and performance. It does not necessarily reflect the chronological order in which the work was completed.

The thesis is structured in the following manner. In chapter 2, I present the quantum and classical theories for scattering an atom from an oscillating potential barrier. These theories are then used as guides for developing the experimental scheme. Chapter 3 introduces the ultracold atom theory describing how BECs behave with a narrow energy spectrum. Chapter 4 discusses the experimental apparatus used to generate BECs. Chapter 5 is devoted to the design, construction, and evaluation of a magnetic levitation system for cold atoms based on a quadrupole magnetic field powered by a high-speed current source. Chapter 6 describes the details of the experimental scheme and evaluates the performance of its various components. The experimental results and associated analysis are presented in chapter 7. Finally, chapter 8 concludes the thesis and reviews the general outlook for the experiment.

CHAPTER 2

Scattering by an Oscillating Barrier

2.1 Introduction

This chapter introduces the basic theory and physics involved in one-dimensional scattering a particle or wave by an amplitude modulated barrier. The theory developed in this chapter makes specific predictions for oscillating barrier scattering regarding the generation of momentum-space sidebands, which is an important motivation for this thesis, as well as the energy range of the sidebands and the role of inter-particle interactions. The quantum generation of sidebands differs significantly from the continuous momentum spectrum predicted by classical physics. Furthermore, the theory developed in this chapter also provides significant guidance for designing the experiment presented in later chapters.

This chapter is structured in the following manner: section 2.2 introduces the basic oscillating barrier model, section 2.3 discusses the classical equations of motion for the system, and section 2.4 qualitatively describes quantum results using the Schrödinger equation for a wave scattered by an oscillating barrier in contrast to the classical regime, as well as the result of atom-atom interactions. Section 2.5 discusses the considerations for designing an experiment to observe sidebands and sections 2.6 and 2.7 discuss the requirements and parameter selection for experimental observation of the momentum sidebands.

2.2 Model

We consider a one dimensional system in which an atom is directed at a potential energy barrier with a Gaussian profile, as shown in figure 2.1. While a flat top barrier is easier to analyze, a Gaussian barrier is more easily produced experimentally by focusing a standard Gaussian laser beam, e.g. produced by the output of a single mode fiber. We define our Gaussian energy barrier $U(x,t)$ in position and time in the following manner:

$$U(x,t) = U_0[1 + \alpha \sin(\omega t + \phi)]e^{-(x-x_b)^2/2\sigma_b^2}, \tag{2.1}$$

where U_0 is the average amplitude of the barrier, x_b is the position of the barrier, and σ_b is the width of the barrier (in the case of a laser generated barrier, the waist radius w_b of the focus is given by $w_b = 2\sigma_b$); the barrier amplitude oscillates at frequency ω and phase ϕ. The relative modulation amplitude is given by α: for $\alpha = 1$ the barrier peak oscillates between 0 and $2U_0$, while for $\alpha \to 0$ the barrier is barely dithered around U_0. We direct atoms towards the barrier from the left with velocity v_0 and momentum p_0. The Hamiltonian H for the atom interacting with the barrier potential is given by

$$H = \frac{p^2}{2m} + U(x,t), \tag{2.2}$$

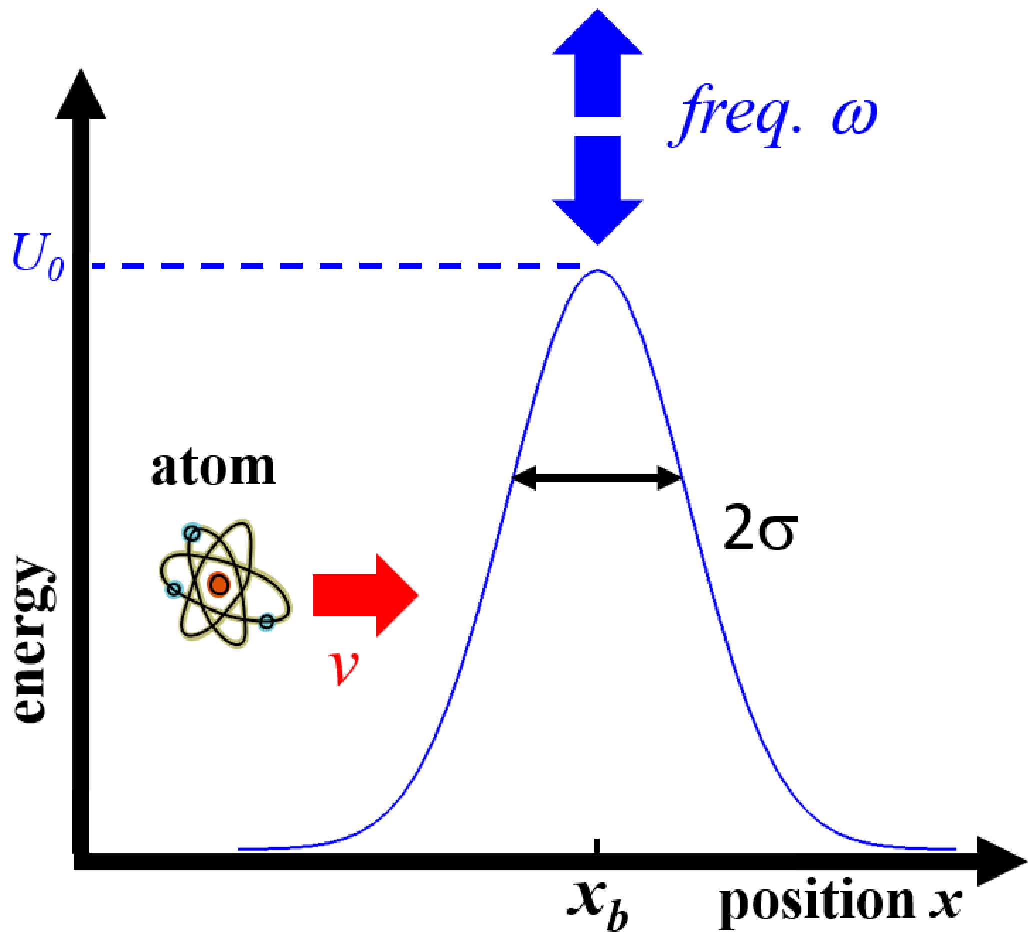

FIG. 2.1: The initial kinetic energy of an atomic wave packet is shifted by interacting with an amplitude-modulated barrier.

where p is the momentum of an atom with mass m. The system can be analyzed in a classical or quantum framework, though in both cases numerical methods must be used. As we will see in the following sections, the classical and quantum dynamics differ markedly, though the range of the predicted motions are in approximate agreement.

2.3 Classical Description

The classical equations of motions are readily obtained from Hamilton's equations using the Hamiltonian in equation 2.2. These equations can be written as:

$$p = m\frac{dx}{dt} \tag{2.3}$$

$$\frac{dp}{dt} = -\nabla U(x,t) \tag{2.4}$$

While analytic results are difficult to obtain, numerical propagation of these equations (eq. 2.3 and 2.4) is straightforward, e.g. with a Runge-Kutta method, and will give the position and momentum of an atom at any time t for a given initial position x_0 and momentum p_0.

If one directs a string of atoms with a same initial momentum p_0 but different starting positions, then these atoms will encounter the barrier at different phases in its oscillation. The outcome of an atom's encounter will depend on this phase (or its initial position), which results in a different final momentum (i.e. momentum after the atom has escaped the barrier region). The starting position can even decide whether the atom is reflected by the barrier or transmitted across it.

2.3.1 The Barrier as an Energy "Elevator"

Indeed, depending on the arrival phase at the barrier, an atom can either gain energy or lose energy as it rides up or down the energy barrier "elevator." This gain or loss of energy is continuous with the arrival phase, so that if one plots a histogram of all the possible final momenta or energy of the atoms (after interaction with the barrier) for a given incident string of atoms, then one finds that there is a strict range of classically permitted final momenta. Figure 2.2 shows in red such a histogram, or probability density, as a function of output momentum; the pink band shows the classically allowed final momentum range. Notably, the histogram is continuous in purely reflective or transmissive scenario[1] (which depends on the initial energy of the atoms, as well as the barrier parameters).

2.3.2 Limiting Cases

We note two interesting limiting cases. First, if the barrier is oscillating very quickly compared to the motion of the atom, then it appears as a time averaged static potential. In this case, the atoms acquire very little if any spread in their final momentum and either transmit completely over the barrier or reflect completely off regardless of their arrival phase. The second case occurs if the barrier is oscillating slowly compared to the motion of the incident atom, i.e. the barrier completes a small fraction of an oscillation during the time that the atom interacts with it. In this case, the arrival time of the atom at the barrier with respect to the phase of the barrier oscillation decides whether transmission or reflection occurs: however, as the barrier is quasi-static, the atom will gain or lose little kinetic energy during the interaction. In both these cases, the final momentum of the incident atom changes little compared to the incident momentum (except for a sign change).

[1]Obviously partial reflection/transmission cannot produce a continuous distribution with momenta of opposite signs.

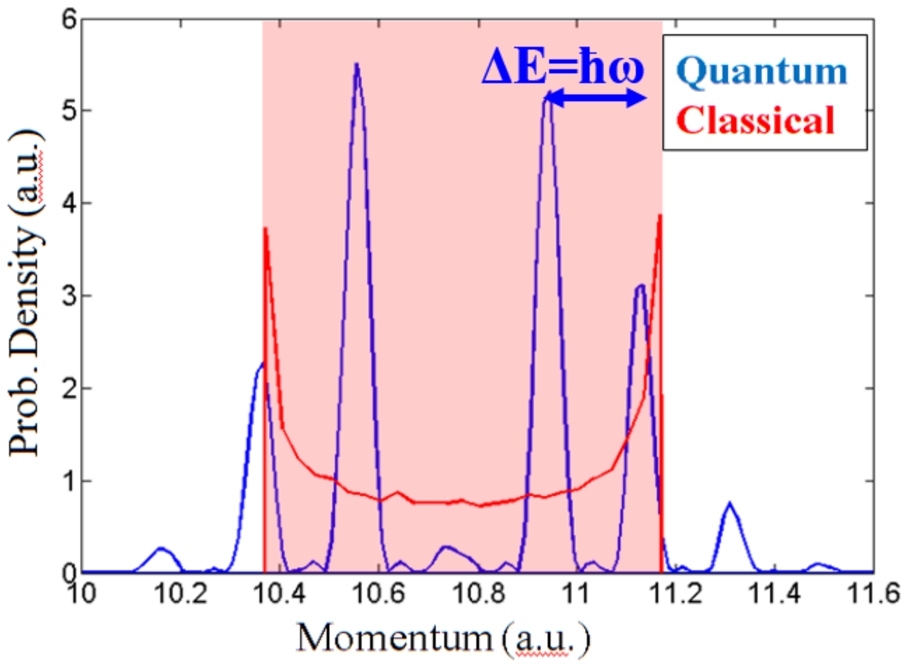

FIG. 2.2: Quantum and classical simulations for the final momentum distribution of atoms scattered (fully transmitted) by an oscillating barrier. The atoms have an incident momentum $p_0 = 10.75$, while the barrier parameters are height $U_0 = 6.61$, dither index $\alpha = 1$, phase $\phi = 0$, width $\sigma_b = 10$, and oscillation frequency $\omega = 2.06$. These parameters were chosen to suppress the scattered carrier momentum. The classical calculation was conducted by M. Ivory.

2.3.3 Generating a Scattered Momentum Spread

In between these two limiting cases, i.e. for multiple barrier oscillations during the atom-barrier interaction time, then the arrival phase of the atom determines the final momentum of the atom. In this case, the final momentum distribution acquires a significant spread, as is illustrated by the red curve in Figure 2.2. This thesis focuses on this "in between" case, in which the classical and quantum predictions for the final momentum distribution can differ significantly. While the final scattered momentum spread is continuous, it typically has hard edges at its upper and lower bounds. we use these edges to define the classically allowed scattered momentum range.

2.3.4 Incident Distribution

When simulating the scattering process to generate plots such as the red momentum distribution in figure 2.2, the incident atoms are chosen to have a specific momentum (i.e. mono-energetic). However, we use one of the following 1D distributions centered on x_0 with width β for the initial atomic positions:

Gaussian (β = standard deviation)

$$P_G(x) = \frac{1}{\sqrt{2\pi}\sigma} e^{-(x-x_0)^2/2\beta^2} \tag{2.5}$$

Thomas-Fermi (β = radius of distribution edge)

$$P_{TF}(x) = \begin{cases} \beta^2 - (x-x_0)^2 \quad for \mid x - x_0 \mid \leq \beta \\ 0 \quad for \mid x - x_0 \mid > \beta \end{cases} \tag{2.6}$$

However, we generally find that the choice of initial position distribution has little effect on the final momentum distribution, since we typically work with situations where β is sufficiently large so that the atoms experience many barrier oscillations. The most significant difference between initial distribution type are the subtle oscillations between Floquet peaks (as can be seen when looking closely at the blue curve in figure 2.2) that are more pronounced with a Thomas-Fermi distribution. This difference is of little consequence to the overall result.

2.4 Quantum Description

We implement a quantum mechanical description of barrier scattering in 1D with the following approach. An atom is described by a wavefunction $\Psi(x,t)$, which we then use to compute the time evolution due to the atom-barrier interaction. In the absence of atom-atom interactions, the 1D Schrödinger equation gives the evolution in time and space for the wavefunction $\Psi(x,t)$ of an atom:

$$i\hbar\frac{\partial}{\partial t}\Psi(x,t) = (-\frac{\hbar^2}{2m}\frac{\partial^2}{\partial x^2} + U(x,t))\Psi(x,t) \tag{2.7}$$

where $U(x,t)$ is the barrier potential given in equation 2.1 and m is the mass of the atom. Atoms incident on the barrier are waves rather than particles. We convert the classical distribution of atomic positions $P_G(x)$ and $P_{TF}(x)$, i.e. eq. 2.5 and 2.6, into an incident wavefunction $\Psi(x)$ by taking the square root of the of the classical distribution $P_{G,TF}(x)$ and multiplying it by the planewave wavefunction $exp(ip_0x/\hbar)$ with initial momentum p_0:

$$\Psi_{G,TF}(x) = \sqrt{P_{G,TF}(x)}e^{ip_0x/\hbar} \tag{2.8}$$

This incident wavefunction is centered on $x = x_0$ and must be propagated with the Schrödinger equation (eq. 2.7) to compute its travel to the barrier, its interaction with the barrier, and then its evolution away from the barrier. As with the classical simulations, the specific incident wavefunction (Ψ_G or Ψ_{TF}) does not significantly affect the scattered momentum distribution, so long as an atom experiences many barrier oscillations during the scattering process. However, it is more appropriate to use Ψ_{TF} to model a quasi-pure BEC and Ψ_G for a thermal ensemble of atoms.

2.4.1 Numerical Propagation Method

Propagation in time of the $\Psi(x,t)$ wavefunction is done numerically using a split-step operator method [44][45] implemented in a FORTRAN program originally developed by the group of Prof. K. Das at Kutztown University. The program incorporates the time variation of the barrier and uses a fast Fourier transform (FFT) to compute the momentum space wavefunction $\Psi(p,t)$ at a given time. The FFT requires a periodic boundary condition in space, so the spatial range R over which $\Psi(x,t)$ is computed must be chosen sufficiently large to avoid significant wraparound of the wavefunction over the course of the full time evolution. In momentum space, the momentum grid density must be sufficiently fine to resolve the narrow momentum features that are typically encountered. Table 2.1 shows the real space and momentum space grid parameters ranges that typically are used in our simulations.

Dimensionless units: The quantum simulations are typically done with dimensionless units, such that $\hbar = 1$ and $m = 1$. This choice is equivalent to picking a scale factor, ℓ_0, based on the ratio of the experimental width of the barrier (σ_b) to the width of the barrier (σ_b') used in simulations. Similarly, we define a useful time/frequency scaling based on ℓ_0:

$$\omega_0 = \frac{\hbar}{m\ell_0^2} \tag{2.9}$$

Parameter	Range
Number of points N	2^{15}-2^{19}
Spatial range R_x	8000-16000
Spatial step size Δx	0.01-0.1
Momentum range R_p	100-400
Momentum step size Δp	$10^{-5} - 10^{-3}$
Time step Δt	0.01-0.1

TABLE 2.1: Quantum split-step operator method parameters. All parameter are in dimensionless units. The real space and momentum space parameters are inversely related, such that $\Delta p = 2\pi/R_x$ and $R_p = 2\pi/\Delta x$. The FORTRAN package 'dfftpack' require that input array sizes be powers of 2.

This leads to the following unit conversions for distance, time, frequency, velocity, momentum, and energy:[2]

$$x = \ell_0 x' \tag{2.10}$$

$$t = \frac{1}{\omega_0} t' \tag{2.11}$$

$$\omega = \omega_0 \omega' \tag{2.12}$$

$$v = \sqrt{\frac{\hbar\omega_0}{m}} v' \tag{2.13}$$

$$p = \sqrt{m\hbar\omega_0} p' \tag{2.14}$$

$$U = \hbar\omega_0 U' \tag{2.15}$$

Once appropriate parameters are found, and the experimental barrier width is known, the theoretical parameters can be converted to real units using these relations. This converts the theoretical parameters from units in which $\hbar = 1$ and $m = 1$, to those in which $\hbar = 6.626 \times 10^{-34}$ J·s and $m = 87 \times 1.67 \times 10^{-27}$ kg for ^{87}Rb.

Benchmarking the quantum simulations: The quantum simulation results have

[2] Quantities in theory units are indicated by an apostrophe.

been tested against semi-classical calculations by Prof. J. B. Delos, Dr. T. Byrd, and Prof. K. A. Mitchell, and reasonably good agreement was found between the two methods [42].

2.4.2 Quantum vs. Classical: Sidebands

The quantum prediction for the scattered momentum distribution differs significantly from the classical one, as shown by the blue curve in Figure 2.2. The most outstanding feature of the quantum prediction is the discrete nature of the final momentum spectrum, which consist of a series of regularly-spaced narrow peaks, separated by significant gaps. In momentum space these peaks are almost evenly spaced, but in energy space their separation is exactly even: the kinetic energy difference between neighboring peaks is given by $\Delta E = \hbar\omega$. We refer to these peaks as sidebands in analogy to the sidebands generated by frequency modulation (FM) of a carrier wave. The atomic wavefunction is essentially a deBroglie matter-wave, whose energy (potential and kinetic), and hence frequency, is periodically modulated at frequency ω by the oscillating barrier potential. The same physics is present when FM modulating a radio frequency carrier signal for radio broadcast transmission (see also the discussion in Chapter 1 or using an electro-optic modulator to add sidebands to a laser). Formally, the peaks are called Floquet peaks or modes, since they are a result of the Floquet theorem for driven quantum systems [4], which is similar to the Bloch theorem for quantum systems featuring a spatially periodic potential. The momentum space wavefunction associated with each peak is called a Floquet state. While the quantum and classical scattered momentum distributions differ significantly, they still overlap considerably. Notably, the bounds of the classical distribution still largely dictate the range of the quantum distribution, as illustrated in Figure 2.2. However, the quantum momentum distribution typically spreads somewhat beyond the classically allowed bounds due to momentum-space "diffraction".

2.4.3 Semi-Classical Picture: Sidebands as Multi-Path Interference

Semi-classical calculations [42] show that the Floquet peaks can be interpreted as the result of constructive interference between atom planewave trajectories with different initial positions. Figure 2.3 shows the classical mechanics calculation for the periodic relationship between the final momentum p_f of an atom based on its initial position x_i for a specific set of parameters (initial momentum $p_0 = 1.8$, barrier dither $\alpha = 0.5$, height $U_0 = 1$, width $\sigma = 10$, and frequency $\omega = 0.1$). The black vertical line shows that several initial positions x_i (open circles) result in the same final momentum p_f: since there are multiple paths to a same final momentum, then quantum mechanically these paths will interfere. Constructive interference produces the Floquet peaks, while destructive interference yields the gaps between the peaks. The semi-classical approach in [42] provides one additional insight into this interference. Figure 2.3 shows that the final momentum p_f is periodic in the initial position x_i: the grey and white bands shows boundaries for the periods. Notably, there are two x_i within a period that result in same p_f (for different parameters there can be more than two, but generally the number must be even, with some exceptions). The semi-classical calculation [42] shows that inter-period interference determines the final momenta of the Floquet peaks (i.e. that they are separated by $\Delta E = \hbar\omega$), while intracycle interference determines the amplitude (or "height") of the peaks.

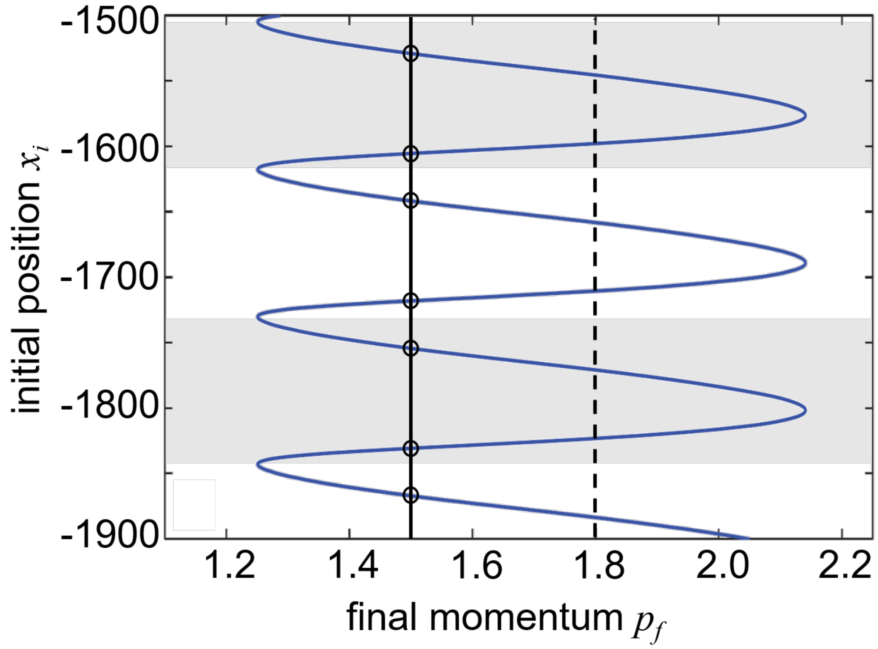

FIG. 2.3: This figure shows the relation between initial position and final momentum for $\alpha = 0.5$, $\omega = 0.1$ and $p_0 = 1.8$ (dashed vertical line). Each point on the curve intersecting the dashed line shows that multiple initial positions can lead to the same final momentum. That is, at a chosen p_f (solid line), paths arrive after beginning at different x_0 (circled points). The interference between the different paths determine peak locations (intercycle) and heights (intracycle). This figure is adapated from [42].

2.4.4 Atom-Atom Interactions

Thus far the description of the atom-barrier scattering process has only involved single particle physics (i.e. equations 2.3, 2.4, and 2.7). Any experimental implementation using many atoms in a same quantum state, i.e. a Bose-Einstein condensate (BEC, see Chapter 3 for a formal theoretical introduction to BEC), must also consider the role of atom-atom interactions. In the context of a BEC, the interactions can be treated using mean-field theory: the interaction of a single atom with all the other atoms in the BEC can be modeled as a pseudo-potential that is proportional to the atomic density $\mid \Psi(x,t) \mid^2$; a proportionality factor g describes the strength of the atom-atom interactions. When this nonlinear pseudo-potential term is included in the Schrödinger equation, it becomes the "nonlinear Schrödinger equation" or Gross-Pitaevskii equation (eq. 2.16).

$$i\hbar\frac{\partial\Psi(\mathbf{r},t)}{\partial t} = \left(-\frac{\hbar^2}{2m}\nabla^2 + U(\mathbf{r},t) + g|\Psi(\mathbf{r},t)|^2\right)\Psi(\mathbf{r},t) \tag{2.16}$$

We note that in this formalism, $\Psi(x,t)$ is a many-body wavefunction for the BEC and has a different normalization definition: $\int \mid \Psi(x,t) \mid^2 dx = N_{BEC}$, where N_{BEC} is the number of atoms in the BEC. The non-linear interaction term is straightforward to include in the split-step operator quantum simulations in order to compute the time-evolution with the 1D Gross-Pitaevskii equation [46]. Simulations of the atom-barrier scattering process in Figure 2.4 show that as the interaction strength g is increased, the Floquet peaks decrease in amplitude and broaden. For sufficiently strong interactions, e.g. $g = 20$ in Fig. 2.4, the peaks are sufficiently broadened and depressed and acquire significant substructure (i.e. ripples) as well, so that the sidebands become somewhat washed out. In the context of an experiment, these simulations suggest that atom-atom interactions can be detrimental to the observation of Floquet sidebands.

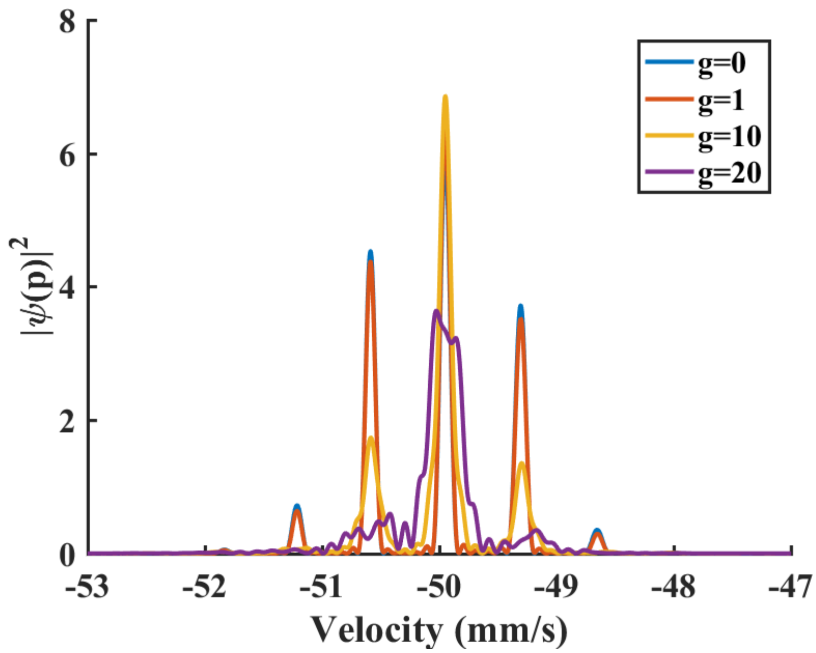

FIG. 2.4: Final momentum distributions with different atom-atom interaction strengths. The negative final velocity indicates a reflection from the barrier. The atoms have an incident momentum $p_0 = 32$, while the barrier parameters are height $U_0 = 1444.1$, dither index $\alpha = 1$, phase $\phi = 0$, width $\sigma_b = 10$, and oscillation frequency $\omega = 13.1$.

However, 1D simulations of the Gross-Pitaevskii equation (eq. 2.16) may be insufficient for accurately describing the effects of interactions during the atom-barrier scattering process. Indeed, interactions can couple motion in different dimensions (i.e. imagine a water balloon bouncing off a wall: at the point of impact the balloon will "pancake" and expand significantly along the axes perpendicular to its motion), so 3D simulations of eq. 2.16 may yield different behavior than the 1D case shown in Figure 2.4. However, 3D quantum simulations of eq. 2.16 are beyond the scope of this thesis.

2.5 Experimental Implementation

Now that we have presented the theoretical predictions regarding the final momentum distribution for atoms scattered by an oscillating barrier, notably the appearance of Floquet sidebands, we discuss how to implement an experiment to observe these predictions. This is a discussion that covers the broad considerations, and not the crux of all the details (such as at the beginning of Chapter 6). The basic objectives of such an experiment are the following:

1. Determine/measure the final momentum distribution.
2. Observe a final momentum distribution with Floquet sidebands.

This first objective requires an experimental setup that can measure a momentum distribution (i.e. velocity distribution). The second objective requires an experimental setup that has the resolution to observe distinct sidebands. This second objective also requires a setup that can access the range of atom-barrier scattering parameters that yields widely separated, distinct sidebands. Figure 2.5 shows a sketch of the basic experimental scheme. The following paragraphs discuss the basic ingredients for implementing the experiment.

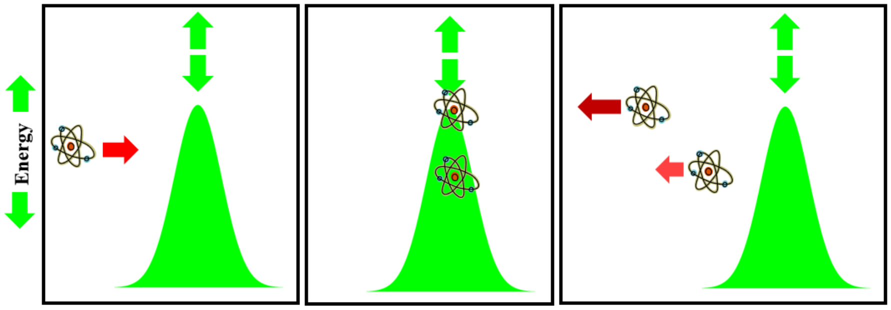

FIG. 2.5: Diagram of atoms reflecting after interacting with an oscillating barrier. Atoms are incident on the oscillating barrier (left). The energy of the atoms is shifted by the barrier (middle). The atoms reflect off of the barrier, moving at a new velocity (right).

2.5.1 BEC: The Atomic Wavepacket

The first ingredient required for an experiment is a mono-energetic planewave of atoms, which will mimic the wavefunctions in section 2.4 (eq. 2.8). A BEC with a velocity kick is the ideal choice, since all the atoms are in the same state with a Thomas-Fermi wavefunction. When a BEC is released from a cigar-shaped trap, it expands relatively quickly along its transverse radial axes due to the release of its stored mean-field energy (from interactions). However, the BEC hardly expands along its axial axis: the momentum spread is close to negligible, so along this axis the BEC is essentially mono-energetic (even after a properly implemented velocity kick along this axis). We note that under the right circumstances, the axial expansion rate can be quite small, i.e. on the same order as the Heisenberg limited expansion rate given by $\Delta x \Delta p_x = \hbar/2$ (see Chapter 3 for more details). Indeed, the quantum simulations in section 2.4 will automatically generate such a Heisenberg-driven expansion, though it is relatively weak for a spatially large (i.e. $\Delta x \sim \beta$ is big or $\Delta x \sim \sigma$ is big) initial wavefunction $\Psi(x, t = 0)$. Using the axial axis of a BEC ensures that the Floquet sidebands will be as narrow as possible (in momentum space). In principle, a sufficiently cold thermal cloud could have a comparably narrow momentum spread, but in practice one then obtains a BEC if the atom number is high enough. The theory of BECs is discussed Chapter 3, while its experimental production is detailed in Chapter 4. As the axial axis of the BEC is horizontal in our apparatus, the BEC must be levitated in order to be observed for long expansion times: the levitation hardware is described in Chapter 5. The horizontal velocity kick imparted to the atoms is described in Chapter 6.

Interactions: As explained with figure 2.4 in section 2.4, atom-atom interactions tend to suppress or even washout the sidebands that we are interested in observing. By using an untrapped BEC in free-flight, interactions should be strongly suppressed. Indeed, the mean-field interaction energy has already been converted to transverse expansion kinetic energy, leaving very little interaction energy remaining. In dimensionless units, we estimate that the interaction strength for our free-flight BEC is on the order of $g_{1D} \simeq 1$, though some uncertainty remains since we are mapping the 3D nonlinear Schrödinger equation onto a 1D version.

Comparison with a prior experiment: An earlier experiment led by Dr. M. Ivory in 2013, as a graduate student in the Aubin group, did not observe sidebands using a different detection technique. We assess that this experiment did not observe sidebands due to significant atom-atom interactions, since the experiment was conducted in an elongated cigar-shaped trap (see section 3.5 on Kohn's theorem for a further assessment of this initial experiment).

2.5.2 Oscillating Barrier

A tightly focused laser beam, blue-detuned and far off-resonance for the BEC atoms, can serve as an optical dipole potential energy barrier. By varying the intensity (or power) of the barrier beam, the barrier amplitude can be modulated sinusoidally as required. The implementation of the barrier is described in Chapter 6.

2.5.3 Measuring the Momentum Distribution: Time-of-Flight Imaging

After scattering off the barrier, the atoms will travel ballistically according to their scattered momentum. Consequently, after a sufficiently long flight time, the final momentum distribution of the atoms will be mapped onto the atomic position distribution, which can then be imaged directly (with absorption imaging). This time-of-flight imaging of the momentum distribution is presented in Chapter 6.

2.6 Differential Velocity

In order to resolve the Floquet sidebands, they must separate faster than the expansion rate of the BEC along the longitudinal (horizontal) direction. In other words, the atom-barrier scattering parameters (i.e. the experiment parameters) should be designed to maximize the differential velocity between neighboring sidebands. The differential velocity between sidebands is the difference between Floquet peaks of the final quantum momentum distribution after interaction with an oscillating barrier in units of velocity. The kinetic energy of the atoms in a given sideband is shifted by an integer number n of energy quanta, proportional to the oscillation frequency of frequency of the barrier:

$$E_n = E_0 + n\hbar\omega \tag{2.17}$$

The velocity of the nth sideband can then be determined from the kinetic energy:

$$v_n = \sqrt{v_0^2 + 2n\frac{\hbar\omega}{m}} \tag{2.18}$$

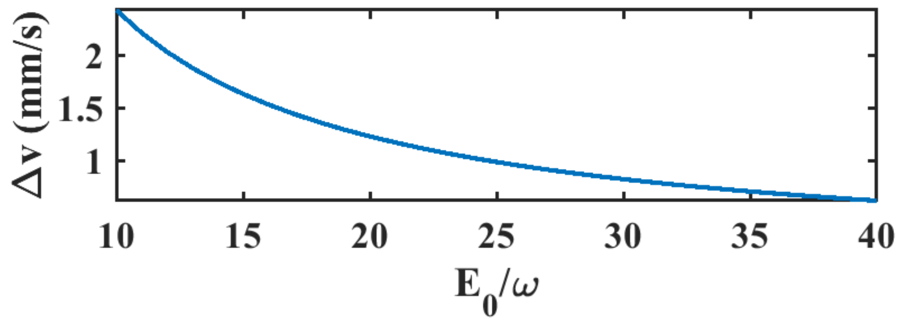

FIG. 2.6: Differential velocity (Δv_0) vs. initial kinetic energy ($E_0 = \frac{1}{2}mv_0^2$) in terms of barrier drive frequency (Δv_0 vs. $E_0/\hbar\omega$). This is calculated based on a modified version of equation 2.19: $\Delta v = (\sqrt{1+1/x} - 1)v_0$, where $x = \frac{E_0}{\hbar\omega}$. For this plot, $v_0 = 4.98$ cm/s, which is a velocity used in the experiment. Section 2.7 explains the selection of an initial velocity.

Therefore, it is simple to calculate the differential velocity between neighboring sidebands.

$$\Delta v_n = v_{n+1} - v_n \tag{2.19}$$

We want to maximize this differential velocity Δv (or at least make it large) so as to separate the sidebands in real space as quickly as possible. Conveniently, equation 2.19 gives us the ability to calculate the differential velocity between sidebands without needing simulation results or varying other Hamiltonian parameters (e.g. barrier energy, oscillation amplitude, and barrier width). Instead, the differential velocity only depends on the initial velocity and the oscillation frequency (Fig. 2.6). A larger differential velocity is obviously desirable for spatially resolving discrete sidebands. Therefore, decreasing the initial velocity or the oscillation frequency appears effective in increasing the differential velocity between sidebands. However, the relative populations of the Floquet states cannot be analytically predicted. So the parameters can be adjusted to increase differential velocity, but those parameters do not necessarily yield any sidebands. This situation is expected. While increasing the oscillation frequency should move sidebands further apart, the atoms will feel the time-averaged potential once the barrier is oscillating sufficiently fast. This result reflects that of the static barrier case. This effect motivates the search for parameters that generate a few, and not too many, sidebands with a large differential velocity to promote neighboring sidebands with significant spatial separations.

2.7 Sideband Generation

A method is required to acquire suitable parameters for spatially resolving discrete atomic sidebands. It is useful to know how many sidebands are generated for a given set of parameters. There are five total parameters that are capable of affecting sidebands: initial velocity v_0, oscillation frequency ω, barrier energy U_0, barrier width σ_b, and oscillation dither amplitude α. This problem can be simplified to reduce the number of parameters we are forced to consider. Oscillation dither amplitude, α, is defined between zero and one. Intuitively, increasing the oscillation amplitude should drive additional sideband generation (this is supported by simulations). Therefore it is best to set this parameter equal to one, and exclude it from a combinatorial analysis. The other parameter that can be excluded is barrier width, σ_b. A spatially localized potential promotes sideband generation over a de-localized one (this assertion is supported by simulations). It was easier to set up and measure the tightly focused beam waist of the laser providing the barrier beam, and then fix the width at the measured value for simulations. Furthermore, if the approach is to determine how large the differential velocity can be increased by solely increasing frequency, this is counterproductive as the sideband population will not be sustained. The quantum simulations are conducted with $m = \hbar = 1$ and the unit conversion between theory and experiment parameters is based on the ratio of barrier widths (see eq. 2.10). The resulting differential velocity in real units is proportional to both barrier width and frequency in theoretical units. So, increasing simulated frequency to increase differential velocity while simultaneously decreasing barrier width to promote sideband production at that frequency is counterproductive and potentially a zero-sum game. The remaining parameter to be varied in a combinatorial analysis is the barrier energy, giving a total of three parameters that should be examined.

Many sets of parameters were simulated.[3] For reasons of convenience and simplicity the resulting number of Floquet peaks[4] were plotted in a surface plot with axes for barrier energy and initial kinetic energy,[5] both in terms of $\hbar\omega$. The parameter that was held constant for a single surface plot was initial kinetic energy E_0 while both frequency ω and barrier energy U_0 were varied. When the initial kinetic energy is changed and another plot is produced, the entire "island" of peaks shifts towards lower differential velocity with lower kinetic energy. Figure 2.7 shows a resulting plot, while figure 2.8 is recolored to target the parameters best suitable to spatially resolve discrete momentum sidebands. Therefore, increasing the initial velocity appears effective in generating sidebands. Unfortunately, increasing the initial velocity is counterproductive to increasing differential velocity (which was suggested in the previous section).

Reflection vs Transmission: We choose to operate the experiment in reflection mode, i.e. the atoms reflect off the barrier, because it was easier in terms of positioning the CCD camera, but also because it resulted in more pronounced sidebands with a larger differential velocity. This result is somewhat intuitive with respect to the FM radio analogy discussed in the previous chapter. Modulating the kinetic energy of the atoms by a greater amount, i.e. larger barrier energy U_0, promotes the generation and population of sidebands. The original version of this experiment was

[3]read: "brute force computation"

[4]I defined a peak to be at least 10% the height of the carrier. It is true that as the carrier population decreases, all other peaks become more prominent by comparison. However, the region in which this applies is not near our region of interest, and therefore ignored.

[5]At the time these parameter sets were simulated, I used the highest experimentally allowable velocity. This limit increased later with new equipment.

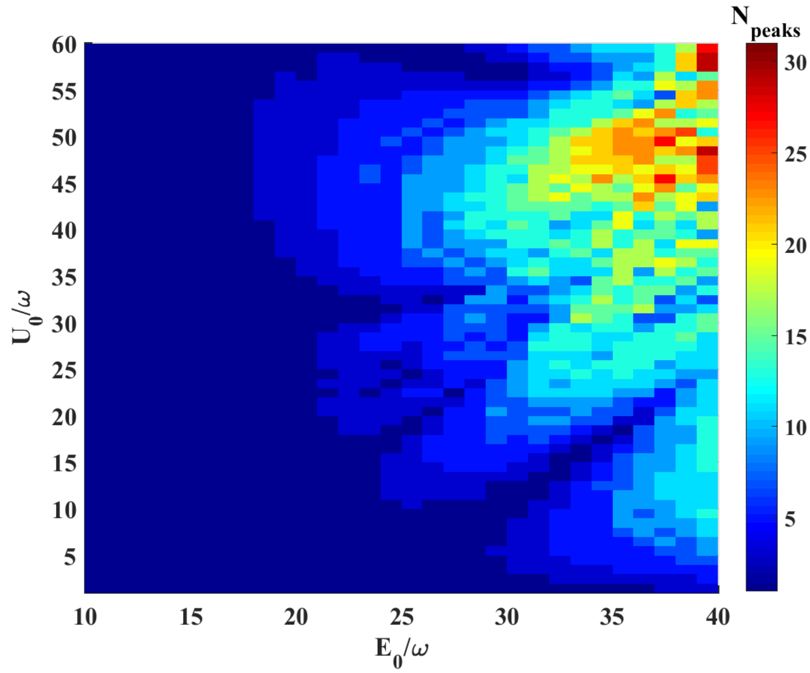

FIG. 2.7: Simulation results of number of Floquet peaks produced by an oscillating barrier as a function of barrier energy U_0 and initial kinetic energy E_0, both in terms of barrier drive frequency ω ($\hbar = 1$).

set up for transmission through the barrier to decrease the laser power required for the barrier and prevent scenarios in which both transmission and reflection occur.

Picking the ideal parameter set is accomplished by finding the parameters that produce 3-5 total Floquet peaks and the largest Δv. Figure 2.6 shows the largest Δv towards lower E_0/ω (to the left). This corresponds to the left-most or lowest E_0/ω that produce sidebands on figure 2.8 shaded in light blue. Table 2.2 shows the parameters selected based on this method.[6]

2.8 Experiment Design

The experiment operates by creating a BEC, releasing it from the atom trap, and immediately accelerating it horizontally with a push coil. A magnetic gradient

[6]Reaching full amplitude without distorting the sine curve and adding extra frequencies proved experimentally difficult. A more realistic value was $\alpha = 0.7$.

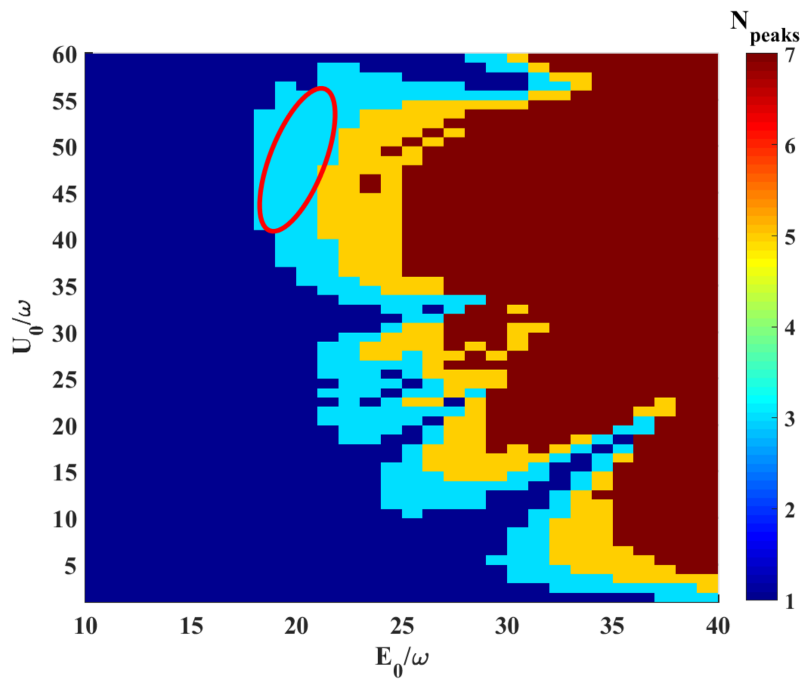

FIG. 2.8: Same plot as Fig. 2.7 but re-colored to highlight the area of interest for our experiment. The experiment is designed to target the light blue regions. The dark blue indicates the presence of one Floquet peak, the carrier, and no sidebands. The red oval shows the region of parameters to target to potentially observe sidebands.

Parameter	Theory Units	Real Units
$\hbar$	1	6.626 $\times 10^{-34}$ J s
m	1	1.45 $\times 10^{-25}$ kg
α	1	1
σ_b	10	1.93 μm
w_b	20	3.85 μm
v_0	13.2	5.0 cm/s
p_0	13.2	7.3 $\times 10^{-27}$ kg m/s
E_0	87.12	1.8 $\times 10^{-28}$ J, $\sim$ 26 μK
ω	4.17	$2\pi \times 13$ kHz
U_0	182.1	3.7 $\times 10^{-28}$ J, $\sim$ 54 μK

TABLE 2.2: Optimal scattering parameters. Theoretical parameters are in dimensionless units. The theoretical units cannot be converted to real, experimental units without a known barrier width σ_b. The conversion is based on the barrier width measured and discussed in Chapter 6.

is turned on to stabilize the vertical position as the BEC propagates towards the focus of the barrier beam. The BEC then interacts with the barrier beam. The horizontal push coil is pulsed again to stop the center-of-mass horizontal motion of the atoms. Then, we wait for the sideband packets to separate from the carrier.

The goal of this experiment was to generate and detect discrete momentum sidebands. Every aspect of the experiment was designed to help promote the production and resolution of sidebands. However, each decision we made had advantages and disadvantages. Our approach is to launch a BEC towards a single oscillating Gaussian barrier and attempt to detect the subsequent sidebands. There is more than one way of doing this.

Original "Discriminator" Method: For example, we initially proposed using a method affectionately called "The Discriminator." The BEC is given an initial momentum to scatter from an oscillating barrier resulting in a spread of final momenta. The BEC then encounters a second static barrier. Depending on the height of the second static barrier, the cloud can either transmit, reflect, or be partially transmitted and reflected. This second barrier will discriminate between sidebands with high and low kinetic energy. When implemented in the past, this method recycled the original barrier through clever use of our trapping potential. Because our atoms are trapped in a harmonic trap, they will interact with the oscillating barrier, reach the top of the harmonic bowl, and then reverse directions to interact with the barrier a second time. On the return trip, however, we choose a static barrier, which will either fully or partially reflect (and transmit) the particles depending on its height. This method is disadvantageous because the confinement of the trap causes an increase in density driven atom-atom interactions that distort the production of sidebands. Unfortunately, to release the atoms from the trap allows them to expand, giving the possibility that there would be no atom density signal due to lifetime issues. The lack of trap also removes the ability to redirect the atoms back towards the same barrier beam, and we do not yet have a second barrier in our toolbox. Therefore, we consider an alternative method.

Direct "Time-Of-Flight" Method: We instead examine the resultant peaks from a single oscillating barrier using a time-of-flight method. This is done by waiting some sufficiently long time to see the peaks manifest themselves in the position space wavefunction. The atoms are released from a relaxed atom chip trap to lower the interactions. A vertical magnetic gradient is applied to counteract the force of gravity and prevent the atoms from falling away from the barrier, out of the camera's field of view. Top and side views of the experimental setup with relevant dimensions are shown in figure 2.9.

In this chapter, I have introduced the theory specific to the quantum pumping experiment and how it influences the setup and design of the experiment. Next, chapter 3 introduces the ultracold atom theory responsible for how BECs behave with a narrow energy spectrum which is required to represent the plane wave for quantum pumping. Chapter 4 discusses the experimental apparatus used to gener-

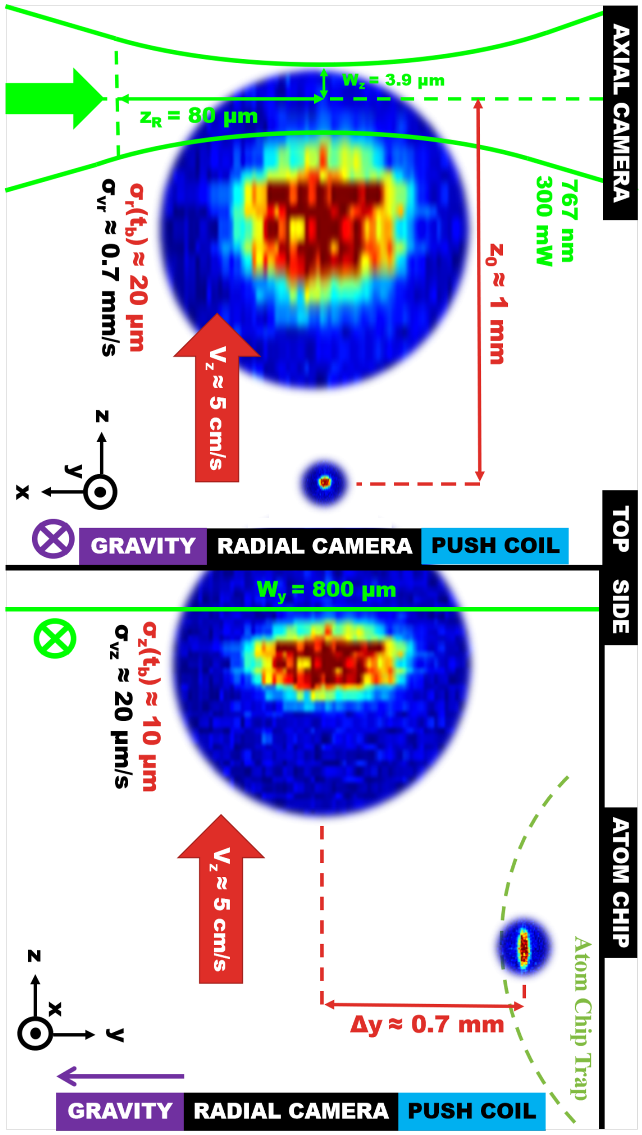

FIG. 2.9: Experiment schematic. Top: Top view of the experiment is shown in which the radial camera and push coil are not in the field of view, but to the right of the image. The axial camera is out of field of view, but above the top of the image. The atoms expand as they propagate approximately 1 mm toward the barrier (767 nm, 300 mW maximum, marked in green with direction of propagation and physical dimensions). Bottom: Side view of the experiment looking into the axial camera. Atoms are released from the chip trap and are pushed to the left towards the barrier (narrow sheet beam propagating into into the image and focused to the plane of the atoms) as they fall approximately 0.7 mm before stable levitation. Diagrams not to scale. Images of atoms used for instructional purposes only (the image is the same, only resized/rescaled to show relative expansion rates). Dimensions, expansion rates, and velocity of atoms listed for axial and radial directions.

ate a BEC. Chapter 5 covers the technical details and development of a device used for magnetically levitating atoms. Chapter 6 discusses the remainder of the experimental setup including the barrier beam and the how the BEC is given an initial velocity. The results are contained in chapter 7 and the outlook for this experiment in chapter 8.

CHAPTER 3

Bose-Einstein Condensate Theory

The purpose of this chapter is to discuss the theory behind the behavior of Bose-Einstein condensates (BEC). The theory is useful for describing the behavior of the BEC that serves as the atomic wavepacket for our experiment. A BEC is composed of bosons (integer spin particles, e.g. atoms) that are all in a single quantum state. A BEC is a distinct state of matter in which classical-like thermal atoms (i.e. relatively short wavelengths) undergo a sharp phase transition to macroscopic occupation of the quantum mechanical ground state (i.e. relatively long wavelength) as the temperature is reduced. A more quantitative explanation for this phenomena is that the BEC phase transition occurs when the de Broglie wavelength (i.e. the wavelength associated with matter exhibiting wave-like behavior, eq. 3.1) is now on a similar length scale as the interparticle distance. The thermal de Broglie wavelength $\Lambda_{dB}(T)$ is given by [47]

$$\Lambda_{dB}(T) = \sqrt{\frac{2\pi\hbar^2}{mk_BT}} \tag{3.1}$$

where $\hbar$ is Planck's constant, m is the mass of the particle (or atom), k_B is the Boltzmann constant, and T is temperature. The fact that Λ_{dB} increases for lower temperatures implies that the BEC transition can be accessed by reducing temperature while maintaining particle density.

BEC was first predicted by Albert Einstein in 1925 in his analysis of a gas of boson particles [48], based on the Bose statistics recently proposed in a paper by Satyendra Nath Bose on photon statistics (and which A. Einstein had translated from English to German for publication in *Zeitschrift für Physik* in 1924) [49]. However, the observation of BEC proved to be considerably more difficult than originally anticipated, due to atom-atom interactions that tend to condense a gas into a solid or liquid at very low temperatures. It was not until 1995, based on ground breaking work in hydrogen [50] and lithium [39], that the first BEC was reliably observed experimentally in the group of Eric Cornell and Carl Wieman at the University of Colorado at Boulder and NIST Boulder using a gas of ^{87}Rb atoms [19]. Not long afterwards, Wolfgang Ketterle's group at MIT conducted measurements characterizing important properties of BECs [38]. For this work, the three were awarded the Nobel Prize in Physics in 2001.

The experiment uses a BEC because of its narrow momentum distribution and phase coherence, i.e. all of the atoms have the same wavefunction. However, a trapped BEC also has significant atom-atom interactions, which manifest themselves as the BEC's internal potential energy, or mean field energy. These interactions and mean field energy are detrimental to the experiment as they tend to wash out the sidebands. Consequently, the experiment is designed to minimize interactions by reducing the BEC density via the conversion of mean field energy to kinetic expansion energy. However, this mean-field driven expansion necessarily increases the momentum distribution of the BEC, so it must be managed carefully in order minimize its impact on the experiment.

The rest of the chapter focuses on the interactions in a BEC with an eye towards minimizing these. Much of the theory presented in this chapter is adapted from chapter 5 of the text by Weidemüller and Zimmerman [47]. Section 3.1 discusses atoms confined in a harmonic trap without interactions. Section 3.2 presents the Gross-Pitaevskii equation that describes a BEC with interactions, and Section 3.3 then goes over the Thomas-Fermi approximation that helps simplify this equation. Section 3.4 reviews the anisotropic interaction-driven expansion of a BEC released from a trap, which is the mechanism that the experiment uses for suppressing interactions. The chapter concludes by going over Kohn's theorem (section 3.5) regarding BEC oscillations in a harmonic trap.

3.1 Harmonic Trap Without Interactions

Before taking on atom-atom interactions, we consider the case of an ideal gas confined by a harmonic trap. The harmonic potential is the most common type of conservative trap for a BEC and ultracold gases (and is used in this experiment) and is given by

$$V(\vec{r}) = \frac{m}{2}(\omega_x^2 x^2 + \omega_y^2 y^2 + \omega_z^2 z^2). \tag{3.2}$$

Where m is the mass of the atom, and $\omega_{x,y,z}$ are the trapping frequencies along the three principal axes of the trap. Atoms in the ground state of the trap have a characteristic size given by the *characteristic length* parameter a_{ho}:

$$a_{ho} = \sqrt{\frac{\hbar}{m\omega_{ho}}}. \tag{3.3}$$

Here, ω_{ho} is the geometric mean of the trapping frequencies: $\omega_{ho} = (\omega_x \omega_y \omega_z)^{1/3}$. In the case of a cylindrically symmetric cigar-shaped trap with radial trapping frequency ω_r, then this expression becomes $\omega_{ho} = (\omega_r^2 \omega_z)^{1/3}$.

The solution to the time-independent Schrödinger equation for the simple harmonic oscillator Hamiltonian $H = -\frac{\hbar^2}{2m}\nabla^2 + V(\vec{r})$ is the well-known harmonic oscillator energy eigenvalues $E_{n_x,n_y,n_z} = \Sigma_{i=x,y,z}(n_i + 1/2)\hbar\omega_i$ and the Gaussian ground state wavefunction

$$\psi(\vec{r}) = \left(\frac{m\omega_{ho}}{\pi\hbar}\right)^{\frac{3}{4}} \exp\left\{-\frac{m}{2\hbar}(\omega_x x^2 + \omega_y y^2 + \omega_z z^2)\right\}, \tag{3.4}$$

This wavefunction is only valid for the ideal gas case in which the atoms in the ensemble do not interact with one another. The size of the wavefunction along each axis can be found by rearranging equation 3.4 to find a Gaussian sigma, $\sigma_i = a_{ho,i} = \sqrt{\frac{\hbar}{m\omega_i}}$. We note that the physical radius or sigma of a cloud of non-interacting atoms in the ground state is given by $\sigma_{idealBEC} = \sigma_i/\sqrt{2}$ (after squaring the wavefunction). These expressions can be used to calculate the aspect ratio of the trap in terms of the trapping frequencies:

$$\frac{\sigma_i}{\sigma_j} = \frac{\sigma_{p_j}}{\sigma_{p_i}} = \sqrt{\frac{\omega_j}{\omega_i}}, \tag{3.5}$$

where σ_{p_i} is the Gaussian width in momentum space. The momentum space width comes from the fact that the harmonic oscillator ground state is a minimum uncertainty state.

When comparing this relation for the ideal gas BEC to the thermal cloud case, a Boltzmann distribution shows that inside the trap [47] the aspect ratio of the atomic cloud is given by

$$\frac{\sigma_i^{thermal}}{\sigma_j^{thermal}} = \frac{\omega_j}{\omega_i}. \tag{3.6}$$

In contrast with eq. 3.5, the momentum distribution of atoms in a thermal gas is isotropic, so that $\sigma_{p_i}^{thermal} = \sigma_{p_j}^{thermal}$ for $i \neq j$. Consequently, a thermal gas released from a trap expands isotropically.

Ballistic expansion of an ideal BEC vs. thermal gas: Consider a BEC composed of an ideal Bose gas held in an anisotropic harmonic trap. A time-of-flight expansion measurement will basically map the momentum distribution of an ensemble onto position space. This expansion is similar to a diverging laser beam in the sense that the beam will have a larger divergence angle for a smaller source. A BEC confined in a tight trap will have a small size, and expand more quickly than a BEC confined in a relaxed trap. The BEC wavefunction will have an elongated shape with an inverted aspect ratio with respect to the harmonic trap. Meanwhile, a comparable thermal cloud will expand isotropically, i.e. in a spherical fashion. The anisotropic demeanor of the BEC expansion is further accentuated in the interacting case as the interaction energy contributes to the kinetic expansion after trap release. This behavior is also a distinctive experimental litmus test for the verification of the presence of a BEC.

3.2 The Gross-Pitaevskii Equation

The purpose of this section is to present the concepts and equations for describing the wavefunction of a BEC composed of interacting atoms. This treatment is based on the Gross-Pitaevskii equation (GPE), which describes the low temperature[1] properties of a dilute BEC with an s-wave scattering length a_s (see below for details) that is much less than the mean atomic spacing. The GPE is the simplest approximation for describing a BEC wavefunction at ultracold temperatures. At temperatures close to $T = 0$, excited states are nearly unpopulated and may be ignored. In the mean-field approximation, the interaction of a BEC atom with all of the other BEC atoms is approximated as a potential energy term that is proportional to the atomic density.

[1] The GPE does not have temperature in it, so technically "low temperature" $\rightarrow$ "zero temperature".

In the s-wave collision limit (i.e. at ultra low temperatures), the interaction energy between two atoms is given by the contact interaction $H_{int} = g\delta(\vec{r} - \vec{r'})$, where $\vec{r}$ and $\vec{r'}$ are the locations of the interacting atoms. At the low temperatures that produce BECs, it is realistic to exclude the higher order interactions as they will not significantly influence the BEC behavior (otherwise the lifetime would be very short due to three-body collisions, likely making BEC production unfeasible). The effective interaction strength between two atoms at low temperatures is a constant:

$$g = \frac{4\pi\hbar^2 a_s}{m}. \tag{3.7}$$

Here, a_s is the s-wave scattering length which characterizes the effective size of an atom involved in an atom-atom collisions. The sign of a_s determines attractive (negative) or repulsive (positive) nature of the interaction. In the case of ^{87}Rb, the interaction is repulsive, and a_s is approximately $100a_0$, where a_0 is the Bohr radius.

To characterize the states of interacting atoms, we use a mean-field treatment(this section largely follows the treatment of Pethick and Smith [51]), and assume that the wavefunction is a symmetrized (as is the case for bosons upon particle interchange) product of single-atom wavefunctions for N atoms. For a pure BEC, all atoms (bosons for ^{87}Rb) are in the ground state, $\phi(\vec{r})$. We therefore write the multi-atom wavefunction for N atoms as

$$\Psi(\vec{r_1}, \vec{r_2}, ..., \vec{r_N}) = \prod_{i=1}^{N} \phi(\vec{r_i}), \tag{3.8}$$

where each single atom wavefunction $\phi(\vec{r_i})$ follows the standard normalization $\int |\phi|^2 d^3r = 1$. We note that in the absence of interactions, $\phi(\vec{r})$ is given by the wavefunction in equation 3.4. Including the contact interaction H_{int} for each atom-atom pair, the multi-atom Hamiltonian can be written as

$$H = H_0 + H_{int} = \sum_{i=1}^{N} \left[\frac{\vec{p_i}^2}{2m} + V(\vec{r_i}) \right] + g \sum_{i<j} \delta(\vec{r_i} - \vec{r_j}) \tag{3.9}$$

where $V(\vec{r_i})$ is the external potential experienced by each atom, and the "$i < j$" prevents an atom from interacting with itself and eliminates double counting.

The energy of the many atom BEC system can be calculated with the relation $E = \langle \Psi | H | \Psi \rangle$. The kinetic energy and external potential energy (first and second terms) are straightforward to compute, but the interaction term (third term) is more involved. The integral in the interaction term can be rewritten in the following manner:

$$\langle \Psi | \delta(\vec{r_i} - \vec{r_j}) | \Psi \rangle = \int \int \phi^*(\vec{r_i}) \phi^*(\vec{r_j}) \delta(\vec{r_i} - \vec{r_j}) \phi(\vec{r_i}) \phi(\vec{r_j}) d^3 r_i d^3 r_j \tag{3.10}$$

$$= \int \phi^*(\vec{r_i}) \phi^*(\vec{r_i}) \phi(\vec{r_i}) \phi(\vec{r_i}) d^3 r_i \tag{3.11}$$

$$= \int |\phi(\vec{r_i})|^4 d^3 r_i \tag{3.12}$$

$$= \int |\phi(\vec{r})|^4 d^3 r \tag{3.13}$$

The energy of the BEC can thus be written as

$$E = N \int d\vec{r} \left[\frac{\hbar^2}{2m} |\nabla \phi(\vec{r})|^2 + V(\vec{r}) |\phi(\vec{r})|^2 + \frac{(N-1)}{2} g |\phi(\vec{r})|^4 \right]. \tag{3.14}$$

The N out front is from the sum over all of the identical atoms. The $(N-1)/2$ coefficient on the interaction term is due to the sum over the different atomic pairs.

For the true wavefunction, there are some atoms that will be in other states due to effects at small interatomic distances, and therefore the total number of atoms in the ground state will be less than N. The depletion of the BEC, or the relative reduction of the number of atoms in the ground state, is of order $(na^3)^{1/2}$, where n

is the density [51]. We ignore this "quantum depletion" effect in the remainder of this chapter.

We now define the BEC wavefunction[2] $\psi(\vec{r})$ in terms of the single atom wavefunction $\phi(\vec{r})$ as [51]

$$\psi(\vec{r}) = N^{1/2}\phi(\vec{r}). \tag{3.15}$$

Conveniently, the atomic density $n(\vec{r})$ is related to the BEC wavefunction via the relation

$$n(\vec{r}) = |\psi(\vec{r})|^2. \tag{3.16}$$

We can readily incorporate the BEC wavefunction $\psi(\vec{r})$ into the equation for the energy (eq. 3.14), if we make the approximation that $N-1 \simeq N$ in the limit of a large number of atoms. This new expression for the energy is also an energy functional since it depends on $\psi(\vec{r})$:

$$E(\psi) = \int d\vec{r}\left[\frac{\hbar^2}{2m}|\nabla\psi(\vec{r})|^2 + V(\vec{r})|\psi(\vec{r})|^2 + \frac{1}{2}g|\psi(\vec{r})|^4\right]. \tag{3.17}$$

We note that the BEC wavefunction $\psi(\vec{r})$ is normalized to the number of atoms N:

$$N = \int d\vec{r} n(\vec{r}) = \int d\vec{r}|\psi|^2. \tag{3.18}$$

The eigenstates of the many atoms BEC system (and in particular the ground state) are determined from the variational principle using variational calculus (i.e. Ritz theorem). A given $\psi(\vec{r})$ is an eigenstate of the system when $E(\psi)$ is at an extremum: we must find $\psi(\vec{r})$ such that $\delta E/\delta\psi = 0$. However, this extremum problem is also subject to the normalization condition in eq. 3.18, so we write the variational

[2] $\Psi \to \psi$

condition with a Lagrange multiplier μ [51]:

$$\frac{\delta}{\delta\psi}(E(\psi) - \mu N(\psi)) = 0 \tag{3.19}$$

It is understood that the variation $\delta\psi$ represents a variation with respect to both ψ and ψ^*, which are treated as independent here. We note also that μ will later take on the role of chemical potential, i.e. mean-field energy.

Application of the variational calculus of equation 3.19 to the energy functional in equation 3.17 results in (after several steps)

$$-\frac{\hbar^2}{2m}\nabla^2\psi(\vec{r}) + V(\vec{r})\psi(\vec{r}) + g|\psi(\vec{r})|^2\psi(\vec{r}) = \mu\psi(\vec{r}), \tag{3.20}$$

which is the time-independent GPE. Setting $g = 0$, one recovers the Schrödinger equation. The potential influencing the atomic dynamics is the sum of the external trapping potential, V and the non-linear term $g|\psi(\vec{r})|^2$ that is density dependent based on the mean field of the atoms. The interaction term generates a potential for the atoms that reflects their spatial distribution. Solving this equation typically involves elaborate numerical simulations, but physical insights can be learned by approximations for different parameters. The eigenvalue is μ, the chemical potential, not the energy per atom given by the Schrödinger equation for the non-interacting case. The time-dependent version of the GPE is similar to the time-dependent Schrödinger equation:

$$i\hbar\frac{\partial}{\partial t}\psi(\vec{r},t) = \left(-\frac{\hbar^2}{2m}\nabla^2 + V(\vec{r}) + g|\psi(\vec{r},t)|^2\right)\psi(\vec{r},t) \tag{3.21}$$

Finally, in the context of ballistic expansion of a BEC released from a trap, it can be helpful to examine the constituents of the energy functional. The total energy of the BEC can be written in terms of the density [47] as

$$E(n) = \int d\vec{r}\left[\frac{\hbar^2}{2m}|\nabla\sqrt{n}|^2 + nV(\vec{r}) + \frac{gn^2}{2}\right] = E_{kin} + E_{ho} + E_{int} \tag{3.22}$$

with these energy contributions: E_{kin} is the kinetic energy, E_{ho} is the potential energy provided by the external trapping potential, and E_{int} is the mean-field interaction potential energy of the atoms. If the trapping potential is switched off nonadiabatically as in a time-of-flight measurement, the term E_{ho} will disappear and the the expansion energy of the BEC will be dominated by $E_{kin} + E_{int}$. In fact, the next section will show that in the Thomas-Fermi approximation, the primary contribution to the expansion energy is E_{int}.

3.3 The Thomas-Fermi Approximation

For sufficiently large atom numbers, accurate expressions for the ground state energy E and wavefunction $\psi(\vec{r})$ of the BEC can be derived by using the Thomas-Fermi (TF) approximation, which consists of neglecting the kinetic energy term in the GPE (3.20). For high atom numbers, repulsive interactions, and a harmonic trap, the BEC wavefunction is basically controlled by the interaction energy ($\frac{E_{int}}{E_{kin}} \gg 1$). Without the kinetic energy term, the time independent GPE (eq. 3.20) becomes considerably simpler:

$$[V(\vec{r}) + g|\psi(\vec{r})|^2]\psi(\vec{r}) = \mu\psi(\vec{r}) \tag{3.23}$$

where μ is the chemical potential. The solution for the condensate density is thus given by

$$n(\vec{r}) = |\psi(\vec{r})|^2 = \begin{cases} \frac{\mu - V(\vec{r})}{g} & \mu - V(\vec{r}) > 0 \\ 0 & otherwise. \end{cases} \tag{3.24}$$

The above equation gives the solution only where the right hand side is positive, and $\psi = 0$ outside that region. This wavefunction is effectively the same as the distribution in equation 2.6. The balance of interaction and potential energies gives a flat effective potential for the atoms. The boundary of the cloud is therefore given by $V(\vec{r}) = \mu$. The physical implication of the TF approximation is that the energy to add a single atom to any location within the cloud does not vary over the length of the cloud, and therefore is same over the entire BEC. The energy to add a single atom is found through the sum of the external potential $V(\vec{r})$ and the interaction contribution $gn(\vec{r})$: This energy is the chemical potential μ.

It is important to understand that the GPE only describes the physics for $T \to 0$, i.e. only the condensate fraction. The physics of any thermal cloud surrounding the BEC is not described by the GPE. Generally, interactions between thermal atoms are small compared to those within the BEC. Furthermore, interactions between the condensate and thermal atoms can generally be neglected. Therefore, this theory only describes atoms that have cooled to BEC. The condensate dynamics within a trap are dominated by interactions as the kinetic energy is comparatively small and negligible in contrast to the interaction energy.

If we apply the TF approximation to a BEC confined in a harmonic trap, then the radii of the condensate along the principal axes are given by

$$R_i^2 = \frac{2\mu}{m\omega_i^2}, \quad i = x, y, z \tag{3.25}$$

The cloud radii, R_i, may be evaluated in terms of experimentally accessible parameters if the chemical potential is known. The normalization condition for ψ allows one to solve for the chemical potential, μ, as a function of the atom number N [51]:

$$N = \int d\vec{r} n(\vec{r}) = \frac{8\pi}{15} \left(\frac{2\mu}{m\omega_{ho}^2} \right)^{3/2} \frac{\mu}{g} \tag{3.26}$$

Manipulating equation 3.26 to solve for μ yields the chemical potential as a function of $\hbar\omega_{ho}$ [51]:

$$\mu = \frac{\hbar\omega_{ho}}{2} \left(\frac{15 N a_s}{a_{ho}} \right)^{2/5}. \tag{3.27}$$

The TF radii, R_i, are found by inserting equation 3.27 for μ in equation 3.25 and solving for R:

$$R_i = \sqrt{\frac{2\mu}{m\omega_i^2}} = a_{ho} \frac{\omega_{ho}}{\omega_i} \left(\frac{15 N a}{a_{ho}} \right)^{1/5}, \quad i = x, y, z. \tag{3.28}$$

The geometric mean $R_{ho} = (R_x R_y R_z)^{1/3}$ is a handy metric for summarizing the spatial size of the BEC [51]. So, combining equations 3.25 and 3.27 we obtain

$$R_{ho} = \left(\frac{15 N a_s}{a_{ho}} \right)^{1/5} a_{ho}. \tag{3.29}$$

Equation 3.29 shows that the average BEC radius R_{ho} is somewhat larger than the trap's ground state radius a_{ho}. For example, with the various traps that we typically use with our apparatus ($a_{ho} \simeq 0.5 - 2\mu$m and $N = 10^4$ ^{87}Rb atoms), R_{ho} is 3-4 times larger than a_{ho}.

Next, we can use the BEC wavefunction obtained from the Thomas-Fermi approximation (eq. 3.24) to calculate the potential and interaction energies of BEC atoms. Importantly, the interaction energy can be used to compute the expansion velocity of a BEC released from a trap. The variational condition of eq. 3.19 can be rewritten as $\mu = \frac{\delta E}{\delta N}$ (i.e. the standard definition of the chemical potential μ).

Furthermore, from eq. 3.27 we know that $\mu \propto N^{2/5}$, so we can combine these two expressions to calculate the energy per atom in the condensate [51]:

$$\frac{E}{N} = \frac{5}{7}\mu. \tag{3.30}$$

We want to see how the total energy is distributed between potential energy and interaction energy. We insert the TF solution given by inserting equation 3.24 into 3.17 and evaluate while ignoring the kinetic energy term. The ratio between the interaction energy E_{int} and the potential energy E_{pot} then becomes [51]

$$\frac{E_{int}}{E_{pot}} = \frac{2}{3} \tag{3.31}$$

Inserting the result of equation 3.30 into the relation $E = E_{int} + E_{pot}$, we find that $E_{int} = \frac{2}{5}E$. If we then take this result and combine it with equation 3.29, we find that the interaction energy per atom is [51]:

$$\frac{E_{int}}{N} = \frac{2}{7}\mu. \tag{3.32}$$

In the case where the confining potential of a BEC is quickly extinguished, then this repulsive interaction energy pushes the atoms apart, thus giving them kinetic energy to drive the ballistic expansion. However, this expansion is not isotropic for a cylindrically symmetric cigar-shaped trap.

3.4 Expansion Rate Calculations

A key requirement for the experiment is that we have a free-space BEC with a small expansion rate, the rate of change of the cloud size, along a given axis (i.e. a narrow velocity distribution) but also strongly suppressed interactions. In particular, we want the $g|\psi(\vec{r}|^2$ term (i.e. $gn(\vec{r})$) in equations 3.20 and 3.21 to be negligible, which the experiment accomplishes by reducing the density n via ballistic expansion of the BEC. More specifically, the experiment uses the anisotropic expansion of the BEC released from its trap to achieve both a low density and a small velocity distribution: the BEC expands quickly along its radial directions (reducing the density), but very slowly along its axial axis, which we then use as the primary axis for the BEC momentum kicks and measurements of the experiment. This section presents calculations of the BEC expansion rate based on the theory developed in section 3.3.[3]

Typically when a BEC is released from cigar-shaped trap, the axial directions expand much faster than the axial one, often to the point that the axial expansion can be hard to detect. Indeed, in chapter 6 (see figure 6.1) we show experimentally that the axial expansion rate is close to negligible. Figure 3.1 shows the radial expansion rate calculated by equating the interaction energy in equation 3.32 with the radial kinetic energy of the cloud (we neglect any axial expansion energy). This is an indication that density-driven interaction energy acquired by the act of trapping atoms, potentially tunable by changing trapping frequency, contributes to the kinetic expansion observed during time-of-flight measurements. This calculation was done for different atom numbers and axial trapping frequencies targeting typical conditions of our ultracold apparatus. While the axial trapping frequency was varied, the radial trapping frequency (1141 Hz) remains constant. Similar calculations are performed to calculate the condensate density (figure 3.2) and the in-trap Thomas-Fermi radius of the BEC (figure 3.3).

Calculating the axial expansion rate by equating the interaction energy to the

[3] Alternatively, [52] gives equations for the ballistic expansion of a cigar-shaped BEC released from a trap

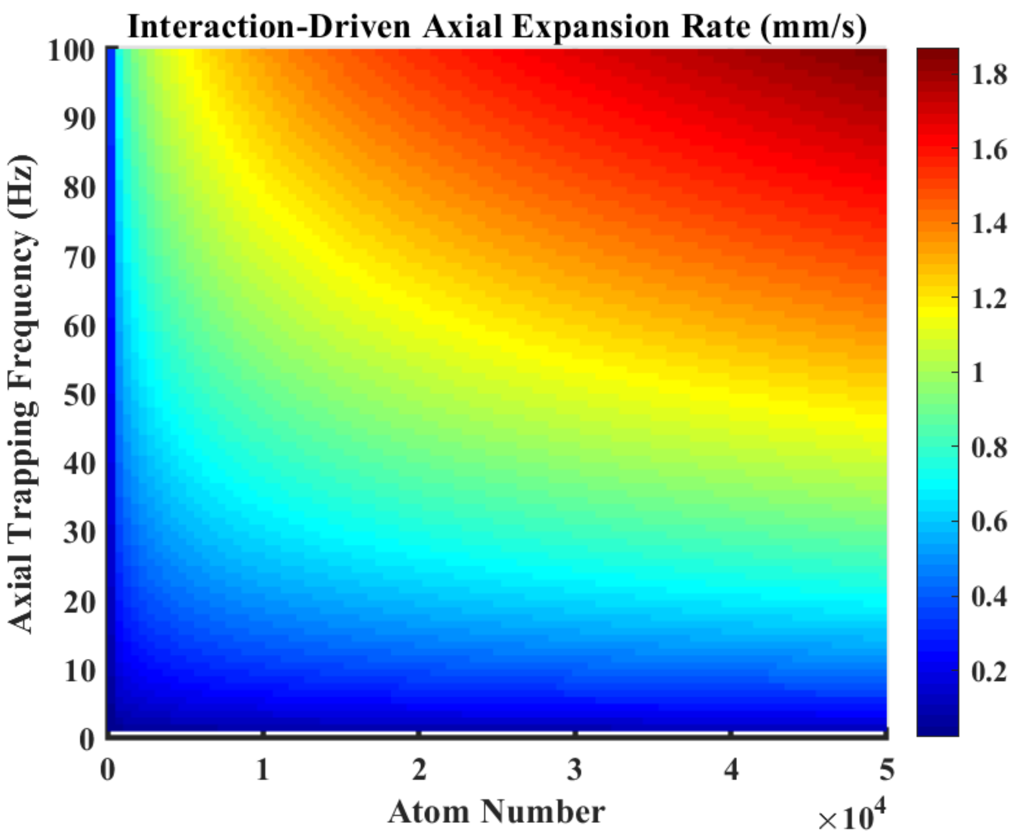

FIG. 3.1: Theoretical expansion rate calculated based on equation 3.32 and plotted as a function of axial trapping frequency and total atom number.

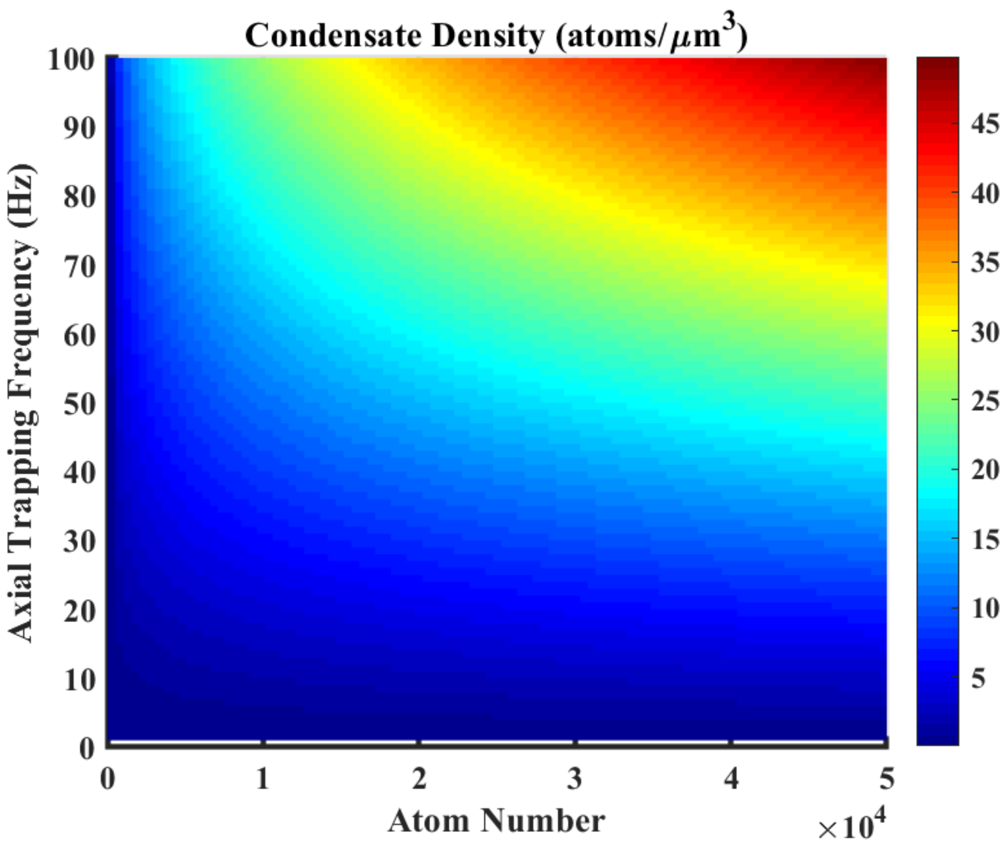

FIG. 3.2: Theoretical in-trap density calculated using the machinery derived in section 3.3 and plotted as a function of axial trapping frequency and total atom number.

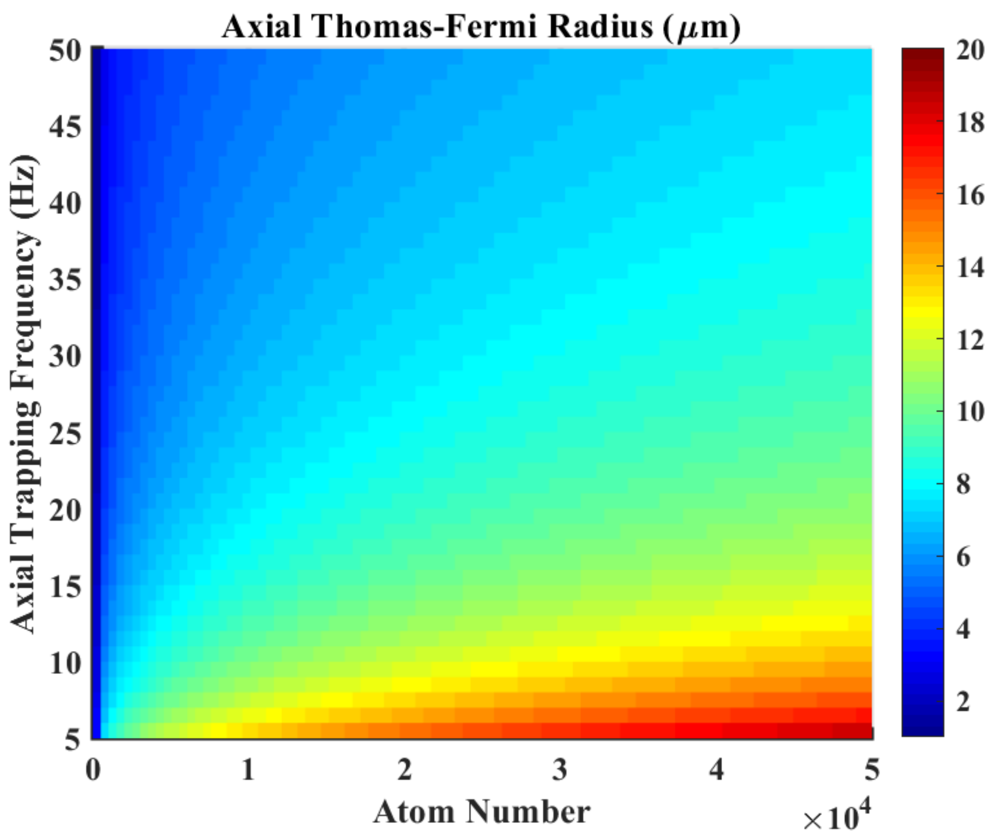

FIG. 3.3: Theoretical condensate radius calculated based on equation 3.29 and plotted as a function of axial trapping frequency and total atom number.

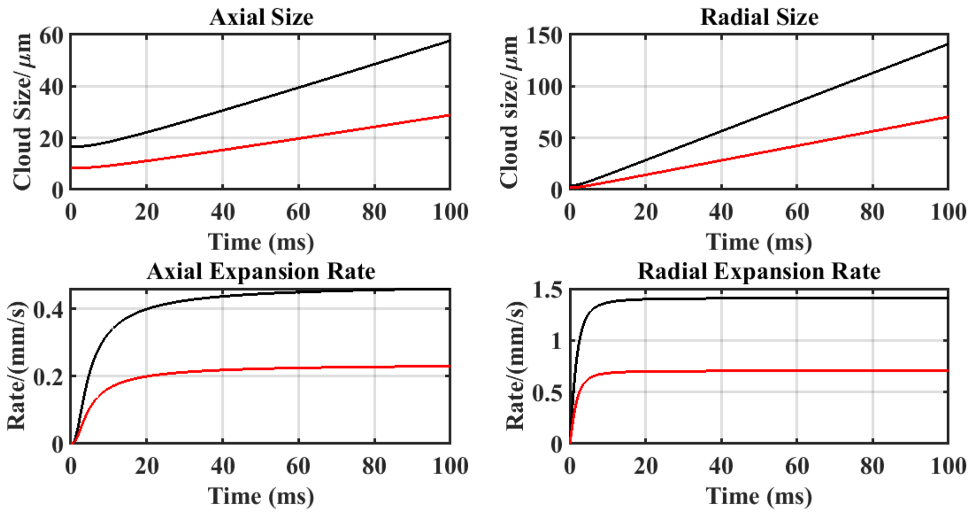

FIG. 3.4: Axial and radial cloud sizes and expansion rates over time as calculated by equations 3.33 and 3.34 using values for our relaxed chip trap ($\omega_z = 2\pi \times 13.5$ Hz and $\omega_r = 2\pi \times 63$ Hz). The initial condensate radius ($\sigma_z(t = 0) = 8.3\ \mu m$, $\sigma_r(t = 0) = 1.8\ \mu m$) is determined by 3.29 and assuming $N = 10^4$ atoms. The black line corresponds to the Thomas-Fermi radius, R_{RF}, according to equations 3.33 and 3.34. The red line represents the approximate Gaussian σ, where $2\sigma = R_{RF}$.

axial kinetic expansion energy (i.e. using eq. 3.32) will not work if the radial expansion is neglected (this is equivalent to a situation where the BEC is held in a tube trap): all of the interaction energy then goes into the axial expansion, the expansion rate will be much larger than what it would be if the BEC were released from a trap. The way to calculate a free space axial expansion rate accurately is to use:

$$r(t) = r_0\sqrt{1 + (w_r t)^2} \tag{3.33}$$

and

$$z(t) = r_0\frac{\omega_r}{\omega_z}\left(1 + \left(\frac{\omega_z}{\omega_r}\right)^2\left(\omega_r t \arctan(\omega_r t) - \ln\sqrt{1 + (\omega_r t)^2}\right)\right) \tag{3.34}$$

where $r_0 = r(t = 0)$ is the initial radial cloud size, and ω_r and ω_z are the radial and axial trap frequencies [52]. Figure 3.4 shows the results of the calculation for both the axial and radial directions.

Interaction Suppression: Interaction strength is a density driven effect, trapped atoms experience a higher interaction strength than un-trapped atoms. The previous experimental attempt was performed in-trap. The conclusion is to perform the experiment outside of a trap. To show that we can effectively reduce interactions, we show the factor by which we have approximately reduced the density of the atoms by comparing cloud size when released from the trap and allowed to expand before interacting with the barrier, relative to the atom cloud size in-trap. So, investigating atom-atom interactions suggests we should design our experiment such that it is performed out of trap. And by doing so, we believe we have reduced interactions by an order of magnitude compared to in-trap.

$$\left(\frac{\sigma_{out}}{\sigma_{in}}\right)^2 = \left(\frac{\sigma_{out}(t = 20ms)}{\sigma_{in}}\right)^2 = \left(\frac{20\mu m}{5.6\mu m}\right)^2 = 12.9 \tag{3.35}$$

3.5 Kohn's Theorem

The group's first experiment on BEC scattering from an oscillating barrier (by Dr. M. K. Ivory) did not successfully observe sidebands. It was originally believed that the problem with the experiment was a contamination of the narrowly defined momentum state as the BEC oscillated inside an harmonic trap. A broad momentum state washes out the fine structure of the sidebands that we intended to resolved. It is now understood through Kohn's theorem [53] that a BEC should not change its size or momentum spread while oscillating in a harmonic trap.[4] In other words, the breathing modes of the BEC are independent from its oscillatory modes.[5]

A cloud of atoms trapped by an arbitrary conservative potential can expand, shrink, deform, and alter its energy spectrum as the center of mass (COM) travels

[4]Dr. Ian Spielman (NIST Gaithersburg) first pointed out Kohn's theorem to us and its application to our experiment (2014).

[5]Discussion adapted from the PhD thesis of Ariel Sommer, Zwierlein group, MIT (2013) [54]

through this potential. In general, the positions and velocities of the atoms relative to the COM of the cloud are coupled to the motion of the COM in the potential. However, for certain potentials, the motion of atoms within the COM frame becomes independent from the COM motion and position: in other words, the position and velocity coordinates of the atoms relative to the COM decouple from the COM evolution. This decoupling can occur even in the presence of atom-atom interactions. The harmonic trapping potential is a specific case in which this decoupling does occur and represent a generalization of Kohn's theorem, often referred to as the "harmonic potential theorem" due to work by J. F. Dobson [55]. In the rest of this section, I give a classical mechanics derivation of this theorem that includes atom-atom interactions. The derivation is adapted from one given by A. Sommers in his PhD thesis (Zwierlein group, MIT, 2013) [54] but with some additional details. The quantum version is covered by Dobson [55].

We consider identical atoms of mass m that are confined by a harmonic potential along the z-axis (with trapping frequency ω_z) and by a transverse external potential $V_{ext,xy}(x, y)$ along the x and y axes. Importantly, the axial and transverse potentials are separable (in our experiment the transverse potential is also harmonic). These atoms also interact with each other via the spherical interaction potential $V_{int}(r)$, where r is the distance between the two atoms; in section 3.2, this interaction potential was the contact potential $g\delta(r)$. The full potential experienced by an atom with index i is thus given by

$$V(x_i, y_i, z_i) = \frac{1}{2}m\omega_z^2 z_i^2 + V_{ext,xy}(x_i, y_i) + \sum_{j \neq i} V_{int}(r_{ij}) \tag{3.36}$$

where r_{ij} is the distance between atoms i and j. If we restrict ourselves to examining the motion along the z-axis, then the equation of motion for atom i is

$$m\frac{d^2}{dt^2}z_i = -m\omega_z^2 z_i - \sum_{j\neq i}\frac{d}{dr}V(r_{ij}\frac{z_{ij}}{r_{ij}}) \tag{3.37}$$

where $z_{ij} = z_i - z_j$ is the z-axis projection of the differential position between the atoms.

Next, we look at the z-axis motion of the COM coordinate z_{cm}, which obeys the standard differential equation for the harmonic oscillator:

$$\frac{d^2}{dt^2}z_{cm} = -\omega_z^2 z_{cm} \tag{3.38}$$

Atom-atom interactions do not affect harmonic motion of the COM as these are internal forces. We can move to the COM reference frame by transforming the atoms' coordinates. The position vector for each atom relative to the COM is given by $\vec{r'}_i = \vec{r}_i - \vec{r}_{cm}$. We can then write equation 3.37 in terms of the relative coordinate by using the substitution $z_i = z'_i + z_{cm}$:

$$m\frac{d^2}{dt^2}z'_i = -m\omega_z^2 z'_i - \sum_{j\neq i}\frac{d}{dr}V(r'_{ij}\frac{z'_{ij}}{r'_{ij}}) \tag{3.39}$$

where $r'_{ij} = |\vec{r'}_i - \vec{r'}_j| = |\vec{r}_i - \vec{r}_j|$ and $z'_{ij} = z'_i - z'_j = z_i - z_j$. Notably, the z_{cm} coordinates have dropped out due to the use of equation 3.38. We see immediately that equation 3.39 for the z'_i coordinate (in the COM frame) is identical to equation 3.37 for the z_i coordinate. We conclude then that the internal dynamics of the system in the COM frame and the laboratory frame are essentially equivalent. We note that dynamics in the transverse directions (in xy plane) are unchanged in the COM frame and the lab frame due to the separable nature of the external potential.

This theorem ensures that the COM motion of a BEC in a harmonic potential is decoupled from the internal properties and dynamics of the BEC, and in particular its kinetic energy and momentum distribution (except for an offset). This theorem shows that the momentum state of the BEC in a harmonic trap should remain intact for experiments. This should exonerate the COM motion as the cause for the lack of sidebands in the first experiment on BEC scattering from an oscillating barrier. As discussed in chapter 2, we suspect in situ atom-atom interactions for washing out the sidebands. Furthermore, we note that presence of the oscillating barrier means that the trapping potential in the first experiment is no longer harmonic: formally, this means that the above theorem no longer fully applies; however, the barrier (centered on the trap) behaves somewhat as a hard wall, so the theorem is still expected to hold for the most part.

CHAPTER 4

Apparatus

The purpose of this chapter is to provide an overview of the setup and procedures involved in creating a Bose-Einstein condensate, and to also cover some of the science behind the cooling as well. It is my hope that this information also serves as a maintenance guide to future students. Ultracold atom apparatuses are very complicated to design, build, and maintain. Our apparatus is no different (see Figure 4.3). Our apparatus has been developed over several years by multiple students. I am the fourth graduate student to conduct an experiment on this apparatus. I was preceded by M. K. Ivory and A. R. Ziltz who constructed the majority of the apparatus, and also C. T. Fancher who I had worked with closely to improve and maintain the performance of the apparatus. I have also worked on projects such as the light induced atomic desorption (LIAD) system, an over-current safety interlock for the atom chip (the Killbox, discussed in section 4.3.1), the oscillating barrier beam (section 6.3), a 3 W microwave amplifier (Dr. Watts), a high current fast switch (the "Levitiathan," discussed in detail in chapter 5), a high current pulse switch (the Kraken, section 6.2), the dark-ground imaging system [56], and optical dipole traps.

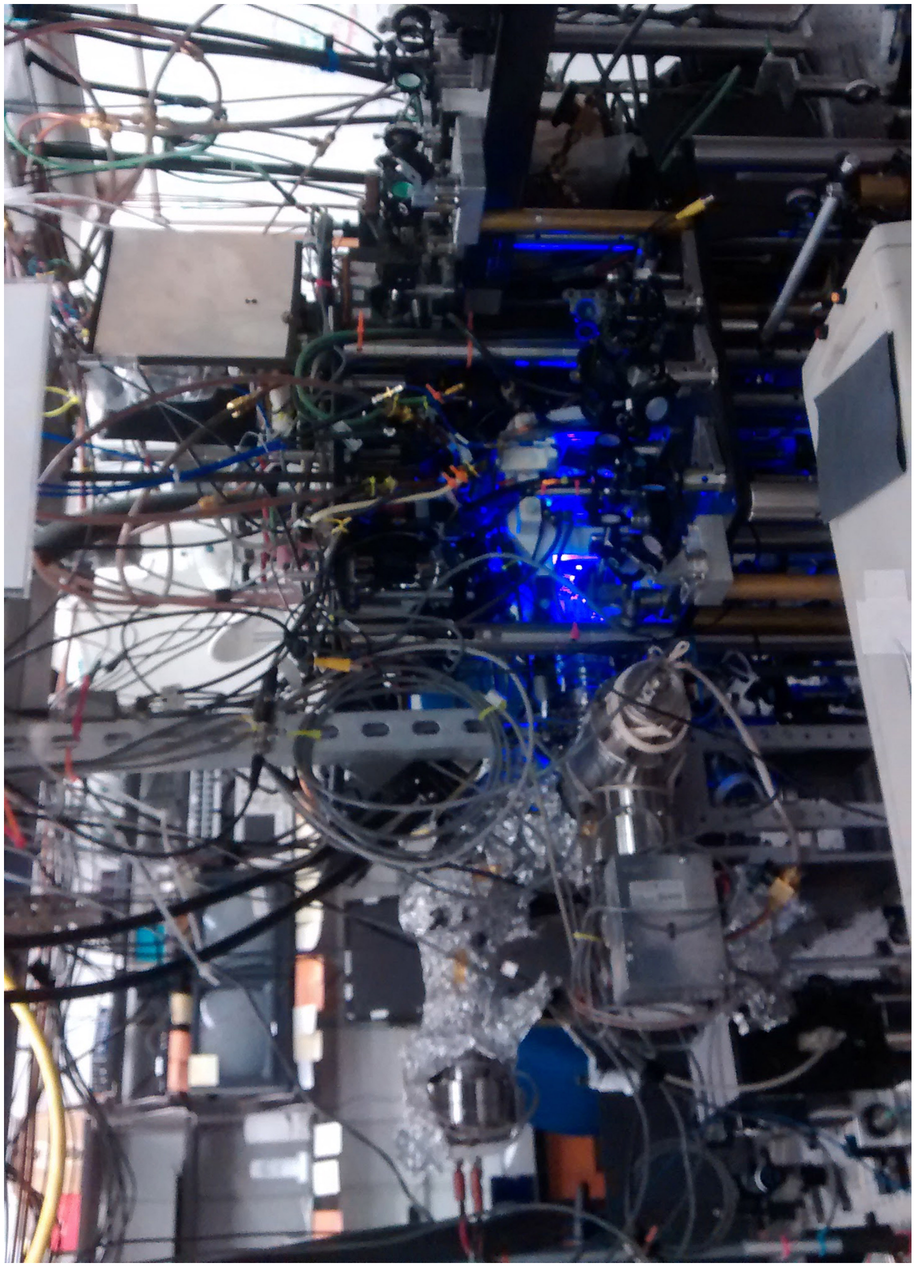

FIG. 4.1: Photo of the apparatus. I believe this photo adds emphasis to the technical conglomeration that is required to operate in harmony to produce a BEC. Figures 4.2 and 4.3 help to visualize the components in this photo.

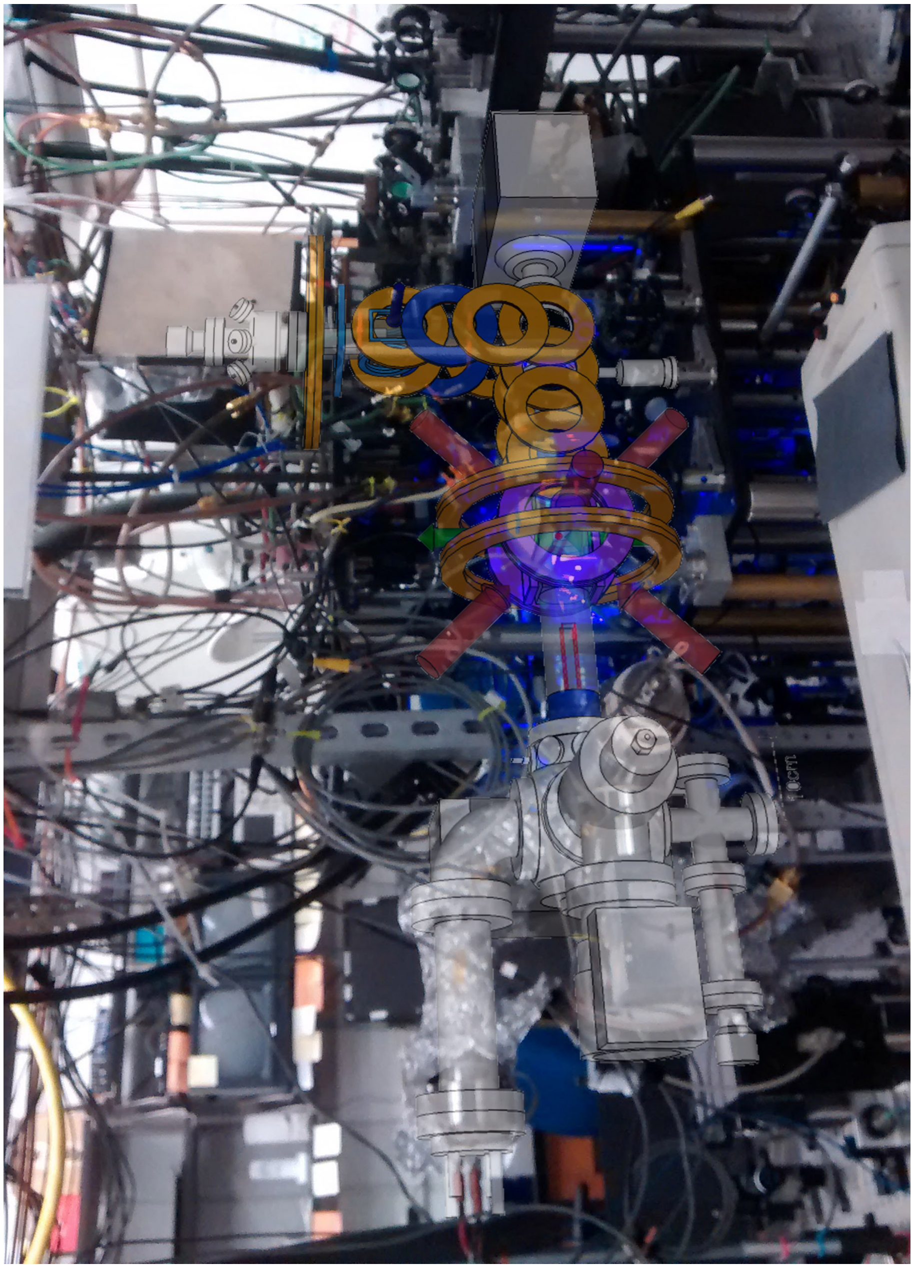

FIG. 4.2: This figure is the same photo as figure 4.1, but with a transparent schematic shown in figure 4.3 overlaid.

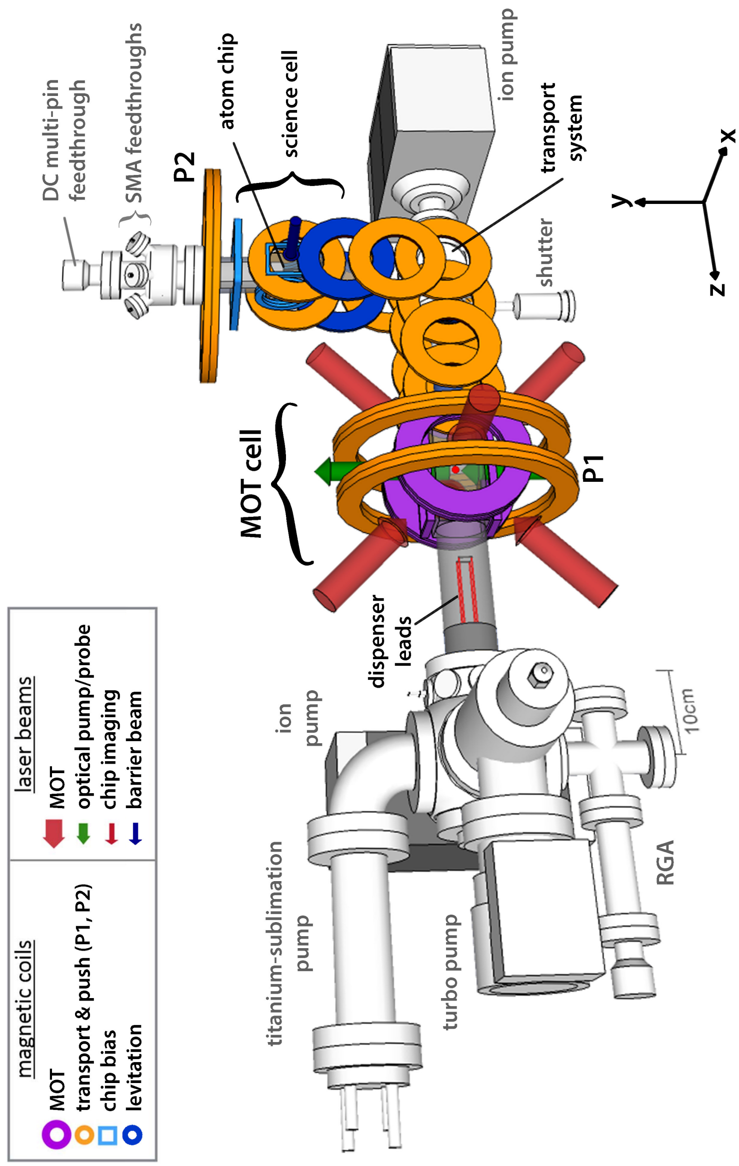

FIG. 4.3: Cutaway diagram of the critical components of the dual-chamber ultracold atom apparatus. Image credit: A. Ziltz [43]. Vacuum parts are shown in white/gray. The small red sphere in the center of the Magneto-Optical Trap (MOT) cell is the MOT, and the Optical Pumping (OP) beam travels up and through the MOT. The arrows represent laser beams for the MOT/OP/Barrier (red/green/blue). The axial pump/probe beam co-propagates with the barrier beam. The coils used for magnetic trapping and transport are highlighted in orange. Coil 6 (discussed in chapter 5) is highlighted in blue. The atom chip is mounted upside down on the gray chipstack.

The layout for this chapter is as follows: Section 4.1 discusses the MOT construction, cooling techniques, and associated laser systems. Section 4.2 describes magnetic trapping of cold atoms. Section 4.3 describes cooling and trapping with the atom chip that ultimately leads to Bose-Einstein condensation with atom number as high as $N_{BEC} = 4 \times 10^4$. Figure 4.1 shows a photo of the apparatus. Figure 4.2 shows the same photo in figure 4.1 with a transparent schematic from figure 4.3 overlayed. Figure 4.3 more clearly shows the diagram of the overall dual-chambered apparatus with different parts indicated by highlighted color. This figure will be referred to multiple times in this chapter.

4.1 Magneto-Optical Trap Operation

4.1.1 Magneto-Optical Trap

The Magneto-Optical Trap (MOT) is the first step in achieving Bose-Einstein condensation. The MOT traps and cools atoms in a room temperature gas to temperatures of 100μK (10 cm/s). This section describes this process and the infrastructure required for this atomic cooling starting point.

The MOT consists of six laser cooling beams oriented across three axes (one horizontal, and two diagonal in our apparatus, fig. 4.3) with pairs of counter-propagating beams. The beams are detuned to the red of resonance such that a moving atom will see the counter-propagating beams at different energies (fig. 4.4). The Doppler effect causes the atoms to see a blue-shifted (red-shifted) frequency when moving towards (away) the beam. By detuning to the red, the atoms are more likely to absorb a photon when travelling towards a MOT beam. After absorbing a photon, the atom will then spontaneously emit a photon in a random direction. For each photon absorbed, the atom recoils (6 mm/s for ^{87}Rb) along the beams direction of propagation. The atom receives a velocity kick when emitting a photon, however the atom will experience a net decrease in speed as the direction of the recoil during absorption is selective, while the emission is random. The rate for this process is on the order of 10^7 events/second, so the atoms experience a dramatic cooling. A spatially varying external magnetic field is added to provide a magnetic gradient. The spatially varying magnetic field creates a spatially varying detuning that controls the strength of the optical trapping force, with a null centered at the magnetic zero. Doppler cooling only affects the velocity of the atoms and does not trap them. The magnetic field and the laser light together provide confinement.

4.1.2 MOT Chamber

The MOT cell consists of a rectangular glass cell that was baked out and is pumped to achieve ultra-high vacuum (UHV). The UHV (10^{-10} Torr range) increases the lifetime of trapped atoms by isolating cold atoms from collisions with background atoms and molecules. We routinely activate a Rb dispenser to replenish this species in the vacuum system. We use a light induced atomic desorption system to dynamically control the background pressure of Rb atoms. This system directs 1.8 W of 405 nm light onto the MOT cell to desorb atoms stuck on its inner surface. This system has been shown to increase the Rb background pressure by over three orders of magnitude, and is considered essential for running the MOT. When not running, the lights are turned off to conserve the atoms inside the vacuum system. Surrounding the MOT cell are homemade multi-layer, water-cooled coils. These coils are connected in an anti-Helmholtz orientation and are used to generate a magnetic quadrupole field gradient used for cooling and trapping (see Figures 4.3 and 4.5). These coils provide a gradient of $\sim$9 G/cm (strong axis).

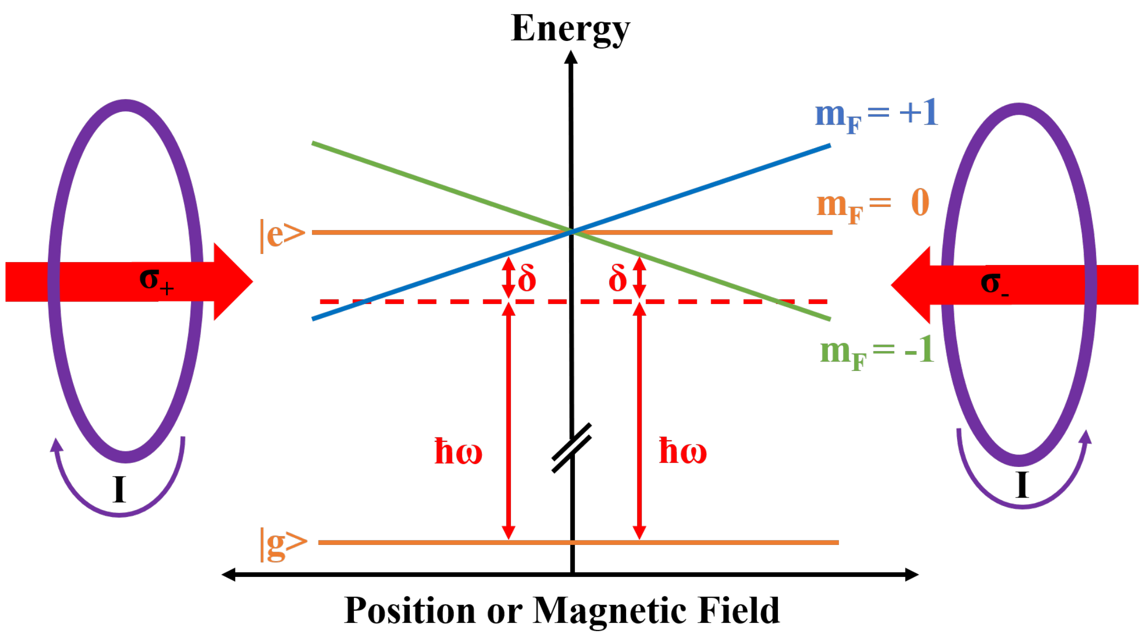

FIG. 4.4: Schematic of a MOT. A linear magnetic field gradient is created along the position coordinate axis by a pair of coils (purple) in arranged in anti-Helmholtz configuration. Zeeman magnetic sub-levels split by the presence of the magnetic field are shown $m_F = 0, \pm 1$ (orange, blue, and green). A pair of counter-propagating laser beams are incident on the center of the MOT from each side with spatially varying detuning δ. The beams have opposing circular polarizations chosen for preferential absorption, but both are at frequency ω. The atoms are confined by magnetic and optical forces restoring their position to the center of the trap. Figure adapted from [57, 58, 21].

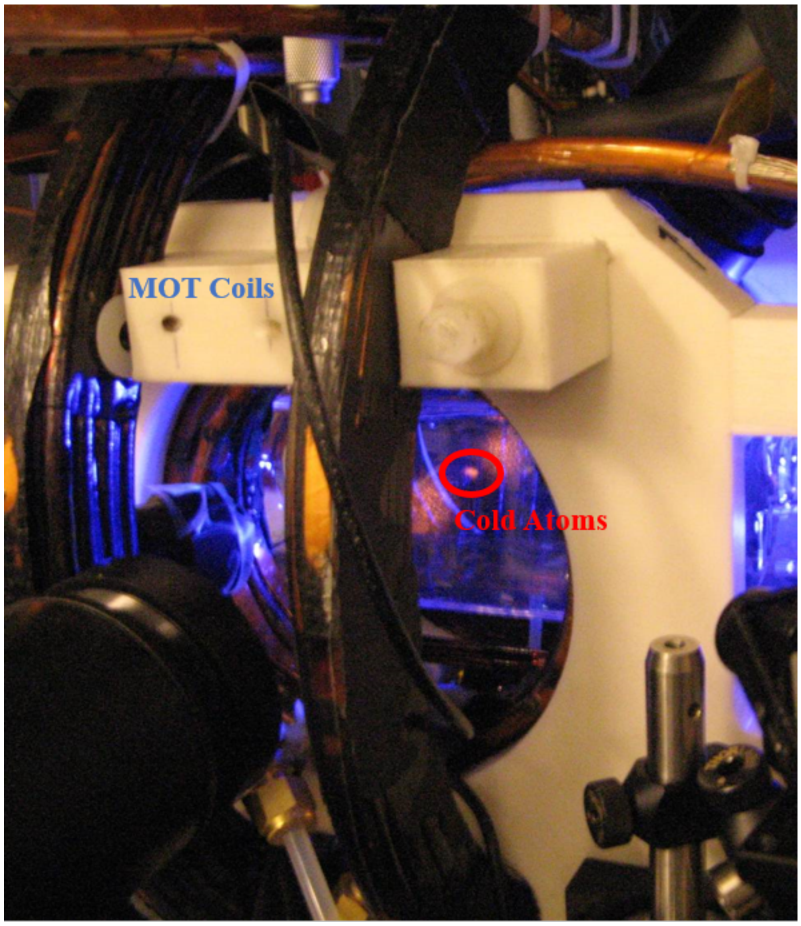

FIG. 4.5: This image is of our vacuum chamber where we trap and cool atoms. The orange colored ball in the center is about 10^9 atoms at a temperature of approximately 100 μK.

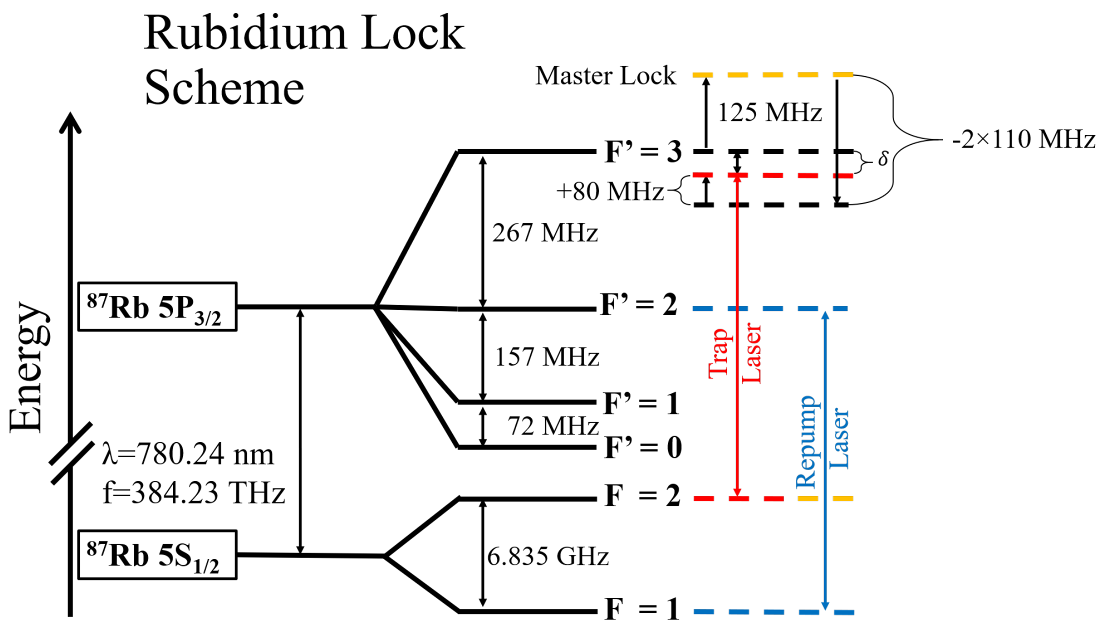

FIG. 4.6: Energy level and laser diagram for ^{87}Rb. The master lock (orange) is offset from the $\left|5S_{1/2}, F = 2\right\rangle \rightarrow \left|5P_{3/2}, F' = 3\right\rangle$ transition by 125 MHz. The trap laser (red) frequency is controlled by a double pass AOM (AOM-1 in figure 4.7) driven at 110 MHz that detunes the master light injected into a diode laser. An additonal AOM (AOM-2, 80 MHz single pass) controls the amplitude of the trap laser light. The repumper light (blue) drives a cycling transition between $\left|5S_{1/2}, F = 1\right\rangle$ and $\left|5P_{3/2}, F' = 2\right\rangle$ states to repump the atoms back to the trap laser cycling transition. Figure adapted from [59].

4.1.3 Laser Systems

The MOT operates on the D2 line (780 nm) of ^{87}Rb, as shown in figure 4.6. The cooling and trapping light is red-detuned ($\sim$20 MHz) from the $5S_{1/2}, F = 2 \leftrightarrow 5P_{3/2}, F' = 3$ cycling transition. Also, we use a repumper laser to drive atoms back into the cycling transition, if they have fallen into a dark state ($5S_{1/2}, F = 1$). The repumper light drives $5S_{1/2}, F = 1 \leftrightarrow 5P_{3/2}, F' = 2$, thus allowing atoms to decay to the $F = 2$ ground state of the cycling transition.

The trap and repumper light are provided by diode lasers. We use a commercial external cavity diode laser (ECDL) (Toptica DLC Pro) as the master laser lock. A free running diode laser (Sanyo DC-7140-201) provides the repumper light.[1] Acousto-Optic Modulators (AOM) provide amplitude (frequency) control of the laser beams in single (double) pass configuration. AOMs are capable of responding on the μs level timescale, which gives us good dynamic control over the laser light. Homemade mechanical shutters made from automotive relays are strategically placed at telescope foci and used for blocking extraneous light from optical fibers that couple laser light from the laser table to the science table. Having two optics tables (see Fig. 4.7) helps to decouple the main apparatus from electrical and mechanical noise, and temperature fluctuations. An additional diode laser is operated in slave configuration as light from the master laser is injected to seed the output, which grants us a significant increase in power. The injection laser lock is set by adjusting the diode current while monitoring the frequency spectrum output by the laser on a Fabry-Perot cavity interferometer. This is unnecessary for the repumper laser, as we require much less repumper light with respect to trap light. Faraday rotators provide optical isolation for laser sources.

The master laser is locked to a saturation absorption transmission line through the use of a pump probe scheme in a Rb vapor cell. The error signal is produced by a lock-in amplifier observing the saturated absorption probe signal. Feedback varying the laser's current and the piezoelectric voltage of its external cavity maintains the lock. Rather than locking the repumper laser with a similar setup, we lock the repumper laser to the already locked master laser (fig. 4.7). This is accomplished by picking off a small fraction of the light from each laser and coupling the mixture into an optical fiber. This fiber delivers the signal to a high speed photodetector capable of detecting the optical beat note, whose frequency is then compared to

[1] Unfortunately, during my tenure, both of these lasers have expired and are unusable as they no longer provide the level of stability necessary for laser cooling atoms. The master laser has been replaced by a well-performing Toptica laser, and the repumper with an adequate, but far less stable, diode laser.

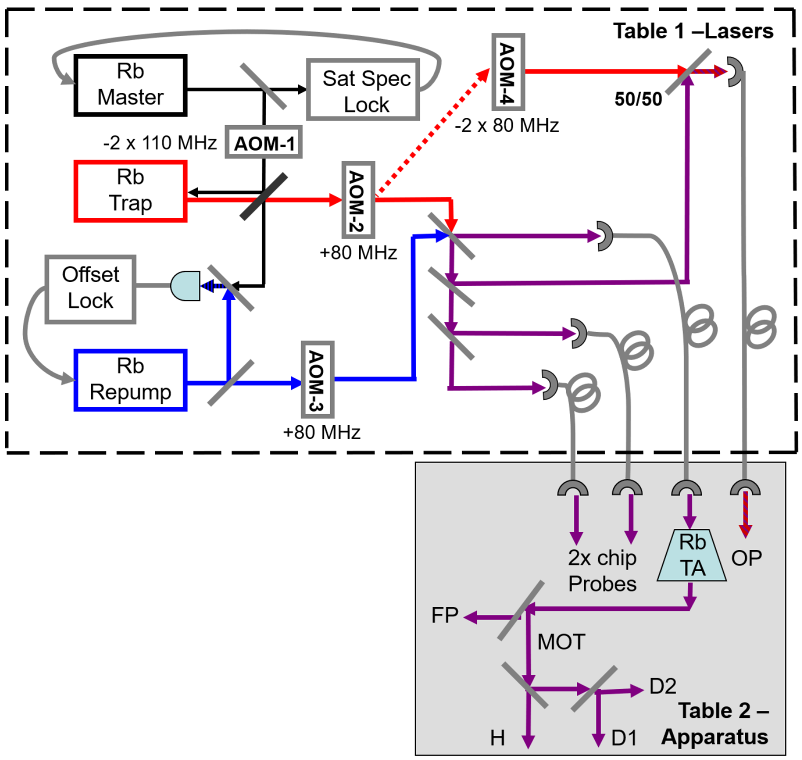

FIG. 4.7: Laser system schematic for a dual species (only Rb shown) apparatus. Multiple lasers, AOMs (Acousto-Optic Modulator), TAs (Tapered Amplifier), optical fibers, and shutters perform the function of the switchyard to control the amplitude and frequency of trap, repumper, Optical Pumping (OP), and probe light. Straight arrows represent free space laser beams. Curved gray arrows represent electrical signal. Gray lines with double loops represent optical fiber paths. The Fabry-Perot (FP) cavity provides frequency spectrum information about the combined beams before they enter the MOT cell. Figure adapted from [43].

a reference to generate an error signal. Feeding back to the diode laser current maintains the offset lock to the master.

We use a Tapered Amplifier (TA) with temperature stabilization to amplify the light destined for the MOT cell used for Doppler cooling. This TA can be seeded with 20-25 mW and outputs 350-400 mW. This allows us to deliver a peak intensity of $\sim$1.4 mW/cm^2 per MOT beam. This combination of laser sources and switchyard components (Fig. 4.7) provides the architecture for producing and controlling the required trap, repumper, optical pumping, and probe (imaging) light.

The MOT cooling beams are created by mixing trap and repumper light and sent from the laser table to the science table via polarization maintaining single mode optical fibers. The light is then amplified through a TA in single pass configuration and the mode is cleaned with lenses and apertures. After this, the beam must be split into six beams, one for each axis and direction. To accomplish this, the MOT beam passes through two linear waveplates and corresponding polarizing beam splitting (PBS) cubes to separate the original beam into three, one for each axis. Each of these is separated once again using a similar setup with a PBS cube. Each of the six beams passes through a quarter ($\lambda/4$) waveplate to create circularly polarized light and is then expanded 1:5 in size by telescopes to produce $\sim$ 2" diameter beams. These large beams are used to provide a fast loading rate for the MOT. The waveplates used to balance the intra-axis power are more important than the inter-axis power balancing waveplates, and are adjusted on a daily basis. The MOT must be aligned once or twice per year. The PhD thesis of Dr. Charles Fancher [57] contains detailed procedural instructions for completing this task.[2] Figure 4.8 shows an image of the MOT with approximately 5×10^8 atoms collected by our CCD camera.

[2]Dr. Charlie Fancher and I recommend listening to "I'll Make a Man Out of You" from the Walt Disney animated film "Mulan" during this process. The realignment process will take about half a day. Place the song on repeat until you're sick of it.

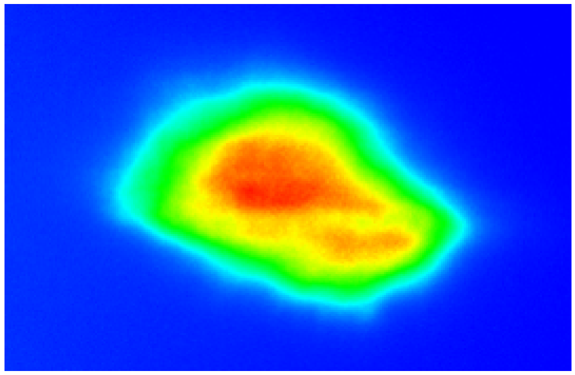

FIG. 4.8: Image of an ^{87}Rb MOT. This is a false-color fluorescence image in which red (blue) signifies more (less) photon counts, which is proportional to the number of atoms. This asymmetry is typical of atoms in the MOT. This structure disappears once the atoms are trapped (fig. 4.11).

4.1.4 Temperature Measurement

It is obviously useful when cooling atoms to have a method for measuring their temperature. In the absence of an ultracold, vacuum thermometer, we require an alternate mechanism for measuring temperature. In a monatomic gas, such as laser-cooled Rb atoms, temperature is a measure of the average kinetic energy of the atoms. This definition implies that we can indirectly measure temperature by measuring their average kinetic energy:

$$K = \frac{1}{2}m\bar{v}^2 = \frac{1}{2}k_B T \tag{4.1}$$

where k_B is the Boltzmann constant, $\bar{v}$ is the RMS velocity of the atom, and m is its mass. Measuring atomic velocity will indirectly determine the temperature. This can be done by releasing atoms from a trap and tracking the expansion of the atom cloud over time, $\sigma(t)$. Atom cloud's RMS size expands according to

$$\sigma(t) = \sqrt{\sigma_0 + (\bar{v}t)^2} \tag{4.2}$$

where σ_0 is the initial cloud size (at t=0). This formula gives us the ability to determine temperature, however it requires multiple destructive measurements. We can perform a 'single-point' temperature measurement, although we regard it as having poor accuracy and generally do not report temperature measurements when acquired in this manner. Based on equation 4.1, temperature can be inferred from a measurement of expansion velocity (i.e. by turning off the MOT and measuring the cloud size at different times-of-flight):

$$T = \frac{m}{k_B}\bar{v}^2 \tag{4.3}$$

In the case of ^{87}Rb, if one uses a velocity in cm/s then $T_{\mu K} = 1.045 \times v^2_{cm/s} \simeq v^2_{cm/s}$.

4.1.5 Optical Molasses

Optical Molasses (OM) is a sub-Doppler laser cooling technique that is applied to the atoms after they have been collected in the MOT. This method is capable of cooling the atoms to temperatures lower than the MOT. OM is also known as polarization gradient cooling, or Sisyphus[3] cooling. This technique cools the atoms by transferring their kinetic energy to a laser light field through the selective absorption of lower energy photons and spontaneous emission of higher energy photons (i.e. giving away more energy than is gained). This method uses three pairs of counter-propagating, circularly polarized beams (like the setup for the MOT light) that combine to create a standing wave of spatially varying polarization (fig. 4.9). The laser light field provides an electric field that causes an AC Stark shift that spatially varies the ground state energy with the polarization. The beams are red-detuned and designed such that as an atom moves through the field it becomes resonant with

[3]In Greek mythology, King Sisyphus was forced to push a heavy boulder up hill, after which it would simply roll back down. His punishment forced him to do this repeatedly for all eternity.

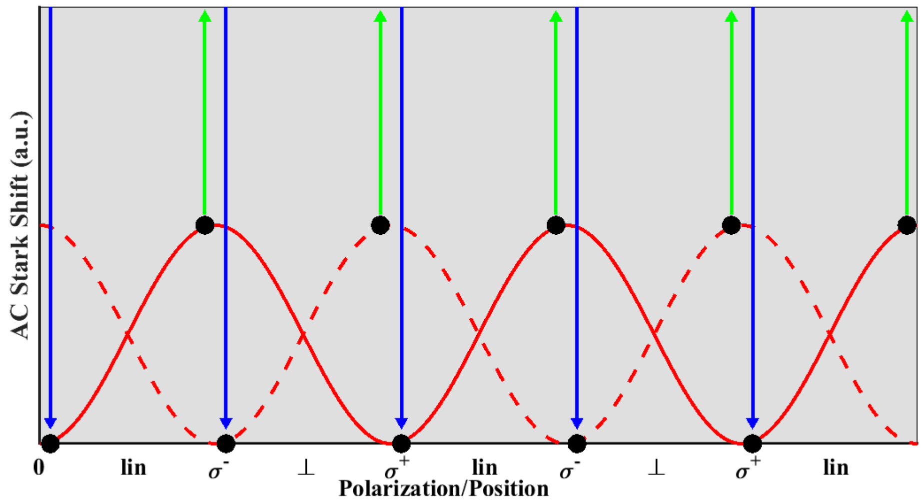

FIG. 4.9: Optical molasses energy diagram. The red sine curves indicate different electronic spin states whose energies are split by an AC Stark shift. The atom is indicated by a black circle. The bottom x-axis labels indicate the standing wave polarization at that location. When the atom reaches the the appropriate σ polarization, it absorbs a photon and transitions to the excited state, and spontaneous emission to the other ground electronic state. The atom continues repeat this process and loses kinetic energy. Fiture adapted from [57, 58, 21].

the cycling transition when the energy of the transition is at a minimum. At this point, the atom is likely to absorb the photon and be pumped to the excited state. When the atom decays through spontaneous emission, it is possible for it to decay to the lower energy ground state. The process occurs again and again, an atom will repeatedly lose more kinetic energy than it gains, thereby cooling it.

We use the same trap light as we do for the MOT to implement OM, but use the trap double-pass AOM to alter the detuning of the light. Waveplates controlling the intra-axis power balancing for each axis are frequently optimized using the counts and cloud size of a magnetic trap acquired through fluorescence imaging as feedback. This is done to prevent a net force from the cooling beams acting on the atom cloud, which would push the cloud away from the center of the magnetic trap (or magnetic zero of the trap). The OM process requires zero field to prevent a DC Zeeman shift in atomic energy levels that may overwhelm the AC Stark splitting. It is for this

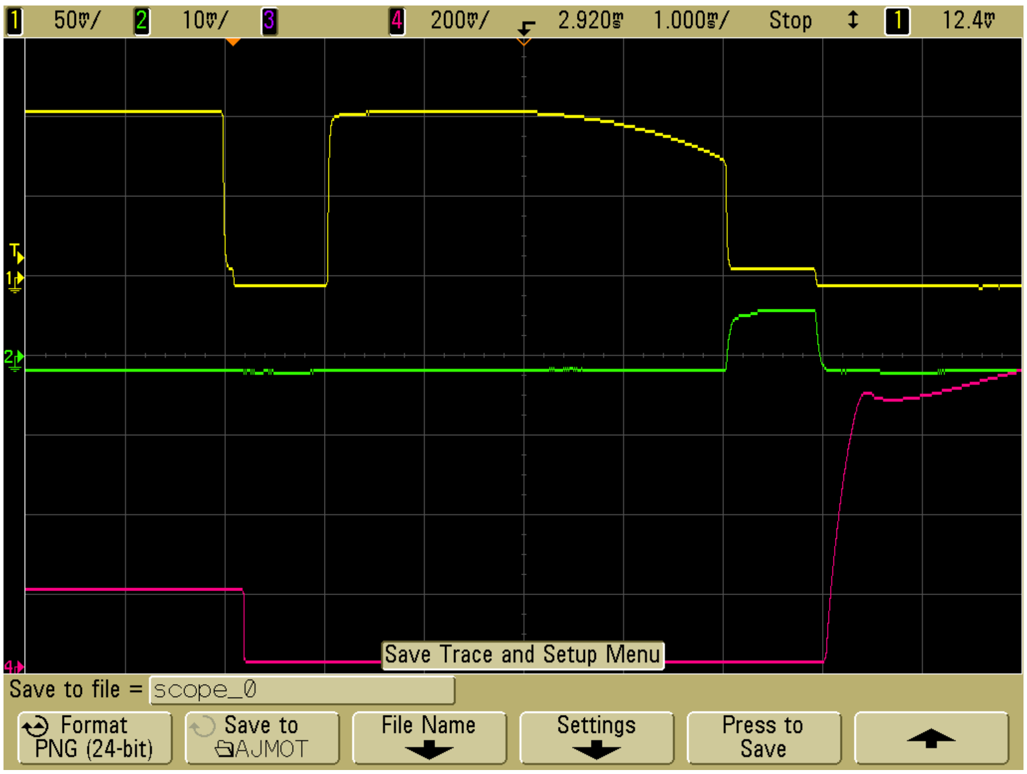

FIG. 4.10: Scope image showing timing diagram for MOT cell cooling dynamics. MOT (OP, or optical pumping, see section 4.1.6) light is shown in yellow (green), and MOT current in pink with a calibration of 50 A/V. The MOT coils are turned off quickly to perform optical molasses and optical pumping. The coils are turned back on quickly to magnetically trap the atoms. Laser light measured via photodiodes.

reason that after loading the MOT sufficiently we turn off the MOT coils quickly (see Fig. 4.10 for timing diagram), as the atom cloud will expand and move away from the trap center during the turn off time. We empirically optimize the duration (2-5 ms) of the OM pulse as too much time allows the cloud to expand too much,[4] and too little time cools the atoms insufficiently. The laser power and detuning is ramped during the pulse. The OM cooling process benefits from decreasing laser power over the duration of the OM pulse.

The OM laser cooling technique allows us to cool the atoms well below the Doppler limit of the MOT, allowing us to reach a temperature of 30μK. However, this scheme is not without its own limitation: OM does not confine the atoms, and thus allows the atoms to wander (admittedly more slowly) away from the laser light. There, the OM stage is kept relatively short to limit the expansion of the cold atom cloud.

The MOST FREQUENTLY ENCOUNTERED PROBLEM while cycling the apparatus is the issue of losing injection laser lock at the OM frequency.[5] The silver lining to this problem is that it is fixed by simply adjusting the injection laser current. However, one may be unaware that the injection laser has lost lock without checking the Fabry-Perot monitor at the OM frequency while the apparatus is not cycling. One may encounter many suspicious performance aberrations that are cause to check the lock.[6]

OM is often used to optimize the power balancing and alignment of the MOT beams. Realigning the MOT (which must be done periodically) is cause to adjust the magnetic trim coils and the waveplates controlling power balancing. There are two possible forces that could simultaneously contribute to moving the atoms away

[4]This causes more heating when adding a magnetic trapping potential later on.

[5]While this is a simple problem to fix, it occurs frequently enough that it is expected to happen at some point during data collection.

[6]And lose one's mind, as lost injection lock is not always the source of a problem.

from the trap center: a magnetic gradient, and a net optical force caused by a power imbalance in the counter-propagating cooling beams. The best way to proceed is to separate the two forces. I recommend decreasing the Rb TA current for less optical power, and consequently less optical force when adjusting the trim coils to zero the magnetic field. This is done by turning off the MOT coils and observing how the atoms disperse on a TV camera. I recommend full power when adjusting waveplates for changing the shape and position of the MOT cloud. Additionally, detuning the trap light towards the OM cooling frequency while free-running the MOT will have an affect on the cloud position, and it is desirable to have the cloud move as little as possible. Making these adjustments is not difficult or frequent, but necessary and time consuming. When optimized, OM performs well and reliably so on a day-to-day basis.[7]

4.1.6 Optical Pumping

The purpose of optical pumping (OP) is to prepare the atoms for magnetic trapping by preferentially populating the $F = 2, m_F = +2$ hyperfine stretched state. OP increases the fraction of atoms that are loaded into a magnetic trap, as some states are anti-trapped or unaffected by an external magnetic field altogether. Atoms are preferentially pumped into the $|2, 2\rangle$ ground state by driving the ^{87}Rb D2 line between $F = 2$ and $F' = 2$. Atoms are pumped into the $m_F = +2$ stretched state, and not the $m_F = -2$ stretched state by using σ^+ light selected by a $\lambda/4$ wave plate. Laser light is sent through the OP path on the laser table by turning off the trap AOM (AOM-2) thus redirecting all of the zero order light to the OP AOM (AOM-4) in double-pass configuration for control of power and detuning. The light is coupled via optical fiber to the science table where it is directed underneath the

[7] Injection lock performance excluded.

MOT cell and aimed upwards at the atoms (green in figure 4.3). The vertical trim coil provides the DC magnetic quantization field for the OP process (see figure 4.3). This beam is also conveniently used for absorption imaging with a CCD imaging system placed above the MOT cell. We perform this short step (∼1 ms) after the OM stage and before turning on the magnetic trap. We have optimized the OP pulse by varying beam power, detuning, pulse time, and the external bias field. We assess performance based on the number of atoms trapped in the magnetic trap and observed through fluorescence imaging. Repump light is typically provided through the MOT beam paths, although the system was meant to ideally operate by providing repump light along the OP path. In practice, we observe a minor improvement using the latter, but at the cost of the system being more susceptible to irreproducibility caused by mechanical shutter timings. OP requires about 1 mW of optical power and is typically reliable. This stage also gives us the diagnostic advantage in that the forthcoming magnetic trap will contain much fewer atoms in the event of an OP problem or lack of light. However, it should also be noted that too much OP light can cause unwanted heating before the atoms are loaded into the magnetic trap. This adversely affects cooling performance during the later step known as forced evaporation.

4.2 Magnetic Trap & Transport

The second stage of atomic trapping and cooling leveraged by our apparatus is magnetic trapping. Once the atoms have been cooled by the MOT, the laser cooling light is blocked and the magnetic field for the MOT is turned off quickly. Then, the atoms are targeted by OM and OP laser pulses. After these steps, a pair of anti-Helmholtz coils that produce the field for the magnetic trap is turned on quickly. These steps are necessary to trap the atoms, cool and trap them in a preferred state

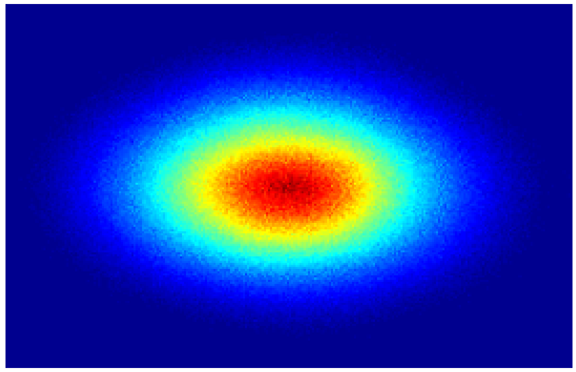

FIG. 4.11: Image of an ^{87}Rb magnetic trap. This is a false-color fluorescence image in which red (blue) signifies more (less) photon counts, which is proportional to the number of atoms.

to avoid unwanted atomic collisions and promote cooling. We use a spin distillation technique to remove any leftover $m_F = +1$ atoms by keeping the coil current to less than 70 A to produce a gradient less than 30 G/cm: this is strong enough to hold $m_F = +2$ against gravity, but not $m_F = +1$.[8] This magnetic quadrupole trap is used to transport trapped atoms to the atom chip for forced evaporative cooling. The magnetic trapping scheme allows us to capture 3×10^8 atoms with a temperature of 60 μK. Although it may seem contradictory to our overall goal for the temperature of the atoms in the magnetic trap to be higher than the temperature after OM, the increase in temperature is due to the addition of the trapping potential. Figure 4.11 shows a representative false-color fluorescence image taken of an ^{87}Rb MOT. The oblong nature of the trapped atoms reflects 2:1 ratio in magnetic gradient between the strong and weak axes of the trap.

Seven anti-Helmholtz coil pairs turn on and off successively (Fig. 4.12) to move the location of the magnetic trap 30 cm horizontally and then 30 cm up through the L-shaped vacuum chamber shown in fig. 4.3. A current multiplexer (known as the "Coilplexer") allows three 2 kW power supplies (Agilent 6571A-J03)

[8]There has been an issue in the past when the coil current was not dropping low enough to remove atoms in unwanted states.

to drive 10 different coils (7 transport coil pairs and 3 push coils). There are safety concerns over the amount of current driven and the power dissipated by these coils. These concerns motivated the construction of over-current and over-temperature safety interlocks. These interlocks are very similar to, and the pioneer versions, of the homemade interlock known as the Killbox (discussed in section 4.3.1) and the interlock incorporated into the high-speed, high-current power supply known as the Levitiathan (see chapter 5). Due to additional concerns over the power supply programming common being connected to the positive output of the supply, the analog control signals for the high current power supply are sent from the sequencer through galvanic isolation buffers (based on ISO124). The same analog isolation electronics was used in the construction of the Levitiathan (see chapter 5). Once transport is complete, we begin driving current through the atom chip to load atoms from the transport trap into a Ioffe-Pritchard trap created with the atom chip. One big water-cooled push coil (labeled P2 in Figure 4.3) is located above the atom chip to produce a vertical magnetic field that helps to load atoms into the atom chip trap located 1.5 cm above the axis of the last transport coil pair (Coil 7).

4.3 Atom Chip

The region beneath the atom chip in the science cell (see Figures 4.13 and 4.14) is the primary place for experiments to be conducted within this apparatus. The apparatus contains several DC and RF magnetic field sources for generating a micro-magnetic trap for forced RF evaporation to quantum degeneracy, and also for experiments. In addition, there are laser beams used as optical probes for imaging systems oriented towards the atom chip for *in situ* and time-of-flight measurements. The tight confinement (high trapping frequencies) of the chip trap ensures quick re-thermalization times for expedient RF evaporation. The anistropic trap generated

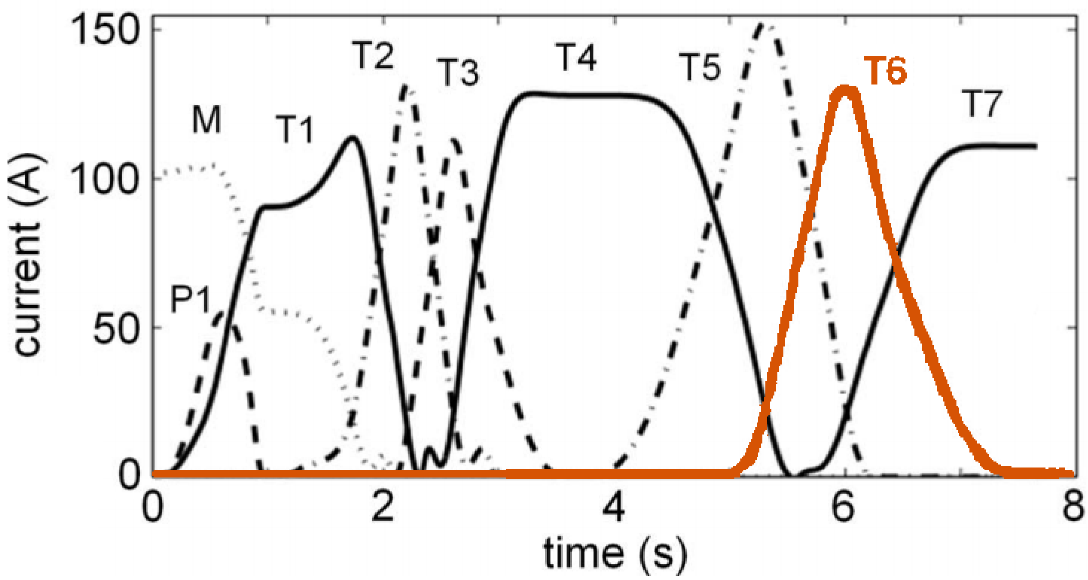

FIG. 4.12: Transport coil illustration and timing diagram. This shows the current traces for the MOT coils (M), push coil, (P), and transport coils 1-7 (T1-T7). Transport coil 6 (T6) is highlighted as it is also used for levitating atoms. The overall experimental scheme with levitation is discussed in chapter 6 and the power supply used to drive the coils is discussed extensively in 5. Figure adapted from [43].

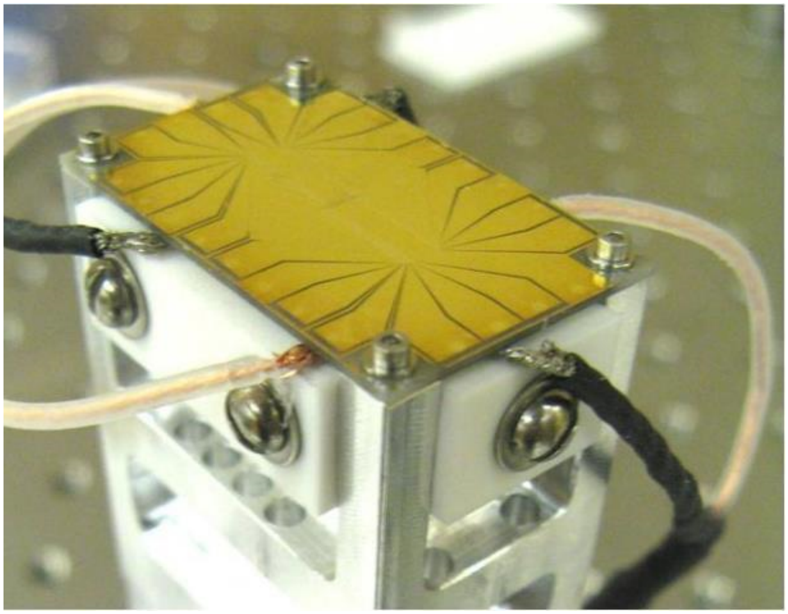

FIG. 4.13: This photo of the atom chip was taken before the chip was installed in the vacuum cell. It measures approximately 3 x 2 cm. The chip was made by Dylan Jervis from the Thywissen group at the University of Toronto.

by the atom chip and other magnetic field sources is equipped to handle experiments that need a trap with an elongated aspect ratio or a quasi-1D trap, RF near-field potentials, or close proximity to a surface for atom-surface force experiments. Typically, the pursuit of different experiments necessitate a modification or change of atom chip, but not retrofits to the full apparatus.

Atoms are trapped by the atom chip by confining them in the Z-wire trap created by a slender Z-shaped wire on the surface of the chip (Figure 4.14). The middle segment of the Z-wire is 50 μm across and the end cap segments are 200 μm across. The Z-wire has a height of approximately 3 μm in the vertical direction above the chip surface. An anisotropic Ioffe-Pritchard trap is generated beneath the Z-wire by a DC current is passed through the wire in addition to an external magnetic field B_{hold}, oriented such that the field is parallel to the surface of the chip and perpendicular to the middle segment of the Z-wire. The endcap segments of the Z-wire guarantee that the magnetic field value at the trap minimum is non-zero

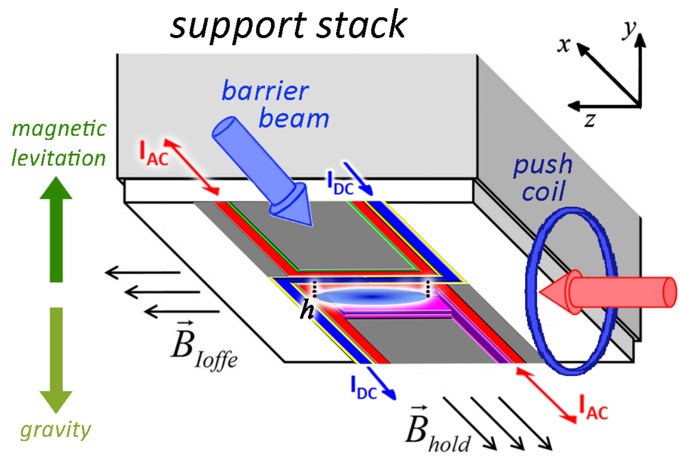

FIG. 4.14: Atom chip schematic. The chip wires are magnified and shown on the chip surface located underneath the chip stack. The magnetic field of the Z-wire (blue, I_{DC}) current and the external magnetic field ($\vec{B}_{hold}$) creates a cigar-shaped Ioffe-Pritchard trap, represented by the atom cloud (blue), at a distance (h) below the center of the chip. An additional magnetic field ($\vec{B}_{Ioffe}$) points axially along the trap and is used to provide the floor of the trap and prevent Majorana losses [60, 61]. The red wires (I_{AC}) on the chip are used for forced RF evaporation. The radial pump/probe beam (red arrow) and axial pump/probe beam co-propagates with the barrier beam (blue arrow). The push coil (blue ring) accelerates the atoms axially as gravity as canceled by magnetic levitation. Figure adapted from [43].

(see fig. 4.15). B_{Ioffe} is a longitudinal magnetic field, parallel to the middle Z-wire segment, used to increase this magnetic field value at the location of the trap minimum. The trap is approximately harmonic in all directions. The axial and radial trap frequencies for Rb have been determined to be $\omega_z = 2\pi\times 9.3$ Hz (50 Hz after sweeping the atoms into the dimple trap) and $\omega_r = 2\pi\times 1.1$ kHz, for $I_Z = 1$ A, $B_{hold} = 20$ G, and $B_{Ioffe} = 4.9$ G. The trap is located 100 μm from the surface of the atom chip. U-shaped wires are used to broadcast RF (3-20 MHz) and μRF ($\sim$6.8 GHz) magnetic fields to produce an RF shield, remove atoms in unwanted states, and for the forced evaporation of trapped atoms. There are more wires on the atom chip that may be used for other purposes and future experiments that are not exhibited in Figure 4.14.

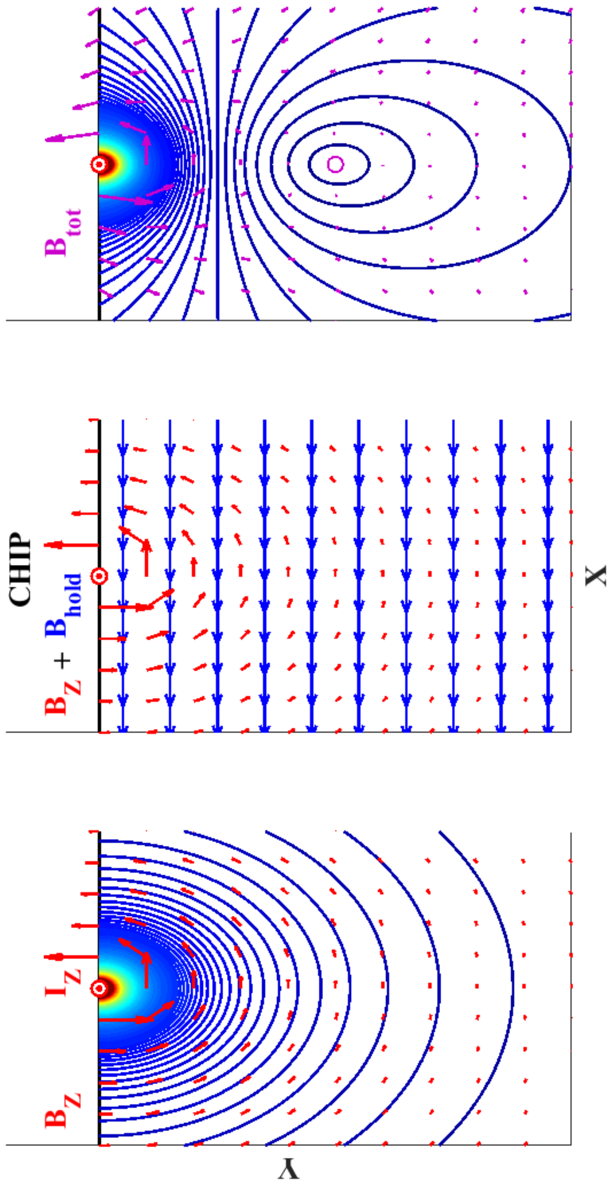

FIG. 4.15: Qualitative atom chip trap magnetic field diagram. Bottom: Current through the z-wire I_z generates a magnetic field ($\vec{B}_Z$, red) with magnitude and direction indicated by the vector field. The colored contour lines qualitatively show magnetic field magnitude. Middle: An external field oriented horizontally called $\vec{B}_{hold}$ (blue) is applied. Top: The resulting magnetic field ($\vec{B}_{tot}$, purple) has a minimum (purple cirlce) that is the trap location.

4.3.1 Safety Interlock

The current that flows through the Z-wire to create an atomic trap is provided by a high-precision, high-speed bipolar power supply (High Finesse, BCS 5/5). The output of the High Finesse is galvanically isolated from the analog control signal (via an internal Texas Instruments ISO124 chip). This feature of the power supply is important for the suppression of noise and ground loops. The ground of the Z-wire is connected to the optics table and vacuum system flange by a wire that is easy to access and modify. A safety interlock system, called the 'Killbox,' (Figure 4.16) is designed to shut off the chip current via a digital TTL control signal in the case of an over-current condition or if the current is on for too long. The High Finesse is internally configured to allow current for a high digital TTL signal. The High Finesse is equipped with a current monitor analog output signal u which is used to detect over-currents, and to integrate the monitored current, and trip if left on too long. Reference potentiometers connected to the other input of each comparator dictate the over-current and over-time settings. Once any of these safety conditions are tripped, the safety interlock will latch (via feedback loop incorporating IC1A, IC1B, and IC1C in figure 4.16) so that current cannot be driven through the device again without a manual reset. If the trip conditions are still active, the interlock will not reset. A fault indicator LED (yellow) will light up on the front panel. It is also common for the Killbox to trip with a false positive when the High Finesse is power cycled. This interlock system guarantees that the Z-wire current I_Z stays at or below 1 A for at most 10 s, which was determined to be safe based on resistive heating measurements.

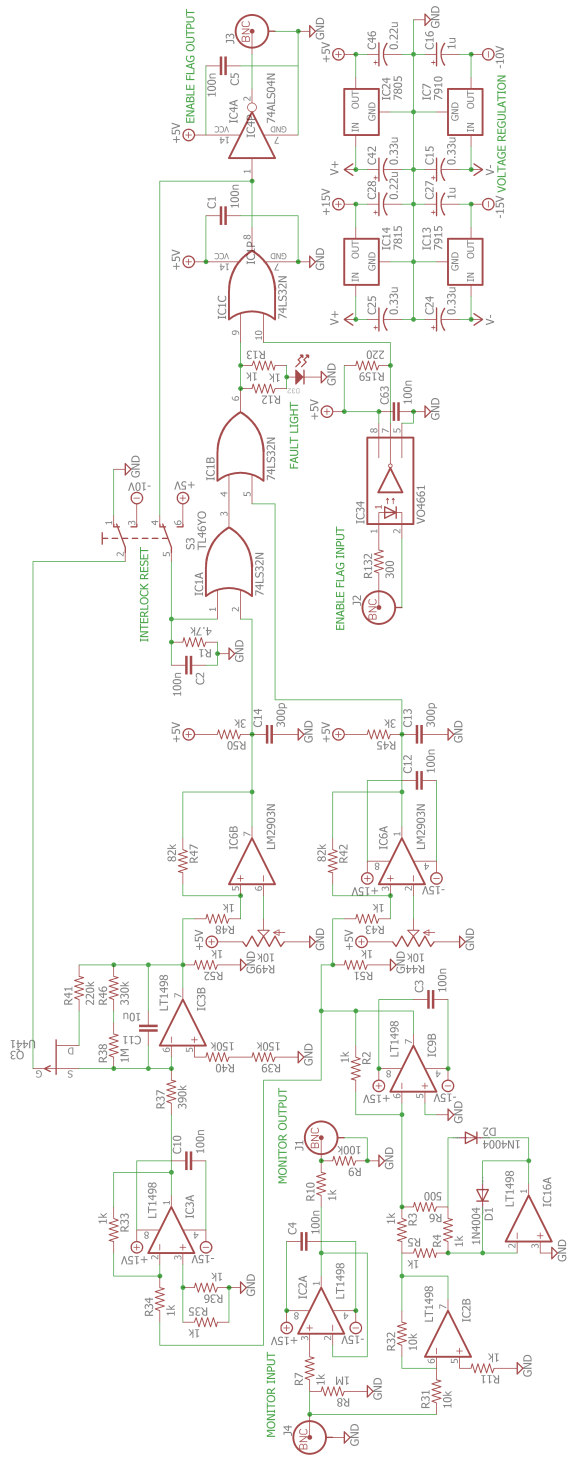

FIG. 4.16: Schematic for the Killbox.

4.3.2 RF Evaporation to BEC

Once the ^{87}Rb atoms have been loaded into the atom chip trap, the final stage of cooling begins. This method of cooling is known is evaporative cooling and is one of the oldest form of cooling known to mankind.[9] This cooling technology can be seen in the typical workplace scenario in which one makes a hot beverage and must wait some time before it is cool enough to drink. During this time, the hottest molecules of the beverage leave the cup, and the average temperature of liquid gradually decreases as this occurs. This technique is actively applied to the atoms in what is known as forced evaporation. A RF signal couples trapped atomic states to anti-trapped atomic states within the same hyperfine manifold. Applying this signal to the atoms causes a change in state, and the anti-trapped atoms are ejected. The atom chip trap is approximately a harmonic potential, in which a spatially varying magnetic field allows for the selective targeting of the hottest atoms. Hotter atoms oscillating in the trap encounter the edges of the trap, where the magnetic field has shifted the resonant frequency coupling to an anti-trapped state. This creates the ability for a particular RF signal to affect the edges of the atom cloud without affecting the center. In this way, the RF signal is known as an "RF knife" because of the manner in which it is capable of cutting into the atom cloud and removing the hottest subset of the population.

A direct digital synthesis function generator (Berkeley Nucleonics, model 645) provides a RF signal for forced evaporation. The function generator helped created our initial BECs when outputting 16 dBm, however this proved to be too much when optimizing the apparatus and resurrecting the ability to generate a BEC. The evaporation signal frequency is swept by the function generator under analog control

[9]For example, blowing on your hot coffee to cool it off.

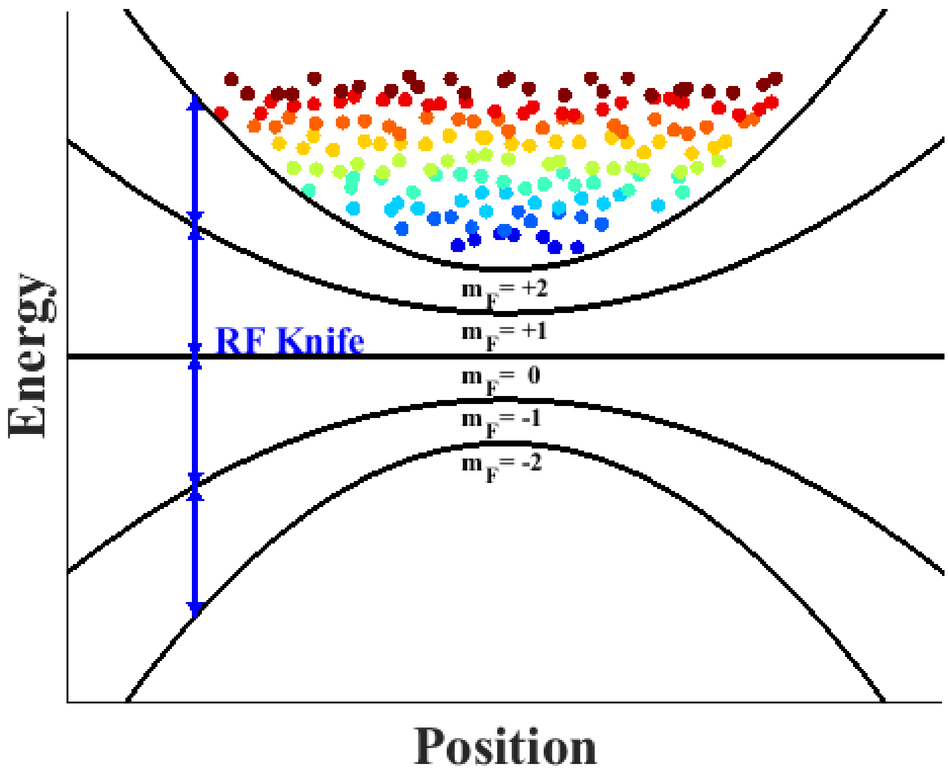

FIG. 4.17: RF evaporation diagram. Atom in the $m_F = +2$ state are evaporatively cooled by selecting the hottest atoms (red) to transition to an untrapped state. When the knife is stopped (without sweeping through the entire cloud), only the coolest atoms (blue) remain in the trap.

during the cooling process beginning at 19 MHz and ends near 3.4 MHz.[10] The RF signal amplitude is controlled by a variable voltage attenuator (VVA) and may be toggled on or off entirely with a RF switch control by a digital TTL signal. The signal is then AC-coupled to the chip and broadcast by one of the U-wires (see fig. 4.14).

During the evaporation process, I_z and $\vec{B}_{hold}$ are adjusted to change the trapping frequency. The trapping frequency is a useful metric for characterizing how compressed the atom chip trap is. This is important because the level of trap compression controls the collision rate and consequently the rethermalization process for the remaining atoms after the RF knife has removed atoms from the trap. $\vec{B}_{Ioffe}$ remains present to prevent Majorana loss (unwanted spin flips at a magnetic zero) and lifts the evaporation transition frequency above environmental noise in the kHz to MHz range. Efficient and slow evaporation pathways are preferable, however the finite lifetime of atoms in the chip trap requires that evaporation take place over a few seconds to yield the largest BEC.

Finally, I assess the performance of our apparatus based on the ability to generate a BEC and the number of atoms in the BEC. The simplest test of whether or not an atom cloud has been cooled to quantum degeneracy is to release the atoms from their trap and check for anisotropic expansion after some time-of-flight. As stated previously, hotter atoms are removed from the ensemble during evaporation. Therefore, a scenario exists in which the evaporation process is performed so inefficiently that end result is not only a lack of quantum gas, but no atoms left in the trap at all. However, even in a relatively efficient evaporation, atoms are still ejected from the trap, decreasing the potential atom number yield for the BEC. Evaporation efficiency will therefore be measured by the increase in phase space

[10]In practice the final frequency may vary on a daily basis when attempting optimum BEC production.

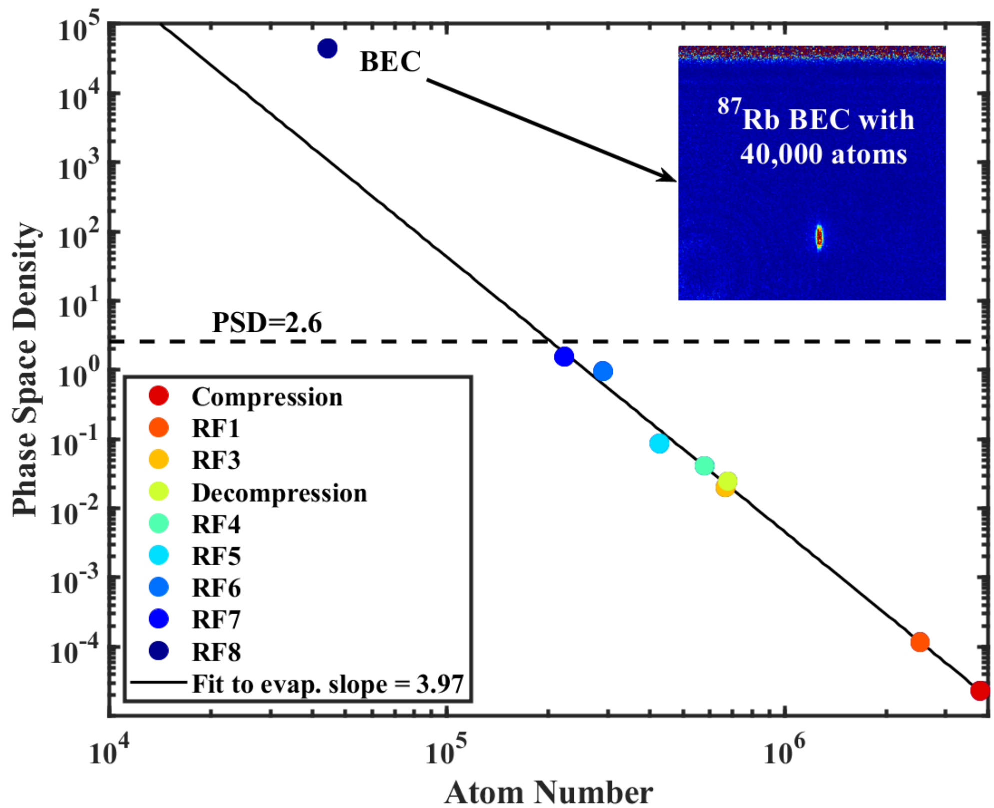

FIG. 4.18: Effective evaporation pathway to BEC. Plot of phase space density as a function of atom number beginning at the initial loading into the Z-wire trap (bottom right), continuing through 6 s of evaporative cooling with a RF knife to quantum degeneracy. The data is fit to: $PSD = N^{-m}$ where m is the evaporation efficiency. The points are larger than the error bars. A BEC of 40,000 atoms was produced. Images were collected using the axial camera with different times-of-flight.

density (PSD) relative to the atom number loss.[11] To track our progress, aid in BEC generation, and diagnose a "sick" apparatus, we plot PSD vs. atom number (N) as shown in figure 4.18. Data like the kind shown in this plot help to guide the choices of parameters (RF frequency, RF amplitude, trapping frequencies, etc.) to optimize the evaporation pathway. After identifying problems with the apparatus (too much RF power, $m_F = +1$ population) we succeeded in producing a BEC with approximately 40,000 atoms under optimal conditions.

4.3.3 BEC Jitter

The purpose of this section is to discuss BEC jitter and the problems it has caused in designing our single barrier scattering experiment. BEC jitter refers to an observed irreproducibility in the vertical position of a BEC after it has been released from the atom chip trap. This jitter is a problem when designing an experiment performed out of trap because our quasi-1D scattering experiment requires that a BEC interact with a tightly focused laser beam. If the vertical position of the atoms is inconsistent, then the atoms interact with the beam in a different location, with a different beam intensity due to the Gaussian profile of the beam. This is a problem because the beam intensity is directly proportional to one of the precisely tuned parameters required to observe a quantum effect. We considered this problem when planning the size of the beam, however making the beam larger is disadvantageous because it decreases the maximum achievable intensity given a finite amount of available beam power.

We initially noticed the problem with a BEC as the position shift on a small

[11] Phase space density is the metric of choice rather than spatial density or temperature because of trade-offs between those two quantities. For example, the temperature of the atoms could be lowered through adiabatic cooling, but in doing so the cloud becomes larger, and less dense. Phase space density is a convenient way of incorporating both. The BEC transition occurs for $PSD_{BEC} = 2.612$ [19] independent of T and n. $PSD = n\Lambda_{dB}^3$, where n is atom number density and Λ_{dB} is calculated via equation 3.1.

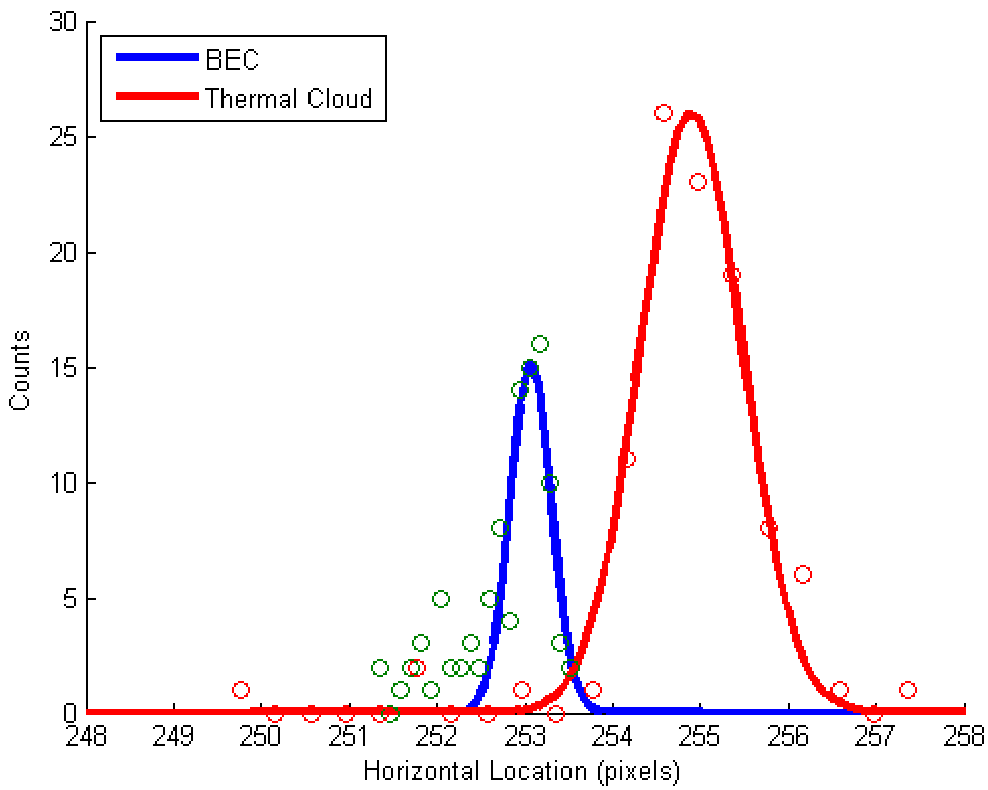

FIG. 4.19: Horizontal (vertical on rotated axial camera) location histogram. Gaussian curve fit to a histograms for each data set. One pixel on the axial camera is 4.65 μm.

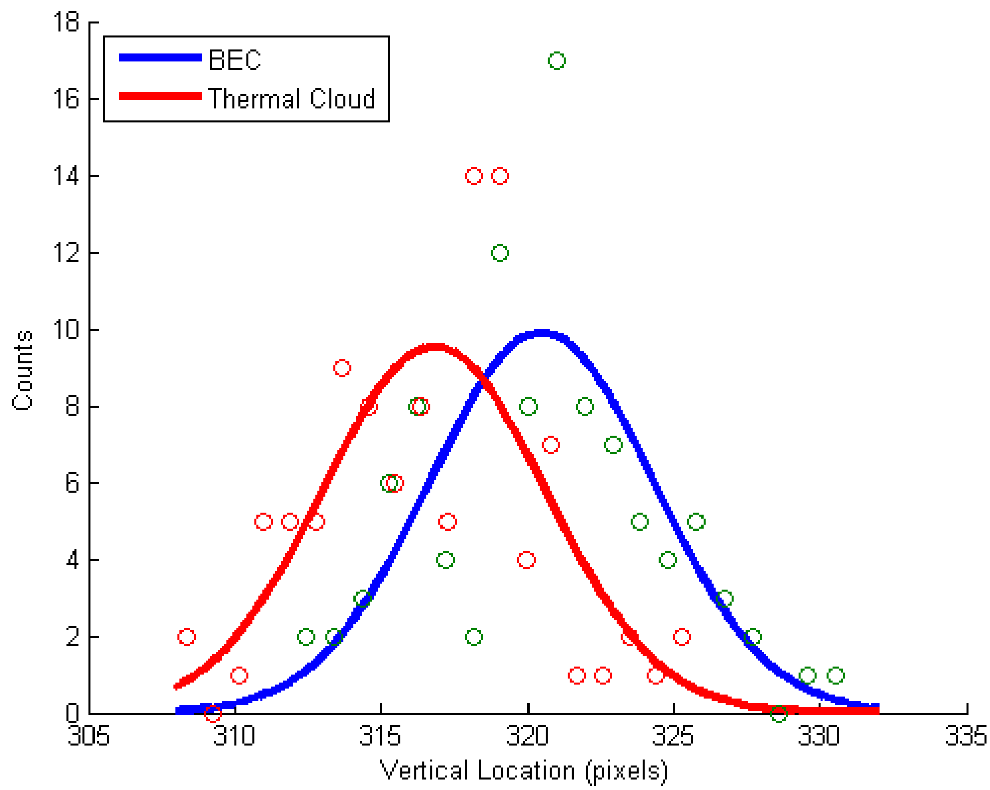

FIG. 4.20: Vertical (horizontal on rotated axial camera) location histogram. Gaussian curve fit to a histograms for each data set. One pixel on the axial camera is 4.65 μm.

cloud is more easily noticeable than an equal shift on a large cloud. However, when the same data for a thermal gas (larger diameter cloud at the same time of flight) was analyzed, it also displayed this irreproducibility in vertical position (see figures 4.19 and 4.20 for comparison between BEC and thermal cloud position distributions). We attempted to identify the cause of the problem by comparing the jitter from atoms released from the chip trap (figure 4.21) and a crossed optical dipole trap (ODT) (figure 4.22). We found that the ODT resulted in a significantly smaller spread in vertical position, and approximately equivalent to the spread in horizontal position. This forces us to conclude that something unique to the atoms being held by the chip or magnetic forces is causing the jitter, as the atoms did not exhibit the same behavior when held entirely by optical forces. Another clue that helps to identify the cause of the problem is the observation that the horizontal position does not exhibit the same level of irreproducibility as the vertical position. This combined with the observation that a magnetic force or gradient is causing this problem suggests that a current source positioned above or below the atoms is the origin of the problem. There are four current sources on at the end of the evaporation cycle: the Z-wire, the hold field, the Ioffe field, and transport coil 7. Coil 7 is used as a push coil to sweep the atoms horizontally into a dimple in the trapping potential during the latter half of RF evaporation to access higher trapping frequencies and a higher collision rate for cooling to quantum degeneracy. Coil 7 is an anti-Helmholtz coil pair with each coil position to either side of the vacuum chamber. While this current source produces a small vertical gradient (very little current, <3 A, is used during evaporation), turning off coil 7 prior to the Z-wire trap did not eliminate the jitter. A similar argument can be made for the Ioffe and hold coils. This leaves only the Z-wire. We propose, although cannot confirm, that the atoms are receiving a small, but irreproducible kick from the Z-wire as it is turned off. The vertical position jitter is shown to be greater at larger times of flight,

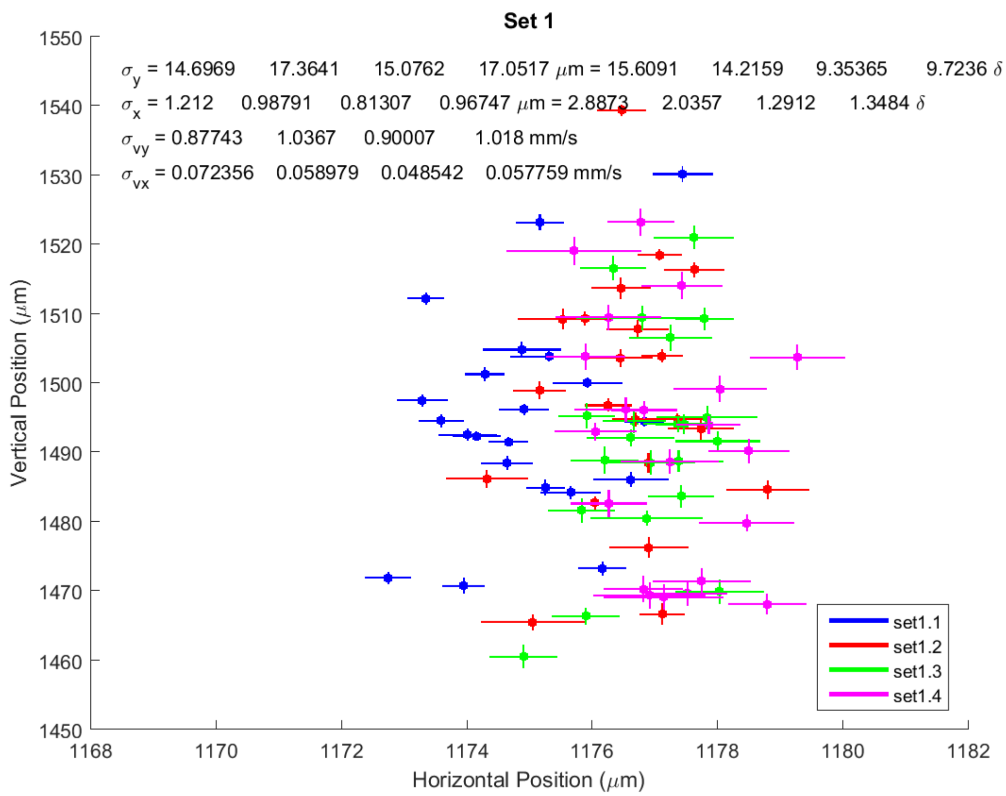

FIG. 4.21: Jitter data for atoms released from the atom chip trap (∼80 images collected). Atom cloud locations are plotted as vertical position vs. horizontal position. Vertical and horizontal error bars are shown. The data points were collected sequentially, without significant pauses. The data set is broken into subsets to track position drift. Standard deviation values for vertical and horizontal positions and sizes are shown in separate columns corresponding to subsets. Note the vertical scale compared to the horizontal.

indicating that the jitter is really a velocity jitter (the relevant data supporting this is more appropriately discussed later, in chapter 5, and figures 5.29 and 5.30). This supports the Z-wire kick theory and it appears that something associated with the turn off of the Z-wire trap causes the jitter (maybe an irreproducible eddy current in the chip).

In an attempt to combat this problem, we varied the trap turn-off procedure and parameters for the Z-wire, Ioffe, and hold. We also changed the linear current ramp to a minimum-jerk trajectory ramp to turn the Z-wire off more smoothly. No

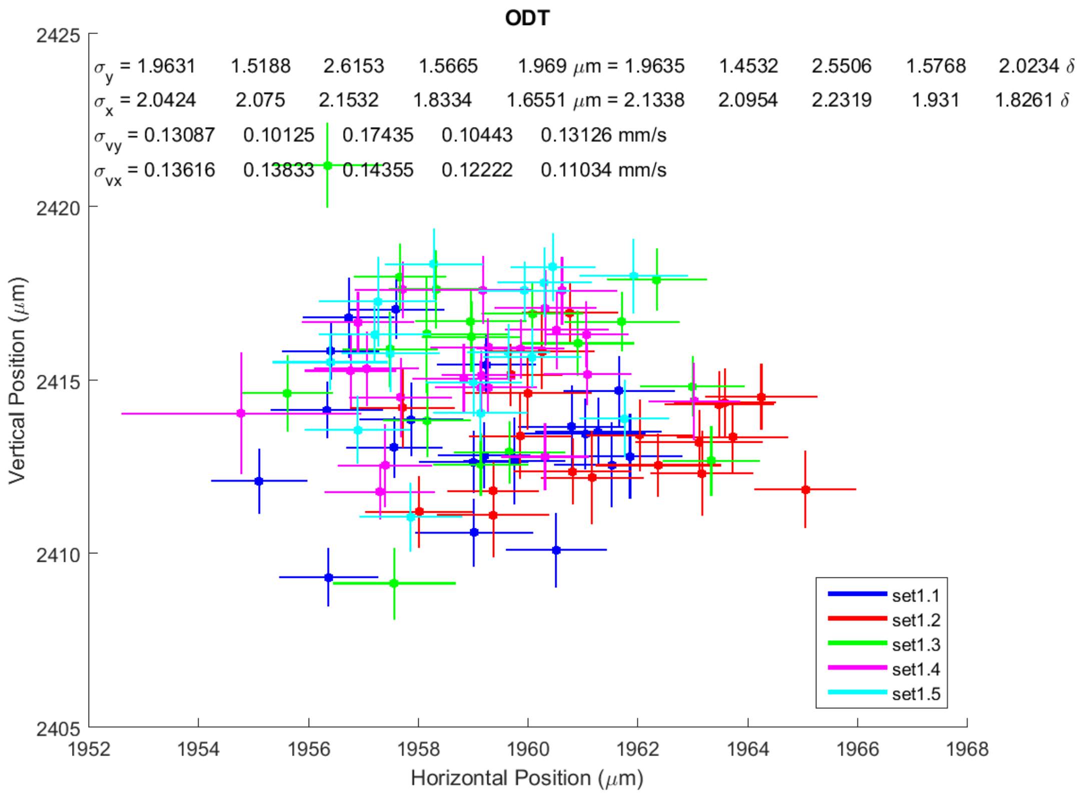

FIG. 4.22: Jitter data for atoms released from an ODT (∼100 images collected). Data is displayed in a similar format to figure 4.21.

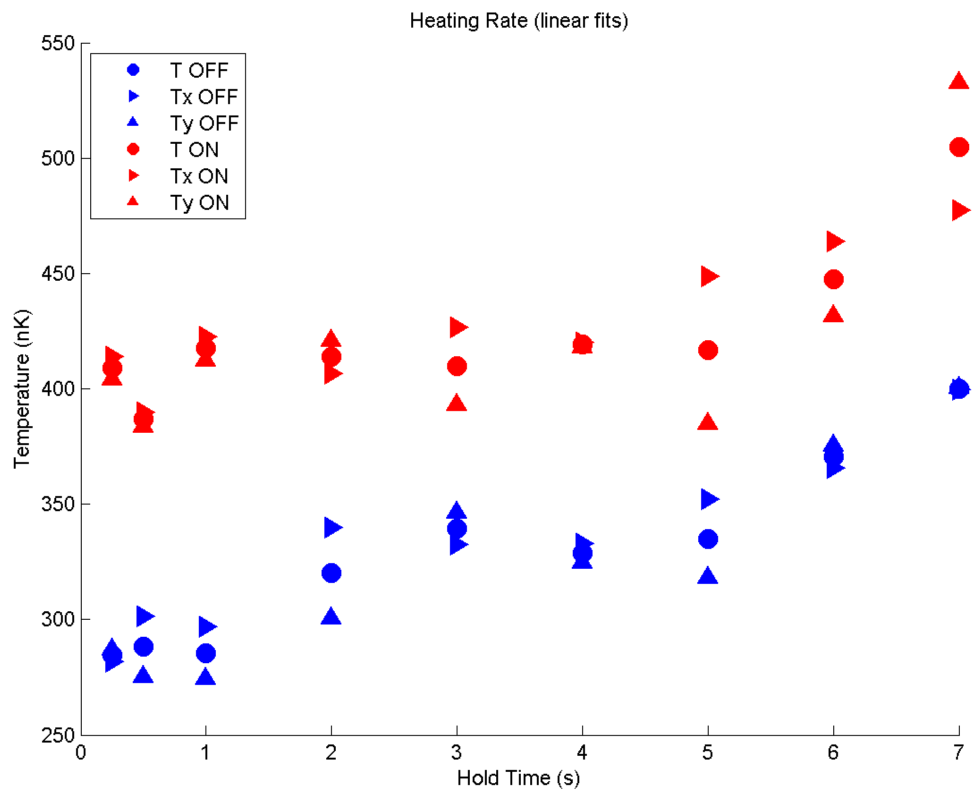

FIG. 4.23: Heating rate displayed as temperature vs. trap hold time. Temperatures are displayed with the Z-wire on (red) and off (blue). Circles display the mean temperature, while triangles show the temperatures derived from the horizontal (T_x) and vertical (T_y) expansion rates.

changes made appeared to be helpful, and the data collection process to produce enough statistics was very time-consuming.[12] We are unsure of the root cause of this problem or how to solve it. We are aware of a physical defect in our atom chip that has prevented the use of higher currents through the Z-wire. It is also possible that this phenomenon limits the effectiveness of our delta-kick cooling attempt mentioned in section 6.1

The obvious course of action is to create a BEC in an ODT. While other research groups [62, 63, 64, 65, 66, 67, 68, 69, 70, 71, 72] have demonstrated that this is

[12]The MOT loading stage was shortened to decrease overall apparatus cycling time, however this causes over-temperature problems in some of the coils when the cycle time is too short.

possible, it is more difficult. Evaporation in ODT is generally accomplished by lowering the trap depth by decreasing the ODT laser power, which also relaxes the trap and consequently the collision rate. The mean trapping frequency of the ODT is $\bar{\omega} = (\omega_x \omega_y \omega_z)^{1/3} = 2\pi \times (164 \times 186 \times 28)^{1/3} = 2\pi\times$ kHz, compared to $\bar{\omega} = (\omega_r^2 \omega_z)^{1/3} = 2\pi \times (1141^2 \times 50)^{1/3} = 2\pi \times 402$ Hz for the chip trap. The result is a lower evaporation efficiency, which necessitates longer evaporation times, which ultimately competes with the lifetime of the trap. We have also measured a heating rate ($\sim 14nK/s$) and overall higher temperature with Z-wire on ($\sim 100nK$) in the ODT that severely hampered our ability to cool in this trap (figure 4.23). We were forced to conclude that cooling to quantum degeneracy is not a viable option in our existing crossed ODT with our initial conditions. The solution to the BEC jitter problem is to continue to use the atom chip trap to generate a BEC with a healthy atom number. The effects of the velocity jitter can be minimized by elongating the vertical height barrier beam used for the quantum pumping experiment such that the atoms feel no significant variation in barrier energy, despite the jitter.

CHAPTER 5

Magnetic Levitation System

In this chapter, I discuss in detail the hardware used to drive an anti-Helmholtz coil pair in the transport system (coil 6 in Figure 4.3 in Chapter 4) for levitating atoms near the atom chip. The transport system is already designed to hold atoms against gravity, and propagate them upwards towards the atom chip. We use the transport coils again to create a magnetic gradient that provides an upward force on the atoms that is proportional to the current through the coils. The chip trap holding the atoms must be turned off to allow the atoms to propagate and perform the experiment and coil 6 must be turned on quickly to prevent the atoms from acquiring a downward velocity between trap release and coil turn-on. In order to prevent this, coil 6 requires 75 amps of current to pass through it the instant the trap is turned off. Turning on the coils before turning off the trap was expected and confirmed to have a detrimental effect on the atoms due to the addition of the magnetic fields. This section presents the design, construction, and characterization of a high current fast switch, named the 'Levitiathan,' [1] that is capable of turning

[1]Levitiathan is the result of merging 'leviathan' and 'levitation'. Other whimsical names for equipment in our lab include Lasersaurus Rex, Purple Haze, Killbox, Dr. Watts, Cinderella, Step-mother, and the BEC Apparatus Magnetic Field (BAMF) Switch

on current through coil 6 in less than 2 ms (this was closer to 1 ms at higher power supply voltages, but ultimately proved unworkable due to power supply instability).

A previously constructed fast switch (named the BAMF switch built by A. Ziltz using Insulated Gate Bipolar Transistors or IGBTs) is used to quickly turn on current through the MOT (Magneto-Optical Trap) coils [43]. This switch consists of multiplexed power sources and solid state transistor switches to make and break the connection to the MOT coils. This device successfully switches current through the MOT coils quickly (<1 ms), but does not have the capability to control and modulate the current with dynamic precision. To clarify, the BAMF switch was used to make or break an electrical connection, and had no ability to control the amount of current.

Since we require fast dynamic control of the current, we chose a new design for the Levitiathan that uses power MOSFETs (Metal-Oxide-Semiconductor Field-Effect Transistors; model: IXYS IXTN200N10L2) to quickly turn on and dynamically modulate current through the transport coil 6. This method was based on previous work by the Spielman group at the Joint Quantum Institute [73, 74, 75], and is an improvement over our previous BAMF fast switch which lacked the ability to modulate current.

This chapter is structured in the following manner. Section 5.1 motivates the purpose of the levitation system in the experiment. Section 5.2 gives a detailed description of the Levitiathan current modulator instrument and circuitry. Section 5.3 describes the operation of the Levitiathan, and how it is integrated into the transport system of the BEC apparatus. In section 5.4, I review the theory of magnetic levitation and discuss how it informs the experimental tuning of our scheme levitation scheme. Finally, section 5.5 presents the performance of the levitation system.

5.1 Motivation

A BEC with small atom-atom interactions requires a lower atomic density than what is found in-trap. The solution to this problem is to conduct the scattering experiment out of the trap to take advantage of the smaller interactions, though the atoms will then fall under gravity. Thus, coil 6 is capable of providing a vertical magnetic gradient that can cancel gravity. Unfortunately, the field generated by Coil 6 adds to the chip trap field causing the trap center to quickly move to a new location that is much further away. Coil 6 can only be turned on after the trap has been turned off. During the time between trap release and Coil 6 equilibrating to the appropriate current, the atoms acquire a downward velocity. The Levitiathan is constructed to turn on current quickly and modulate in such a way as to halt the vertical motion of the atoms to achieve levitation. An initial levitation test using coil 6 in slow turn-on mode successfully levitated atoms from a dipole trap (no BEC) using 70 A of current (see Figure 5.1).

A rapid turn-on of current is essential for achieving atomic levitation from the chip trap on short time scale. Our high current supply (Agilent 6571A-J03) cannot respond to programming changes faster than 50 ms, limiting the turn-on speed and levitation performance. Figure 5.2 shows an attempt at levitation with such a slow current source. Also, coil 6 must be turned off before absorption imaging takes place, though the speed at which the current turns off is not critical. Instead, we prefer to avoid long-lived eddy currents caused by a rapid turn-off. Additionally, the transport coil multiplexer (this “coilplexer” device is used for directing current to various transport coils during the transfer of atoms from the MOT cell to the chip cell) can be used to stop the flow of current through coil 6.

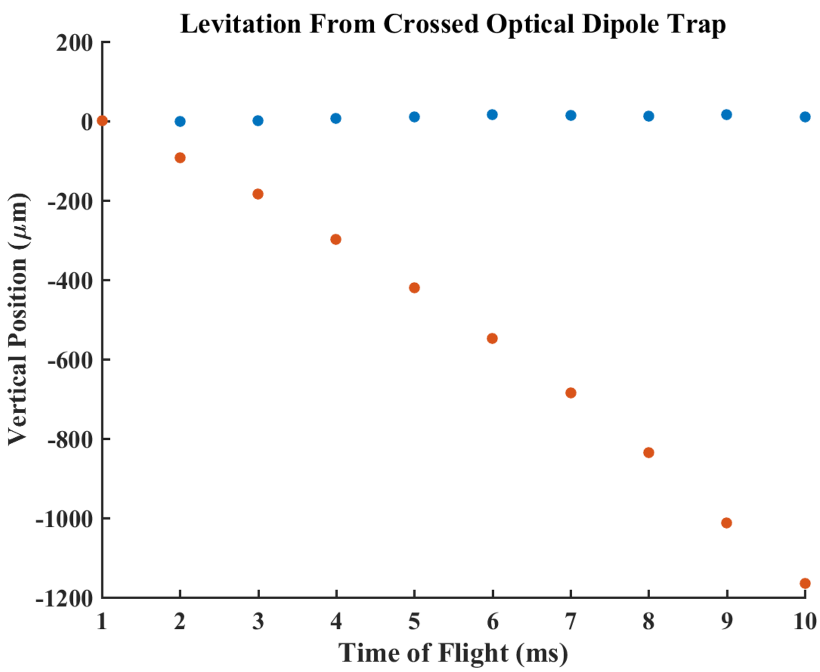

FIG. 5.1: Magnetic levitation of cold atoms released from an optical dipole trap. Red dots shows atoms falling under gravity after being released from the optical dipole trap. Blue dots show atoms levitating after being released from the same trap in the presence of a magnetic gradient provided by coil 6.

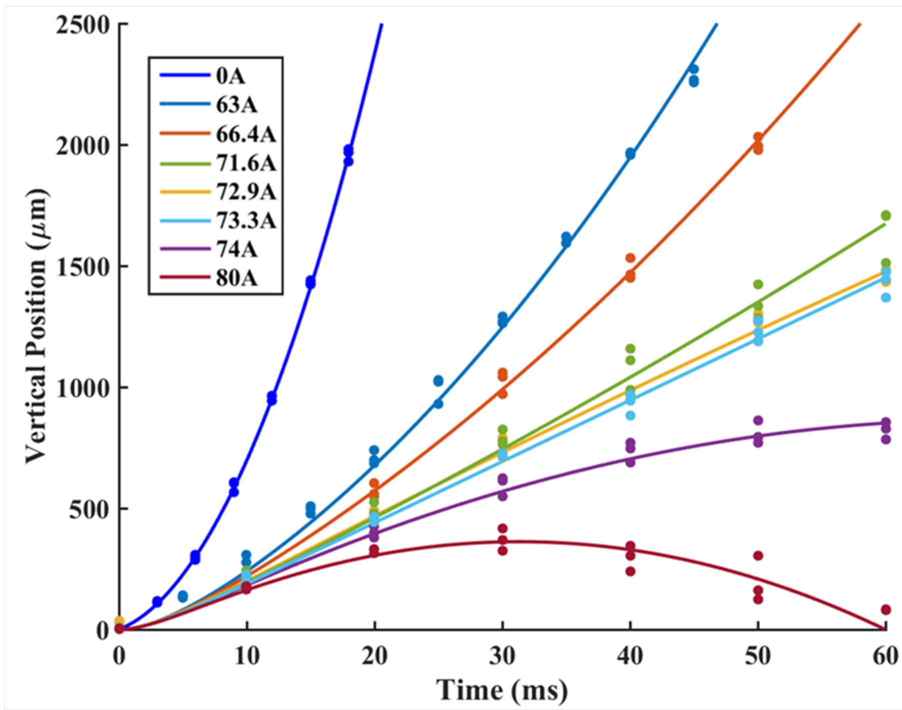

FIG. 5.2: Ultracold atoms falling under suppressed gravity as levitation coils turn on slowly. The positive vertical direction is down, away from the atom chip in the apparatus (This may seem counter-intuitive, but it is actually in keeping with the pixel numbering on the axial camera).

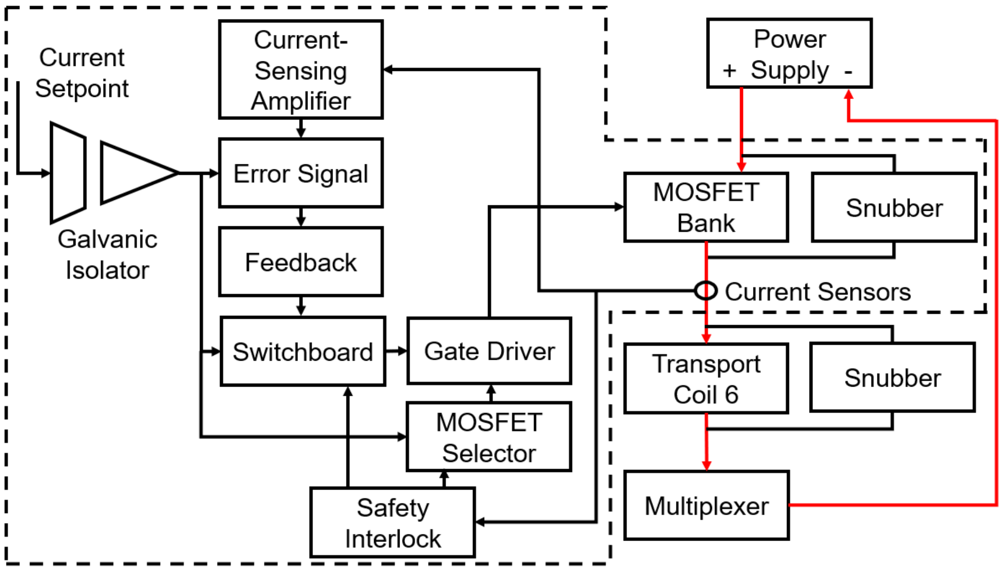

FIG. 5.3: Block diagram of the levitation system. Components included inside the Levitiathan are enclosed by the dashed line. Red lines indicate thick wires carrying large currents, while the black lines indicate are small wires carrying low current control signals.

5.2 Design and Theory of Operation

The Levitiathan has been designed to safely and reproducibly provide a fast turn-on and good current control. It is important to understand its operation before it can be modified, repaired, or reconfigured for anything other than its intended use.

The Levitiathan converts an existing power supply (providing a constant voltage source) into a high-speed current source for driving inductive loads (see Figures 5.3, 5.4, and 5.5[2]). A bank of several power MOSFETs in parallel is used to dynamically regulate current through an inductive load while the power supply is operated in constant voltage mode. An error signal is generated by comparing a control input with the current measured by a current sensor. Proportional-integral (PI) feedback is used to drive the gate voltages of the MOSFETs to stabilize the system to the

[2]The component labels for the full schematic in figure 5.5 may or may not match the component labels in the following subcircuit schematic figures.

FIG. 5.4: Levitiathan current modulator with constituent components.

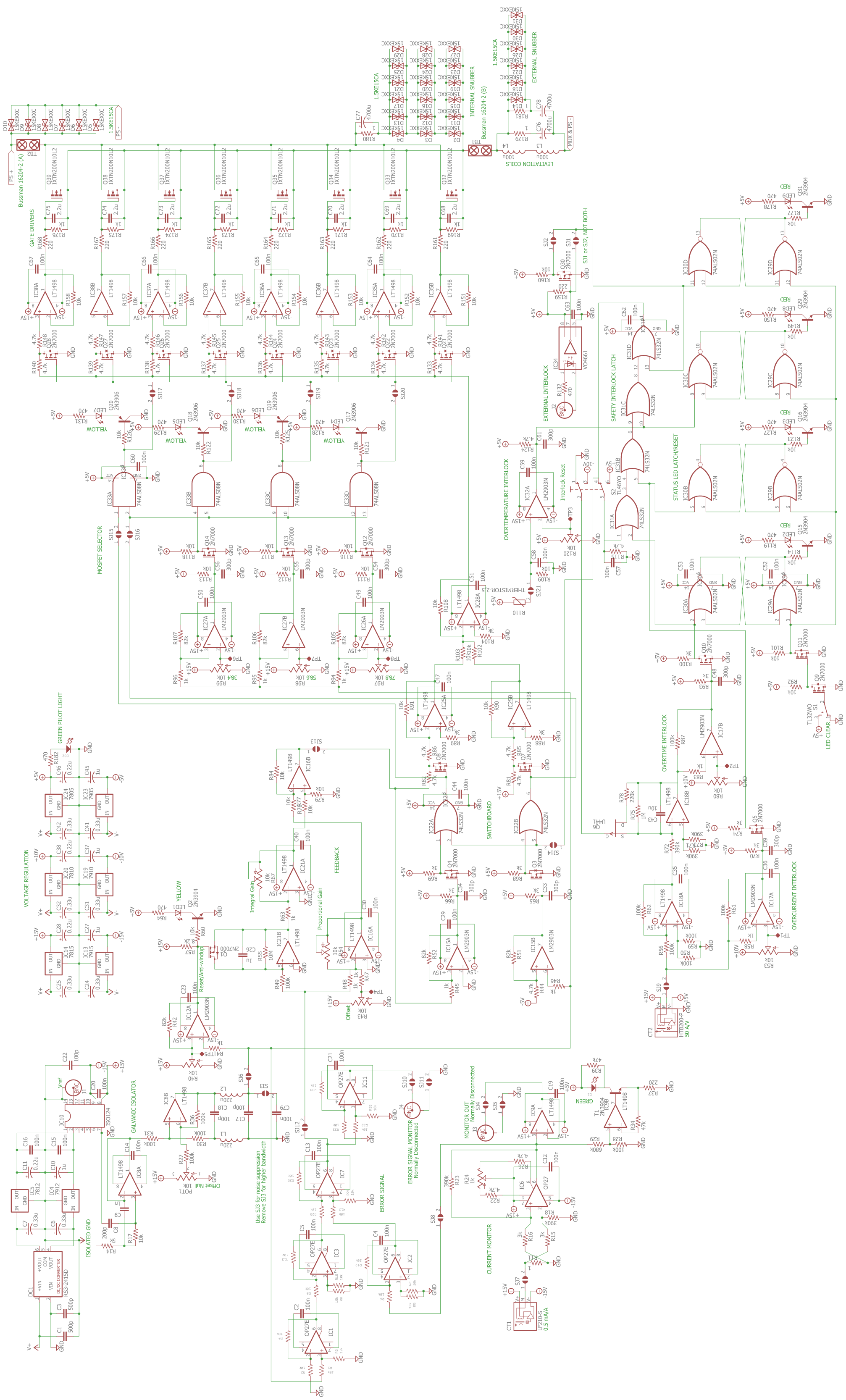

FIG. 5.5: Full schematic of the levitation current modulator. The block diagram for the schematic is shown in figure 5.3.

desired current. Before turn-on, the power supply is programmed to operate in constant voltage mode. Once the current has the desired level, the power supply can be programmed to gradually lower the output voltage to reduce the amount of power the MOSFETs must dissipate, so long as the current is not limited.

Effectively making or breaking the electrical circuit with the power MOSFETs induces a voltage spike across the coils given by $\Delta V = L \cdot \frac{dI}{dt}$. The MOSFETs can tolerate up to 100 V between the drain and source. When the circuit is broken by the MOSFETs, the coil must dissipate its stored magnetic energy. To protect against high voltages, snubbers using transient voltage suppression (TVS) diodes (1.5KE15CA) were placed in parallel with both coil 6 and the MOSFETs. I will now discuss in greater detail each of the components of the Levitiathan design shown in figure 5.3.

5.2.1 Isolation

Coil 6 is powered by an Agilent 6571A-J03 power supply (153 A, 14.3 V). The current and voltage settings of all of the programmable power supplies in the lab, including this Agilent, are independently controlled by the Adwin sequencer. The Agilent 6571A-J03 power supplies have a enable/disable button in addition to the front panel power switch. The default setting after power up is disabled. This is an easy way to disable the power supply instead of switching it off.

Extensive effort has been taken to ensure that the remote programming inputs are electrically isolated from the experimental ground and Adwin sequencer for safe operation. Apart from preventing ground loops, the isolation is need because the programming input grounds on the Agilent are directly connected to the power supply positive output. If any of our coils were to contact each other or the optics

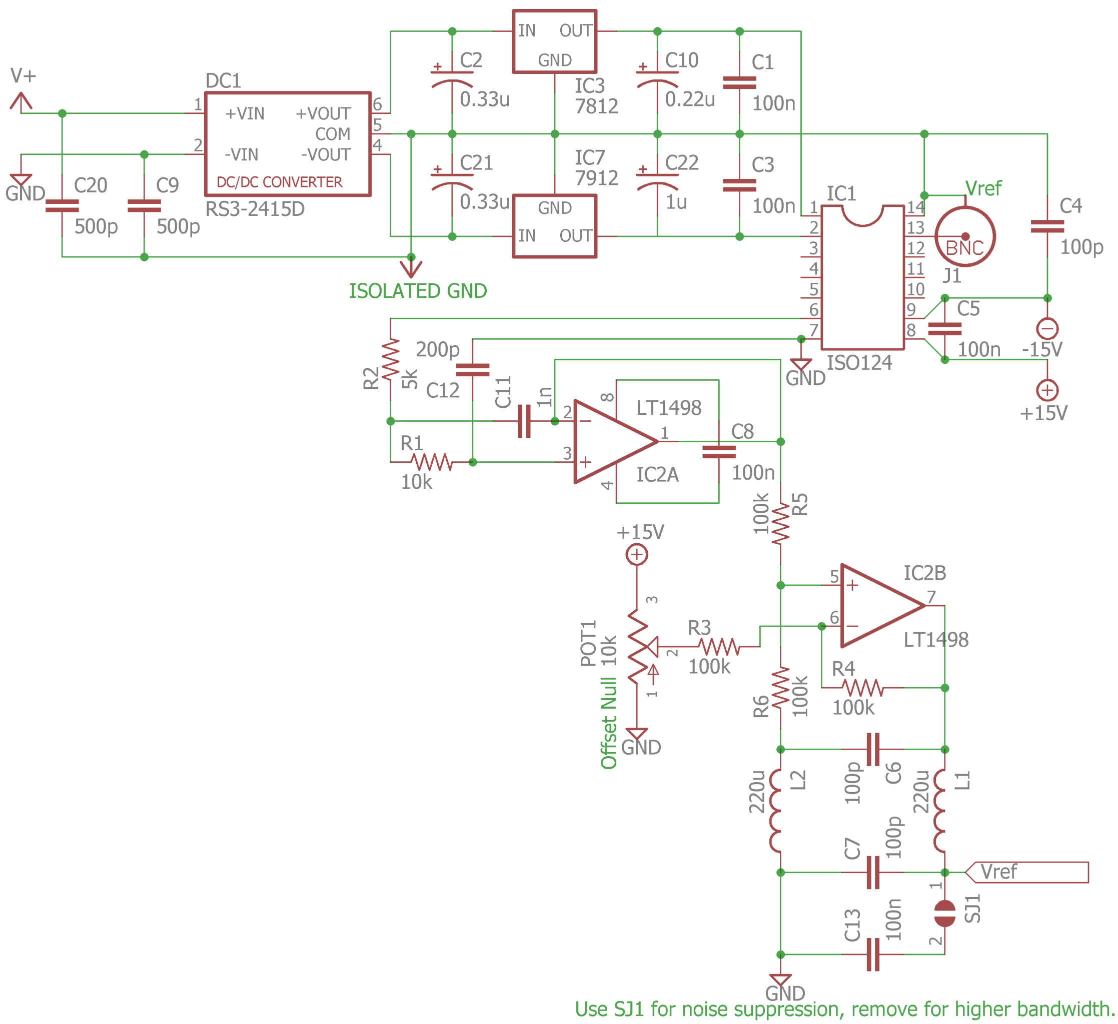

FIG. 5.6: Schematic of the galvanic isolator circuit. Jumper SJ1 may be used to achieve lower noise at the cost of bandwidth. This circuit buffers the signal V_{ref} received from the Adwin sequencer via BNC jack. The output signal labeled V_{ref} connects to the error signal, feedback, switchboard, and MOSFET selector circuits (figures 5.10, 5.11, 5.12, and 5.13).

table, it could potentially send high current back through the Adwin sequencer.[3] To prevent such carnage, the analog control signals for programming the Agilents and the fast switch are connected to the Adwin sequencer through a galvanic isolation buffer (Texas Instruments, ISO124), schematic shown in Fig. 5.6. Similarly, the only digital input to the switch is also isolated with an optocoupler.

5.2.2 Power Supply

An Agilent 6571A-J03 was used to develop the power supply. This was a 2 kW power supply with 14.33 V and 153 A maximum outputs. This model power supply was originally used for the switching of a 200 μH anti-Helmholtz coil pair. We required a power supply that could generate $\sim$75 A through these coils either quickly ($\sim$ 3 μs), or with good current control, and this power supply was capable of neither. I also discovered during development that the power supply, with MOSFET current regulation, could only remain on at its maximum voltage setting for a short time, that is several seconds, before blowing a fuse (F308, 0.5 A time-delay). This fuse feeds power to an H-bridge modulating the primary transformer that regulates the output voltage. Agilent/Keysight was unable to help us solve this issue. The acceptable workaround was to either pulse the current for a short time, or operate the supply at a lower output voltage. I later discovered that operating the supply at maximum voltage with MOSFET current regulation would cause noise on the supply's output voltage. This may be consistent with the aforementioned fuse blowing if the transistors in the H-bridge driving the transformer require more current to regulate the output voltage. A higher voltage is preferable because the performance of the device is faster.

[3]Such an unfortunate event has happened to the Thywissen group (University of Toronto).

5.2.3 MOSFETs

The IXYS IXTN200N10L2 power MOSFET was chosen to regulate current for its extended Forward Bias Safe Operating Area (FBSOA). A MOSFET used in this capacity can be viewed as a voltage controlled variable resistor. A higher power supply voltage decreases the turn-on time, so is therefore preferable for performance. However, the MOSFETs experience the excess voltage drop and must be able to dissipate a large amount of power. Eight MOSFETs have been used in parallel instead of just one, effectively distributing the power. To help dissipate the power, the MOSFETs are mounted on a copper plate 3/8" thick.

All eight MOSFETs cannot be used simultaneously under all conditions. If the desired current is too low, too many MOSFETs will increase the noise on the current. I believe this is due to some instability in the MOSFET near the conducting/insulating transition. More active MOSFETs requires them to operate closer to the transition than with fewer MOSFETs. To counter this problem, I have designed a MOSFET selector that turns off some MOSFETs incrementally as the current is lowered. These settings are adjustable with internal potentiometers. The MOSFETs, like all transistors, have a parasitic capacitance (Miller capacitance). This capacitance is present between all three terminals of the MOSFET. When combined with the inductance of the wires connected to the terminals of the MOSFET, a parasitic oscillation can appear on the drain-source voltage (V_{DS}) and the current. This oscillation can appear as a high amplitude, high frequency (MHz range) that is capable of burning out the protection diodes across the drain and source. It is helpful to use more than one TVS (Transient Voltage Suppression) diode in parallel to protect the MOSFETs. To prevent the oscillation, I used coaxial cable to deliver the gate signal to the MOSFETs. The gate driver was designed with carefully chosen values to help mitigate the high amplitude oscillations. I also added a ferrite bead to the wires carrying the gate signal. The drain and source are attached with thicker gauge twisted pair wire. Later, a snubber circuit was added to help suppress transient voltages between drain and source.

5.2.4 Current-Sensing

The current sensor is used to measure the current flowing through the MOSFETs (which is in series with the load) and use that information to provide feedback to the MOSFET's gates, delivering and stabilizing the requested amount of current. The LEM LF 210-S was selected for its relatively low noise and cost. Unlike the LEM HTB 200-P sensor used in the safety interlock for this device, as well as in the coil multiplexer ("coilplexer") and the BAMF switch, the LEM LF 210-S produces an output current rather than a voltage proportional to the measured current. To convert this current into a voltage, I constructed a current-sensing differential amplifier (adapted from The Art of Electronics, Horowitz & Hill, Third Edition, figure 4.91, page 278). The amplifier consists of a current shunt and a differential amplifier, shown in Fig. 5.7.

5.2.5 Protection Diodes

Transient Voltage Suppression (TVS) diodes are connected in parallel with the drain and the source of the MOSFETs to protect the MOSFETs from the induced voltage generated from fast inductive switching. These diodes were later incorporated in a voltage snubber connected in parallel with both the MOSFETs and the coils. 1.5KE15CA TVS diodes were chosen because they were also placed in parallel with the power supply. They have a 15V clamping threshold, which is slightly above the maximum output voltage of the supply.

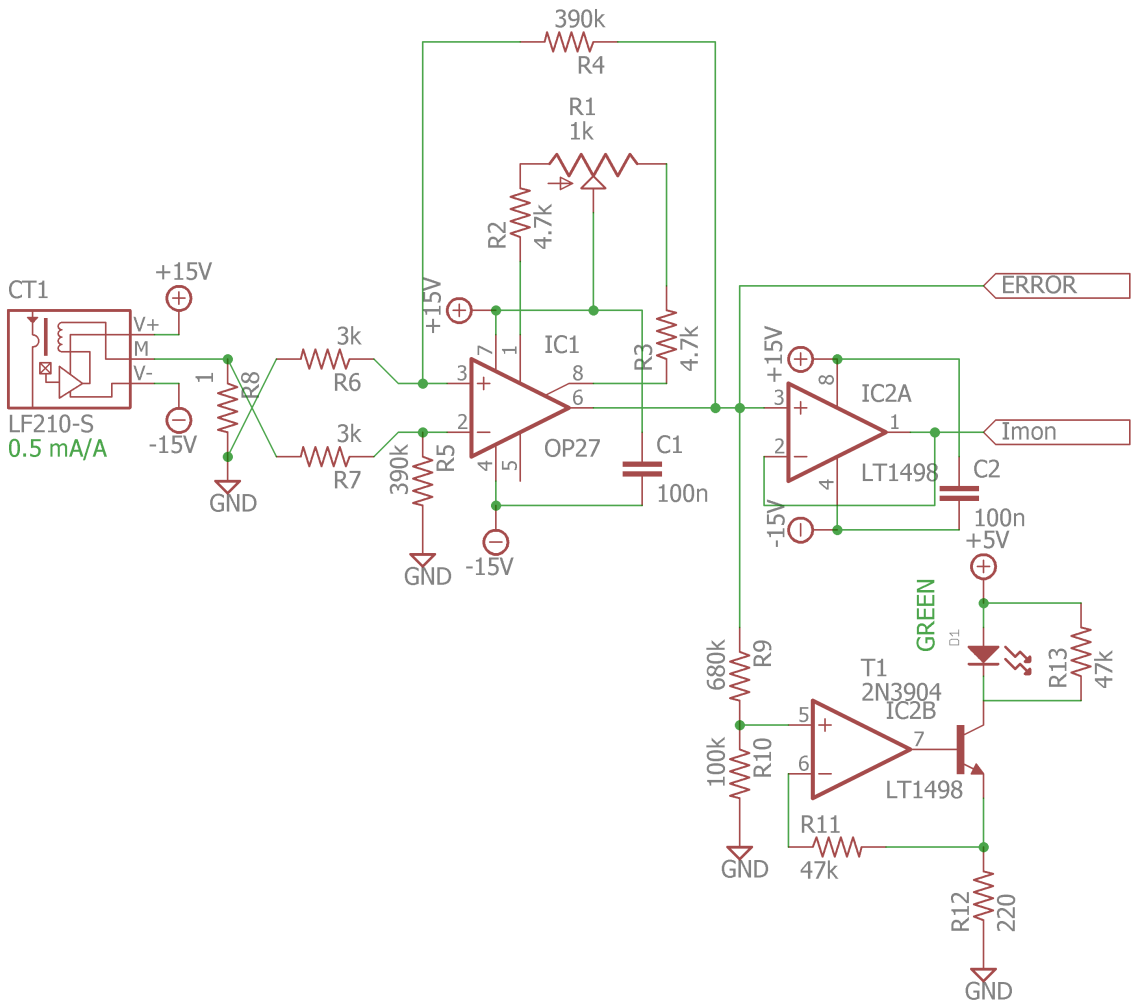

FIG. 5.7: Schematic of the current-sensing amplifier circuit. The LED (D1) brightness is proportional to the current. The signal labeled ERROR connects to the error signal circuit (fig. 5.10) to input the measured current. The I_{mon} signal is meant to connect directly to a BNC jack on the front panel. The jack is not normally connected, but can be with provided jumper connections. Plugging a device into the I_{mon} jack will connect said device to the Levitiathan ground, which is also connected to the Agilent power supply's negative terminal. It is strongly advised to use an isolation transformer when monitoring this signal with a scope. Therefore, this jack is normally left unconnected internally. During the experiment, this monitor was not necessary because a current monitor was already available for coil 6 via the coilplexer.

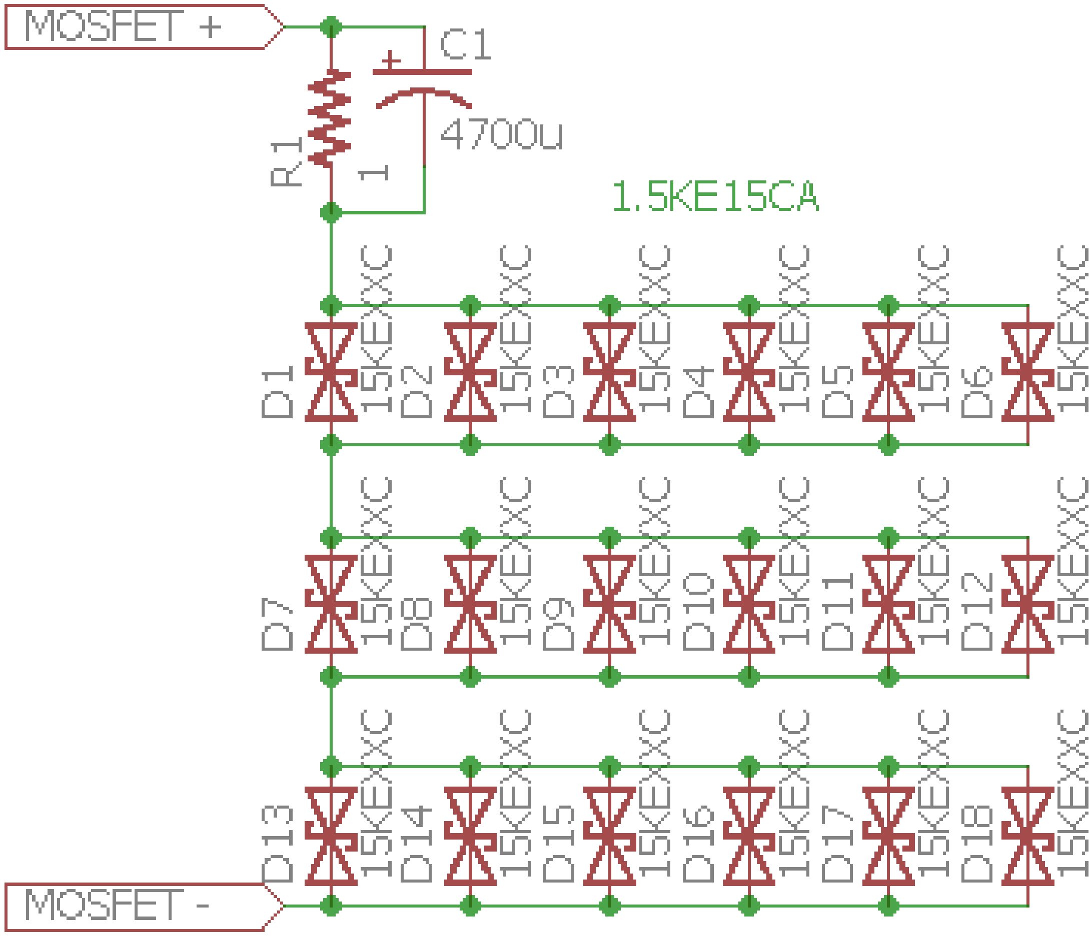

FIG. 5.8: Schematic of the snubber circuit in parallel with power MOSFETs.

5.2.6 Snubber

Snubbers are energy-absorbing devices that can be used to suppress the transient voltages caused by fast inductive switching. The design can be widely varied. Diode snubbers with optional resistors can be used to clamp a transient voltage, while RC snubbers use a large capacitor that charges during the voltage spike, and later discharges through the resistor. Different combinations of resistors, capacitors, and diodes were tested empirically for their suppressing ability. See schematics (figures 5.8 and 5.9) for details.

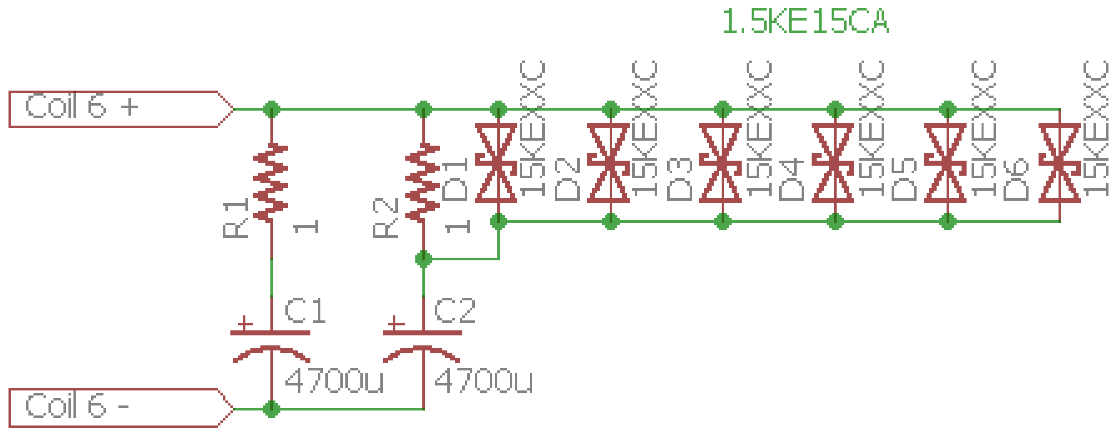

FIG. 5.9: Schematic of the snubber circuit in parallel with the levitation coils.

5.2.7 Feedback

A PI feedback circuit (figures 5.10 and 5.11) was designed to stabilize the current by modulating the gate voltage appropriately. This circuit had the task of not only stabilizing the current, but to also be capable of turning it on quickly. This requires either derivative gain for PID feedback, or a large proportional gain. The circuit is designed with the latter, but has additional space for a derivative gain stage to be added if necessary. An offset was added to the proportional amplifier and set at ~ 3 V, as the MOSFETs do not begin to conduct until the gate reaches ~ 4 V. This was done to shorten the delay between receiving a signal and the current beginning to turn on. The integrator opamp was fitted with a MOSFET reset switch that is held closed to prevent premature integration. This is referred to as the anti-windup integrator. A 2N7000 MOSFET is used to short the integration comparator for anti-windup. This MOSFET's gate is driven by a comparator with ± 15 V output.

5.2.8 Switchboard

The switchboard (Fig. 5.12) is designed to relay the appropriate signal to the MOSFET gate driver. When the current through the load is being controlled by

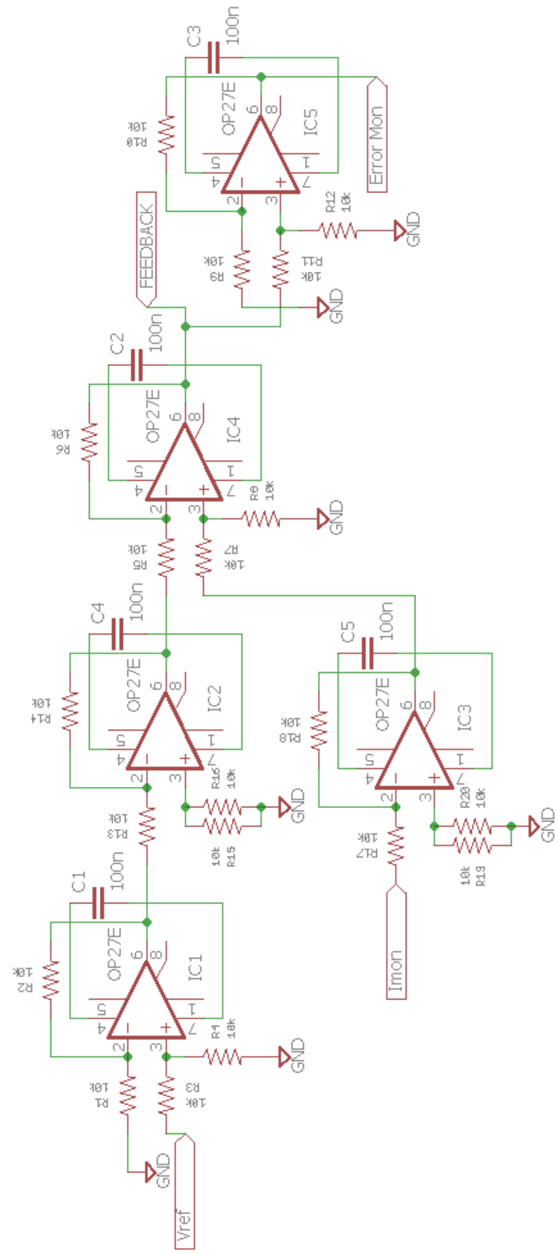

FIG. 5.10: Schematic of the circuit that generates an error signal for feedback. This circuit receives the current setpoint via V_{ref} from the galvanic isolator circuit (fig. 5.6). The current monitor signal labeled I_{mon} in this figure is received from the error signal circuit (fig. 5.10). The resulting error signal is sent to the feedback circuit (fig. 5.11) via the signal labeled FEEDBACK. The Error Mon. does not connect to a jack on the front panel and is instead an unterminated jumper connection inside the Levitiathan housing. This error monitor is buffered through a differential amplifier to help prevent an accident that might damage an oscilloscope.

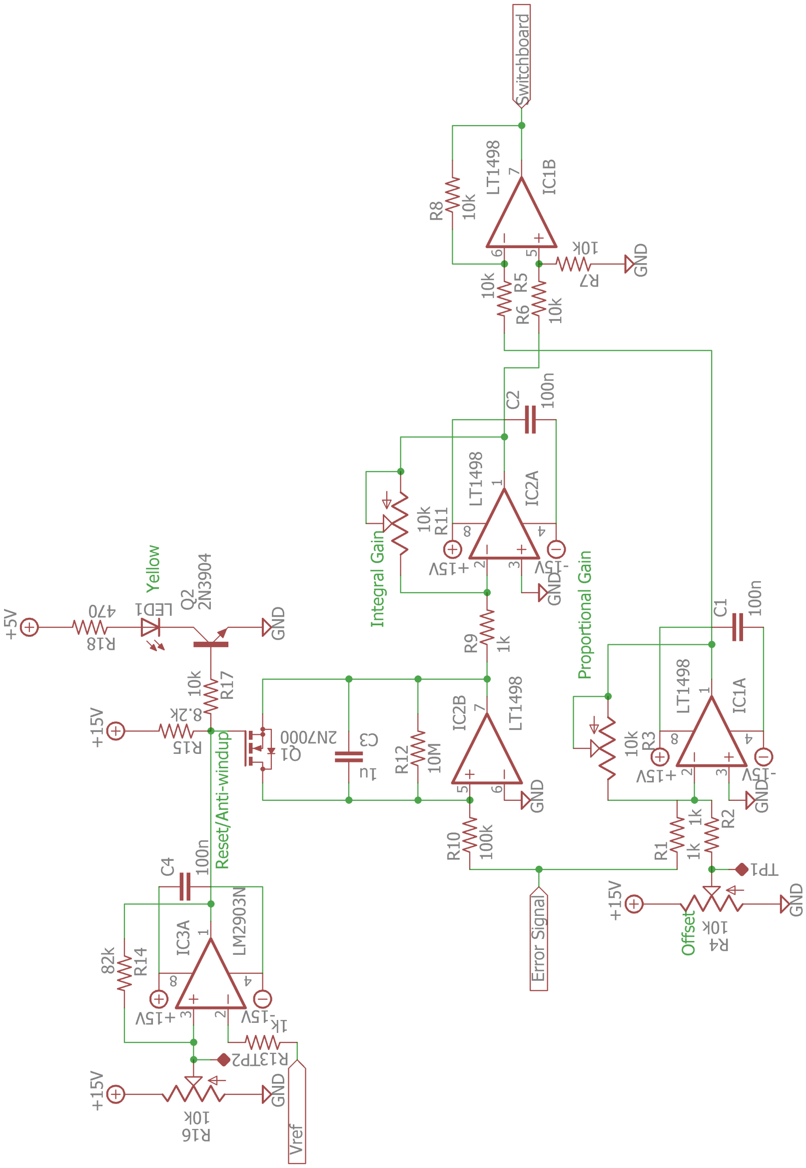

FIG. 5.11: Schematic of the feedback circuit. This circuit takes the Error Signal from the error signal circuit (fig. 5.10) and uses proportional and integral amplifiers to reduce it to zero by controlling the power MOSFET gates. Proportional and integral gain settings are control by trimpots R3 and R11 respectively. The signal controlling the MOSFET gates is routed through the switchboard and MOSFET selector circuits (figures 5.12 and 5.13). The V_{ref} signal comes from the galvanic isolator circuit (fig. 5.6) and is input to a comparator to determine a threshold (set by R16, with test point TP2) for delivering current. The resulting digital signal is used to ‘reset’ the integrator to prevent it from ‘winding up’ when no current is desired through coil 6. Allowing the integrator to wind up negatively affects the response time and current turn-on. LED1 is used to indicate when the anti-windup feature is active.

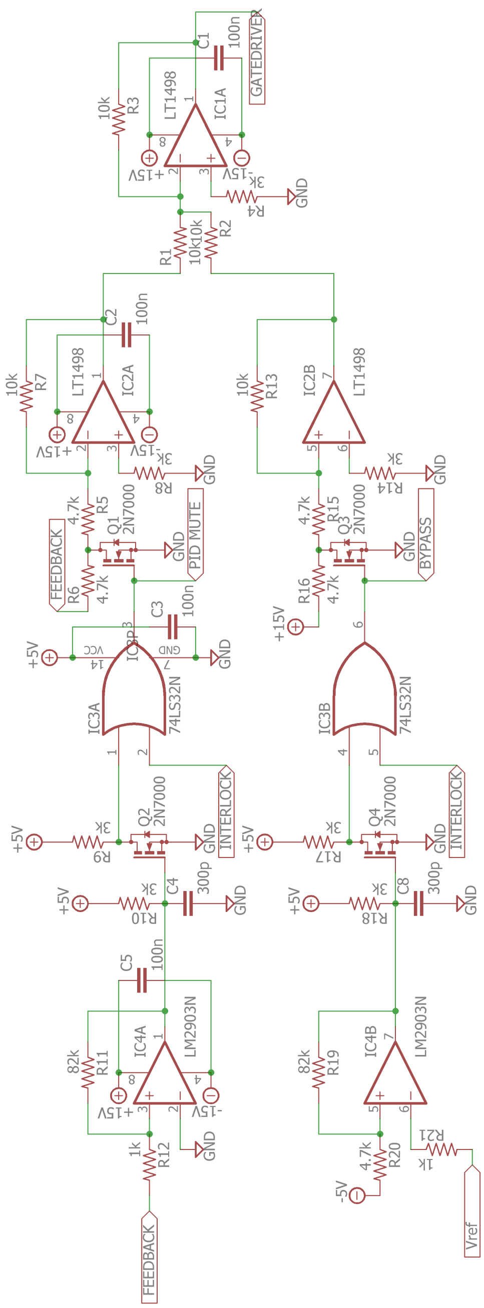

FIG. 5.12: Schematic of the switchboard circuit. The switchboard serves to route the signal from the feedback circuit (fig. 5.11) depending on the desired mode the Levitiathan is meant to operate in, and determined by the V_{ref} signal from the galvanic isolator circuit (fig. 5.6). The INTERLOCK signal is received from the safety interlock circuit (fig. 5.18) and used to mute the feedback signal in the event of a fault. BYPASS and PID MUTE signals are sent to the MOSFET selector circuit (fig. 5.13) and input for MOSFET selection logic. The output (GATEDRIVER, pin 1 of IC1A) will either be the feedback signal or +15 V (used for bypass mode to keep MOSFETs in a fully conducting state) and is sent to each individual gate driver circuit (fig. 5.14).

the MOSFETs and the feedback, then the feedback is connected to the gate driver. If the MOSFETs are meant to be run in bypass mode (i.e. MOSFETs act as fully closed switches), then the feedback signal is disconnected from the gate driver, and a constant +10V signal is relayed instead. However, in the event of a safety interlock trip, or an active mute, the switchboard will disconnect these voltage signals from the gate driver. This switching is done using a 2N7000 MOSFET and LT1498 opamp to create an analog switch.

5.2.9 MOSFET Selector

This circuit (Fig. 5.13) is used to connect either 2, 4, 6, or 8 MOSFETs to a gate signal. In bypass mode, all 8 MOSFETs are connected to a constant +10V signal to hold them in a fully conducting state. If the mute is active, then none of the MOSFETs are connected to a feedback signal. If the MOSFETs are intended to control the current, then at minimum 2 MOSFETs are always connected. For higher currents, 4, 6, and 8 MOSFETs are incrementally connected to a gate control signal.

5.2.10 Gate Driver

MOSFET gates draw no steady current. However, the gates must be charged to function, and will draw a small amount of current for a brief period of time. Therefore, using an opamp to source enough current to drive a transistor is not necessary. In addition, the LT1498 used to drive a MOSFET can source 20-30 mA of current. Each MOSFET has an individual opamp to drive its gate because an opamp has superior decoupling power to that of a simple resistor. Each gate driver (Fig. 5.14) is built using an analog switch for individual digital control over each MOSFET. The gate (decoupling) resistor was set to 220 Ω for stability. 470 Ω was

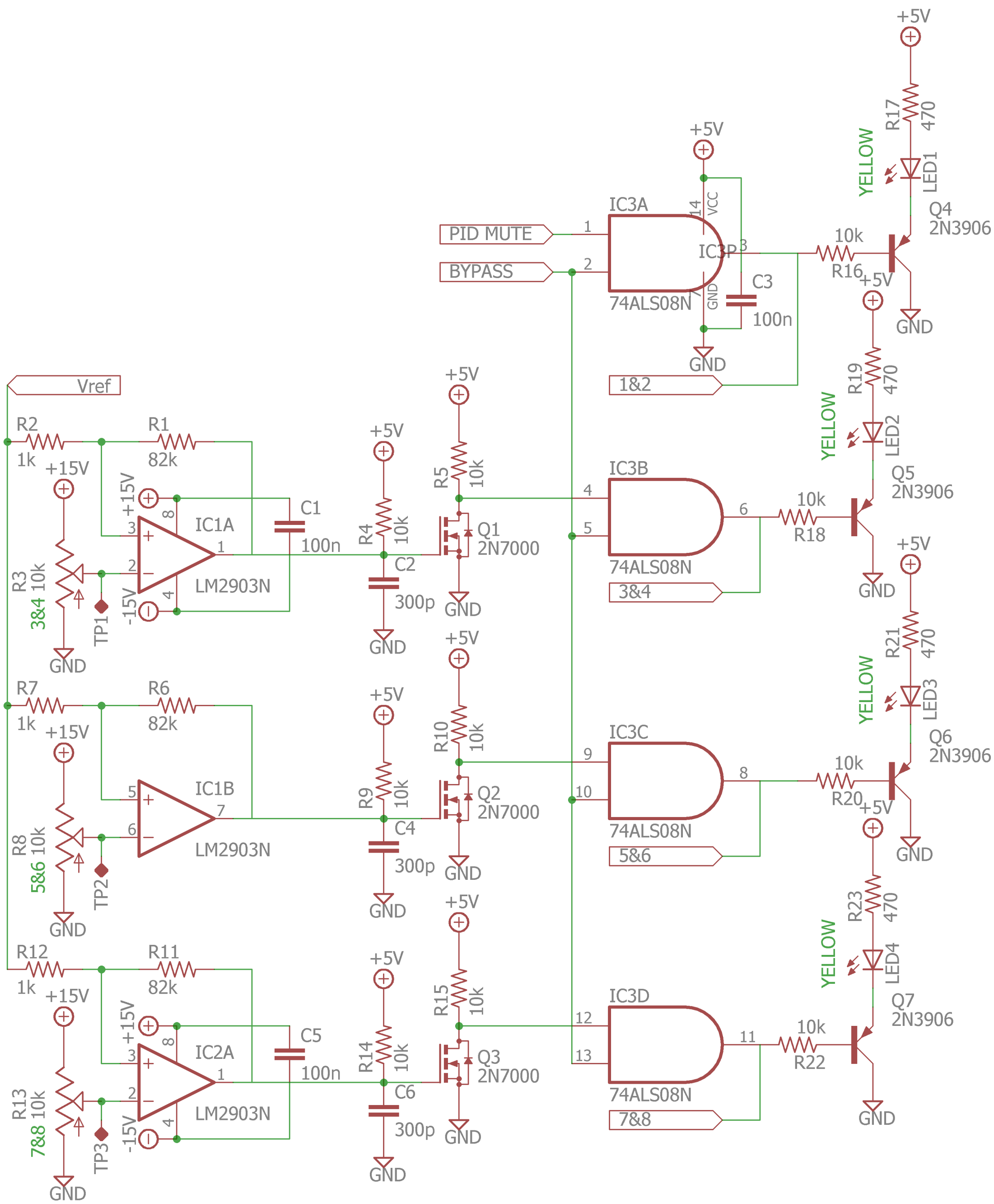

FIG. 5.13: Schematic of the MOSFET selector circuit. The V_{ref} signal from the galvanic isolator (fig. 5.6) is compared to thresholds set by trimpots R3, R8, and R13 (monitored via test points TP1, TP2, and TP3) to determine which MOSFETs will be activate for the desired current to be modulated. Signals BYPASS and PID MUTE from the switchboard (fig. 5.12) contribute to the logic that toggles each MOSFET. Output signals are labeled '1&2', '3&4', '5&6', and '7&8' (monitored via LED1, LED2, LED3, and LED4) and sent to the 8 individual MOSFET gate driver circuits (fig. 5.14).

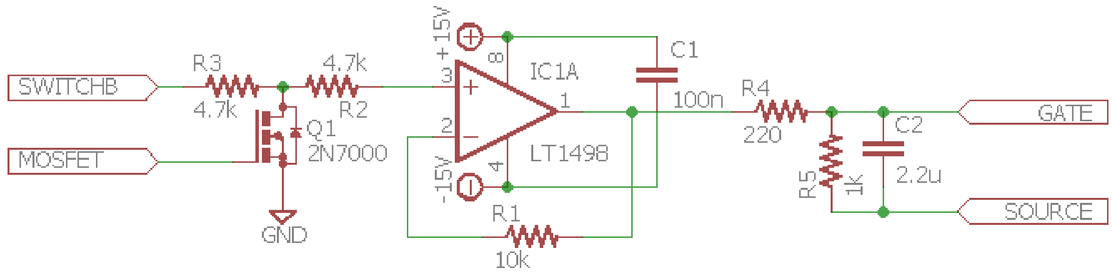

FIG. 5.14: Schematic of the gate driver circuit. The signal carrying the instructions for the MOSFET is received from the switchboard (fig. 5.12) and output to the MOSFET gate and referenced to the source. The signal is toggled via the input labeled 'MOSFET' and is received from the MOSFET selector circuit (fig. 5.13, signals '1&2', '3&4', '5&6', and '7&8'.)

found to be too unstable, and $\sim 100\ \Omega$ was less stable than $220\ \Omega$. The conclusion drawn was to leave that resistor value at $220\ \Omega$, and never change it. To maintain stability, the gate resistor must be paired with a capacitor to make a low-pass filter. Without this capacitor, the MOSFET behavior tends to become unstable, but too large a capacitance will reduce the speed at which a coil can be switched on. A value of $2.2\ \mu$F was chosen to achieve the minimum required stability so as not to sacrifice too much performance. One last resistor (1 kΩ) was added to help the gate discharge when the gate voltage is sent to zero to shut off the current.

5.2.11 Safety Interlock

The safety interlock (figures 5.15, 5.16, 5.17, and 5.18) is designed to halt current by disconnecting the MOSFET gates from a control signal in the event of overcurrent, overtime, or overtemperature. A separate current sensor (LEM HTB 200-P), which outputs a voltage scaled to 50 A/V, is used to detect overcurrents, and to integrate the monitored current and trip if left on too long. A thermistor is embedded in the copper mounting plate for the MOSFETs. The thermistor is one leg of a voltage divider that feeds a comparator input. A reference potentiometer connected to the other input of the comparator is set such that the safety interlock

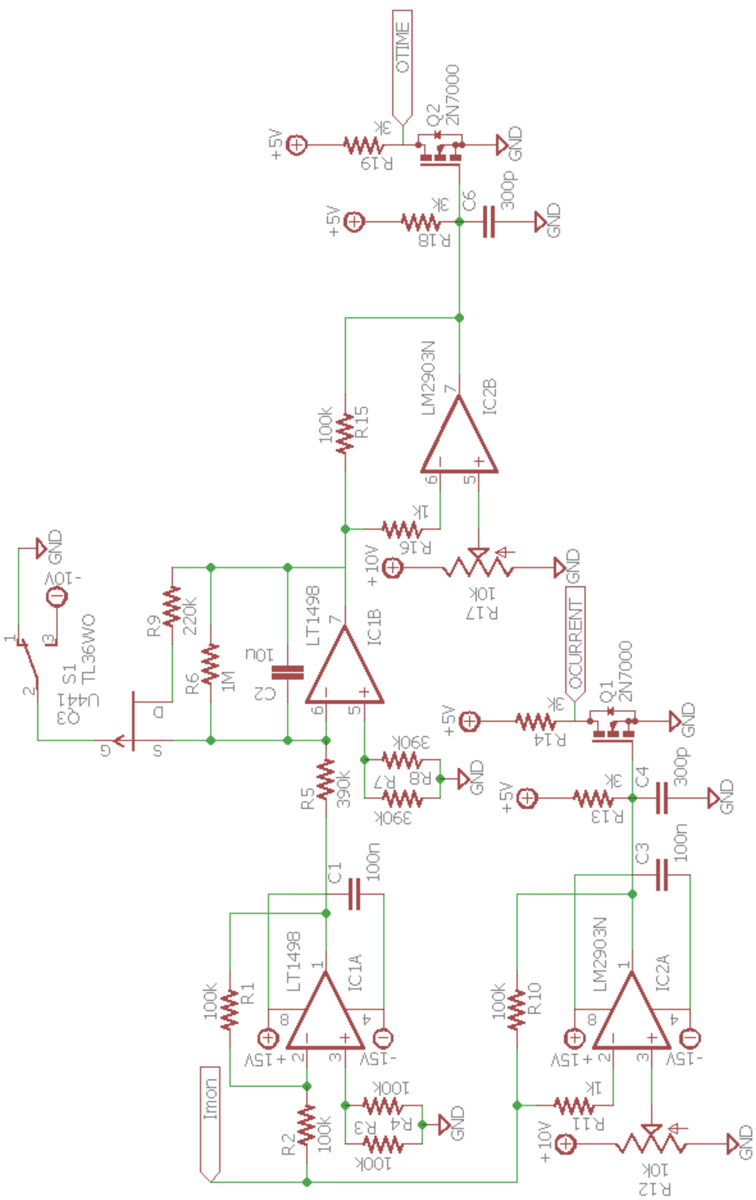

FIG. 5.15: Schematic of the current interlock circuit. A current transducer inputs the signal I_{mon} to the circuit and compares it to a threshold set by trimpot R12. The signal is also integrated by IC1B (reset by S1) and compared to a threshold set by trimpot R17. The digital output flags ‘OCURRENT’ and ‘OTIME’ indicate when the over-current or over-time interlocks have tripped. These signals are sent to the interlock logic circuit (fig. 5.18).

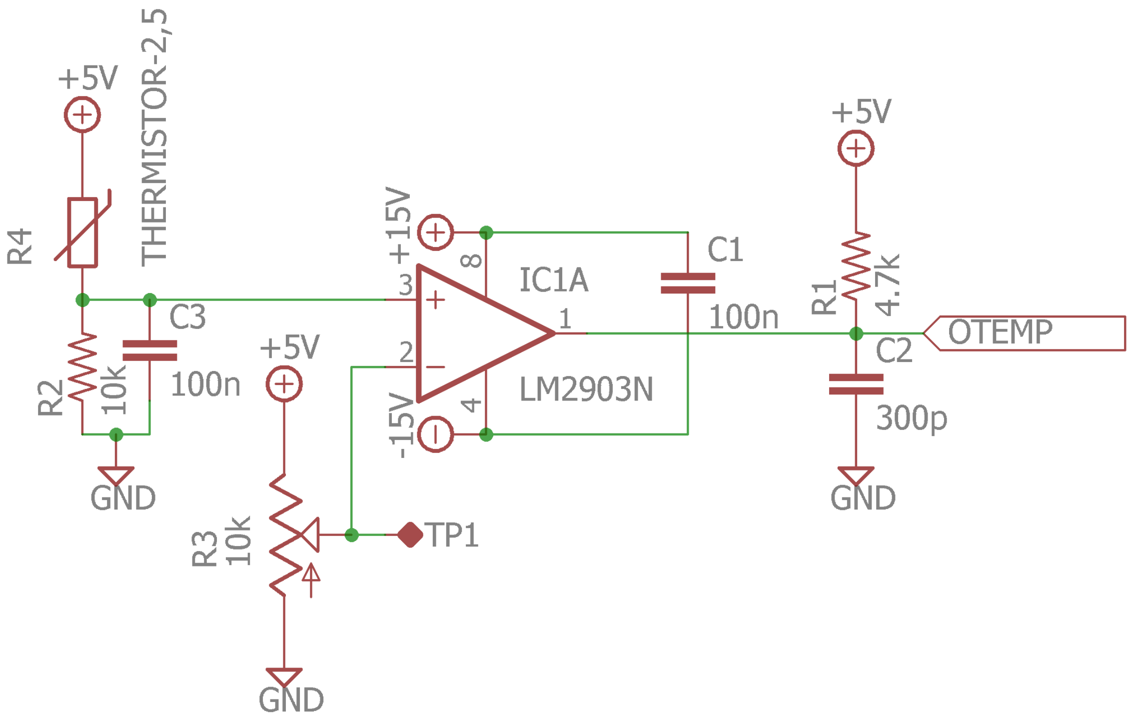

FIG. 5.16: Schematic of the temperature interlock circuit. A voltage divider made with a thermistor inputs a voltage that is compared to a threshold set by trimpot R3. The digital output flag 'OTEMP' indicates when the over-temperature interlock has tripped and is sent to the interlock logic circuit (fig. 5.18).

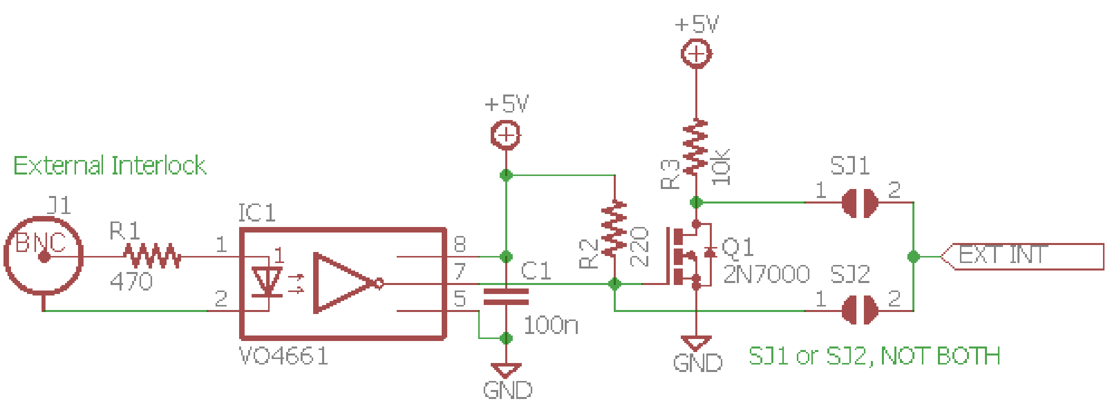

FIG. 5.17: Schematic of the external interlock circuit. BNC jack J1 can accept an external interlock signal. The jack is isolated from the Levitiathan ground via IC1 (a VO4661 optocoupler). The signal 'EXT INT' is sent to the interlock logic circuit (fig. 5.18). Either jumper SJ1 or SJ2 can be selected to invert or relay the original signal as desired.

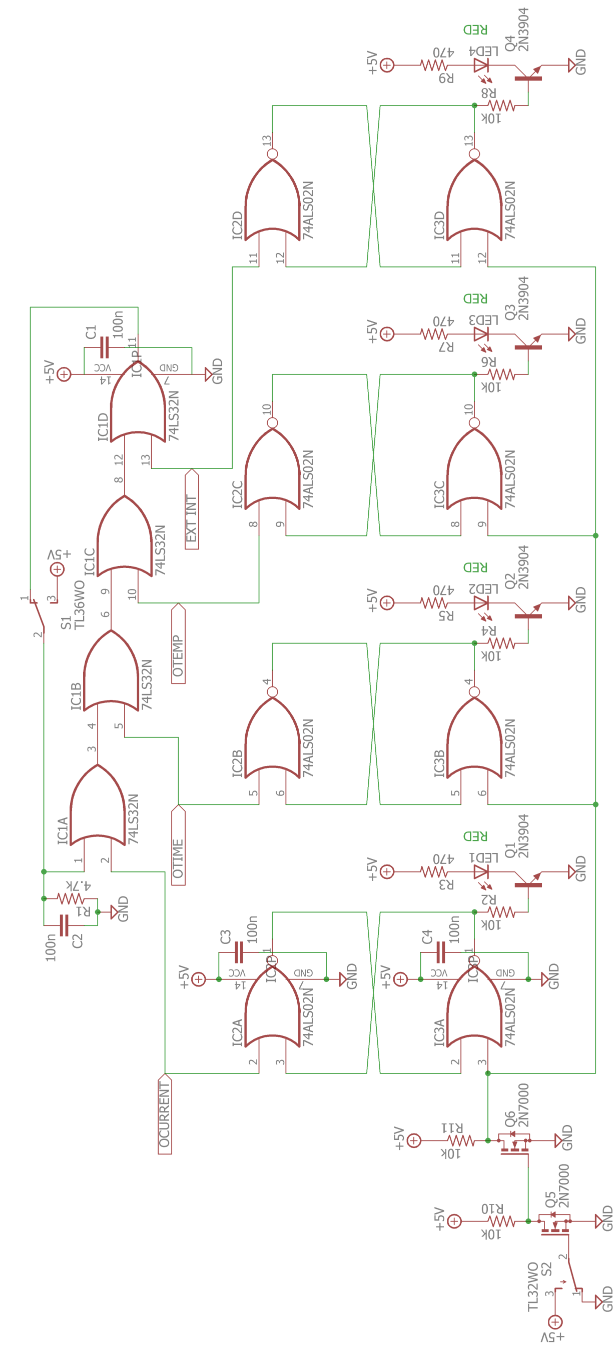

FIG. 5.18: Schematic of the interlock latch circuit. Safety interlock flags 'OCURRENT', 'OTIME', 'OTEMP', and 'EXT INT' (from figures 5.15, 5.16, and 5.17) are input to pins 2, 5, 10, and 13 of IC1. IC1A, IC1B, IC1C, and IC1D are OR gates chained together to create a latch (reset by S1). LED1, LED2, LED3, and LED4 indicate which fault condition has tripped the interlock (reset by S2, where S1 and S2 are a single DPDT switch). IC2 and IC3 are NOR gates (NAND gates can also be used) connected to create 4 RS (set-reset) flip-flop circuits to reset the LEDs. This latches the LEDs so that they do not turn off immediately after a fault conditions returns to normal.

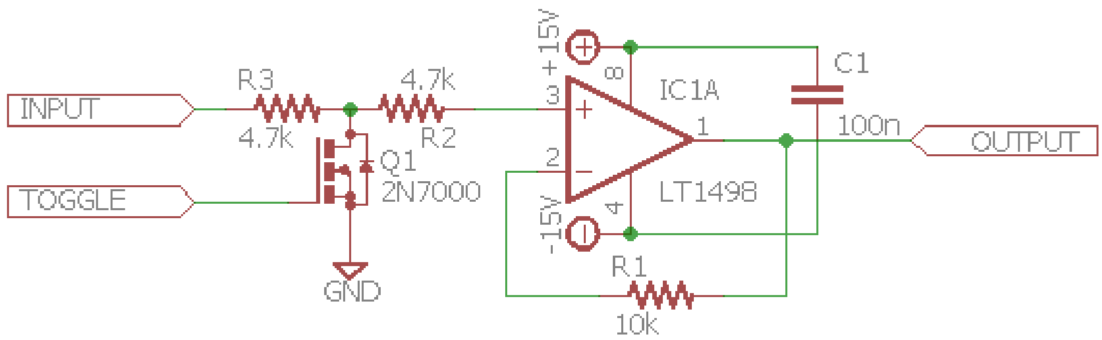

FIG. 5.19: Schematic of the analog switch circuit. This circuit is a major component of the gate drivers (fig. 5.14) and used multiple times throughout the Levitiathan. The output follows the input when the toggle is low. The output is muted when the toggle is high.

will trip when the thermistor reaches 37 degrees Celsius. Once any of these safety conditions are tripped, the safety interlock will latch so that current cannot be driven through the device again without a manual reset. If the trip conditions are still active, the interlock will not reset. A LED corresponding to the type of fault will light up on the front panel.

5.2.12 Analog Switch

Analog switches like the one shown in Fig. 5.19 are used throughout this device to connect/disconnect different signals. There are commercially available ICs capable of this task like the DG211 and DG403. The DG211 worked better empirically than the DG403, however the DG211 signal still sustained a voltage drop. To counter this, I designed my own analog switch. Consider the opamp follower. If the feedback resistance and input resistance are both increased, but still equal, then the circuit will still function as a simple unity gain follower. Consider dividing the input resistor by two, and placing two of those resistors in series. There should be no change. If we place the drain of a 2N7000 MOSFET between the two input resistors and connect the source to ground, the MOSFET will be capable of

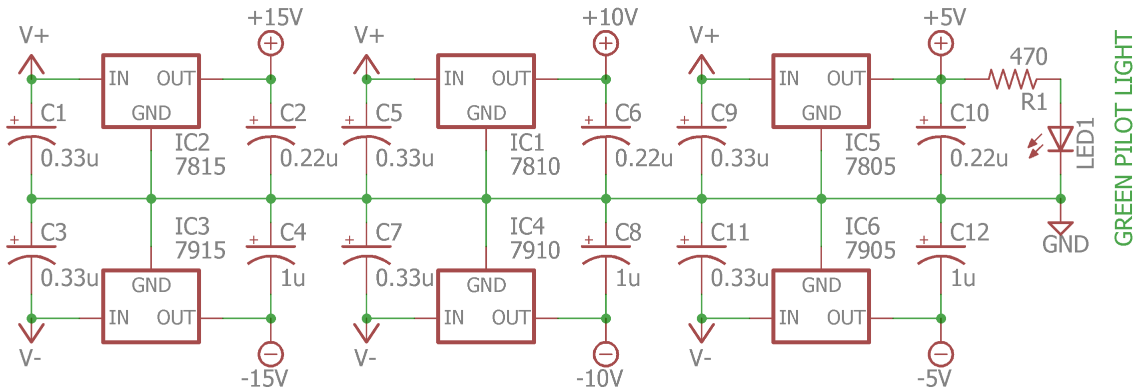

FIG. 5.20: Schematic of the voltage regulators.

shorting the voltage to ground. Now the analog switch can be toggled with a TTL sent to the MOSFET gate. This scheme resulted in a smaller voltage drop than the DG211. The disadvantage of this setup is that it is only capable of relaying voltages with one sign (positive in the above example, negative if you reverse the drain and source[4]). However, only positive signals are sent to the power MOSFET gates, this analog switch works and is used several times in the design of this device.

5.2.13 Voltage Regulation

The voltage regulator circuit board (Fig. 5.20) holds $\pm 5, 10, 15$ V and feeds power to all components (with the exception of the input side of the galvanic isolation chip). Each regulator is bolted to the case so it acts as a heat sink. Each regulator is isolated from the case as pin 2 of the TO-220 package is connected to the heat sink surface of the regulator.

[4]This circuit is listed as a “Bad Circuit Idea” in The Art of Electronics, Horowitz & Hill, Second Edition. The reason for this is the schematic specifically shows positive *and negative* input voltages. The book also has examples of other FET-based analog switches that work. However, failure to pay attention to similarly subtle nuances will result in the destruction of the FET. *Citation: personal experience.*

5.2.14 Terminal Blocks

A terminal block (16204-2) connects the drain and source of the power MOSFETs to the rest of the system. The drain is connected to the positive output terminal of the power supply and the source is connected to coil 6 of the transport system. This allows the device to function as a high side switch and has the advantage of speeding up the entire power supply. Now, the high speed power supply is available to each load that the coilplexer can connect to this supply.

5.2.15 Thermal Concerns

The front panel shows everything the fast switch requires for regular use. There are 3 switches, one for main power, one fault reset, and a separate momentary switch to clear the fault LEDs after latching. Toggling the fault reset switch to the down position will disable the device and the Mute status LED should light up. The up position allows the device to operate normally until the safety interlock detects a fault. Once faulted, the reset switch must be toggled for the device to allow current to pass again. If the reset switch is toggled but the fault condition still exists (e.g. over-temperature) the device will not reset until all fault conditions are cleared. The LED clear momentary switch does not affect the function of the device, instead it clears the fault LEDs and may be used at the operators discretion. If a fault occurs, the MOSFETs will be held insulating to prevent any current from flowing. The coilplexer has its own fault signal connected to an external safety interlock (built by C. Fancher) and thermocouples are connected to the coils for a temperature interlock. When an over-current or over-temperature fault occurs in this system, all Agilent high-current power supplies are shut down via solid state relays used to interrupt the AC lines powering them.

5.3 Setup and Control

5.3.1 Installation

The Levitiathan is meant to operate in conjunction with another power source, either a power supply operated in constant voltage mode, or a battery. This device is capable of function as either a low, or high side switch. When functioning as a high side switch, take the appropriate caution when connecting two grounds together, as they may not be at the same potential. Because a power supply and MOSFET-based multiplexer were already installed to drive the existing coils, we had the option of installing this device with a second power supply, both in parallel with the original supply, or use the original power supply with this device as a second low side switch, or use the original power supply with this device as a high side switch. We chose to do the latter, making this device a high side switch between the power supply and the load. This had the added advantage of improving the operation of everything connected to the multiplexer and driven by that power supply, rather than just the coil pair of interest.

5.3.2 Operation

A single analog control input is used to regulate the current from the power supply.[5] The input is galvanically isolated from the rest of the device to prevent current from the power supply potentially damaging another device. An error signal is generated by comparing the control input with the output of the current-sensing amplifier. PI feedback is used to drive the gate voltages of the MOSFETs. A switchboard and MOSFET selector interrupts the feedback signal depending on the operating mode and number of active MOSFETs. The safety interlock will

[5] This has the advantage of requiring only one channel from the Adwin sequencer. Analog and digital channels can be a limited commodity.

FIG. 5.21: Photo of the front panel of the Levitiathan.

stop the flow of electrical current in the event of over-current, over-time, and over-temperature. A manual reset is required after a safety interlock fault.

The current control input should be between -10 V and +10 V. Different ranges of input voltage correspond to different operating modes for the device. A status LED in the left column of LEDs should light up indicating which operating mode is active. -10 V to -5 V places the device in "Bypass" mode which instructs the gates to hold all MOSFETs fully conducting. Current is controlled by the power supply in this mode, useful for the programming changes already done by the sequencer that do not require speed. -5 V to 0 V places the device in the "Mute" operating mode which instructs the gates to hold all MOSFETs fully insulating, preventing any current from flowing through the device. Any positive control voltage scales to a desired current regulation with 0-10 V corresponding to 0-150 A. There are 4 settings set by internal potentiometers. At low currents, anti-windup is turned on for the feedback system. At different current settings, a different number of MOSFETs are used to regulate current. At maximum current, all 8 MOSFETs can be active, while only 2 are used at low current. The status LEDs in the right column indicate whether anti-windup is active and how many MOSFETs are conducting. The mode, current, safety interlock faults, anti-windup, and number of active MOSFETs can be monitored using the status LEDs on the front panel shown in figure 5.21.

5.4 Levitation Kinematics

The conditions for atomic levitation are null acceleration and velocity. In order to achieve these conditions as soon as the atoms are released from a trap, the levitation coil current must reach a value I_g that cancels gravity in a very short amount of time. For example, to prevent the atoms from moving downwards by one pixel on our axial camera (4.65 μm), the coils need to turn on in approximately 3 ns! Even after significant improvements in speed and current control over the levitation coils, the current required cannot be provided that quickly. Performing a simple turn on to I_g will create a zero net force on the atoms, but the atoms will have acquired a downward velocity during the slow turn on. The alternative to a simple turn on is to overshoot the current that cancels gravity in an attempt to push them upwards as gravity begins to pull them down. Once any downward velocity is canceled, the coil current should be lowered to cancel gravity, thereby stabilizing the vertical position of the atoms from that point forward. The drawback to this scheme is that the atoms will take longer to stabilize, and move some distance before their motion is canceled. The change in position is acceptable as the location of the barrier can be adjusted to account for it. However, it is desirable to minimize the time required to achieve levitation to prevent unnecessary expansion in atom cloud size before the atoms can interact with the barrier. This can be done by adding a pulse of current greater than I_g before equilibrating to I_g. To minimize the time to achieve levitation, this overshoot pulse is intended to be of high magnitude and short duration. Tuning the current dynamics to achieve levitation must be done empirically since the magnetic gradient provided by the levitation coils is not sufficiently well known.[6]

However, if the current turn-on dynamics are incorrect, then levitation will not occur. A theoretical analysis of how the current turn-on dynamics affect the Levitiathan can help guide the empirical tuning of the current turn-on curve. The potential energy of the atoms falling in the presence of a magnetic gradient is

$$V(y,t) = mgy - \vec{\mu} \cdot \vec{B} = mgy - \mu_B byI(t) \tag{5.1}$$

where b is the magnetic gradient per Amp and assumed to be constant. The magnetic term in equation 5.1 assumes that the atoms are in the stretched state ($|F=2, m_f=2\rangle$ for ^{87}Rb) and that the DC Zeeman shift is purely linear. The Lagrangian for the system is

$$L = T - V = \frac{1}{2}m\dot{y}^2 - mgy + \mu_B byI(t). \tag{5.2}$$

The equation of motion for the system is thus

$$\ddot{y}(t) = -g + \frac{\mu_B b}{m} I(t). \tag{5.3}$$

We can obtain the velocity and position of the atoms by integrating equation 5.3:

$$\dot{y}(t) = v_0 - gt + \frac{\mu_B b}{m} \int_0^t I(t')dt' \tag{5.4}$$

$$y(t) = y_0 + v_0 t - \frac{1}{2}gt^2 + \frac{\mu_B b}{m} \int_0^t \int_0^{t'} I(t'')dt''dt' \tag{5.5}$$

[6]More specifically, the gradient varies slightly over space. It varies slowly enough that theoretical calculations are useful, but enough that empirical tuning is required.

There exists a current I_g that results in zero net force on the atoms. This current I_g produces a magnetic gradient force equal and opposite to gravity.

$$I_g = \frac{mg}{\mu_B b} \tag{5.6}$$

We can use I_g to rewrite the equations for velocity and position (eq. 5.4 and 5.5) in a way that makes it easier to interpret the effect that dynamic changes in the current $I(t)$ will have on atoms:

$$y(t) = y_0 + v_0 t + \frac{\mu_B b}{m} \int_0^t \int_0^{t'} (I(t'') - I_g) dt'' dt' \tag{5.7}$$

$$\dot{y}(t) = v_0 + \frac{\mu_B b}{m} \int_0^t (I(t') - Ig) dt' \tag{5.8}$$

The resulting velocity of the atoms can be interpreted as the area enclosed between the current in the coils $I(t)$ and I_g. This knowledge was used to help calibrate the gradient produced by the coils, and the data used for this is shown in Fig. 5.22. The bottom subplot depicts the current trace as a function of time and is proportional to the acceleration or force the atoms feel due to coil 6. Integrating once (twice) shows the velocity (position) that should be added or subtracted to the atoms by this coil. This figure does not account for the effect of gravity, as I_g must also be known to correct for gravity. The points on the uppermost subplot correspond to the points on figure 5.23, which represent the times at which our camera collected images used to derive position information. This data is useful for measuring the magnetic gradient ($b = 0.206$ G/cm/A) produced by coil 6 in the region occupied by the atoms during levitation. Observing the overall time dependence of both the coil 6 current and the vertical position of the atoms[7] helps to decouple net forces

[7] Unfortunately, the position and velocity jitter does add some irreproducibility to this measurement, and makes tuning the current dynamics to achieve levitation more difficult. My solution to this problem was to listen to "You Can't Always Get What You Want" by the Rolling Stones.

and acquired velocities as observed in position changes. We initially attempted to tune the levitation dynamics by estimating I_g and varying the initial overshoot to encourage levitation (this was a long process and A. Rotunno was very helpful). This method proves difficult because of our inability to track atoms in real time. If we observe a change in position between arbitrary times t_1 and t_2, we do not know if the change in position is caused by a non-zero net force on the atoms, or if the net force is zero and the atoms are traveling at a constant velocity acquired between trap turn-off and levitation coil turn-on.

A useful method for determining I_g is to turn on current to different values, like in the bottom subplot of figure 5.22, and applying a quadratic fit to the position data to quantify the effective acceleration felt by the atoms. Plotting the effective acceleration as a function of coil current allows I_g to be determined based on the current at which the atoms feel zero effective acceleration once the coils have turned on (figure 5.23 bottom). Once I_g is known, the current dynamics must be tuned to prevent the atoms from maintaining a constant velocity after the net force is extinguished. This is done by current an initial overshoot pulse above I_g. The area of the pulse is the quantity of interest that will cancel the atoms velocity. To prevent unwanted expansion and loss of optical depth, it is preferable that this overshoot pulse by high magnitude and short duration. The time of the overshoot can be adjusted such that the velocity will diminish. The results of tuning this overshoot pulse can be seen in figure 5.24. Similar data for different pause times can be found in Appendix B. For each of these data sets, an optimum overshoot pulse time was found. This gives a set of optimized current traces in figure 5.25.

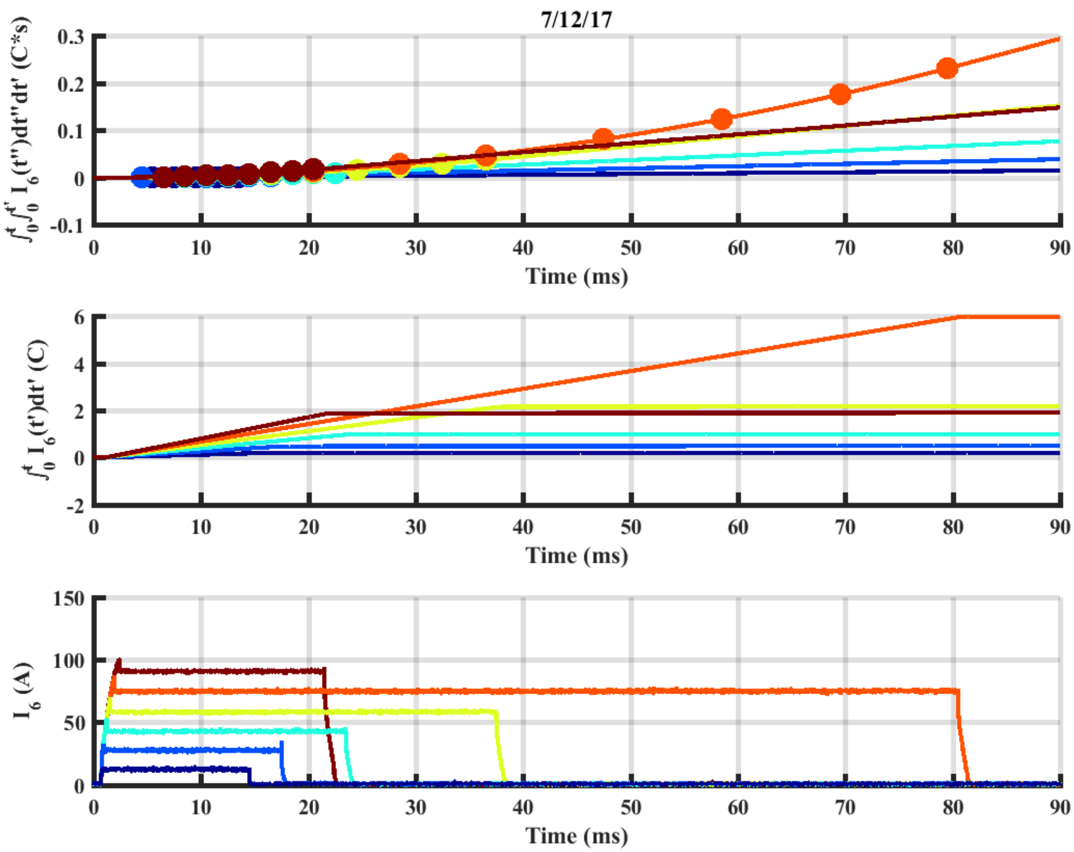

FIG. 5.22: Integrating once (twice) levitation coil current $I(t)$ generates a quantity proportional to the velocity (position) of the atoms. Different colors indicate different coil current traces shown in the bottom subplot, and the colors are consistent throughout all subplots. The color scheme in this figure matches that in figure 5.23. However, I_g in this stage of calculations was yet unknown. It is assumed to be the equilibrium current for each respective trace to perform the integration for "velocity" and "position".

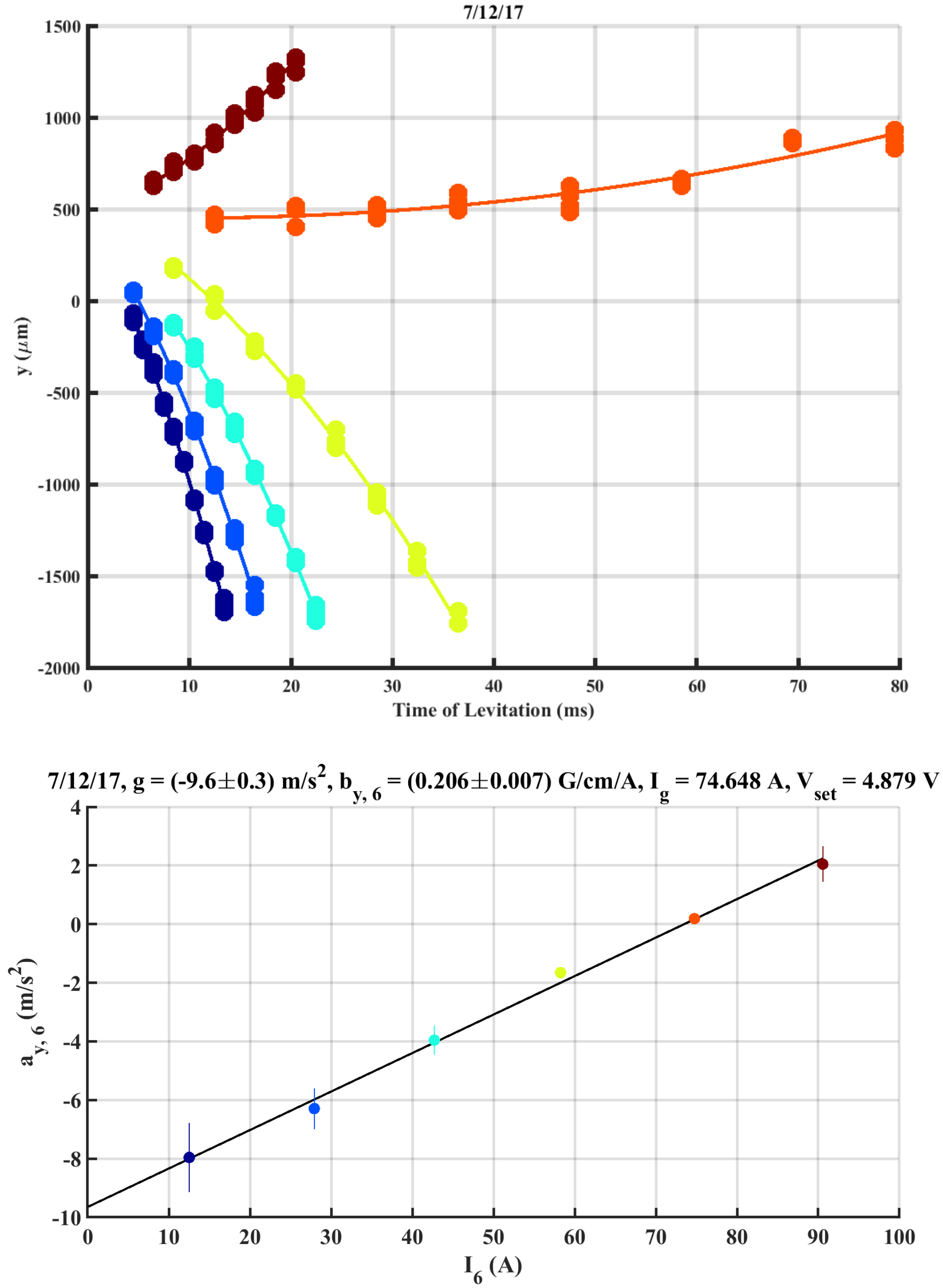

FIG. 5.23: Top: Location of the atoms as levitation coils equilibrate to different current values. Bottom: Acceleration for each current I_g used to collect data. The colors of the points match the curves in the top figure. The correct value of I_g was determined by interpolating the linear fit for zero acceleration ($a_{y,6} = 0$). The colors of the points correspond to the current traces, $I_6(t)$, in figure 5.22 (bottom).

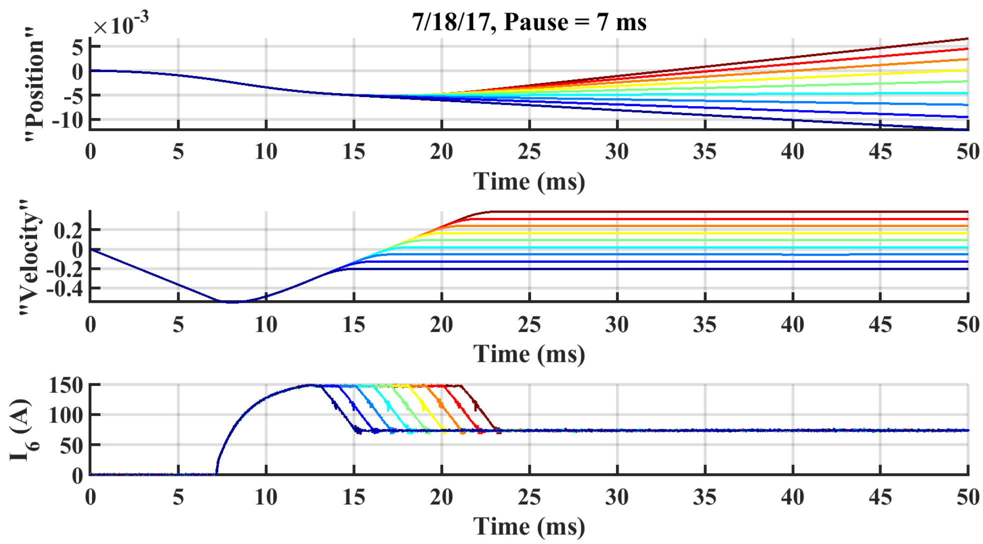

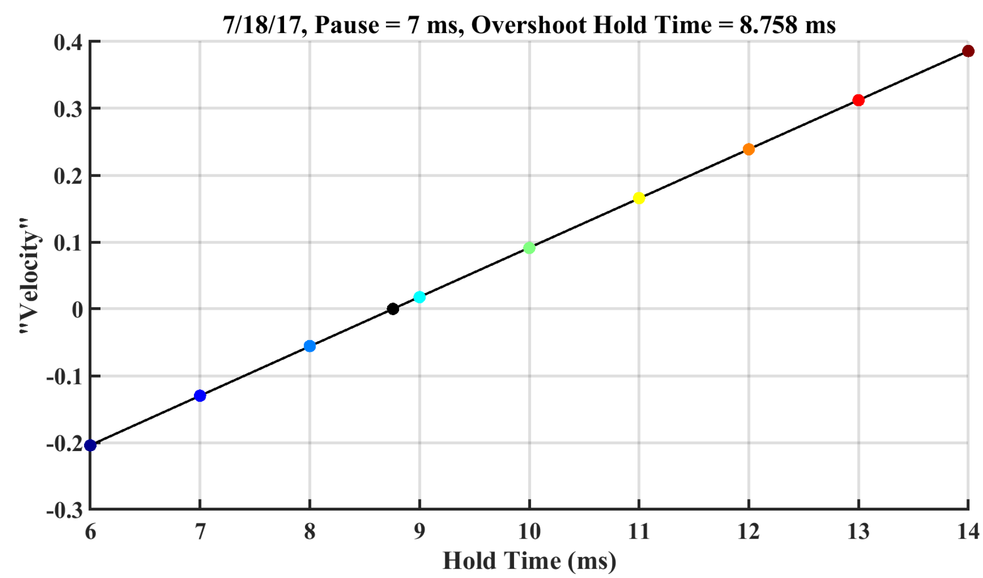

FIG. 5.24: Top: After waiting 7 ms to accommodate a potential push pulse, coil 6 is turned on. Various amounts of time were waited to extend the overshoot pulse to determine how long the pulse should be to cancel the velocity the atoms would have. Bottom: Velocity the atoms would achieve calculated by integrating the current traces. This is plotted against the overshoot pulse hold time to determine the pulse time that will cancel the atoms velocity.

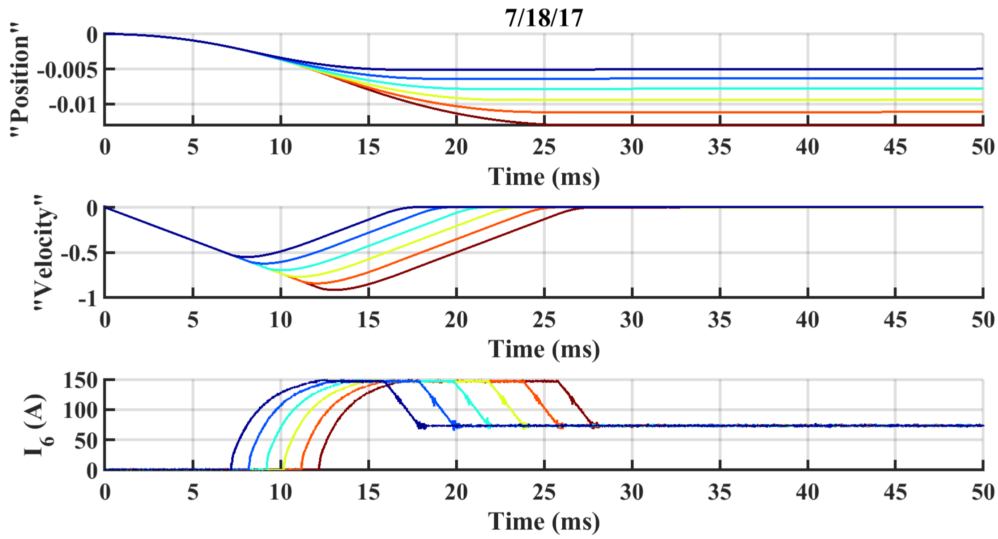

FIG. 5.25: Optimal levitation current schemes. Pausing longer allows for a longer push pulse, or allows the atoms to reach an equilibrium depth further from the chip. In practice, it is better to perform the experiment quickly before allowing the atoms more time to expand.

5.5 Performance

The performance of the Levitiathan is compared to the performance of the power supply alone. Using the power supply and its analog programming inputs for current and voltage, the power supply could reach 75 A in 50 ms. The switch was able to reduce this to 1 ms, however it would produce a subtle overshoot in the current before stepping down to 75 A. Figures 5.23 and 5.26 show the effect that the levitation coils can produce on the atoms after they are released from the chip trap. Different equilibrium currents will result in a different net force in the vertical direction. The desired current value is one that produces a force equal and opposite to that of gravity while the current dynamics during turn-on are manipulated to ensure that the atoms have no velocity at the time the current equilibrates. Figure 5.27 shows the analysis for the magnetic gradient, which has been determined to be $b = 0.212$ G/cm/A based on the data in the figure.[8].

[8]This data gives a slightly different value than the analysis of the data in the previous section

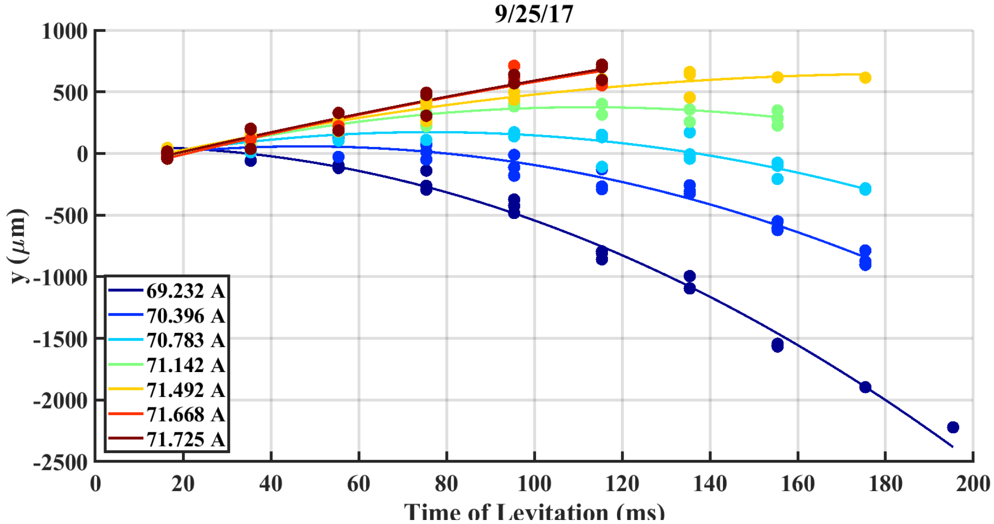

FIG. 5.26: Top: Ultracold atoms can be levitated with the proper current dynamics. Jitter in atomic position can be clearly seen here. The atoms are visible on the camera for a longer amount of time (when compared to figure 5.23) using a relatively narrow range of I_g currents while empirically tuning the dynamics for levitation.

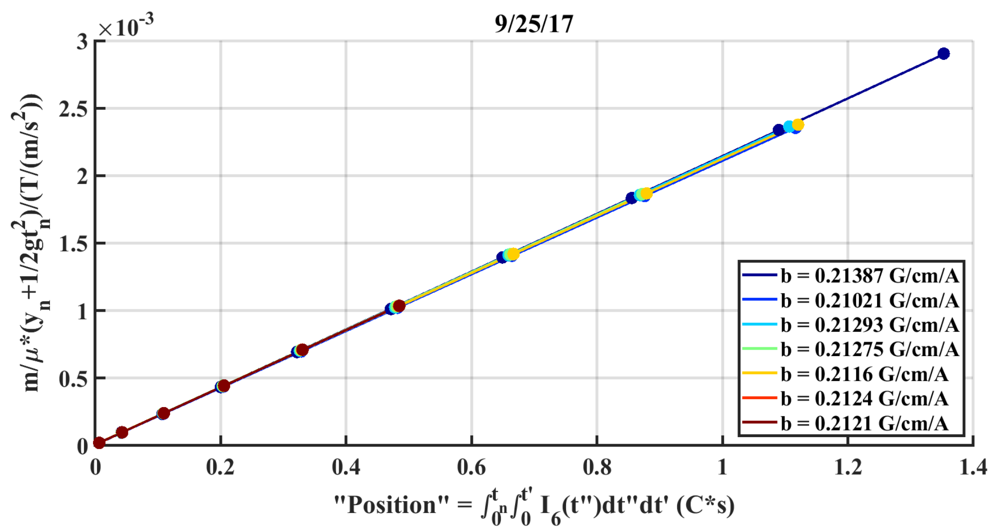

FIG. 5.27: Equation 5.5 can be plotted such that the magnetic gradient b is the slope of the curve. This analysis can be applied to each point in the datasets from the data plotted in figure 5.26. This data is then fit to determine the value of b, which has been done for each dataset. The colors for the datasets shown in the legend match those in figure 5.26.

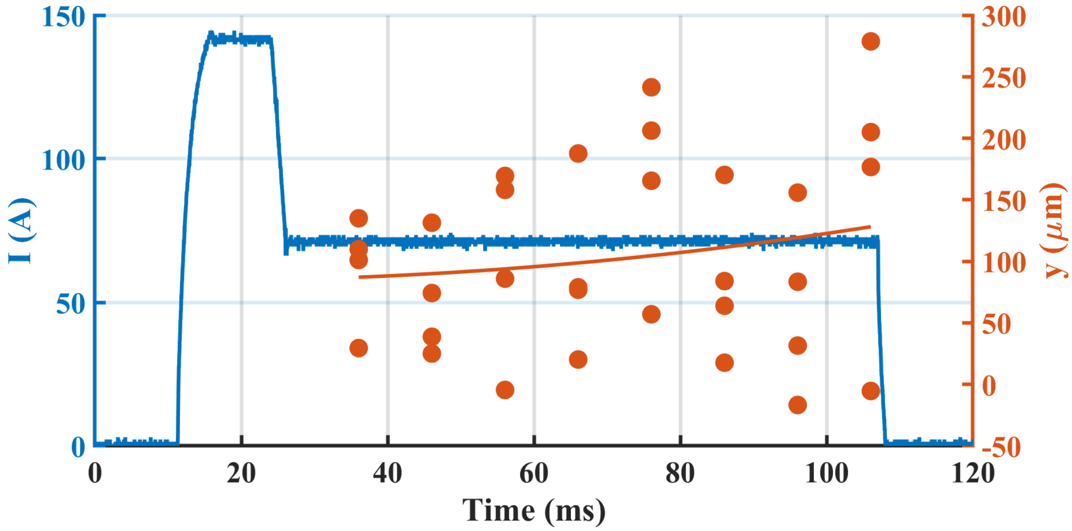

FIG. 5.28: Ultracold atoms can be levitated with the proper current dynamics. The blue trace is the current $I(t)$ plotted on the left axis. The orange points are position data accompanied by a fit (orange line) using the derived equations of motion for this system and are plotted on the right axis. The atoms are released from the atom trap at $t = 0$. The turn-on of coil 6 is delayed for a suitable amount of time to allow a current pulse from the push coil (discussed in section 6.2). The current between 30 and 100 ms is I_g. The position data also shows the jitter worsening over time.

Figure 5.28 shows how the atoms behave in the vertical direction with a reasonable levitation scheme. This data shows that the levitation works reasonably well to stabilize the vertical position of the atoms, however, the data also shows considerable jitter.

5.5.1 Jitter

Other sections of this document have addressed important quantities that affect our experiment, like BEC jitter (section 4.3.3) and expansion rate (section 3.4, and later in section 6.1). The introduction of the magnetic gradient provided by coil 6 to levitate the atoms is a mechanism that can potentially alter the characteristics of the system. This motivates a second analysis of BEC jitter. The use of the levitation system also provides access to BEC cloud sizes at much longer times-of-

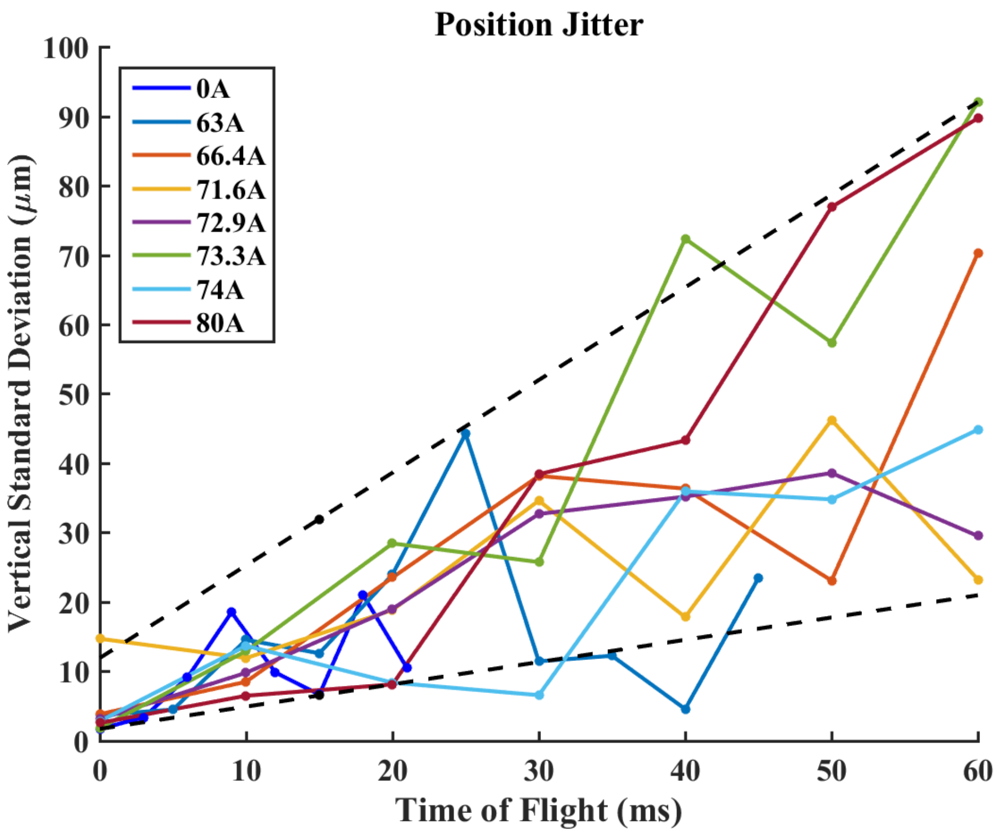

FIG. 5.29: Standard deviation of vertical position of atoms vs. time of flight for different coil 6 currents. The dashed lines are guides for the eye and show the apparent upper and lower bounds as time-of-flight increases.

flight than were previously available due to the atoms falling past the field of view of the camera. This information helps to characterize the type or source of jitter previously stated to be a velocity jitter, and ascertain the effect of coil 6 on the jitter, if any.

In figures 5.29 and 5.30, coil 6 was allowed to turn on and equilibrate to the current values listed in the legend, and no levitation scheme was used for this test out of concern that it might have corrupted the results. These jitter results are relatively consistent with what has been previously established. Figure 5.30 shows that the horizontal jitter is relatively small, especially when compared to the vertical jitter in figure 5.29. For reference, the vertical scale on figure 5.30 is 10 μm, which

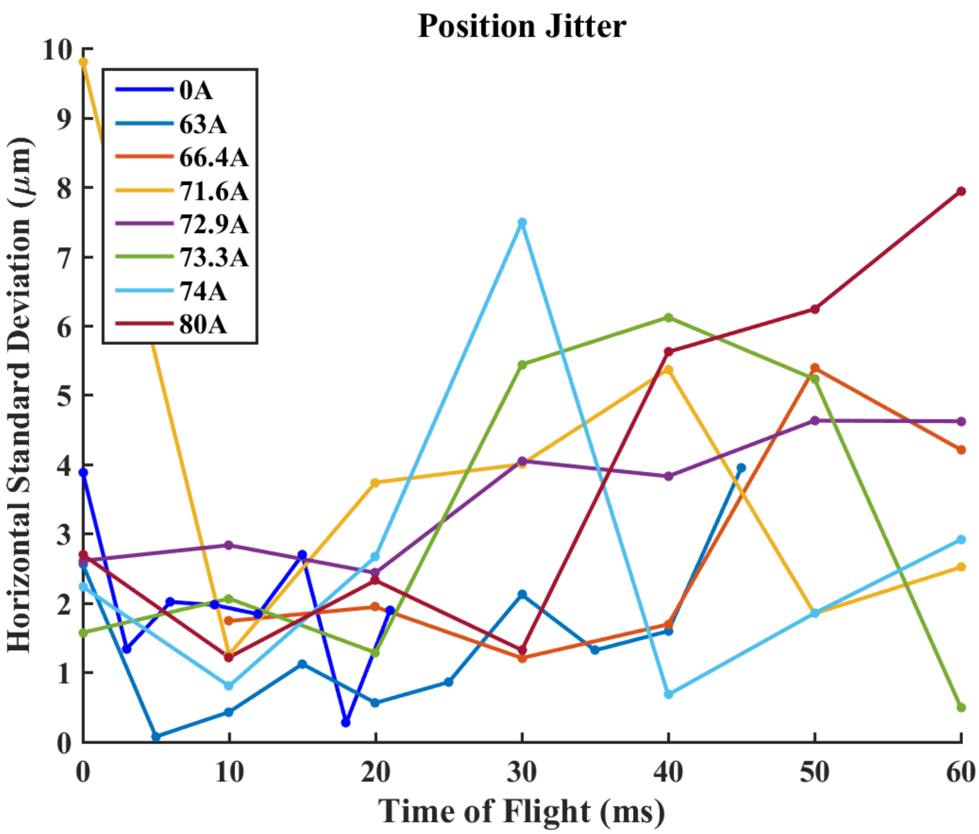

FIG. 5.30: Standard deviation of horizontal position of atoms vs. time of flight for different coil 6 currents.

is about two pixels on our axial camera (4.65 μm/pixel) where as in figure 5.29 it is 100 μm. The vertical spread of atom location shown on figure 5.29 is much larger than the horizontal equivalent. However, the spread in position increases with time-of-flight. This indicates that the jitter is not a position jitter, but a velocity jitter. Therefore, we conclude that the atoms receive an inconsistent initial velocity kick that results in a larger difference in position at later times. The horizontal data appears that it may also support this result, but with less confidence due to the smaller overall jitter in that direction.[9]

5.5.2 Deformation of the Cloud

This section addresses the effect the levitation field has on the shape of the cloud and its expansion velocities. The curvature of the magnetic field produced by the levitation coil (coil 6) can modify the shape of the cloud and its expansion rate over the course of long levitation times and we believe that these effects were relatively small. To investigate this, we examined the size of the atom cloud after being pushed, while being levitated, and before and after interacting with a static barrier. Inserting the static barrier has a disadvantage in that it is more difficult to identify the levitation coils or the static barrier as the cause. However, in the interests of time and this test really only serving as a quality check of the system, and not data collection for the primary experiment, this course of action was more expedient.

The data in figure 5.31 shows the affect on cloud size in the axial and vertical radial directions. We had anticipated only positive values for σ_{vz}, σ_{vy} that indicate expansion. However, in lieu of the equation used to define cloud size as a function

[9] At this time, I have no explanation for the relatively large initial jitter for 71.6 A (yellow traces on figures 5.29 and 5.30).

of time:

$$\sigma(t) = \sqrt{\sigma_0 + (\sigma_{vi}t)^2} \tag{5.9}$$

for $i = y, z$, the imaginary values simply correspond to the magnitude of compression. This data shows a near zero expansion/compression in the axial direction for both incident and reflected atom clouds. This would lead us to believe that the levitation field is not causing a significant effect on the atomic expansion rate. In contrast to the axial data, the vertical radial direction also shows little to no expansion in the incident cloud. However, the reflected cloud shows a much increased expansion rate after interacting with the static barrier. This data supports the assertion that the levitation field has little to no affect on the axial expansion rate, which bodes well for the experiment, while the vertical expansion caused by the barrier is very negative for imaging. An additional piece of evidence for a small axial expansion rate is found in chapter 7, figures and for a $f = 0$ barrier frequency. Since the overall expansion rate is low for this point, it suggests that the push (discussed in chapter 6), levitation, and static barrier do not have a significant effect on the axial expansion rate.

5.5.3 Horizontal Drift During Levitation

This section quantifies the amount of horizontal motion that the levitation produced. The magnetic field coils surrounding the atom chip can be used to tune some of the motion imparted to the BEC by the levitation coils. A side effect of the levitation coils is that it caused some small wander in the horizontal direction. The Ioffe coils are capable of affecting the horizontal motion of the atoms during levitation.

However, for the final experiment I did not tune chip bias fields such as the Ioffe to compensate for any wander. I left this out for two reasons: 1) the wander

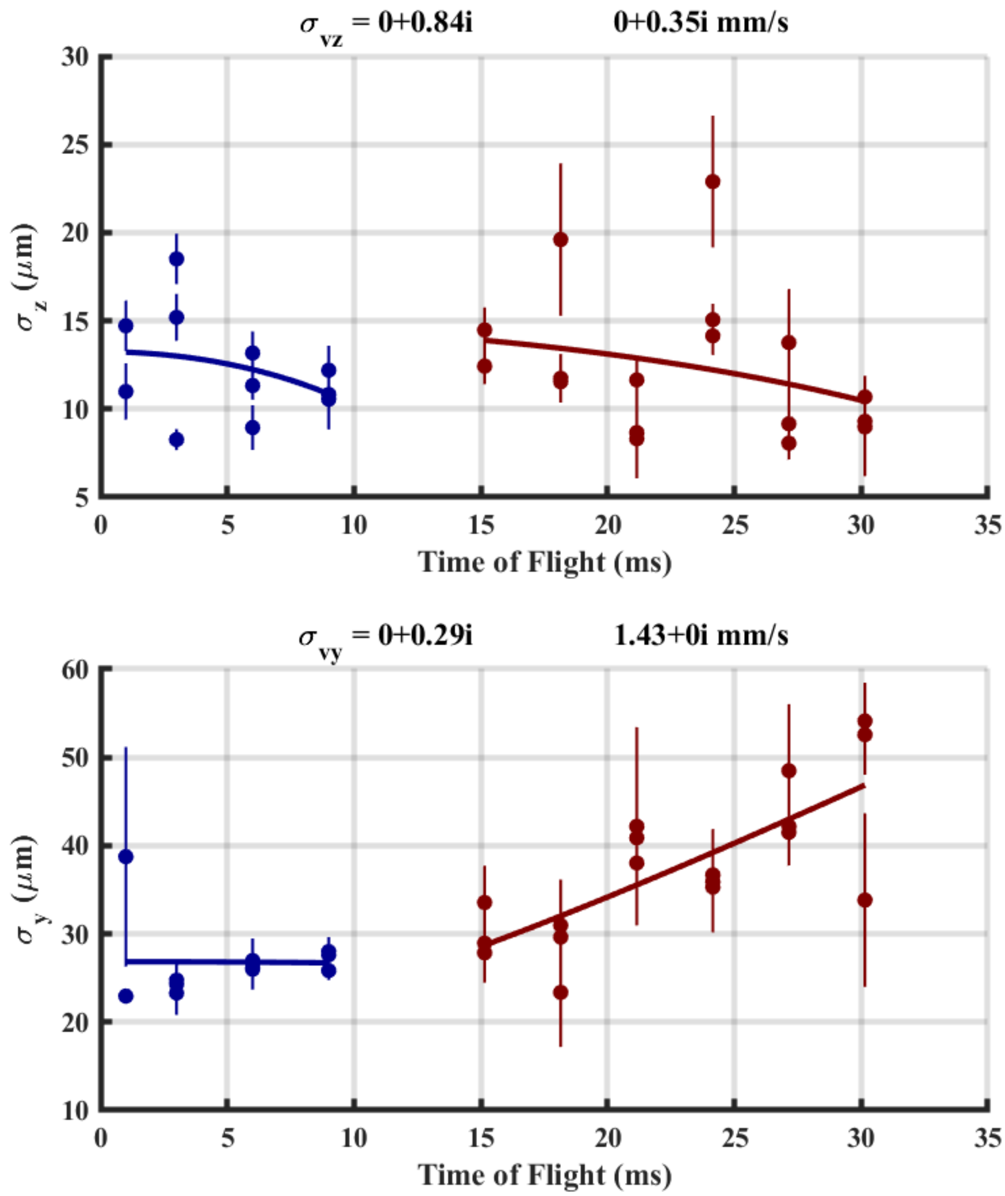

FIG. 5.31: Effect on a BEC after being pushed, levitated, and interacting with a barrier. BEC cloud size data was collected for the axial (top) and radial (bottom) directions (σ_z and σ_y). The data was fit to $\sigma(t) = \sqrt{\sigma_0 + (\sigma_{vi}t)^2}$, where $i = y, z$ The blue curves show the atoms behavior before interacting with the barrier, and the red after.

was relatively minor, and 2) the levitation dynamics required empirical tuning to finally get right and the two degrees of freedom for levitation (equilibrium current through coil 6, and overshoot pulse time) were coupled to one another. This made the empirical tuning a little more difficult, and when the Ioffe and potentially the Hold fields were added, they were all coupled to one another. Collecting enough data to eventually optimize all four fields empirically would've been a difficult and time-consuming nightmare. However, I do have good data plots previously made that show different atomic trajectories at various Ioffe currents. I think that may be useful to include. I do not have analogous plots for the Hold field, but its effect was less significant and it mostly influenced the radial direction (we cared much more about the axial direction, which the Ioffe influenced). The only note I will add is that the Ioffe was left on until coil 6 was turned on, then turned off to mitigate any effects, and then turned on before coil 6 was turned off so that there was always an external field present. This was done to avoid the possibility of the atoms passing through a magnetic zero and scrambling the spin state.

The original intention was to tune the Ioffe during levitation. As such, I choose to display the data here that may be useful for controlling the Ioffe field in the future. Figure 5.32 shows the affect the Ioffe field has on the atoms in the axial direction. Only positive currents were used, although negative currents can also be applied to the Ioffe coils with a bipolar current supply. The Ioffe coils were powered by a bipolar current supply early in our apparatus history. Since then, the AC Zeeman experiments have motivated larger currents through the Ioffe field. As a result, we have since configured the Ioffe to be used with a unipolar current supply, and as this calibration data shows, we would require the bipolar supply to counter extra axial motion.

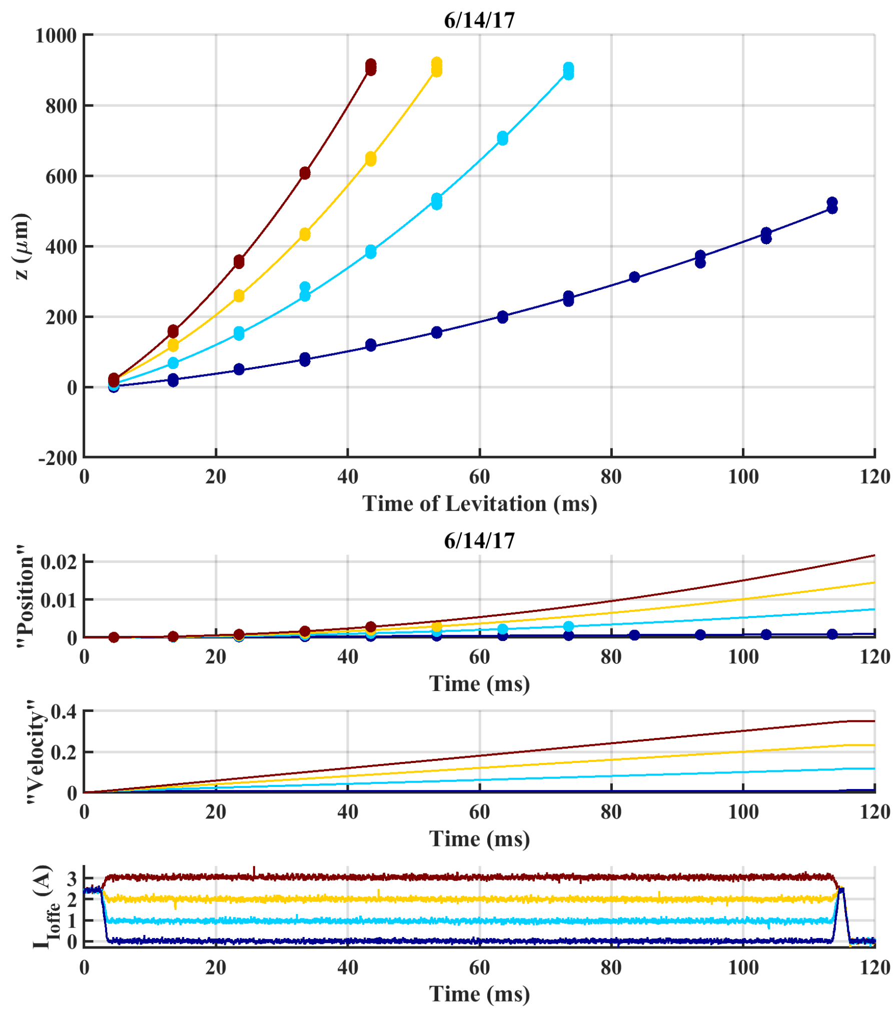

FIG. 5.32: Top: Axial coordinate of atoms during levitation as a function of different Ioffe coil currents shown in bottom. Bottom: Additional plots of Ioffe current traces with single and double integrals.

CHAPTER 6

Experimental Setup

This chapter describes the main experimental components that are used for implementing the experiment to observe scattering of a BEC by an oscillating barrier. While chapters 4 and 5 describe the apparatus for producing a BEC and then levitating it, this chapter focuses on components needed to give the BEC a momentum kick, optical system for generating the laser barrier beam, and the detection method for observing the scattered momentum distribution.

The basic experimental scheme was sketched in chapter 2 (section 2.5) and proceeds according the following sequence:

1) Narrow momentum distribution: BEC. After being generated in a relaxed chip trap, the BEC is released and allowed to expand ballistically to reduced its density and associated atom-atom interactions.

2) Initial momentum kick (and levitation) The BEC is briefly accelerated horizontally by a magnetic push coil towards the oscillating barrier. Once the atoms are pushed, the levitation system is activated to levitate the atoms during their interaction with the barrier and the subsequent ballistic travel (horizontal) of the scattered atoms.

3) Oscillating barrier A tightly focused, blue-detuned laser beam generates a repulsive barrier potential for the atoms. The beam power is modulated by the use of an acousto-optic modulator system.

4) Detection After interaction with the modulated barrier, the scattered atoms are allowed to propagate horizontally for a time-of-flight period to map the momentum distribution onto a position distribution. As most of the atoms are reflected by the barrier beam (for the chosen experimental parameters), the detection phase focuses on the reflected atoms.

This chapter is structured according to these four essential experimental steps and characterizes their performance (chapter 5 describes the levitation system separately). These steps are then combined to run the full experimental sequence and observe scattering of a BEC by an oscillating barrier, which is presented in the next chapter (chapter 7).

6.1 Narrow Momentum Distribution

We use an untrapped BEC as our atomic source for the experiment: atom-atom interactions are strongly suppressed in this case. We relax the chip trap adiabatically so that is only weakly confining (trap frequencies: $\omega_r = 2\pi \times 63(3)$ Hz and $\omega_z = 2\pi \times 13.5(5)$ Hz [21]), and then abruptly turn off the trap, thus releasing the BEC. Once released from the trap, the BEC expands at a rate dictated by its temperature and the trap shape. Because the trap is cigar-shaped, the BEC expands anisotropically. This expansion rate can compete with the differential velocity between sidebands, Δv, making separate sidebands difficult to resolve and detect. That is, separate wave packets moving at different speeds are expanding faster than they are separating. The solution to this problem is either increasing the differential velocity between sidebands, or reducing the expansion rate. We have observed that a BEC released from our atom chip trap will expand in the transverse radial directions, and little to not at all in the axial direction, as shown in figure 6.1: The data shows that the axial horizontal standard deviation width (Gaussian fit) of the BEC expands at the rate of $\sigma_{vz} = 0.019$ mm/s, which is much less than the expected differential sideband velocity of $0.5-1$ mm/s; the radial expansion rate of the BEC is $\sigma_{vy} = 0.69$ mm/s, which is comparable to the expected differential sideband velocity. The experiment has been oriented to propagate the BEC towards the barrier in the axial (horizontal) direction to take advantage of the smaller expansion rate. For a short time while putting together the experiment, we did consider implementing a method for reducing the radial expansion velocity. Delta kick cooling [76][77][78][79][80] is a method that could substantially reduce the radial expansion rate of the BEC by briefly flashing on a weak trapping potential as the BEC expands: however, our experimental attempts at implementing this technique did not yield a sufficient reduction in expansion rate.

BEC Trap Considerations: Atom-atom interactions distort the sideband picture and cause larger expansion rates. It was therefore in our best interest to conduct the experiment with untrapped atoms. Unfortunately, once the atoms are released from the trap they also fall due to gravity. The lab-built custom power supply used to levitate the atoms (discussed in the previous chapter) would have been unnecessary if the atoms could be held in an Optical Dipole Trap (ODT). The magnetic field generated by the levitation coils adds detrimentally to the fields used for the atom chip trap. Therefore, we turned the trap off before turning on the levitation coils, requiring them to turn on quickly.

The ODT uses no external magnetic fields to hold the atoms, so the levitation coils do not interfere with the trap. The proposed scheme would have been to load atoms into an ODT, turn on the levitation coils while the atoms remain unaffected,

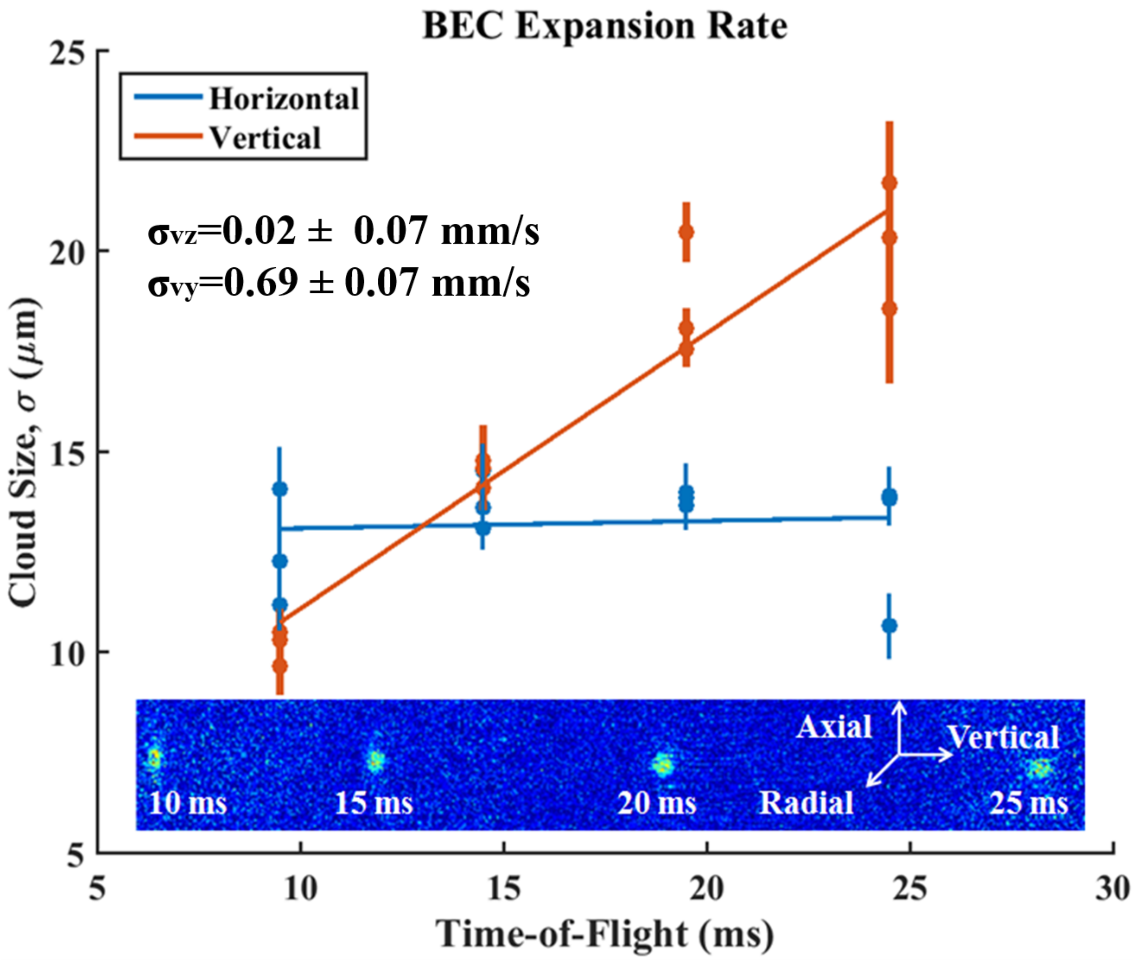

FIG. 6.1: Expansion rates for a BEC released from an atom chip trap. The horizontal (axial) expansion rate is minimal compared to the vertical. Inset: Absorption images of a BEC falling during time of flight.

then when the trap is turned off the atoms would not drop as gravity is counteracted by the coils. The problem with this plan was the inability to cool atoms to BEC in the ODT. Atoms could be cooled to BEC in the atom chip trap, but we observed unwanted heating when loading into the ODT that increased the temperature of the atoms above the BEC transition temperature to yield an ultracold thermal gas.

Forced evaporative cooling can be implemented in an ODT, however it is much less effective than in the chip trap due to much smaller trapping frequencies. Higher trapping frequencies increase the collision rate which helps rethermalize the atoms during forced evaporation. The Z-wire of our atom chip was used to produce a potential gradient (i.e. external force) meant to remove the hottest atoms from the ODT. While attempting to cool the atoms in the ODT we discovered that the field produced by our Z-wire causes an increased heating rate (see figure 4.23). We also attempted to evaporate by decreasing the ODT beam power to lower the trap depth, but this also proved ineffective in generating a BEC. For these reasons, we decided to abandon the ODT in favor of the lab-built high speed power supply described in chapter 5 (i.e. the Levitiathan).

6.2 Initial Momentum Kick

Once the BEC has been released and is slowly expanding, it must be briefly accelerated towards the barrier. A single coil (built by M. Ivory [21], see Table 6.1) is oriented next to the vacuum chamber to produce a magnetic gradient in the horizontal direction to impart an initial velocity to the atoms. A high-current switch was constructed to gate the current pulses applied to the push coil. After the atoms are released from the trap, a current is pulsed through the coil for 5 ms. The magnitude of current dictates the velocity of the atoms. Additionally, if needed, the coil can be used in combination with another magnetic field to reverse the acceleration direction or bring previously accelerated atoms to a halt. The coil and high current switch combination is capable of accelerating the atoms to 60 mm/s, nearly double that of the first generation experiment. The higher velocity is useful for generating sidebands with a larger differential velocity (see sections 2.6 and 2.7).

Parameter	Value
Inner Radius	4.6 cm
Outer Radius	8.0 cm
Number of turns	31
Inductance	40 μH

TABLE 6.1: Parameters for the push coil.

6.2.1 Current Pulse Control

Another high-speed, high-current device similar to the Levitiathan discussed in the previous chapter was built to gate the current pulses through the push coil that accelerates the atoms. This switch is named the Kraken,[1] and is similar in design to the Levitiathan, but is meant to be operated in a digital, on/off, fashion. Removing current sensing feedback made this device easier to build. The design did retain the MOSFETs, gate driver, snubber, current monitor, and safety interlock (Fig. 6.2, 6.3 & 6.4).

The Kraken was originally meant to be operated in series with the transport coil multiplexer ("coilplexer"), however the multiplexer's safety interlock proved too restrictive for our needs. changing the interlock set-points was an ill-advised option as it changes the settings for every other load connected to the same power supply. Instead, the push coil and Kraken switch are installed in parallel with one of the

[1]The name came from the idea that the current would "crack on" very quickly, and we kept the theme of naming equipment after nautical beasts.

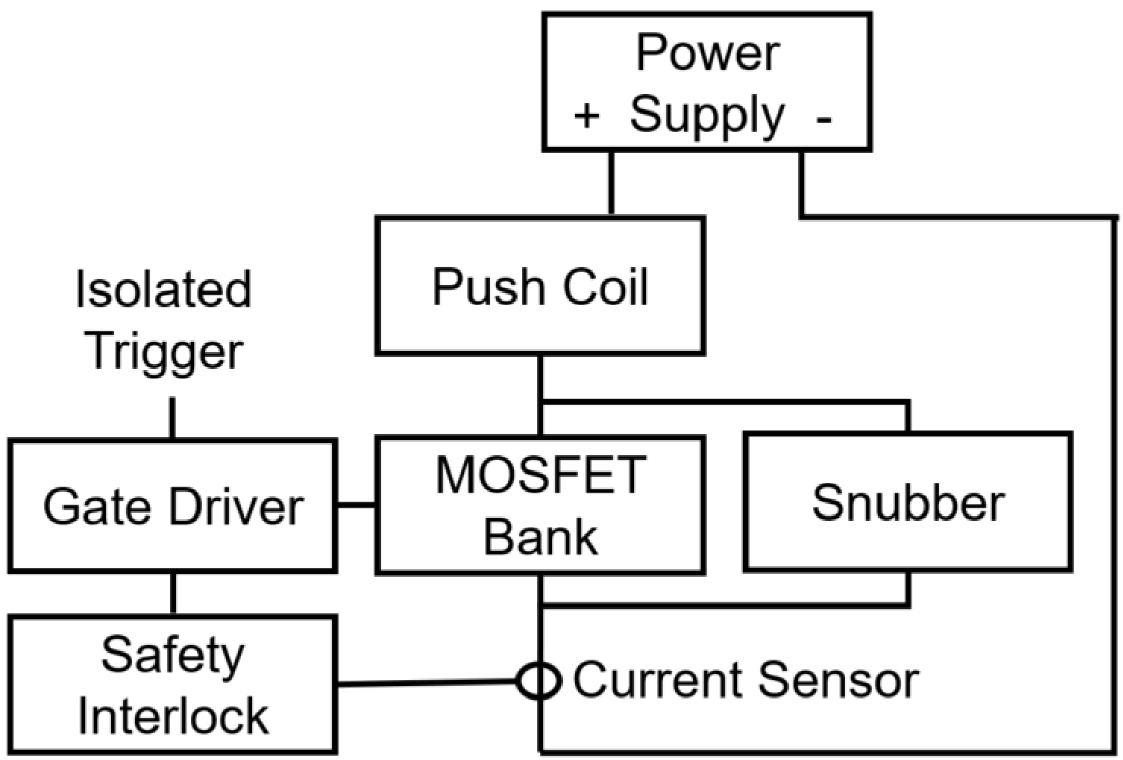

FIG. 6.2: Block diagram for the high speed, high current switch called the "Kraken". The power supply is an Agilent 6571A #J03, 14 V and 150 A (i.e. power supply C of the transport system).

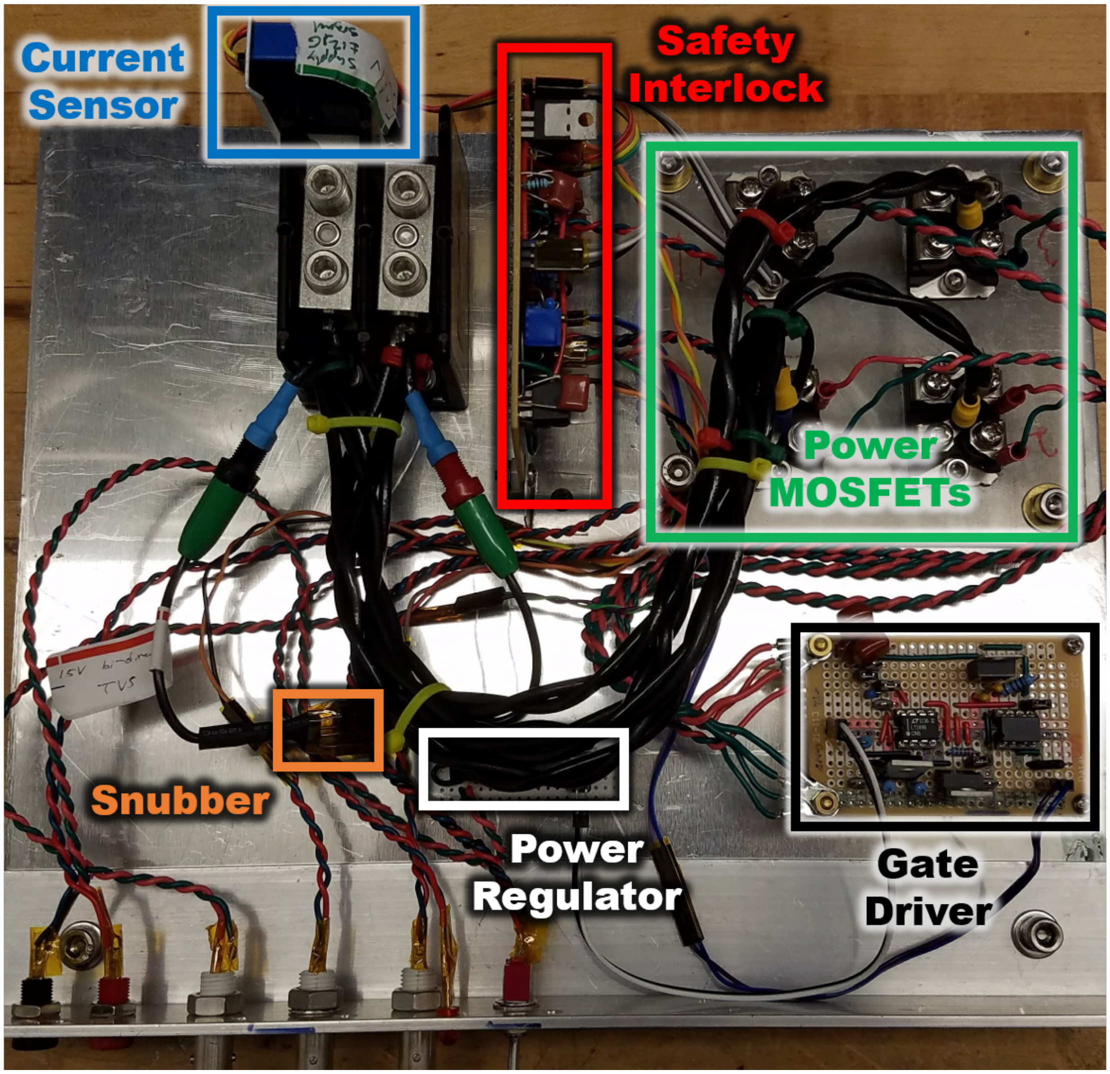

FIG. 6.3: Photo of the Kraken high current switch. The switch is built on an aluminum baseplate and uses a high current terminal block (top left) for handling the input and output wires. The photo shows the placement of the four high current MOSFET switches and their gate driver circuit, as well as the current sensor and the associated safety interlock. The power regulator board and the snubber for the MOSFETs are also shown.

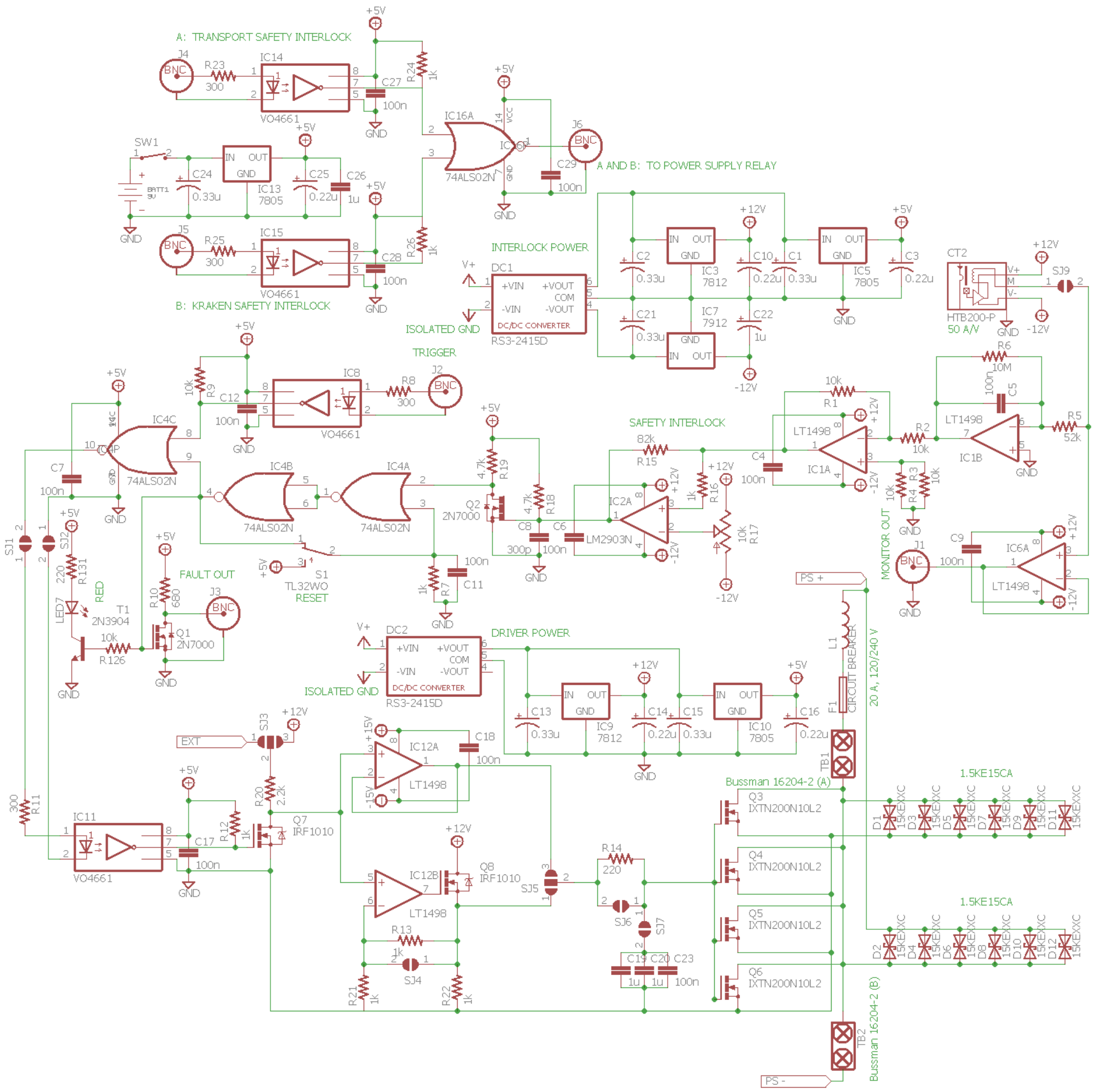

FIG. 6.4: Kraken schematic. The diagram shows the circuits for the four MOSFETs (IXTN200N10L2) and associated snubber, their driver, as well as the current sensor (LEM HTB200) and associated over-current interlocks.

transport system's high current power supplies. The Kraken's local safety interlock allows it to be operated independently of the coilplexer. The current sensor was added later to replace the one built into the coilplexer. A 20 amp circuit breaker is also connected in series with the push coil. The power supply voltage is programmed before the switch is triggered and controls the magnitude of the current pulse. The current pulses used were 5 ms long and more than 100 amps. The breaker takes approximately one minute to trip at 20 amps, but will allow high magnitude, 5 ms pulses as long as the peak current is not too high (~ 200 A).

6.2.2 Performance & Calibration

To use the push coil effectively for our experiment, it was necessary to determine how fast the atoms move for different push pulses. Figure 6.5 shows a variety of push pulses used to determine the velocity imparted to the atoms. If we assume that the magnetic gradient normalized per amount of current produced by the coil is homogeneous over the region the atoms are located during the pulse, then we can predict the initial velocity of the atoms using a similar method as was used in Chapter 5. We can adapt equation 5.4 for this situation:

$$\dot{z}(t) = v_0 + \frac{\mu_B b_P}{m} \int_0^t I_P(t')dt' \tag{6.1}$$

The direction of motion for the atoms in this case is the axial (z) direction and the b_P and I_P refers to the magnetic gradient and current for the push coil, not coil 6. This shows that the final velocity is proportional to the area enclosed by the pulse, or the charge pumped through the push coil during the pulse. Figure 6.5 shows the resulting final velocity as a function of charge through the push coil (the charge Q is given by $Q = \int_0^t I_P(t')dt'$). This data shows that the relationship is indeed linear, and allowed us to calibrate the push coil. Using this data, the magnetic gradient

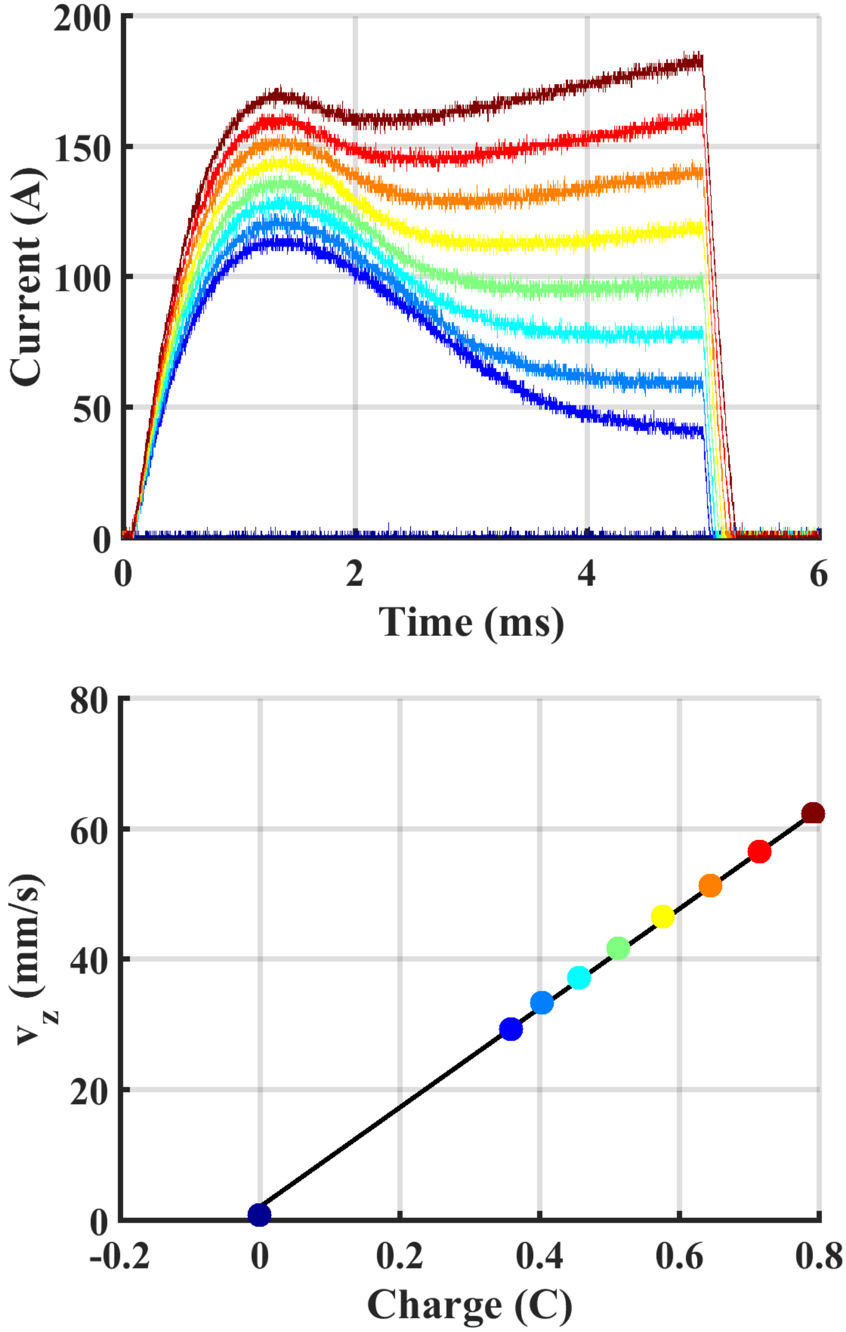

FIG. 6.5: Top: High current push pulses for generating initial velocity. The different color curves show the time evolution of the push coil current for different current request settings (on the power supply controlled by the Kraken switch). The Kraken switch is programmed to be on for 5.0 ms for all curves. The charge pumped through the coil was reproducible at the level of 0.1%. Bottom: Atomic velocity scales linearly with the amount of charge (in Coulombs) that flows through the push coil during push pulses. The colors of the points match the colors of the current traces on the top figure. The linear fit to the data gives a slope of 76.0 ± 0.6 mm/s/C, and is equal to $\frac{\mu_B b_P}{m}$ in equation 6.1.

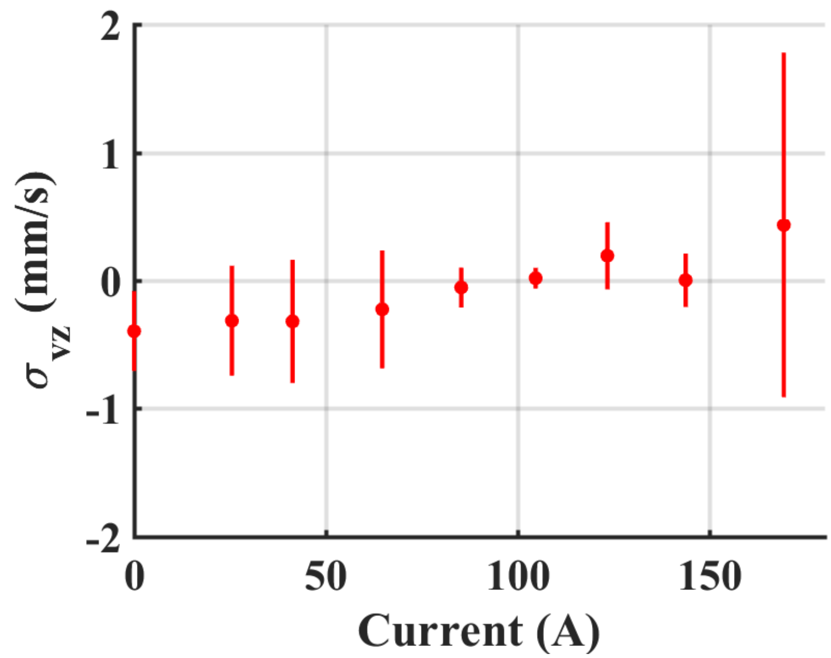

FIG. 6.6: Expansion rate of atoms as a function of peak current of the push coil pulse.

produced by the push coil was determined to be $b_P = 0.119 \pm 0.001$ G/cm/A. Additionally, we have the option of shaping[2] the pulse by choosing the duration and adjusting the pulse height correspondingly. We chose to keep the pulse short and high magnitude to prevent the atoms from potentially moving to a region where the magnetic gradient produced by the coil is no longer homogeneous. Short pulses were also beneficial because they minimized the amount of time the atoms take to reach the barrier, thus reducing the expansion of the BEC (and thus limiting the associated reduction in optical depth, i.e. imaging signal). Figure 6.6 shows the effect the push coil has on the atoms after accelerating them. The data points in the $I > 100$ A range reflect the push pulses used. I have reduced confidence in the highest current data point with a large error bar. A better benchmark for any atomic expansion due to the accelerating field can be seen in chapter 7 in figures 7.7 and 7.9. The $f = 0$ points correspond to a static barrier. That data not only

[2] I use this term loosely, as we had only coarse dynamic control with this setup.

accounts for expansion due to a push pulse, but also from interacting with a static barrier. Additional data collected from the push coil can be found in Appendix C.

6.3 Oscillating Barrier

This section details the design, characterization, and operation of the amplitude-modulated barrier. The barrier is provided by a tightly-focused, blue-detuned laser beam. According to two-level dressed atom theory, the potential the atoms feel due to off-resonance laser light is proportional to the intensity of the light, and inversely proportional to the detuning[3], or:

$$U(\mathbf{r}) \propto \frac{\mathbf{I}(\mathbf{r})}{\delta} \tag{6.2}$$

Here $\delta = \omega_{laser} - \omega_0$ is the detuning of the laser in rads/s; ω_{laser} is the laser's frequency, and ω_0 is the frequency of the closest atomic transition. Red-detuned light produces a potential well, while blue-detuned light creates a barrier for the atoms. The intensity profile $I(\vec{r})$ of the laser determines the shape of the barrier. We note that a tightly localized oscillating barrier (due to a tightly focused laser) not only maximizes the amplitude of the barrier (for a given laser power), but also also tends to promote sideband production (discussed in section 2.7). Single mode lasers feature a Gaussian beam profile as described by:

$$I(r) = \frac{2P}{\pi(w_x^2 + w_y^2)} e^{-2\left(\frac{x^2}{w_x^2} + \frac{y^2}{w_y^2}\right)} \tag{6.3}$$

I is the intensity, P is power, w is the beam waist radius, and r is the coordinate describing the distance from the central axis of the beam. Gaussian beams also change their beam waist when propagating over a distance z along the optical axis,

[3]When taking the well known rotating wave approximation.

such as when directed through a lens, or when a beam is converging or diverging in general. If w_0 is the waist radius at a focus located at $z = 0$, then the beam waist changes according to:

$$w(z) = w_0 \sqrt{1 + \left(\frac{z}{z_R}\right)^2} \tag{6.4}$$

In equation 6.4, z_R is called the Rayleigh length and it is defined by:

$$z_R = \frac{\pi w_0^2}{M^2 \lambda} \tag{6.5}$$

The Rayleigh length determines the region over which the focus shows relatively little change in beam waist (or when $w(z) = \sqrt{2} w_0$). It is important to note that a small focal waist radius, w_0, is desirable to tightly focus the beam for this experiment. However, a large Rayleigh length, z_R, is also desirable so that the atoms feel a quasi-uniform potential along the axial direction. Equation 6.5 shows that these two quantities and their respective desirable trends are in direct contradiction of one another. When making decisions regarding this trade-off, we chose to focus the beam as tightly as possible to promote sideband generation with a spatially localized potential and high barrier energy. The term M^2 also appears in equation 6.5 and represents the *beam quality factor* [81] in laser science. Fortunately, there is no trade-off in regards to this parameter as there is no upside to having a poor quality laser beam. However, creating a high quality beam is sometimes difficult. To this end, the beam was spatially filtered by coupling it through a single mode optical fiber, as shown in figure 6.17 and discussed more in section 6.3.2.

Regarding the spontaneous emission generated by the barrier beam, equation 6.2 seems to imply that the barrier energy can be made as large as desired by tuning the wavelength closer to resonance. In this case, the spontaneous emission, according to equation 6.6 [82] becomes severe and heats up the atoms.

$$\gamma_p = \frac{s_0\gamma/2}{1 + s_0 + (2\delta\gamma)^2} \tag{6.6}$$

6.3.1 Focusing & Wavelength

The size of the focused beam providing the oscillating barrier sets the scale for the other parameters in this experiment, and a more tightly focused beam promotes the generation of sidebands. Furthermore, the potential energy amplitude of the barrier is proportional to the intensity of the beam at the focus, and inversely proportional to the detuning of the beam from resonance. Resonance is the D2 line for ^{87}Rb at 780 nm. The original wavelength choice for the barrier beam was 532 nm. A beam detuned further from resonance requires more power to create a barrier of sufficient energy. Although a smaller wavelength can be focused more tightly, we have chosen to change the barrier wavelength from 532 nm to 767 nm, provided to us by the potassium laser cooling light used in our dual-species apparatus. This lowers the power requirements for creating a barrier. Furthermore, 767 nm is sufficiently detuned from the Rb D2 line, that very little scattering occurs for atoms interacting with the barrier. Simulation results indicate that the number of photons scattering through the barrier interaction would be on the order of ten. In addition, we have a recently constructed laser amplifier (set up by S. Du) for 767 nm that provides more power for the barrier beam. We have a new focusing lens, diffraction-limited, that has been used to focus the 767 nm beam as tightly as possible. The beam size has been measured with a knife-edge style measurement technique and the waist radius is 3.9 μm (Fig. 6.7). This is an improvement over the previous 4.4 μm and should be sufficient for the experiment, based on converting the simulation results from theoretical to experimental units. Multiple measurements were made to determine

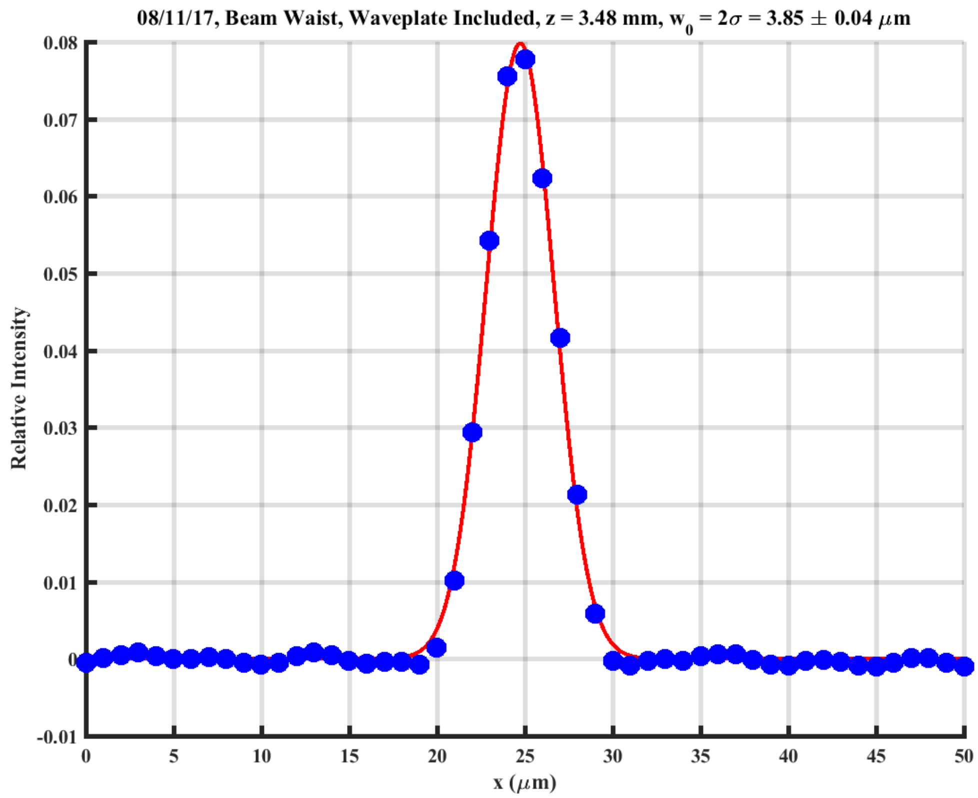

FIG. 6.7: The beam waist was measured at the focus of the beam. Here, the x direction is transverse to the beam, while z is the direction of propagation of the beam.

parameters required to construct a Gaussian beam model for the laser beam. Figure 6.8 shows the setup used for the beam profile measurement. The focusing lens used was the AL2550-B from Thorlabs. This lens was chosen to focus the barrier beam, because it is an aspheric lens designed to provide near-diffraction-limited performance by reducing wavefront error. A 1 μm pinhole was dragged across the beam to measure the beam profile. After hitting the pinhole, the beam was then focused onto a photodiode eye. This photodiode signal was sent to a LeCroy WaveSurfer oscilloscope equipped with math functions to divide the photodiode signal by a second photodiode monitoring the power fluctuations of another beam which was always left unblocked. The data was collected as quickly as possible by using a homemade

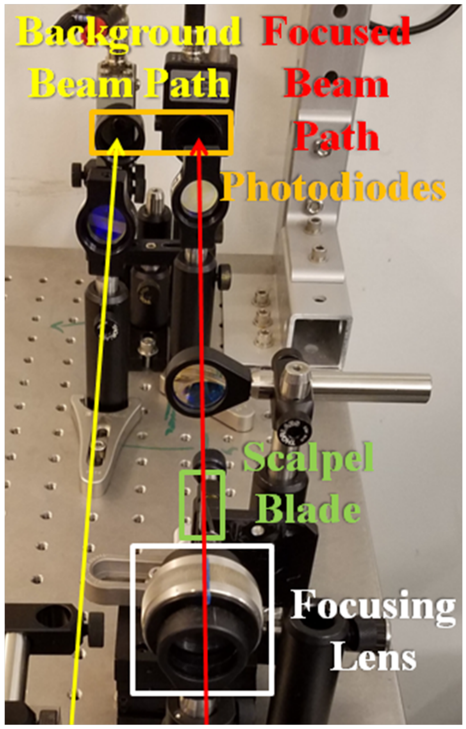

FIG. 6.8: Optical setup used to measure the beam waist at and near the focus of the barrier beam. Initial measurements were done with a new scalpel blade with a knife-edge measurement technique. The measurement was improved by replacing the scalpel blade with a 1 μm pinhole purchased in July 2017. Final measurements were collected with a piece of glass placed after the lens to simulate the vacuum cell of the apparatus.

trigger box to trigger the scope which had been programmed to save trace data with each new trigger.[4] A Thorlabs DM10 manual differential adjuster was used to drive the translation stage that the pinhole was mounted on. This component provided us with quality data (Fig. 6.7) with many points over a focused beam occupying a small cross-sectional area. Figures 6.11, 6.9, and 6.10 are similar to figure 6.7. Different cross-sections have been overlayed for different locations along the beam's axis. The different figures mentioned were collected at different vertical locations while portions of the beam above and below this location were blocked. The center locations on three of these plots is shown to wander. I believe this happened during

[4]This triggering scheme was used because the data was saved in the memory of the scope for post data-collection analysis (i.e. so I could take data quickly).

data collection, although I am unsure whether the beam was wandering, or if the act of turning the micrometer was enough to move the setup ever so slightly, about 5 μm. My guess is that the latter is responsible. A few of the red colored traces on figure 6.11 had been collected after the rest of data. Upon analysis of said data, I decided it was worthwhile to collect more. I suspect the longer pause in between collecting those two portions of data are responsible for the wander. The width of the beam at each of the z locations (for Fig. 6.11) can be plotted versus z location to produce figure 6.12. For whatever reason, the fit of the bottom plot of figure 6.12 gave reasonable values (albeit with large error bars), while the fit for the top plot of figure 6.12 did not. This was done in an attempt to measure the Rayleigh length and M^2 value of the beam. Notably, figure 6.12 shows that the waist radius varies little along the z-axis over a range of ~ 100 μm centered on the focus.

Figure 6.13 is similar to figures 6.11, 6.9, and 6.10. The z axis location of the pinhole was held constant as the blade was repeatedly swept through the beam horizontally at different vertical locations. All of the data can be used to produce a Gaussian beam model for λ =767 nm based on equation 6.3 with experimental values for the $w_{x,0}$, w_y, and M^2 parameters (see table 6.2). Figure 6.14 shows intensity maps based on this Gaussian model and the parameters of table 6.2.

Parameter	Value
Wavelength: λ	767 nm
Beam Quality Factor: M^2	1.1 ± 0.7
Vertical beam waist: w_y	795 μm
Horizontal beam waist: $w_{x,0}$	3.85 ± 0.04 μm
Power: P	~ 300 mW
Polarization	σ^-

TABLE 6.2: Barrier beam parameters.

Vertically Elongated Beam: Figure 6.15 shows the layout for the optical el-

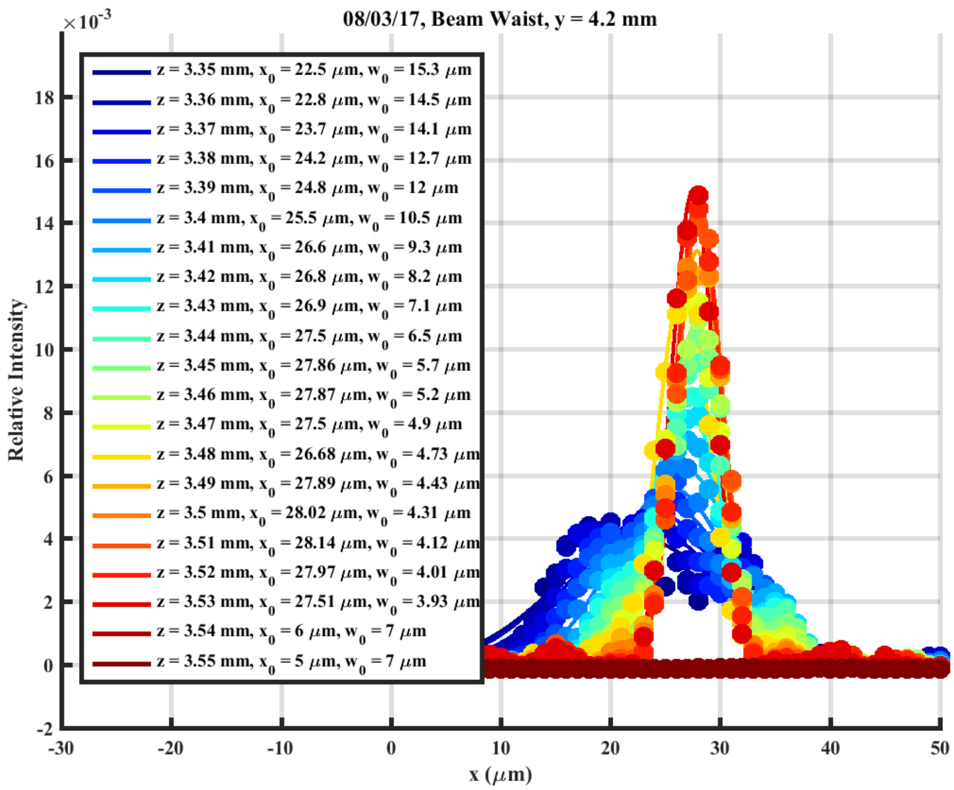

FIG. 6.9: Multiple beam waist measurements transverse to the beam repeated along the direction of propagation of the beam. The vertical location was held constant at about 0.6 mm above the vertical center of the beam. (4.2 mm relative to figure 6.13) Legend includes axial location, center transverse location, and beam waist. The difference in beam center location may be due to beam wander during the course of the measurements. Without more advanced equipment, it is not possible to speed up the data collection process. However, this may illuminate the degree to which the beam wanders over time.

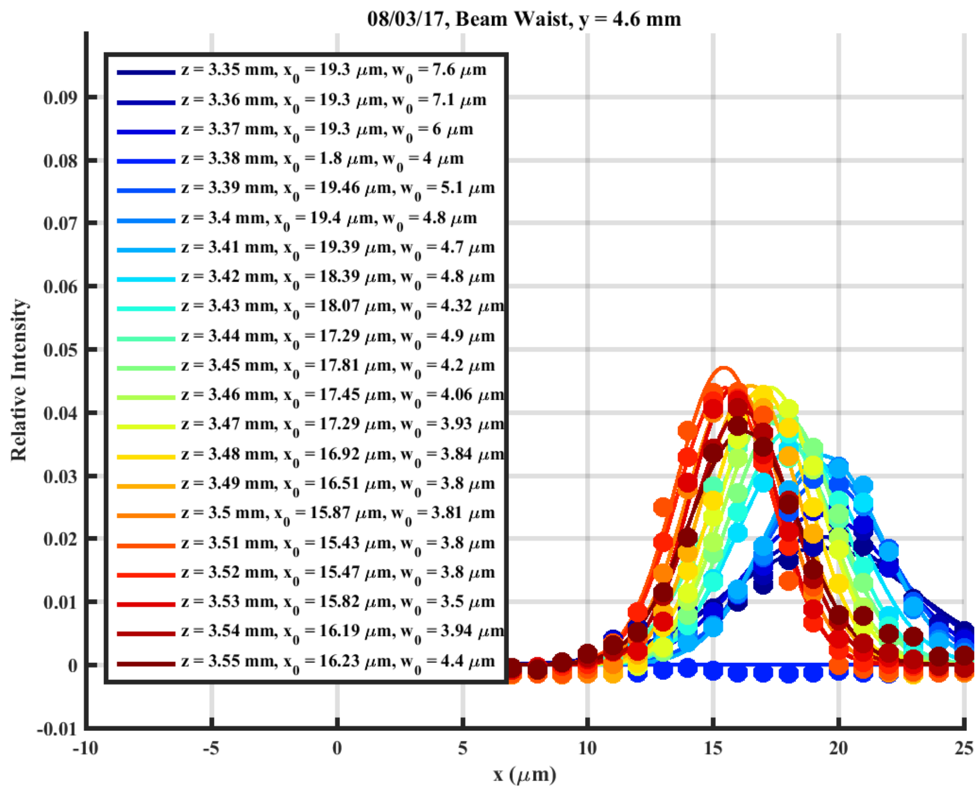

FIG. 6.10: This is qualitatively similar to figure 6.9. Multiple beam waist measurements transverse to the beam repeated along the direction of propagation of the beam. The vertical location was held constant at about 0.6 mm below the vertical center of the beam. (4.6 mm relative to figure 6.13) Legend includes axial location, center transverse location, and beam waist. The change in beam location is likely due to beam wander during data collection.

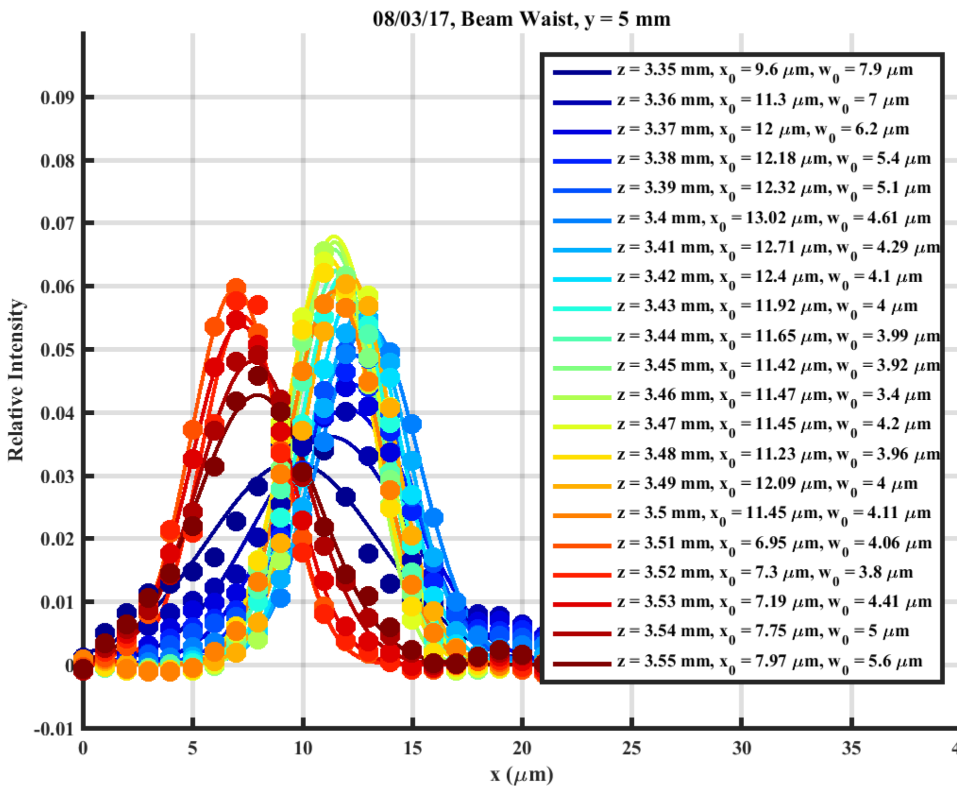

FIG. 6.11: This is qualitatively similar to figure 6.9. Multiple beam waist measurements transverse to the beam repeated along the direction of propagation of the beam. The vertical location was held constant at the vertical center of the beam (5.0 mm relative to figure 6.13). The legend includes axial location, center transverse location, and beam waist. The handful of data series with centers significantly different than the rest were collected the following day, after a bout of data analysis suggested collecting additional data series would be beneficial. This is highly supportive of the notion that the beam wanders over time.

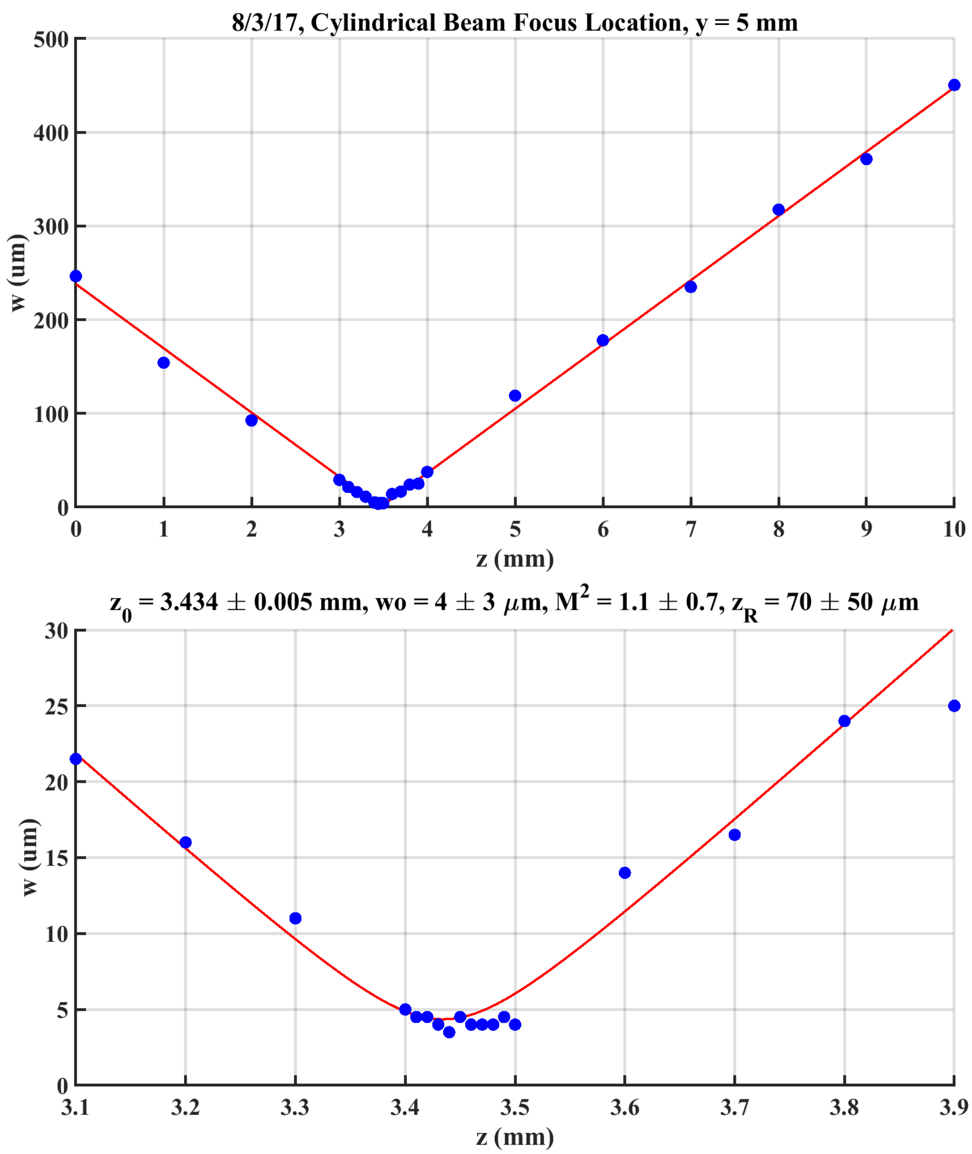

FIG. 6.12: Top: Beam waist vs. axial location. The data is fit (red) to the function given by equations 6.4 and 6.5. Bottom: This figure shows the same data as the top, but the axes are scaled to view the focus of the beam. The data was fit (red, using eq. 6.4 and 6.5) using only the points shown.

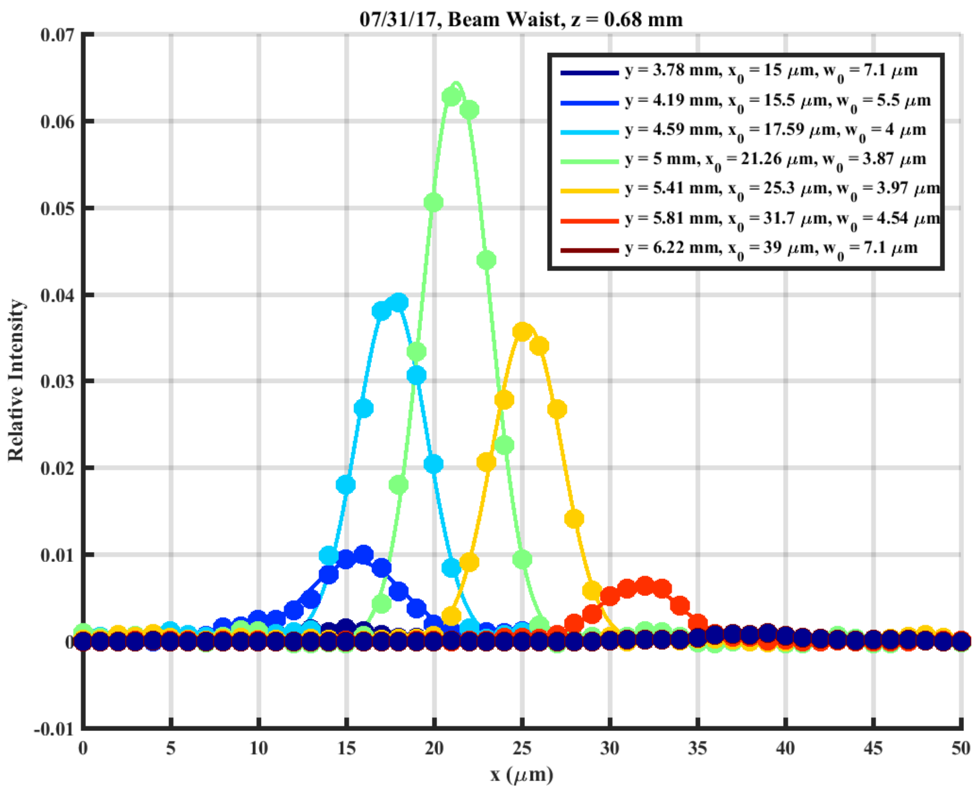

FIG. 6.13: Beam waist measurements along the vertical y direction of the beam. The legend includes vertical y location, center transverse x location (horizontal), and the beam waist radius w.

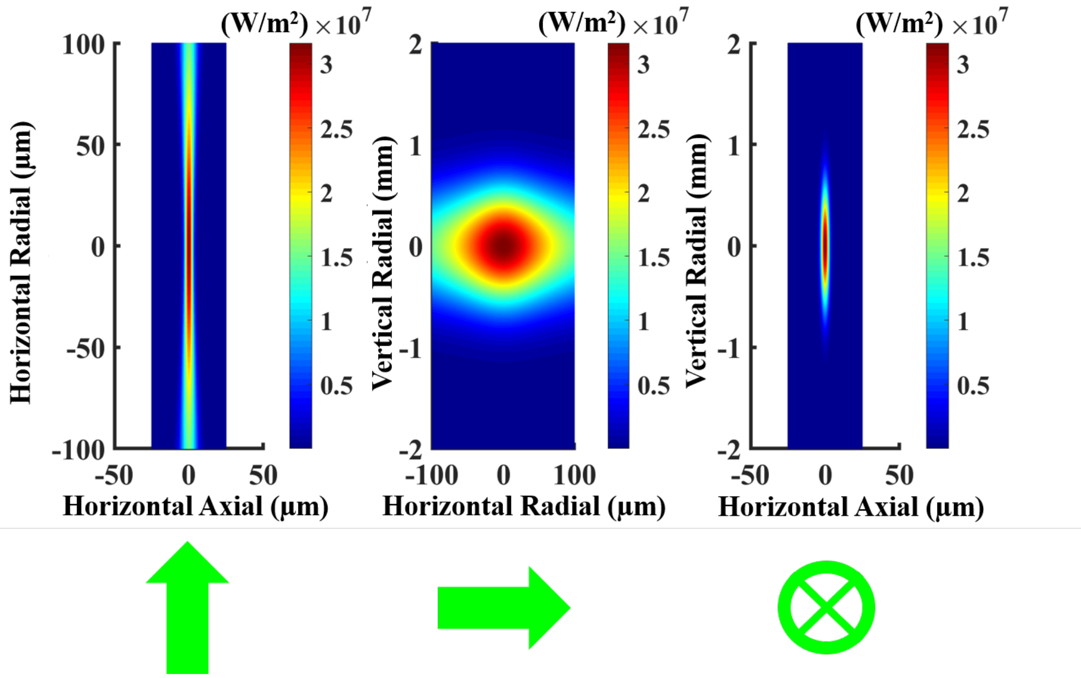

FIG. 6.14: False color plot modeling the barrier beam based on measured data and Gaussian beam modeling equations 6.3 ,6.4, and 6.5. Axes labels for x, y, and z correspond to the labels x, y, and z used in previous figures showing barrier beam measurements. The color bars indicate intensity in SI units, or W/m^2. This model is made for $\lambda = 767$nm, $M^2 = 1.1$, $w_y = 795$ μm, and $w_{x,0} = 3.85$ μm (see Table 6.2). The green arrows indicate the direction of propagation for each center cross-section panel.

ements used to generate the barrier beam. A cylindrical lens (Thorlabs ACY254-250-B, $f = 250$ mm) is create a beam that is focused in the vertical direction and unchanged in the horizontal. When the beam reaches the focusing lens (Thorlabs AL2550-B, $f = 50$ mm), the beam has maintained its original horizontal waist. The beam is made intentionally large to assist focusing the beam to the smallest size possible. The vertical direction of the cylindrical lens is meant to function as a telescope when combined with the focusing lens. This gives the vertical beam waist an overall magnification. Elongating the beam in the vertical direction ensures that the atoms will not experience a significant potential difference over the vertical height of the atom cloud (and subsequent jitter).

6.3.2 Frequency Control

The barrier beam requires a mechanism (Fig. 6.17) to stabilize the beam intensity and control the oscillation. This is accomplished by using an Acousto-Optic Modulator (AOM) that is capable of dynamically controlling the amount of beam power that is sent to the Tapered Amplifiers (TA) that amplify the beam. Variable Voltage Attenuators (VVA) control the AOM. We required the use of two VVAs because a single one (Mini-Circuits ZX73-2500+) was too slow (Fig. 6.16), and our high-speed VVA (Hittite HMC346G8, lab-built) did not have the required range to sufficiently attenuate the beam. The solution was to use both VVAs in series. The slow VVA adds a delay that is long enough to disrupt proper feedback operation. To work around this problem, we calibrated the fast VVA and programmed an arbitrary waveform generator (ARB, Siglent SDG5122) to control the fast VVA with a feed-forward technique. To complete control of the waveform, a photodiode monitors the barrier beam before it enters the vacuum cell and provides information to perform feedback stabilization on the beam using the slow VVA. The problem of the delay

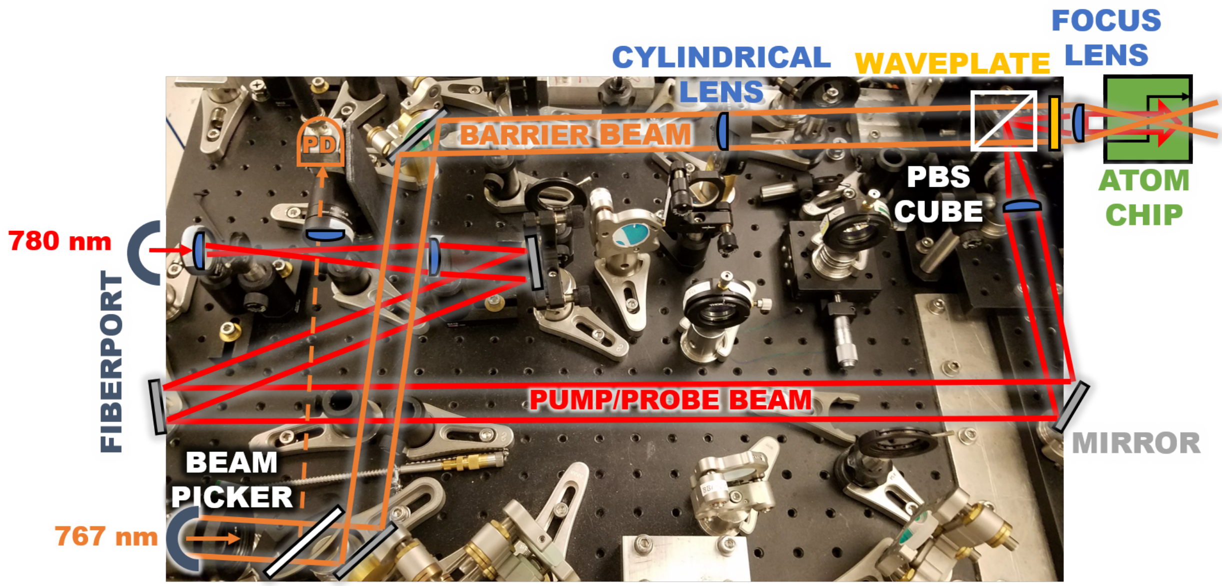

FIG. 6.15: Gaussian barrier beam scheme. The barrier beam (orange, 767 nm) is delivered to the system through a polarization-maintaining optical fiber (dark gray). The beam is combined with the axial imaging pump/probe beam (red, 780 nm) on a PBS cube (white). The blue-detuned focused sheet of light is produced with a cylindrical lens (Thorlabs ACY254-250-B, $f = 25$ cm) that focuses the beam in/out of the page followed by a $f = 5$ cm aspherical lens (Thorlabs AL2550-B) that collimates the beam in/out of the page and focuses the beam up/down on the page. An AR-coated and angled 90:10 beam picker picks off a small reflection for monitoring and controlling power on a photodiode (PD, orange). Alignment is done with two mirrors and a translation stage (Thorlabs SM1Z) that the aspherical lens is mounted to for adjustments of the focus along the axis of propagation. The mirros are elliptical and the beam picker is 2" in diameter. These were chosen so that the large beam would not be clipped on any of the optical elements. The beam was made intentionally large to focus as tightly as possible.

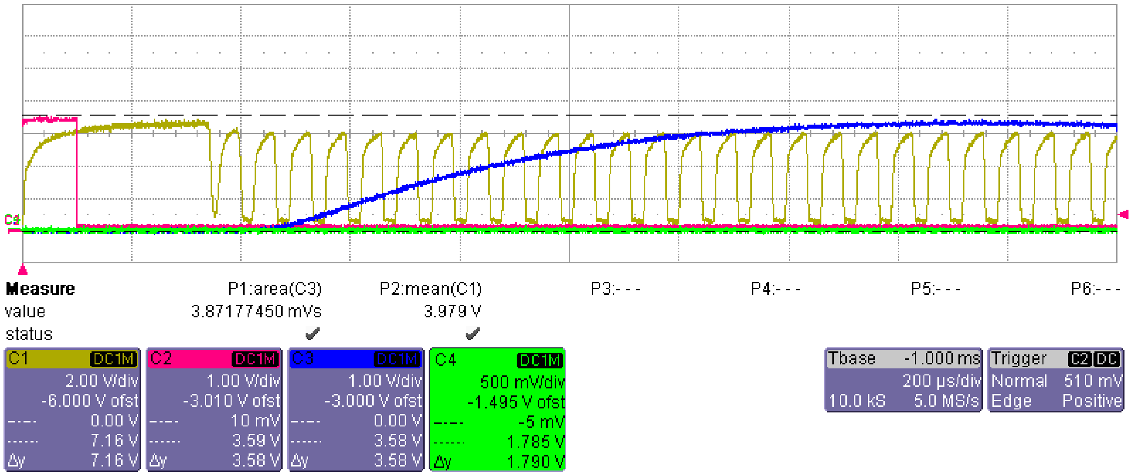

FIG. 6.16: Saved scope image of a photodiode signal (yellow) showing a non-sinusoidal barrier signal.

introduced by the slow VVA is solved by adding a relative phase between the ARB channels controlling the feed-forward to the fast VVA and the feedback setpoint for the slow VVA. This produces an oscillation in barrier intensity in the form of a sine curve (Fig. 6.18), albeit with a smaller amplitude than we had preferred.

6.3.3 Setup & Calibration

The barrier optics were used to align the beam so that it passes underneath the atom chip. The beam focus was placed in the horizontal plane of the atoms and aligned by launching atoms at the barrier with oscillation turned off (i.e. a static barrier), and adjusting the lens for optimum reflection (Fig. 6.19). Barrier energy was measured by launching the atoms at the barrier with a known kinetic energy as determined by time of flight velocity measurements (Fig. 6.19) and measuring atomic transmission and reflection across the barrier as a function of kinetic energy.

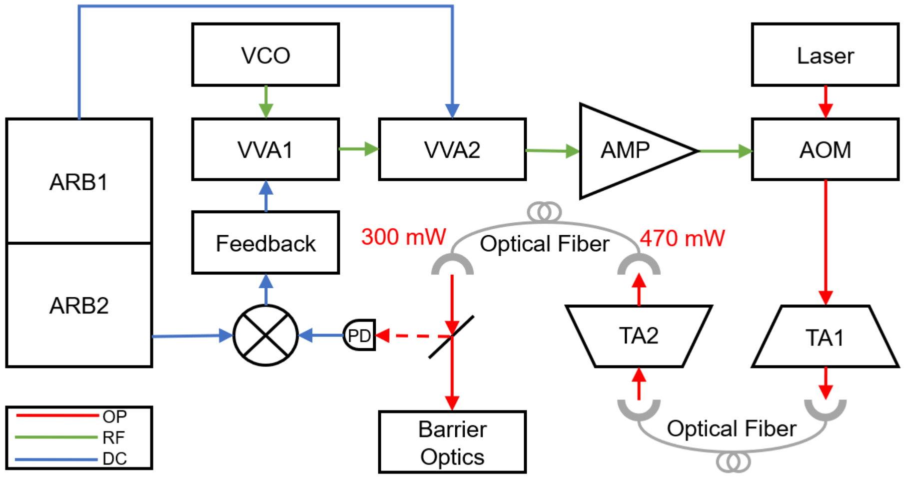

FIG. 6.17: Block diagram of the barrier intensity control systems. ARB1 and ARB2 signals are generated by a two channel ARB generator. The optical signal (red) is generated by a 767 nm diode laser which is amplified and becomes the barrier beam. The barrier beam power is oscillated sinusoidally, by measuring the optical power with a photodiode (PD), which is compared to a sinusoid signal to generate a DC-20 kHz error signal (this signal and related ones are shown in blue), which is then fed back to the VVAs to control the optical power via RF (green) to the AOM (see main text for details).

6.3.4 Optics & Alignment

The final optical setup constructed for the barrier beam also incorporated the absorption probe (on the platforms next to the atom chip). In particular, considerable time was spent aligning and also adding significant translational, but no rotational, control. A good quality PBS cube was added for fixing the polarization of the barrier beam and the probe beam. This cube also allowed convenient mixing of the barrier and axial probe beams. Due to the precision alignment required by the barrier beam with respect to the probe, the optical setup was designed such that the barrier beam transmitted through the cube, while the probe reflected off it. A waveplate was also added for polarization control. Polarization was chosen to favor the imaging system. The quantization field during barrier interaction is the magnetic field generated by the levitation coils. This combination set the determined

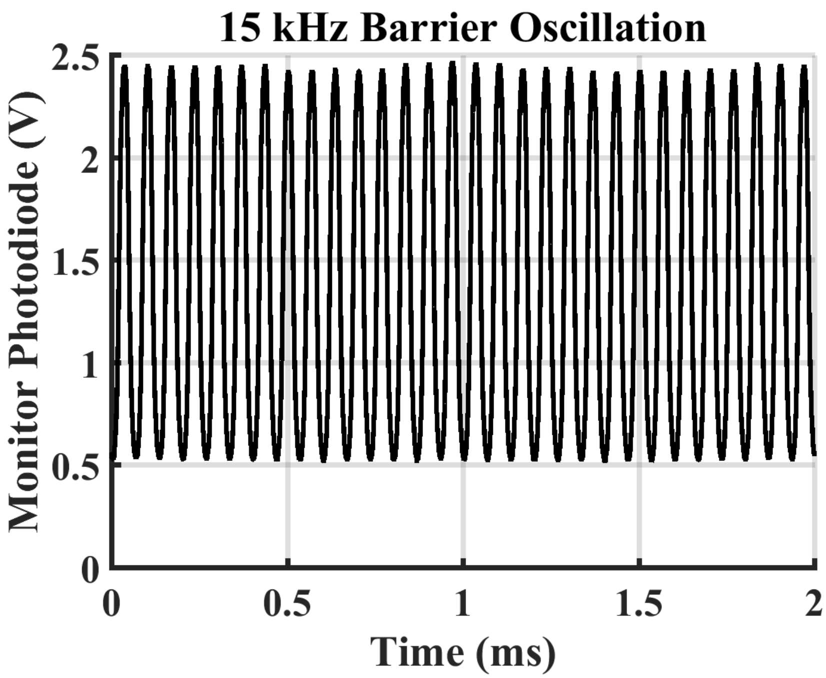

FIG. 6.18: Barrier oscillation monitored via photodiode. The oscillation frequency is $f = 15$ kHz. The barrier amplitude (in energy) is proportional to the photodiode signal (after removing an offset due to photodiode pre-amp). There appears to be a slow modulation (period ~ 1 ms) of the oscillation amplitude if you look at the top of the oscillations. This might be an aliasing effect (from the scope), though it is less apparent at the bottom of the oscillations. Data collected with a LeCroy WaveSurfer digital oscilloscope (5 MHz sample rate).

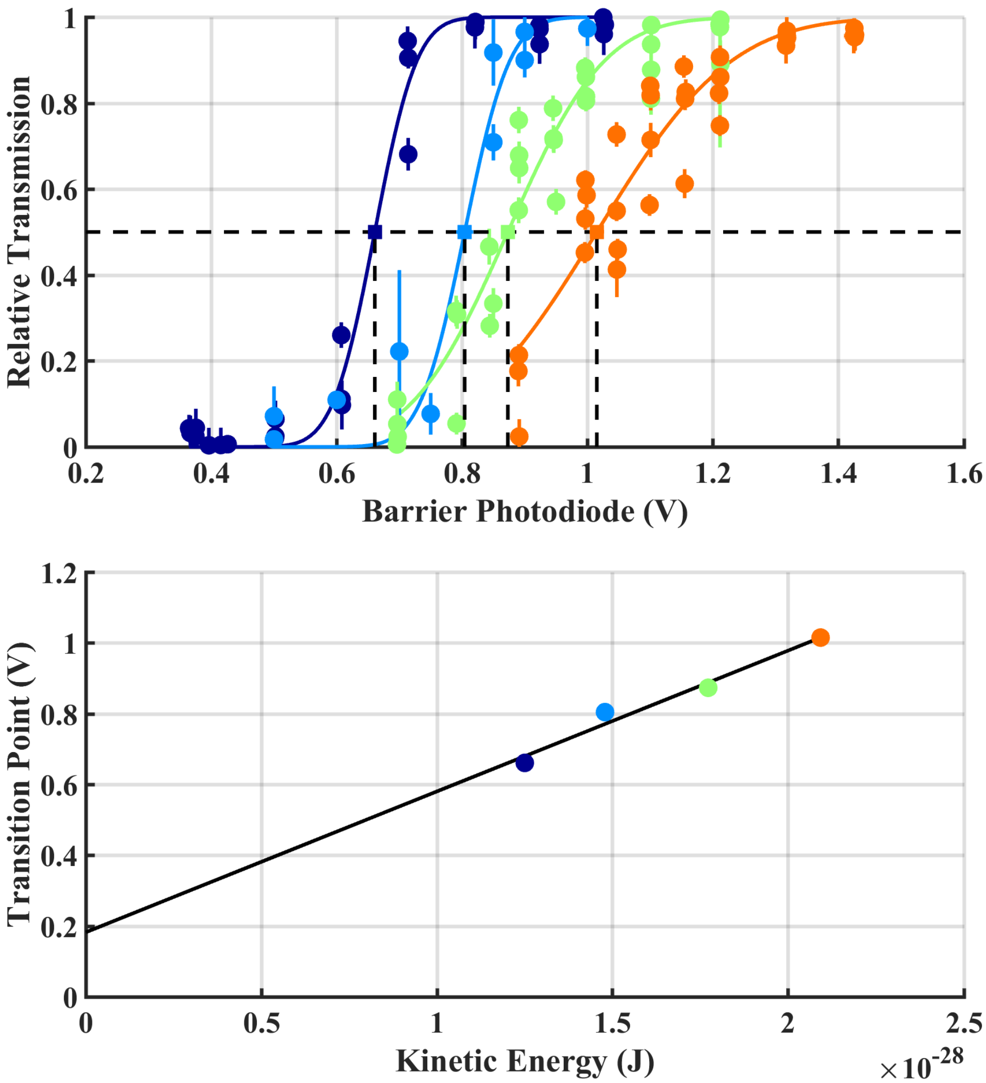

FIG. 6.19: Top: Calibration of the barrier beam potential energy. The plot shows transmission curves for different incident atomic kinetic energies (different colors). The data and fits show atomic relative transmission vs the barrier photodiode signal (in Volts) for a static barrier. The square points indicate the 50/50 transition point according to the fit curve. The data was fit with an error function (erf). Bottom: Median transmission point photodiode voltage vs initial kinetic energy of atoms incident on barrier. The colors of the points correspond to the colors of the curves in the top figure. For reference, a kinetic energy of 1×10^{-28} J corresponds to $E_{kinetic}/k_B = 7.2$ μK. (The offset is due to photodiode preamp.)

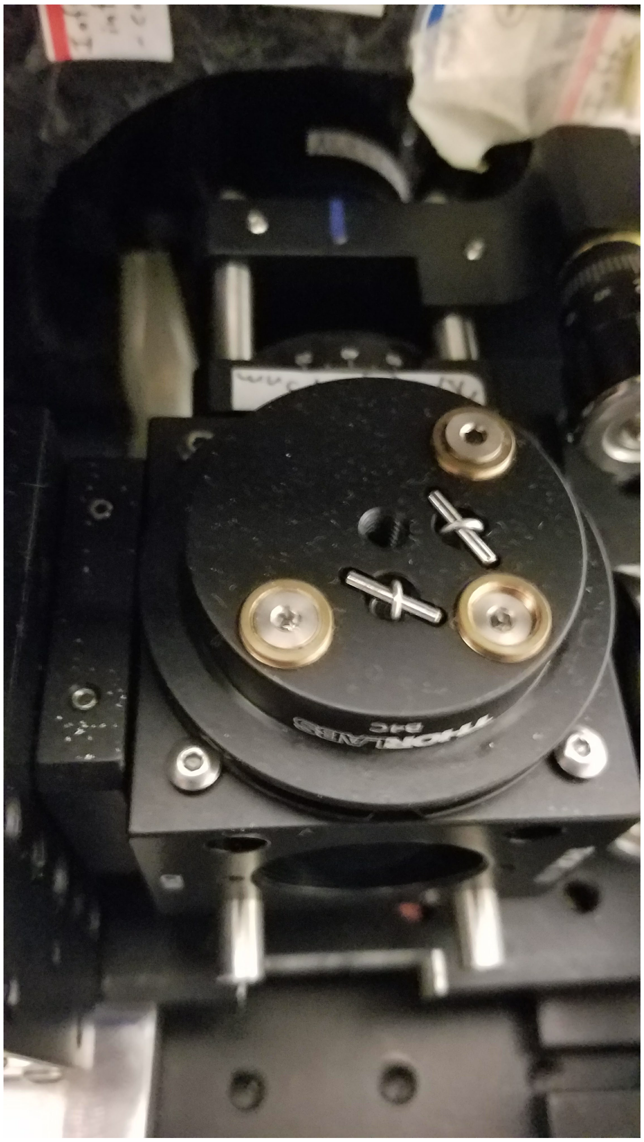

FIG. 6.20: Photo angled top-down of optical assembly. With respect to this photo, the barrier beam travels from bottom to top, while the axial probe is incident on the right side of the cube housing.

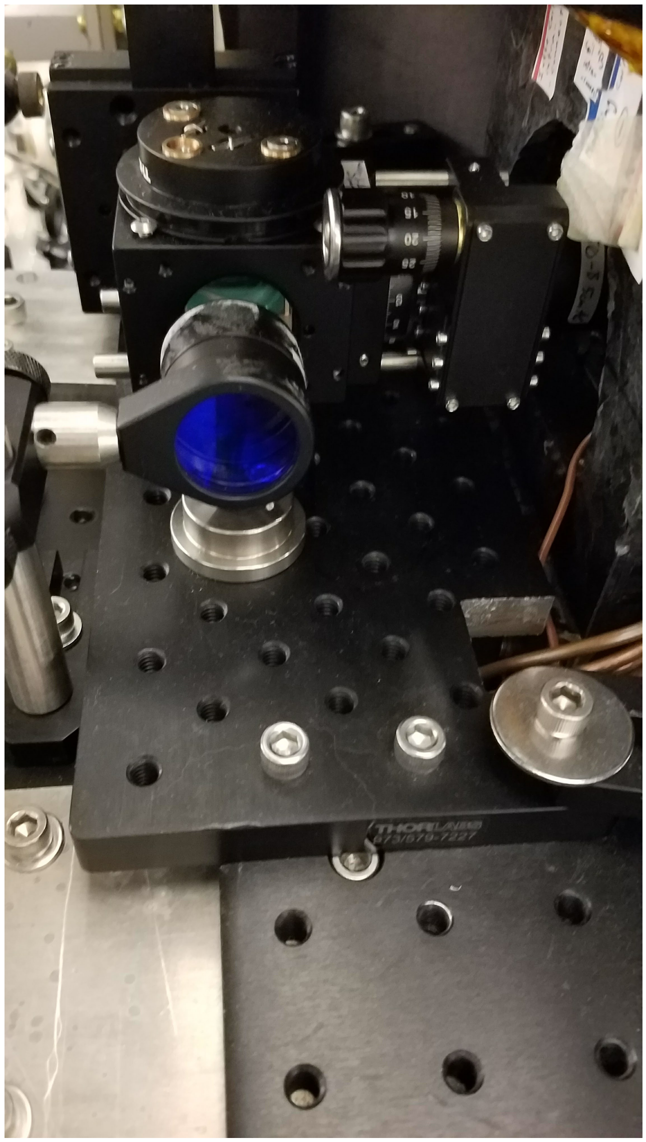

FIG. 6.21: Side view of optical assembly. With respect to this photo, the barrier beam travels from left to right, while the axial probe travels from bottom to top to the cube housing where it reflects to travel to the right, towards the science cell.

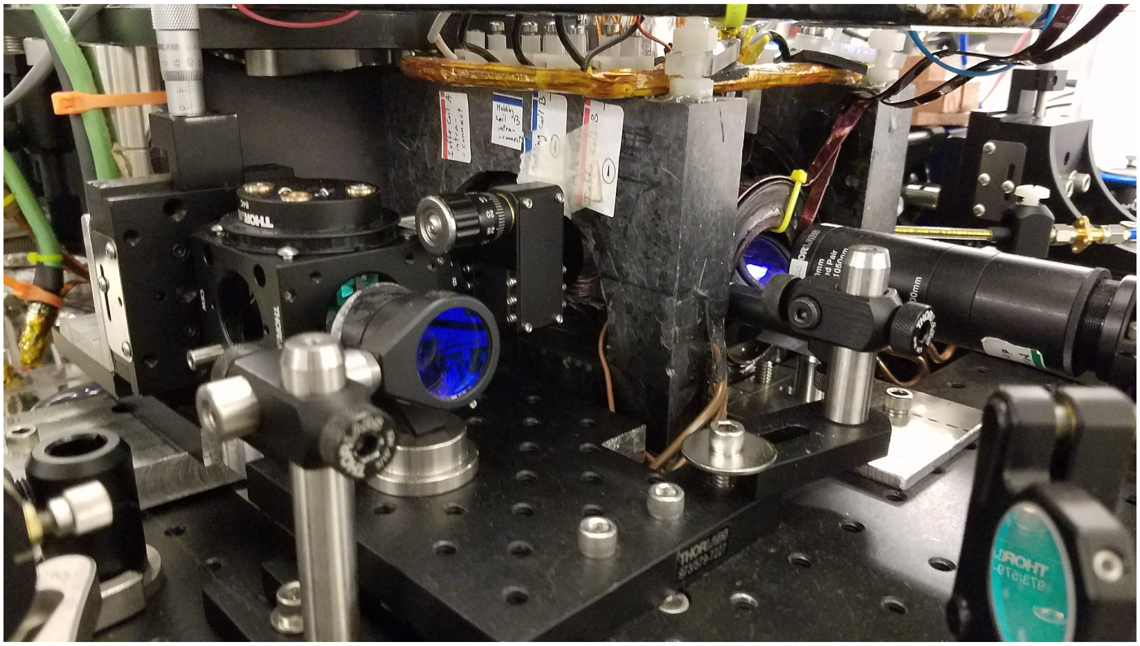

FIG. 6.22: Angled photo of the gizmo.

the effectiveness of the barrier beam given the polarization.[5] The final cage system device was compact, and gave the control that was required. This system should be reused and possibly expanded upon if the need to tightly focus a beam arises again.

The cube was mounted upside down to a tilt-plate inside a cage system. This gave the ability to rotate and tilt the cube to control the angle of the probe beam. After the cube, both beams pass through a waveplate and then the focusing lens. An additional lens to collimate only the probe beam is placed an appropriate distance from the cube to balance the focusing caused by the lens intended to focus the barrier beam. The focusing lens (Thorlabs AL2550-B) itself is mounted on a Z-axis translation stage for fine control (Thorlabs SM1Z). This entire setup was mounted to a translation stage oriented vertically to easily move the beam up and down, and then bolted to the platform near the science cell.

The following is a brief, and hopefully helpful, description of the alignment

[5]The only solution to this problem is to use a dichroic waveplate to set the polarization for the 780 nm imaging beam and 767 nm barrier beam independently.

procedure used for setting up and aligning the barrier beam. The first step is to determine the location at which to align the barrier beam. The criteria for determining this is when the atoms are properly prepared to interact with the barrier. This occurs when the atoms are no longer accelerating after they have been pushed to move axially at a constant velocity, and their vertical position has been stabilized so that they no longer fall under gravity. The atoms are finished accelerating before the levitation coils are turned on, so figure 5.28 provides guidance for determining when the vertical position has stabilized. The location of the atoms can be found easily by collecting an image at the appropriate time after turning off the levitation coils and waiting a minimal time of flight. We do not expect accurate atom numbers from analyzing these images, however the location of the atoms will be accurate. We compensate for the atoms falling vertically for a short time between levitation coils turning off and the camera taking an image (~ 1 ms of time, which is not very significant, but still accounted for). For alignment purposes, it is easiest to roughly center the camera on this location. This can be done by adjusting the camera position and empirically monitoring the atoms on the camera. With the camera in position, the beam was roughly adjusted to the height of the camera's optical axis and coarsely leveled according to the beam's height above the platform (the two platforms on either side of the chip are approximately the same height above the optics table). This was done with the beam at a low power setting with camera settings adjusted and a filter removed accordingly to view the beam on the camera. The waveplate before the optical fiber can be adjusted to redirect some of the beam to a beam dump and away from the camera to protect it. The beam should be initially aligned as a collimated beam, without any lenses or the "Gizmo" (figures 6.20, 6.21, and 6.22) installed. An aperture was closed about the center of the beam to make the alignment process easier. The beam can be aligned using the camera location as a target. To provide two points to align to, the camera can be moved along its optical axis via translation stage. With the camera sitting at opposite ends of the translation stage, two targets are available to align the beam to. A more precise, but similar, alignment method can be used that has been used previously to align the sensitive dark-ground imaging system. The beam is adjusted with one alignment mirror to hit the target location or center of the camera. The camera lens is then removed and the other mirror is used to align the beam to the center, or the dark-ground mask (which can be adjusted to be in the center of the camera, on the optical axis).[6] This process was iterated until the beam was aligned. After the collimated beam is aligned, the "Gizmo" should be set to the same height as the beam via a vertically oriented translation stage. The "Gizmo" was then installed with the focusing lens placed along the optical axis and bolted to the table in the location that best maintains the beam location on the camera (especially the horizontal location). The vertical location of the beam was easily adjusted with the vertical translation stage. The cylindrical lens (Thorlabs ACY254-250-B) was installed to focus the beam to a sheet, rather than a point. the cylindrical lens is round and mounted in a rotation stage to easily adjust the angle of the sheet beam to orient it vertically. At this point, the barrier beam is the proper shape and coarsely aligned to the atoms. Moving atoms are required to adjust the focusing lens to the optimal location. Atoms were launched at the barrier with scheme previously described (i.e. push pulse, and then levitation). The barrier is set to high power with the camera appropriately protected from the beam power. The lens focus is adjusted for maximum reflection of atoms. Reflection is easy to confirm, as the atoms appear in a different location on the camera than if they transmit through the beam. The beam power can be lowered to fine-tune the lens focus as the atoms will only reflect when striking a barrier with enough energy. This process was iterated until the beam no

[6] There is a correct way to pair the mirrors with the adjustment. Using the wrong mirror will cause the beam to diverge from the desired beam trajectory. If this happens, adjust the opposite mirror with the lens on/off.

longer had sufficient power to reflect the atoms when optimally aligned. The beam location and orientation was periodically checked using the camera and appropriately adjusted (mostly vertically) to maintain performance. It is also noteworthy that the method of aligning the lens focus is disadvantageous as it requires the disappearance of reflected atoms to know when the lens has been moved too far. The disappearance of atoms is inherently a difficult method in general, as the disappearance of atoms is not always due to the active adjustment. However, it was useful to check for the presence of transmitted atoms to confirm that the atoms disappeared at the reflected location due to low barrier energy, and not lack of atoms. Blocking the barrier beam as a test is effective to confirm transmitted atoms as the scenario in which both transmitted and reflected atom clouds appear have less optical depth as 2 $N/2$ atom clouds than one cloud with N atoms.

6.4 Detection

The primary objective of the experiment is to measure the velocity distribution of the atoms after interaction with the oscillating barrier. In order to simplify the experiment we focus only on the reflected atoms, which for our parameters includes all of the atoms. This is because the barrier energy chosen to promote sideband generation is so high that the atoms do not have enough energy to transmit through it. If, after interacting with the barrier, the reflected atoms are allowed to propagate for a significant time of flight, then the velocity distribution will map onto the spatial distribution of the atoms: the propagation time must be sufficiently long that the atomic cloud becomes substantially larger than its initial size (immediately after reflecting off the barrier). In fact, the time of flight determines the resolution with which the velocity distribution can be observed: indeed, the longer the time of flight, the more time that the sidebands have to separate from the carrier atoms.

The spatial distribution can then be imaged by absorption imaging with a resonant collimated probe beam (D2 lines cycling transition $F = 2, m_F = 2 \rightarrow F' = 3, m_{F'} = 3$ at 780 nm) that is directed roughly along the same axis as the barrier beam.

Due to how the barrier beam and probe beam are combined, the probe beam is linearly polarized. The Hold field is turned on to function as a quantization field and the magnetic levitation field is turned off before imaging. While the expansion of the atomic cloud reduces its optical depth, thus leading to a significantly reduced absorption, the signal remains sufficient to obtain an absorption imaging signal. In order to increase the signal, the vertical pixels are summed to only look at the axial distribution (horizontal). The maximum time of flight is determined by the quality of the absorption image. In some cases, multiple images are taken to improve the signal to noise and extend the time of flight (e.g. if one is looking for sidebands).

In order to block the barrier beam from entering the imaging system, several narrow bandpass filters are employed (780 nm passed, 767 nm blocked). The choice of filter significantly affects the imaging. Considerable effort was expended in testing out different filters and combinations of filters in order to minimize interference fringes at 780 nm due to reflections between the filters and other optical elements in the imaging system. Ultimately, the arrangement that worked best was the following: Thorlabs FBH780-10, Neutral density filter with $OD = 0.2$,[7] and a second Thorlabs FBH780-10. This filter combination resulted in a significant reduction in probe light onto the CCD ($\sim 50\%$), which was compensated for by increasing the probe power (seen by the atoms) by an equivalent amount.

[7]The ND filter is used to additionally lower the barrier laser beam power reaching the camera, and to prevent a cavity between the two FBH780-10 filters.

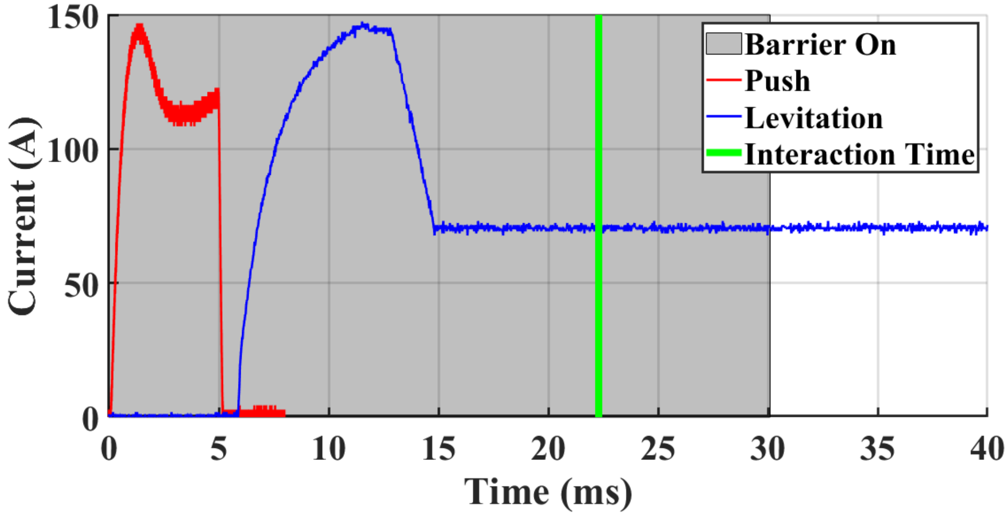

FIG. 6.23: Plot of current vs. time for the push coil (red) and levitation coils (blue). The shaded gray block indicates a region in which the barrier is on, while the green line indicates the time at which the atoms interact with the barrier. The time-of-flight after interaction was then variable for the experiment before an image was collected. (For an initial velocity $v_i = 5.0$ cm/s.)

6.5 Summary of Experimental Sequence

The overall procedure for the experiment is to cool atoms to BEC in our atom chip trap. The chip trap is then relaxed to lower the expansion rate, and then turned off. Once the atoms are released (t=0, fig. 6.23), the push coil is pulsed to start the atoms moving in the horizontal direction. The levitation coils are turned on to provide an upward force greater than that of gravity to slow the atoms down, and then is lowered to cancel gravity (i.e. levitate the atoms). The atoms propagate until they interact with the barrier. The atoms retroreflect from the barrier. Finally, after a time of flight, the camera collects an absorption image. A detailed version of the equipment timings is shown in an image of the Adwin sequencer panel for the experiment in Appendix D.

CHAPTER 7

Results & Discussion

7.1 Introduction

In this chapter, we characterize the scattering from a single oscillating Gaussian barrier and attempt to observe quantum behavior. The basic objective of this early experiment is to detect quantum Floquet peaks, or sidebands, emerging in momentum space. Our approach is to launch a BEC towards a single oscillating Gaussian barrier and attempt to detect the subsequent sidebands. We examine the resultant images after atoms interact with a single oscillating barrier using a time-of-flight method.

In this chapter, I review the results of this experimental scheme and display the effect the barrier has on the expansion rate of the atoms. Included in this chapter are discussions of experimental parameters, data collection and analysis. Preliminary attempts to observe sidebands are shown, as well as resulting trends when the barrier oscillation frequency is altered. The phase dependence of the barrier is investigated to show minimal effects at higher frequencies. The barrier also affects the behavior of the atoms in transverse directions.

7.2 Expansion Rate & Mean Velocity

7.2.1 Data Collection

The goal of this experiment is to resolve discrete momentum sidebands mapped onto a position space wavefunction. Due to difficulties in maintaining optical depth at the long times of flight required to resolve discrete atomic clouds, a relatively easier[1] alternative can be used to determine the effect on atoms interacting with a modulated barrier (barrier frequency and other experimental parameters are contained in Table 7.1). Measuring the initial expansion rate post-interaction does not require long integration times and cloud size data can be collected immediately after the atoms leave the barrier. The expansion rate is determined by fitting the ROI (Region Of Interest) sum along the vertical axis of an atom cloud and applying a Gaussian fit (fig. 7.1) to the resulting horizontal (axial) profile to determine the width of the cloud.[2] Once the cloud size is known for a variety of times of flight, the expansion rate is determined by finding how quickly the cloud increases in size over time (this is a linear relationship at long times). Figures 7.2 and 7.3 are examples of such expansion. Data was collected for multiple barrier frequencies and two initial atomic velocities, hereby referred to as the "Faster Velocity" (v_i = 5.3 cm/s) and the "Slower Velocity" (v_i = 5.0 cm/s).[3] Both figures show short to long times of flight, after barrier interaction, from top to bottom. The data has been filtered with a Gaussian convolution and each mean position has been subtracted so that the size of the clouds can be visually compared. These figures show that the atom cloud does indeed expand over time. There is a trade-off when attempting to characterize expansion. Clouds that expand very little require longer flight times, and still might

[1] This was not easy.

[2] We typically describe the width of the atoms by using the σ parameter ("standard deviation") of the Gaussian curve. Waist radius/diameter could also be used, as long as the convention is consistent for determining the expansion rate.

[3] This is a 6% change. We expect subtle differences between the two sets of parameters.

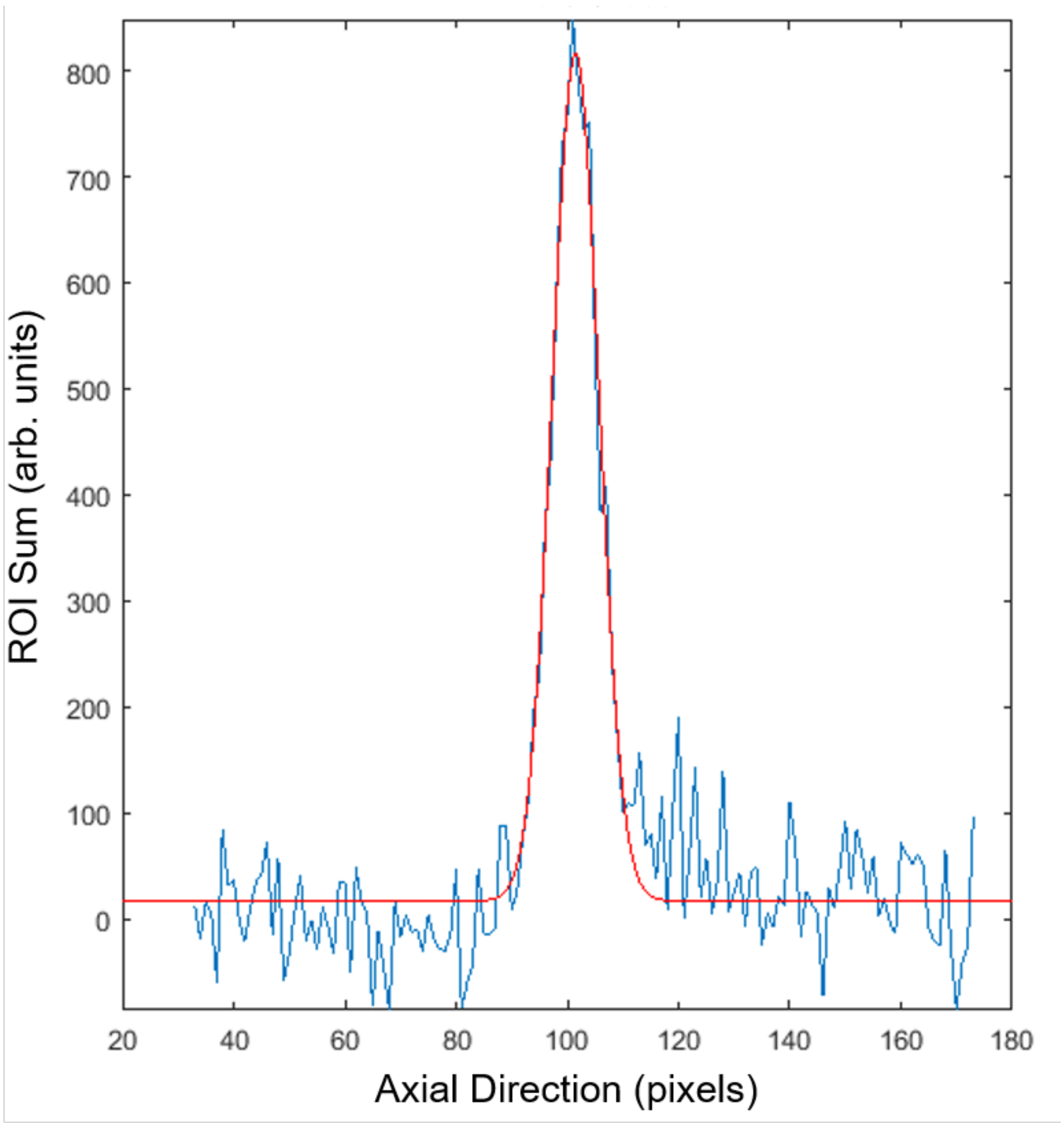

FIG. 7.1: This is an example of a Gaussian fit (red) to ROI sum (blue) to show the data analysis process. This data was collected with f = 13 kHz and 13.3 ms time-of-flight. The initial velocity used to collect this data is $v_i = 5.0$ cm/s. Not all of these fits would be considered "good" Gaussian, but the data can be loosely fit by a Gaussian.

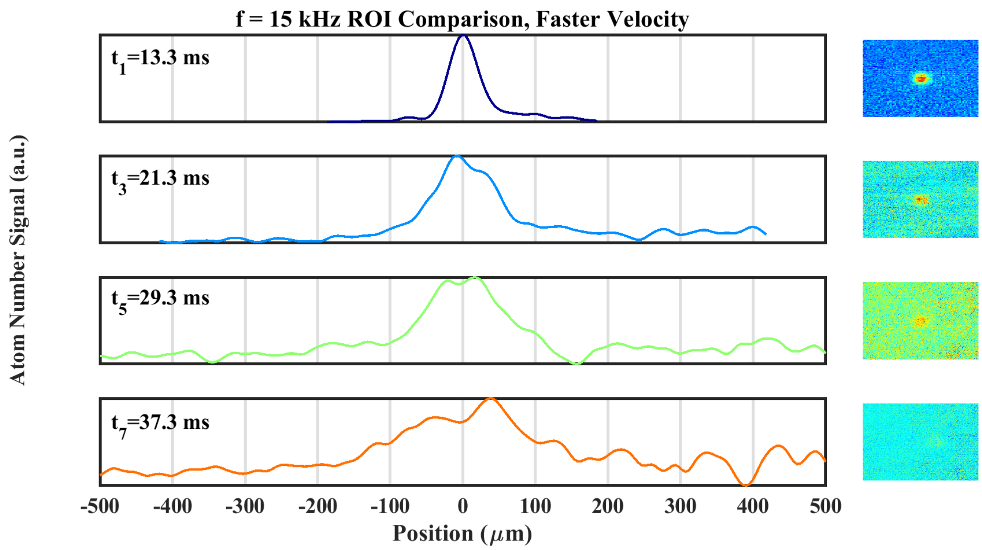

FIG. 7.2: This plot shows the filtered ROI (Region of Interest) sum for multiple times of flight (t_n). The atom cloud clearly expands over time in the axial direction. The data shown was collected for the faster initial atomic velocity and a barrier modulation frequency of 15 kHz.

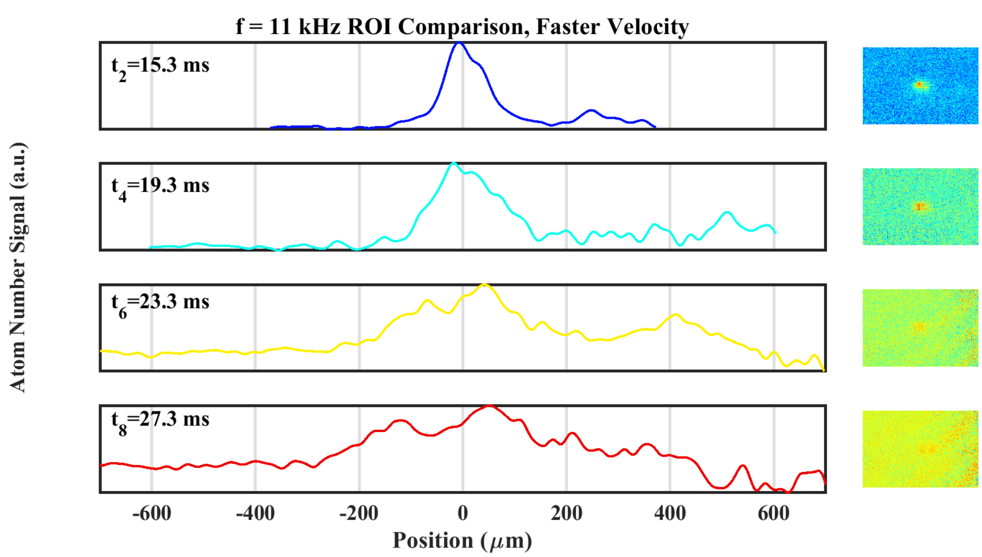

FIG. 7.3: Qualitatively similar to Fig. 7.2, but with a barrier modulated at 11 kHz. Some fringes caused by the imaging system can be seen at low optical depths.

show a negligible increase in cloud size. Clouds that expand very rapidly distribute the finite number of atoms over a larger area, decreasing optical depth and thereby reducing image quality. These clouds cannot be observed at long times due to lack of signal. However, the difference in expansion rate becomes qualitatively obvious when comparing clouds that have expanded very little over a long period of time versus clouds that have grown to a substantial size in a relatively short amount of time. Additional plots similar to figures 7.2 and 7.3 can be found in Appendix A.

Parameter	Value
Barrier Width: $w_b = 2\sigma_b$	3.85 μm
Barrier Frequency: ω	$2\pi \times 0 - 15$ kHz
Barrier Dither: α	0.75
Atom Initial Velocity: v_i	5.0 or 5.3 cm/s
Mean Barrier Energy: U_0	~ 54 μK

TABLE 7.1: Experimental parameters. Barrier frequency was varied with 1 kHz steps while all other parameters were held constant. This was done for two velocities: 5.0 and 5.3 cm/s. Barrier dither, α, was intended to be as close to 1 as technically possible. The parameters were chosen through a combination of optimization and restrictions placed upon us by the apparatus. The barrier beam cannot be focused more tightly than it is. The barrier frequency can be increased at the cost of barrier amplitude dither. The initial velocity can be increased as the power supply and pulse times allow. The barrier energy can only be increased by providing more laser power without the ability to focus the beam smaller.

7.2.2 Preliminary Data

An example of cloud size expanding over time can be seen in figure 7.4 (top), which shows the preliminary axial expansion rates from oscillating and static barriers compared to no barrier. The expansion rate for the static barrier case is negligible and similar to the rate when no barrier is present. This lack of expansion indicates that the presence of the static barrier is not causing momentum broadening and corrupting the well defined energy state of the BEC (e.g. through atom-atom interactions possibly). The oscillating barrier caused an expansion, as expected, indicating that the oscillating barrier has modified the kinetic energy distribution of the BEC that interacted with it. Notably, for this preliminary data set, the barrier modulation was non-sinusoidal (fig. 6.16). The corresponding vertical expansion rates for the preliminary data set are shown in figure 7.4 (bottom). The BEC innately has a larger expansion rate in the vertical direction than the axial direction. This is due to the BEC being held in a cigar-shaped trap. However, the presence of a barrier, either static or oscillating, causes an increase in the vertical expansion rate of the atoms. The increased vertical expansion causes a decrease in the overall optical depth of the atom cloud, thus reducing our effective imaging resolution, and increasing the difficulty of resolving discrete sidebands at long times of flight. The difficulty in resolving discrete sidebands, with parameters that we believed would generate sidebands with a large differential velocity, motivated an attempt to also observe a large expansion rate with a more sinusoidal barrier drive frequency (see Fig. 6.16 for the non-sinusoidal behavior).

In an attempt to observe a variety of shifts in kinetic energy, we fixed the initial atomic velocity to $v_i = 5.0$ cm/s (slow) and measured expansion rates for multiple barrier frequencies. Figure 7.5 (top) shows axial cloud size vs. time for different barrier drive frequencies. This data is then fit to determine the axial expansion rate. It is also noteworthy, and not unexpected, that the larger expansion rates also have larger error bars (the error bars are calculated by extracting the one sigma confidence interval from the fits). Large cloud sizes observed at low optical depths lower the confidence of the fit. Figure 7.5 (bottom) shows the axial expansion rate σ_v vs. barrier drive frequency. As we would have expected, the static barrier case, $f = 0$, has minimal expansion. The expansion that it does have is comparable to the small, but non-zero, expansion that one obtains by simply releasing the BEC from the chip trap (see Fig. 7.4). At larger frequencies, $f = 13$ kHz for example,

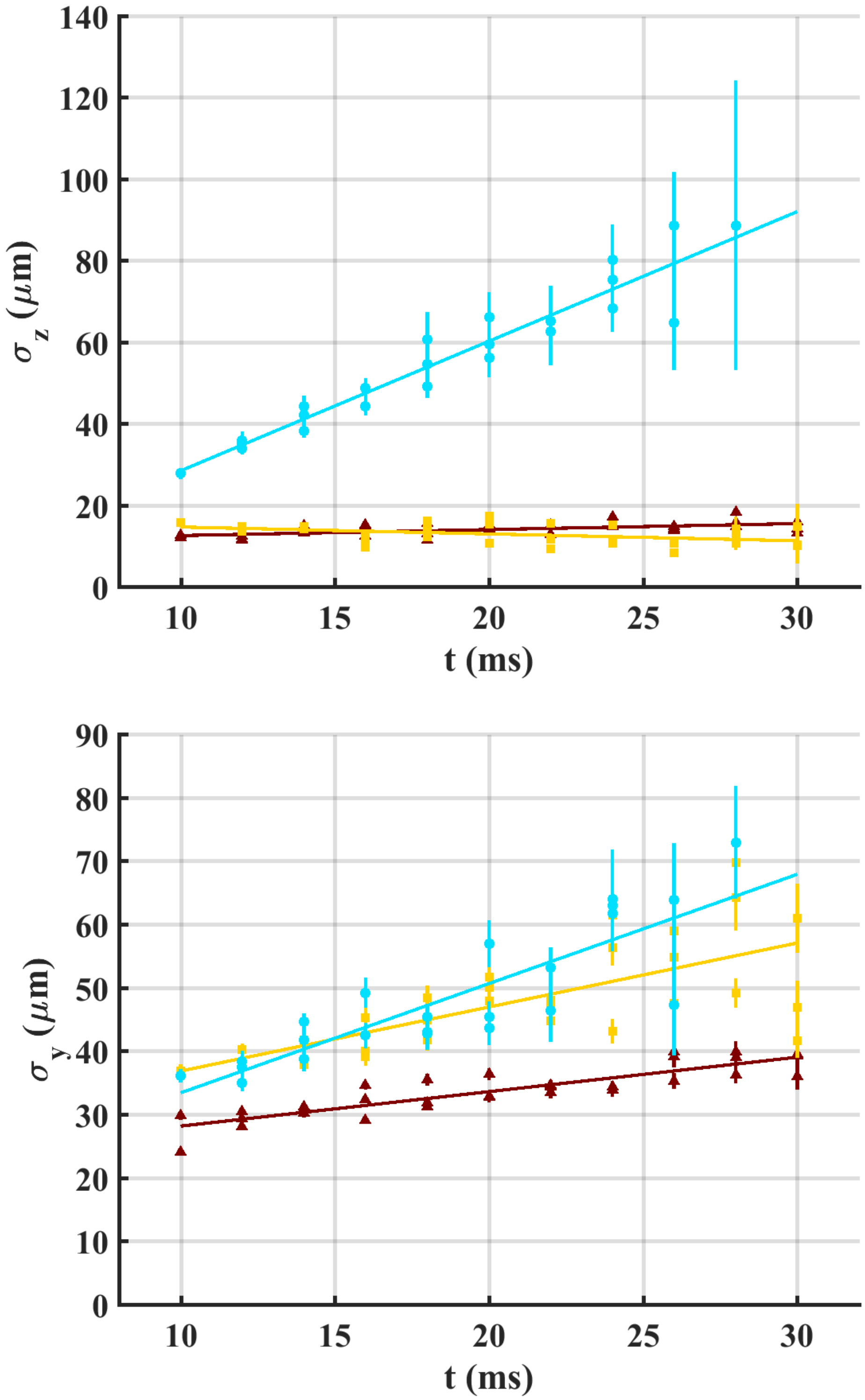

FIG. 7.4: Preliminary axial (top) and vertical (bottom) expansion of atom clouds comparing no barrier (brown), static barrier (yellow), and oscillating barrier (blue) with $f = 13$ kHz, $v_i = 5.0$ cm/s (slow).

the expansion rate is low, much like the static barrier case: this is also expected as the atoms should feel a time-averaged potential when encountering a barrier modulated at high frequencies. The data shows that larger expansion rates occur at lower frequencies. At medium frequencies (~ 4 kHz), the expansion rate is much higher, showing that the barrier redistributes the kinetic energy of more atoms at these frequencies. We would expect that a faster velocity or a shorter atomic packet would have less time to interact with the barrier and vice versa. We would also expect that atomic packets that interact more with the barrier would have a stronger coupling to other Floquet states, that is, the expansion rate should be larger than otherwise. To summarize, the qualitative shape of the data agrees with intuition. The disadvantage of the larger expansion rates occurring at lower frequencies is that those lower frequencies correspond to smaller differential velocities between sidebands. Therefore, the expansion rate is driven by the production of higher order sidebands, not by sidebands further offset from the carrier. This is unfortunate because spatially resolving discrete sidebands requires longer times of flight for smaller differential velocities.

We can also examine the mean velocity of the atoms after interaction with an oscillating barrier. While observing the mean velocity does not provide information to support or refute the discrete sideband model, it can be analyzed and the behavior of the velocity with respect to the barrier frequency can be explained. Figure 7.6 (top) shows the cloud position vs. time for different frequencies plotted on figure 7.6 (bottom), which shows the velocity vs. barrier drive frequency. The atom clouds that were analyzed were reflected from the barrier,[4] and the negative sign is omitted. The position vs. time data is easily fit to find the velocity of the atoms. This data shows that at some frequencies the barrier has altered the mean velocity

[4]High barrier energy was chosen for the purposes of sideband generation. The atoms do not have enough kinetic energy to transmit through it.

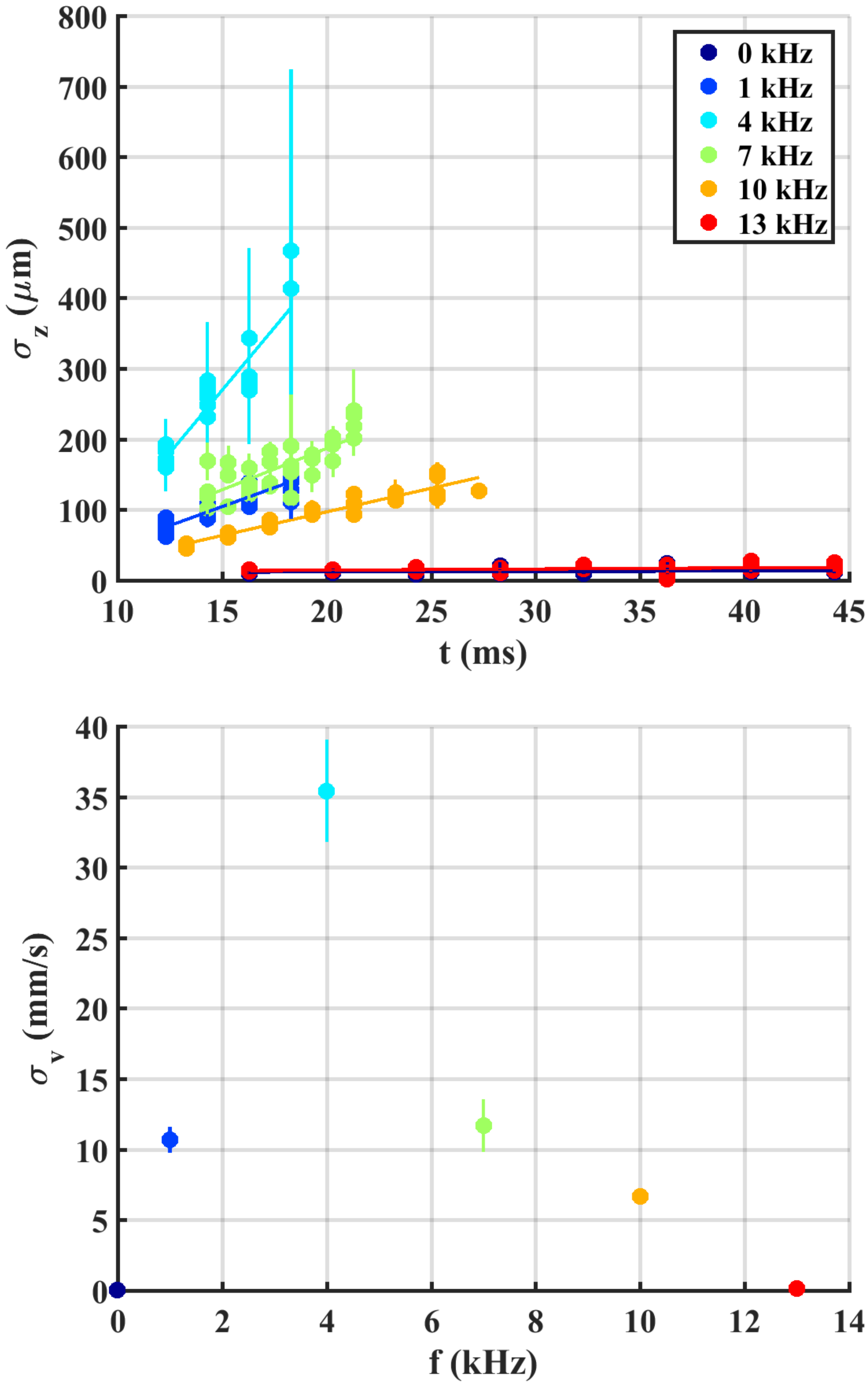

FIG. 7.5: Preliminary axial cloud size vs. time (top) for the frequencies in the axial expansion rate as a function of barrier drive frequency (bottom). The initial velocity is $v_i = 5.0$ cm/s.

of the atoms. We would expect that the static barrier would conserve the initial kinetic energy of the atoms, otherwise the barrier beam does not provide a conservative potential. At high frequencies, the atoms should again feel a time-average of the oscillating barrier potential, and the reflected atoms should move away from the barrier with the same initial speed with which they initially moved towards the barrier. At medium frequencies, the final mean velocity is different than the initial, similar to the expansion rate increasing at medium frequencies in figure 7.5 (bottom). While figure 7.6 (bottom) only has a few points, I would note that all of the velocities at medium frequencies are larger than the initial velocity, and none of them are smaller. Assuming this to be true, this can be explained by the initial kinetic energy of the atoms in relation to the mean barrier energy and its oscillation amplitude. Recall the oscillating barrier potential:

$$U(x,t) = U_0 \left[1 + \alpha \sin(\omega t + \phi)\right] e^{-(x-x_b)^2/2\sigma_b^2} \tag{7.1}$$

If the oscillation amplitude, α, is 70%, then the barrier energy will oscillate between $0.3U_0$ and $1.7U_0$. However, the initial kinetic energy is about $\frac{1}{3}U_0$. Therefore, the barrier tends to only increase the mean kinetic energy of the atoms. This is equivalent to the atoms entering an elevator on the ground floor, and there is nowhere to go but up.[5]

7.2.3 Full Spectrum Frequency Data

We collected data at additional frequencies, to further investigate these effects. Figure 7.7 is qualitatively similar to 7.5. They show similar behavior for the axial expansion rate, but for additional frequencies and also for an initial velocity of

[5] There is no "basement" to go to without the presence of a red-detuned optical dipole potential in this elevator analogy.

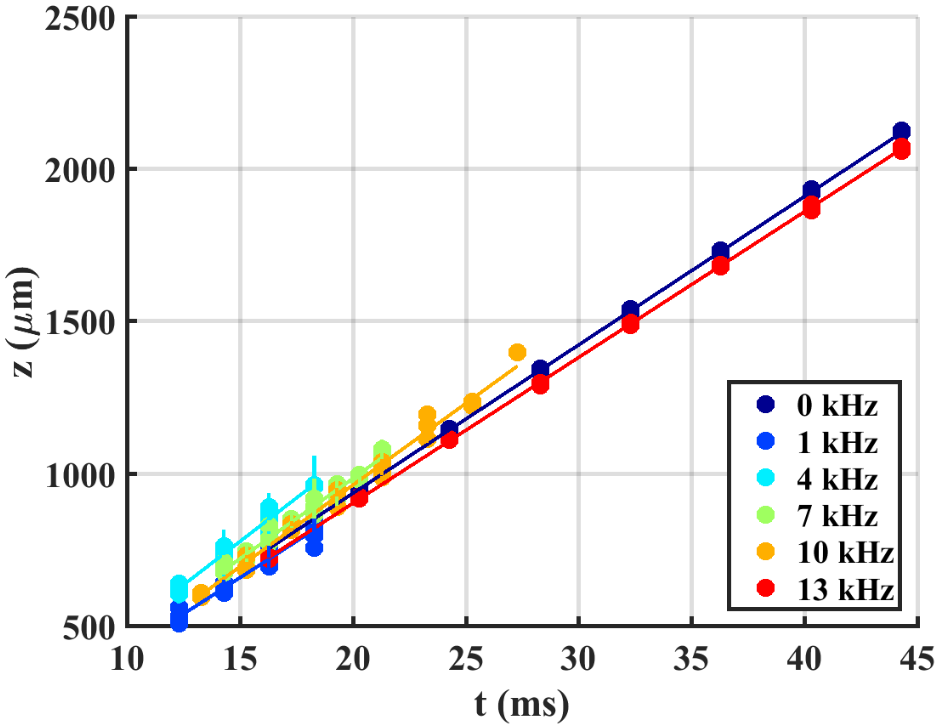

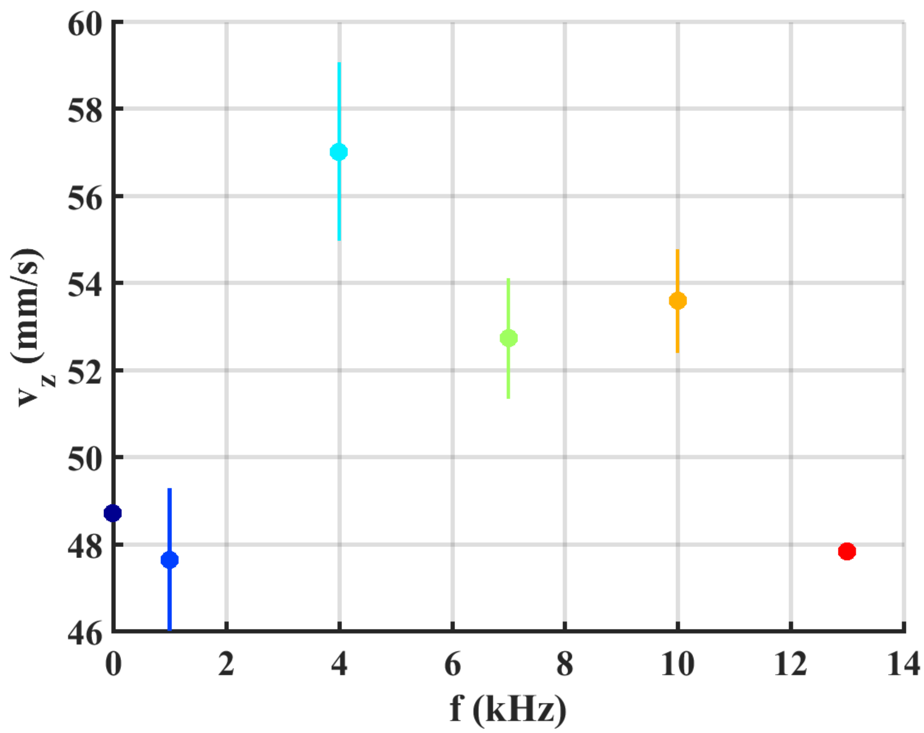

FIG. 7.6: Preliminary axial position vs. time (top) for the frequencies in the axial velocity of atoms reflected from the barrier as a function of barrier drive frequency (bottom). The initial velocity is $v_i = 5.0$ cm/s. This shows different quantities, but is the same dataset as in figure 7.5.

$v_i = 5.0$ cm/s (fig. 7.9 is for $v_i = 5.3$ cm/s). Once again, the colors of the fit lines correspond to the points on the frequency curve. The corresponding results from quantum simulations have also been plotted (blue square markers). This data reinforces the supposition made in the previous section that the expansion rate decreases to a value close to the static barrier case at high frequencies, while the intermediate frequencies show an increase in expansion rate. Notably, the expansion rate is also consistently higher than the theoretical prediction at mid-high frequencies.

Similar data for the final mean velocity is shown in figure 7.8 is qualitatively similar to 7.6, but with additional frequencies. The velocity data also supports the statement made in the previous section that the final atomic velocity returns to the initial velocity if the barrier oscillation frequency is very low, or relatively high (e.g. $f = 10$ kHz). The frequencies shown in the preliminary data ($f = 1, 4, 7, 10, 13$ kHz) agree relatively well with this data. However, some frequencies ($f = 3, 6, 8$ kHz) show a smaller final than initial velocity. I do not have an explanation for this, although the error bars are very large, and do extend to include velocities above the initial.

Figure 7.9 shows similar behavior for the axial expansion rate, but for the faster initial velocity of $v_i = 5.3$ cm/s (fast). Similar data for the final mean velocity is shown in figure 7.10. The data from this initial velocity also supports the observations from the previous section. The expansion rate data appears smoother than corresponding slower velocity data, with the exception of two potential outliers at $f = 4, 6$ kHz. The expansion rate at mid-high frequencies is, once again, consistently higher than the theoretical prediction.

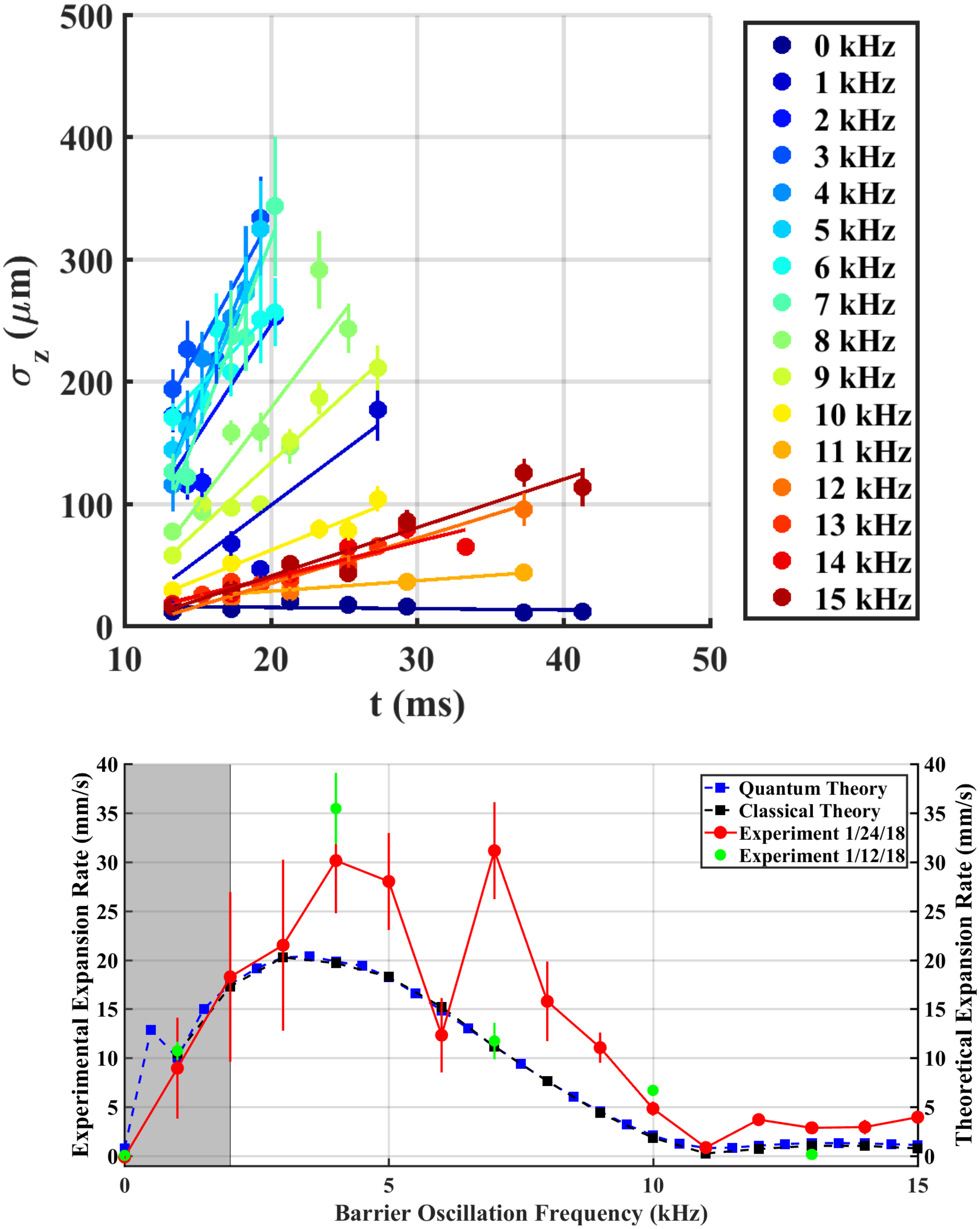

FIG. 7.7: Qualitatively similar to Fig. 7.5. Axial cloud size vs. time (top) for a slower initial velocity. The bottom figure shows axial expansion rate as a function of barrier drive frequency for a slower initial velocity (v=5.0 cm/s). Experimental data (red) is compared to quantum (blue) and classical (black) predictions. Preliminary data (green) from Jan. 12, 2018 is also overlayed. The gray shading indicates the region of low frequencies over which the resulting expansion rate may differ for different barrier oscillation phases.

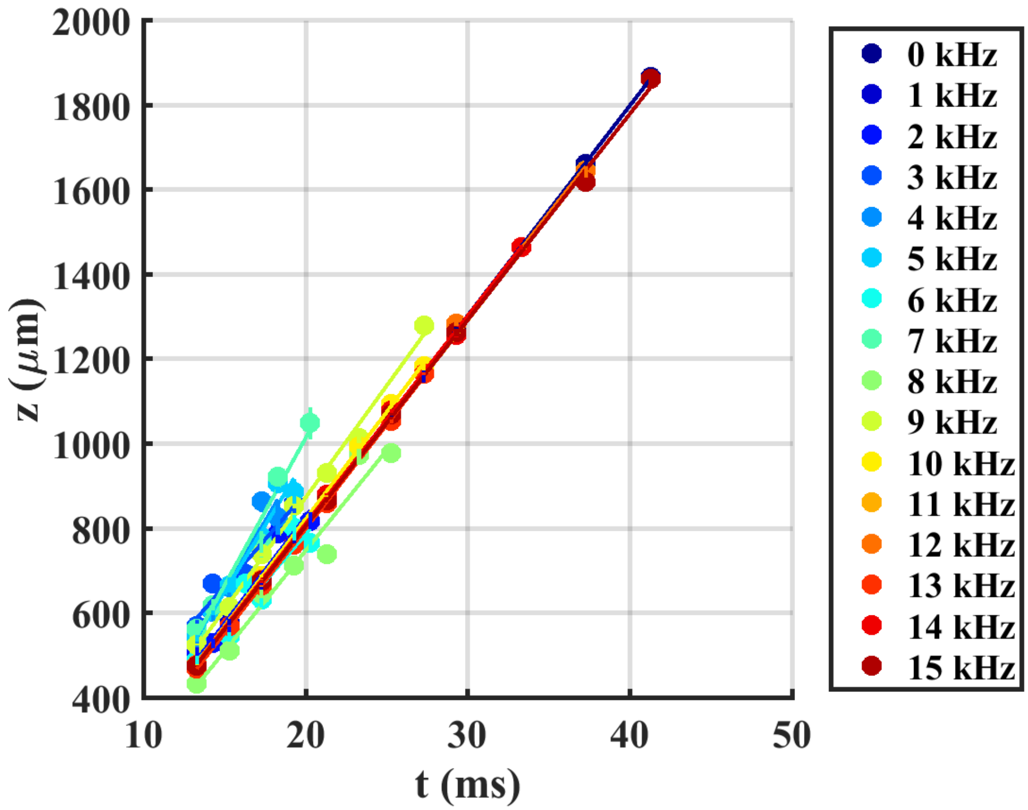

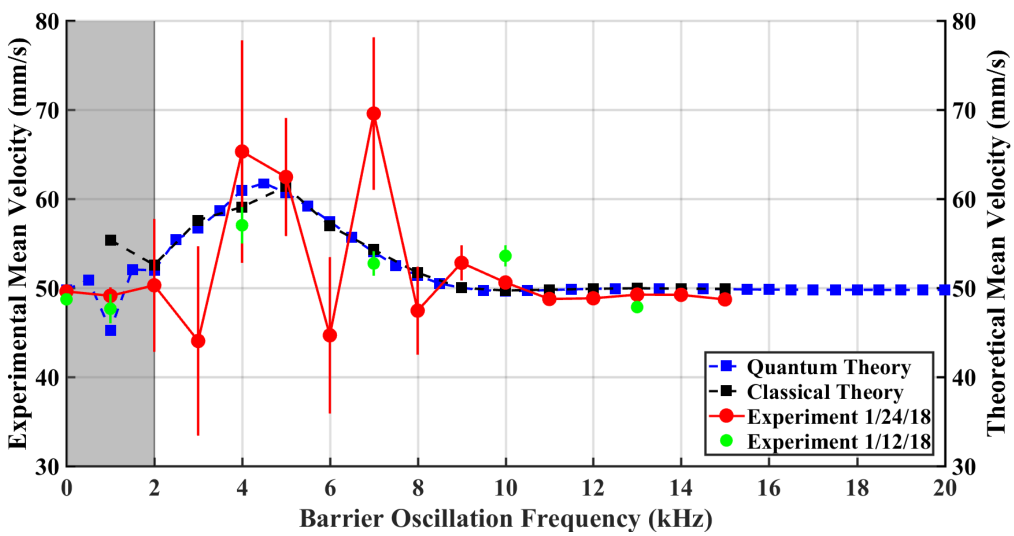

FIG. 7.8: Qualitatively similar to Fig. 7.6. Axial position vs. time (top) for a slower initial velocity. The bottom figure shows the axial velocity of atoms reflected from barrier as a function of barrier drive frequency for a slower initial velocity. Experimental data (red) is compared to quantum (blue) and classical (black) predictions. Preliminary data (green) from Jan. 12 2018 is also overlayed. The gray shading indicates the region of low frequencies over which the resulting velocity may differ for different barrier oscillation phases.

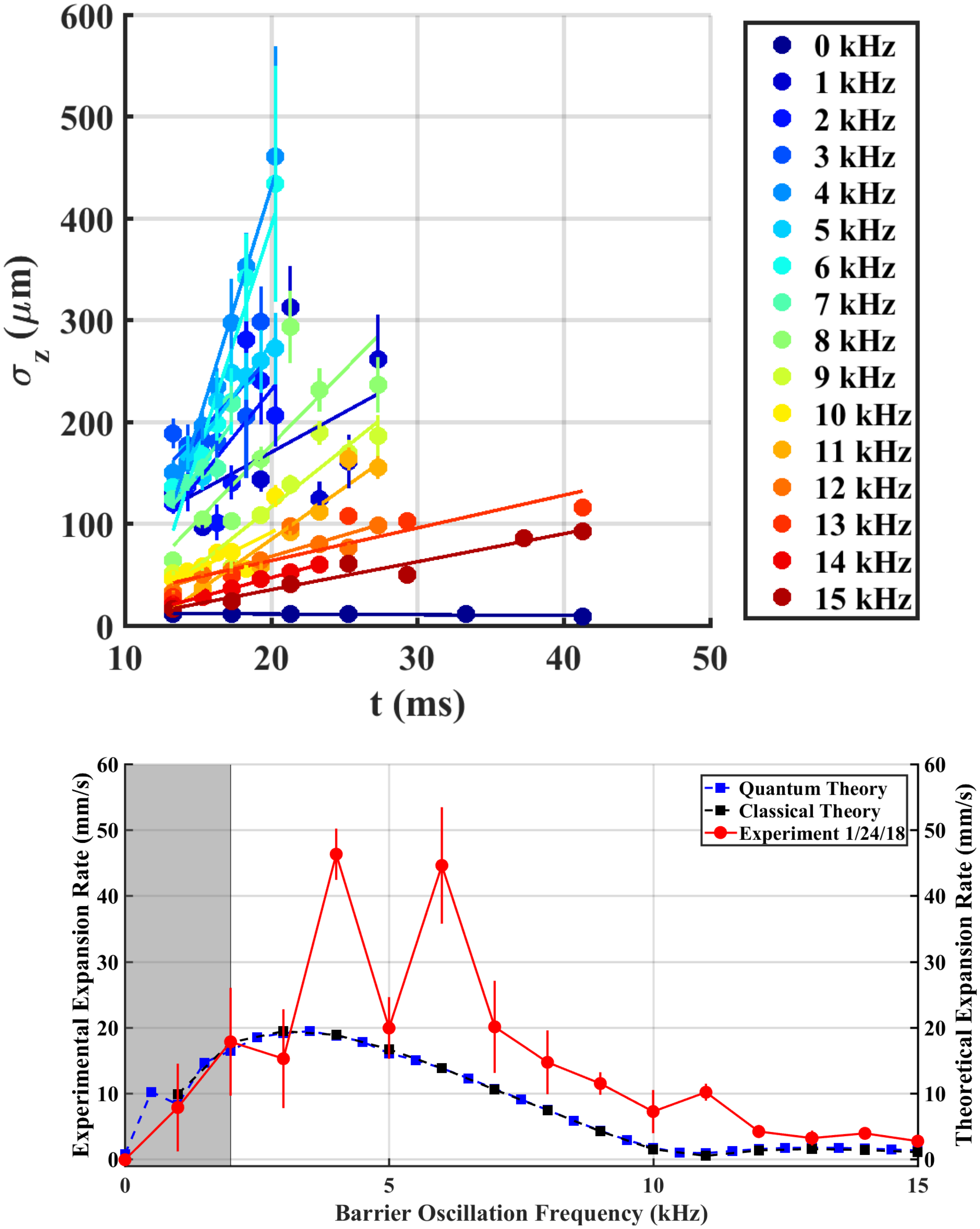

FIG. 7.9: Qualitatively similar to Fig. 7.7. Axial cloud size vs. time (top) for a faster initial velocity. Axial expansion rate (bottom) as a function of barrier drive frequency for a faster initial velocity (v=5.3 cm/s). Experimental data (red) is compared to quantum (blue) and classical (black) predictions. The gray shading indicates the region of low frequencies over which the resulting expansion rate depends (theoretically) on the barrier oscillation phases.

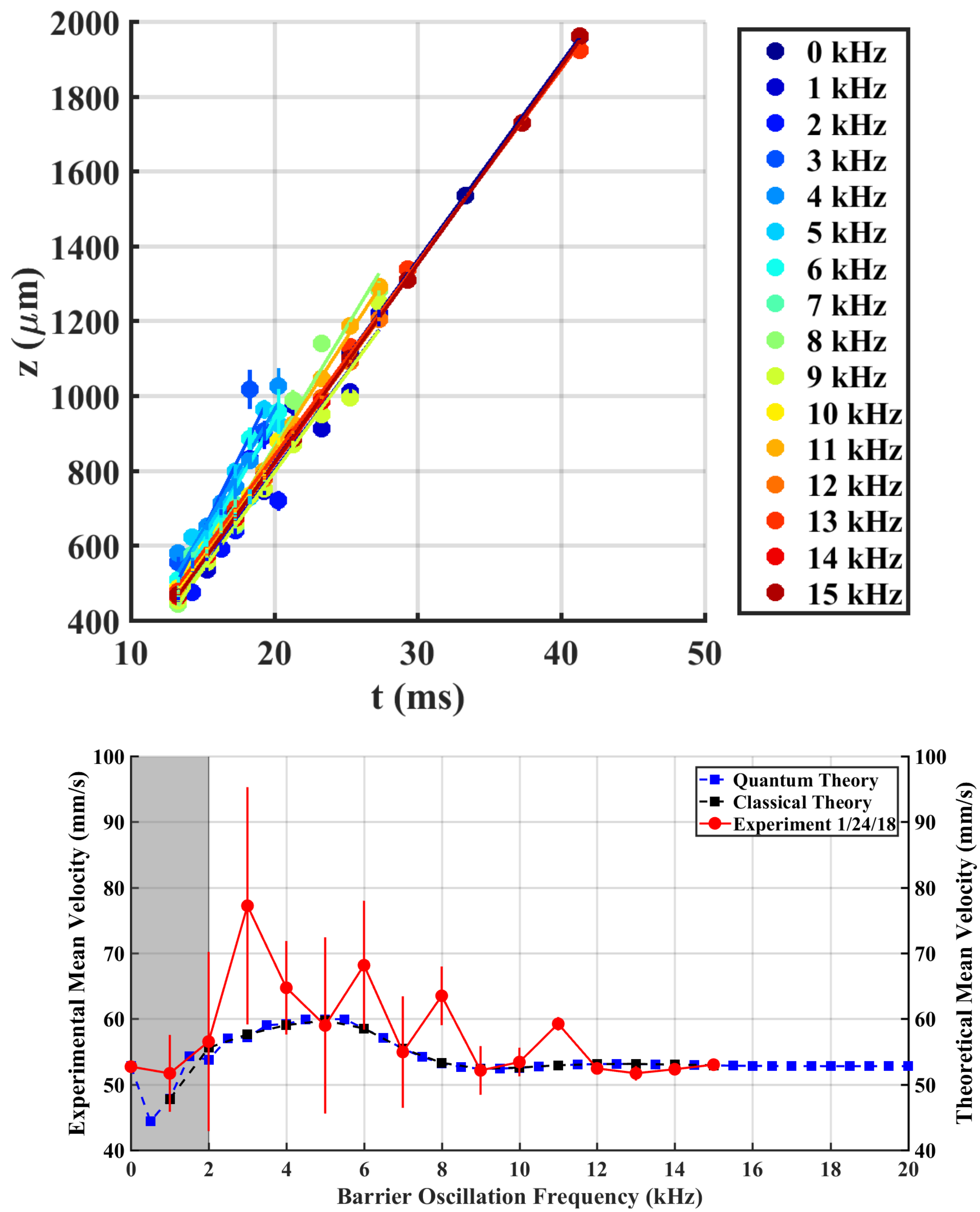

FIG. 7.10: Qualitatively similar to Fig. 7.8. Axial position vs. time (top) for a faster initial velocity. Axial velocity (bottom) of atoms reflected from barrier as a function of barrier drive frequency for a faster initial velocity. Experimental data (red) is compared to quantum (blue) and classical (black) predictions. The gray shading indicates the region of low frequencies over which the resulting velocity may differ for different barrier oscillation phases.

7.2.4 Comparison to Theory

It is helpful to compare these results to both classical and quantum theoretical predictions and ascertain whether or not our experimental data agrees with simulation results. This section will examine the expansion rate as a function of frequency for both initial velocities (5.0 cm/s and 5.3 cm/s), and then compare the final mean velocity as a function of frequency.

Scattered expansion rate: Figure 7.7 (bottom) shows the expansion rate vs. barrier frequency for the slower initial atomic velocity (v=5.0 cm/s). The quantum and classical theory agree very well (only reflected considered, but there is usually no transmission), although it is noteworthy that only the reflected atoms are considered when calculating the expansion rate, because only images of the reflected atoms are collected by the camera. There are no transmitted atoms at higher frequencies (> 5 kHz). The fraction of transmitted atoms is also small when transmission begins near 5 kHz. The classical expansion rate is determined by calculating the standard deviation of the classical momentum distribution. The quantum mechanical expansion rate is shown on the right side of equation 7.2 and calculated using equation 7.3.

$$\sigma = \sqrt{\langle k^2 \rangle - \langle k \rangle^2} = \sqrt{\langle \psi | k^2 | \psi \rangle - (\langle \psi | k | \psi \rangle)^2} \tag{7.2}$$

$$\sigma = \sqrt{\int \psi^*(k) k^2 \psi(k) dk - \left(\int \psi^*(k) k \psi(k) dk \right)^2} \tag{7.3}$$

The experimental data shows qualitative agreement with the simulation results, however the experimental data seems to be consistently larger than the theoretical prediction. This could be caused by the presence of density driven repulsive atom-atom interactions, however this is only a supposition, and is unlikely. We can also compare the full spectrum frequency data collected on Jan. 24, 2018 with the preliminary frequencies ($f = 1, 4, 7, 10, 13$ kHz) collected on Jan. 12, 2018. The frequencies $f = 1, 4, 10, 13$ kHz agree reasonably well between these data sets collected on different days, although $f = 4$ kHz resulted in an expansion rate about 50% higher than the theoretical prediction. However, $f = 7$ kHz disagrees by nearly 100%, causing some doubt about the reproducibility of this experiment. The Jan. 12 data agrees very well with the theory for $f = 7$ kHz, while the Jan. 24 does not. I would also point out that the experimental data set collected on Jan. 24 shows a local minimum at $f = 11$ kHz, and while subtle, also appears in the theoretical prediction. Unfortunately, it is difficult to prove that the experimental data truly exhibits this feature without having more data.[6]

Figure 7.9 (bottom) shows the same curve, only for the faster velocity (no data for that velocity was collected on Jan. 12). This curve qualitatively agrees with the theoretical prediction, except for two very large outliers at $f = 4, 6$ kHz. Once again, the expansion rate data is consistently larger than the theory. Overall, I believe that the only trend that we can be confident of is that at relatively high frequencies, the expansion rate is decreasing and small, comparable to the static barrier case. And at medium frequencies, the expansion rate is larger, indicating a greater shift in kinetic energy.

The theoretical and experimental expansion rates are not equivalent (by definition). We have done some analysis that shows that they differ somewhat quantitatively. In figures 7.7 and 7.9, the theory curves (quantum and classical) show the standard deviation of the final velocities (or velocity space wavefunction). The experiment shows the expansion rate of the Gaussian width (i.e. σ) of the atoms' position distribution as determined by a Gaussian fit of the atoms axial distribution (after an ROI sum). If the experimental atomic distribution is Gaussian, then the theory and experiment definitions should be the same. However, if the experimental

[6]It is obvious to point out that more data may not help without reproducibility, which may be an issue to concern ourselves with.

or theory distribution is not Gaussian (and we know that they are not), then these are not the same. However, we chose this approach in using a Gaussian fit to quantify the width of the experimental ROI sums, as this method is robust. However, if this method is applied to the position distributions of the classical simulations (which largely agree with the quantum for $f < 8$ kHz), the result is not the standard deviation of the final velocities, but rather an expansion rate that is about 25% larger. To clarify, we are not entirely sure how to reconcile the theory and experiment definitions. However, we note that the theory data would agree better with the experimental data if increased by about 25%. To account for this, figures 7.7 and 7.9 have been given two vertical axes each. The left axis is for the experimental "Gaussian fit width expansion rate, while the right axis can be for the theory using the standard deviation of the final velocities. Using the two axes is meant to emphasize that theory and experiment curves are not showing the same expansion rates, but rather two comparable but still different expansion rates. To summarize, experiment and theory agree on the frequency ranges where the scattering is large and where it is small. On figure 7.7, we find significant scattering over the range 1-10 kHz and much less scattering (though non-zero) over the 11-15 kHz range): theory and experiment agree on this qualitative behavior. Theory and experiment also agree that there is a minimum in scattering at 11 kHz, (though this is just a one point result, and we, unfortunately, cannot make this assertion with a large amount of confidence). The result is similar for figure 7.9.

The quantum simulation showed a small amount of transmitted atoms for frequencies that were 5 kHz or lower. Any transmitted atoms were excluded in the theoretical calculation of the expansion rate. Transmitted atoms were rarely detected during the experiment. However, the predicted transmission percentage is very small. Furthermore, when we have simultaneously observed atom clouds that have been transmitted and reflected, we noted that the transmitted cloud is larger in the vertical direction than the reflected cloud. This leads us to believe that the transmitted cloud is expanding faster in the vertical direction than the reflected cloud. A larger expansion rate and small atom number contribute to a very low optical depth that is likely responsible for these transmitted clouds having gone undetected.

Average scattered velocity: The final mean velocity as a function of barrier frequency can also be compared to theory just as the expansion rate was in figures 7.7 (bottom) and 7.9 (bottom). Figure 7.8 (bottom) shows the resulting mean velocity after barrier interaction for different frequencies. The classical and quantum theory curves agree well for most frequencies. At very low frequencies, the oscillation phase of the barrier starts to matter relative to the position and velocity of the atoms. The experimental data shows some agreement with the theory, with notable outliers being $f = 3, 6, 7$ kHz for the data set collected on Jan. 24. The frequencies for which these outliers occur do not match the frequencies where outliers occurred in figure 7.7 (bottom), with the exception of 7 kHz. Had the outliers matched on the two different data sets, then it might have indicated some systemic anomaly or something we do not yet understand about the theory had these outlying frequencies matched. The data set collected on Jan. 12 appears to match the theory results well, although $f = 10$ kHz is higher. The only valid conclusion that might be drawn here is that the mean velocity is shifted (not claiming a trend up or down) over roughly the same frequency range where the expansion rate increases. Figure 7.10 (bottom) shows the final mean velocities for the faster initial velocity. There are outliers on this plot as well occurring at $f = 3, 4, 6, 8, 11$ kHz. Arguably, only 8 and 11 kHz do not have error bars that overlap the theoretical data. This data shows some qualitative agreement with theory, but unlike figure 7.8 (bottom), the outliers on this plot are consistently larger than what the theory predicted.

The experimental results for the final mean velocity differs greatly for low frequencies. I believe this to be an indication that the barrier phase is capable of influencing the resulting momentum distribution, while at higher frequencies the phase has a negligible effect. I expect the carrier velocity to remain constant while sidebands are added to the distribution for high enough barrier frequencies.

7.2.5 Atom Number Dependence

Results are independent of N_{BEC}, indicating that interactions are not strong. One of the main objectives in designing this new version of the experiment was to make sure to minimize atom-atom interactions. Figure 7.11 shows an attempt to quantify the strength of atom-atom interactions, including with the barrier present. The data shown is atom cloud size vs. N_{BEC} for no barrier (circles), static barrier (squares), and oscillating barrier (triangles). The color of the marker on the plot indicates the time-of-flight. This was done because it is inappropriate to compare atom cloud sizes that were not collected at the same time-of-flight. The reason for this is because the atom-atom interactions are quantified by measuring the expansion rate. This plot gives information about the expansion rate as a function of atom number, and because each cloud has a different number of atoms, it is better to include each point, rather than fit the cloud size over time. However, cloud sizes from different times should not be compared, as it is natural for an atom cloud to be large given more time to expand. The axial cloud size is more important to the experiment because a large expansion rate in that direction will obscure sidebands. It is desirable for the vertical expansion rate to be small to maintain optical depth and imaging quality during the experiment. The data in figure 7.11 shows that the axial expansion rate increases with atom number, however the slope of the trend is small, showing that the expansion rate is not too sensitive to changes in atom number. Lastly, this data reflects one key conundrum for this experiment. Superior imaging quality requires as many atoms as possible when imaging at long times, especially when anticipating multiple atom clouds totaling the original number, N_{BEC}. This data shows that too many atoms could adversely affect the axial expansion rate, creating a scenario in which observing sidebands is impossible. This situation creates a trade-off in which we would prefer to have as many atoms as possible, with as small an expansion rate possible, but those two goals are conflicting. To summarize, we believe our results are less dependent of N_{BEC}, i.e. interactions are not important. One of the main objectives in designing this new version of the experiment was to minimize atom-atom interactions. We investigated how the atom number influences expansion rate or σ of position distribution (cloud size). σ_y does depend on N_{BEC} according to fig. 7.11 (bottom). This is somewhat expected from initial BEC expansion from the trap. Figure 7.12 shows a smaller, but non-zero, dependence for σ_z (axial) on N_{BEC}.

7.3 Atomic Cloud Structure

Figure 7.13 shows an example of the appearances of multiple clouds after the atoms have interacted with the barrier driven at $f = 8$ kHz. During data collection, we paid particular attention to any structure within the atomic cloud. This helped support our original goal of resolving discrete quantum mechanical sidebands, albeit we also collected data for parameters for which we did not expect to observe sidebands.[7] For parameters with which we conducted a thorough search for sidebands, we collected multiple images (hundreds in some cases) at the same time of flight in order to average the frames to improve the signal to noise. The Region Of Interest (ROI) sum in the axial direction was analyzed with spatial filters to improve our

[7] I am not suggesting that we did not generate sidebands, but that the differential velocity between them would have been small enough to make resolution and observation difficult or not possible for the short time of flights we were imaging at.

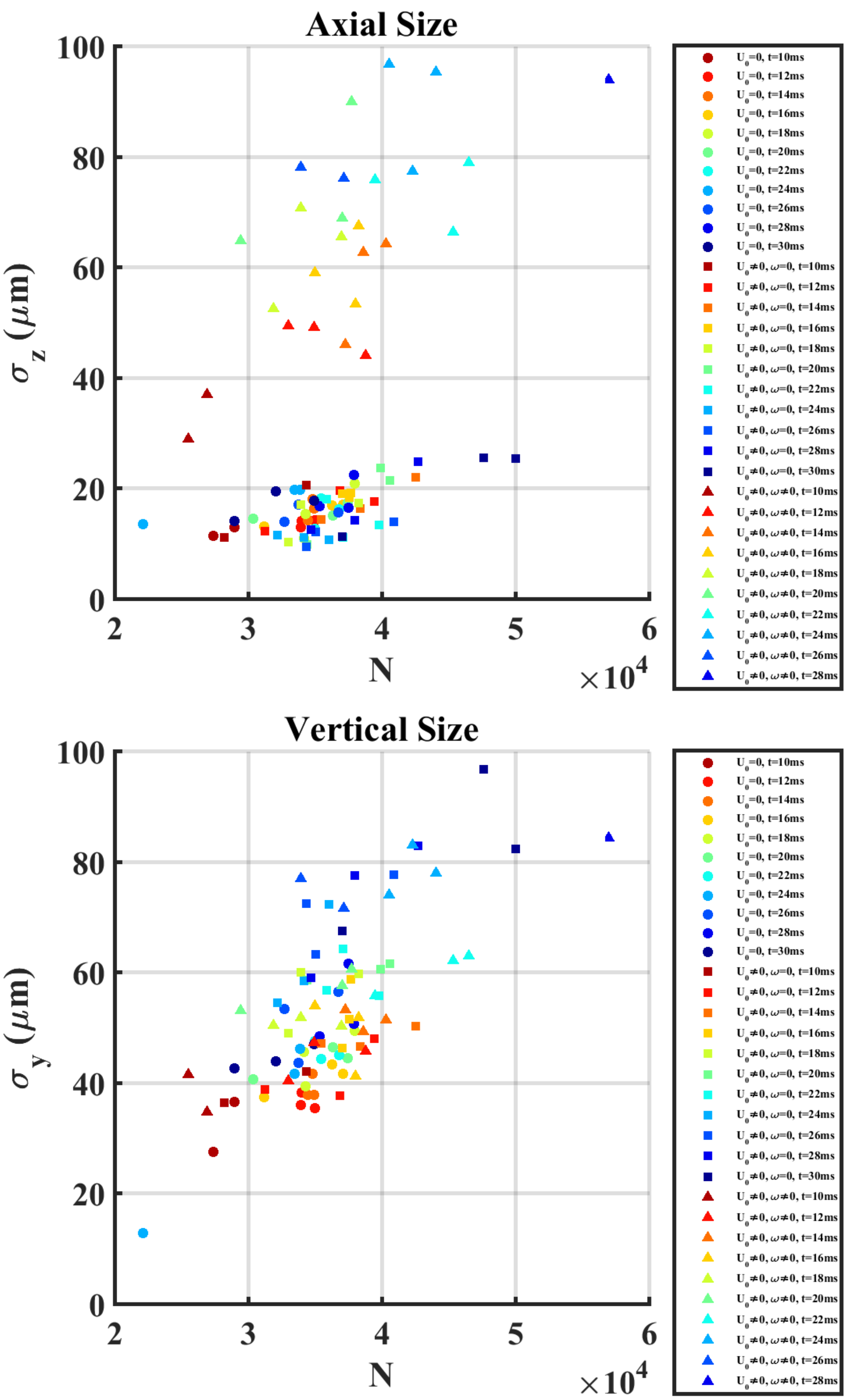

FIG. 7.11: Axial/vertical (top/bottom) atom cloud size vs. atom number. The expansion rate is compared indirectly by measuring atom cloud size at a constant time-of-flight. Data is shown for no barrier (U_0, circles), static barrier ($U_0 \neq 0$, $\omega = 0$, squares), and oscillating barrier ($U_0 \neq 0$, $\omega \neq 0$, triangles). Color indicates the time-of-flight (see legend).

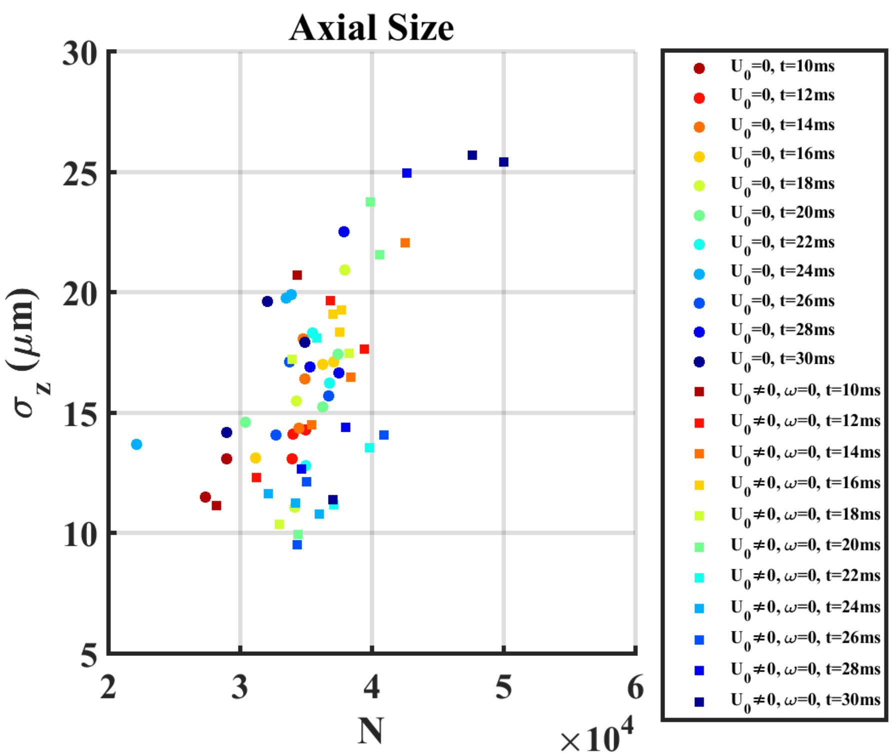

FIG. 7.12: Axial atom cloud size vs. atom number. The expansion rate is compared indirectly by measuring atom cloud size at a constant time-of-flight. Data is shown for no barrier (U_0, circles) and static barrier ($U_0 \neq 0$, $\omega = 0$, squares). Color indicates the time-of-flight (see legend). This is a re-scaled version of figure 7.11. The slope is approximately 10^{-3} μm/atom.

ability to detect signs of sidebands. For some parameters with which we did not expect to observe sidebands, we were able to observe some interesting atomic cloud structure. Figure 7.13 shows an example of multiple atomic clouds resulting from interaction with the oscillating barrier. While the observation of discrete momentum sidebands mapped onto position space would manifest itself as multiple clouds, we do not believe this to be indicative of sidebands for these parameters and time of flight. The time of flight is simply too short and the predicted differential velocity between sidebands is too small for these multiple clouds to realistically be discrete sidebands. In the absence of spatially resolved sidebands, we look for any features to potentially categorize our results as following either quantum or classical theory. The quantum mechanical picture generates discrete Floquet peaks in momentum space, but a convolution operation reveals the envelope of the wavefunction. The same can be done for the position space distributions. At shorter times of flight, the quantum mechanical theory reveals fine fringes in the position distribution, due to the presence of multiple momentum peaks beating against one another in the same location. In most cases, this envelope resembles the classical distribution. We focus on the cases in which this envelope significantly differs from the classical distribution in an attempt to distinguish between quantum and classical models for our experimental data. Figures 7.14 and 7.15 focuses on such scenarios. Figure 7.14 shows the data from quantum and classical theory overlayed with filtered data from $f = 15$ kHz at a relatively long time of flight. The quantum data has propagated for a long enough time that the fringes have disappeared and the convolution only smooths some sharper edges of the curve. This theory shows one prominent carrier peak accompanied by two smaller sidebands. Meanwhile, the classical distribution is a common twin-horned shape.[8] They both have approximately the same overall

[8]We have more commonly referred to this as "batman ears." I consider this to be a more charismatic terminology through the mere mention of batman. Duh.

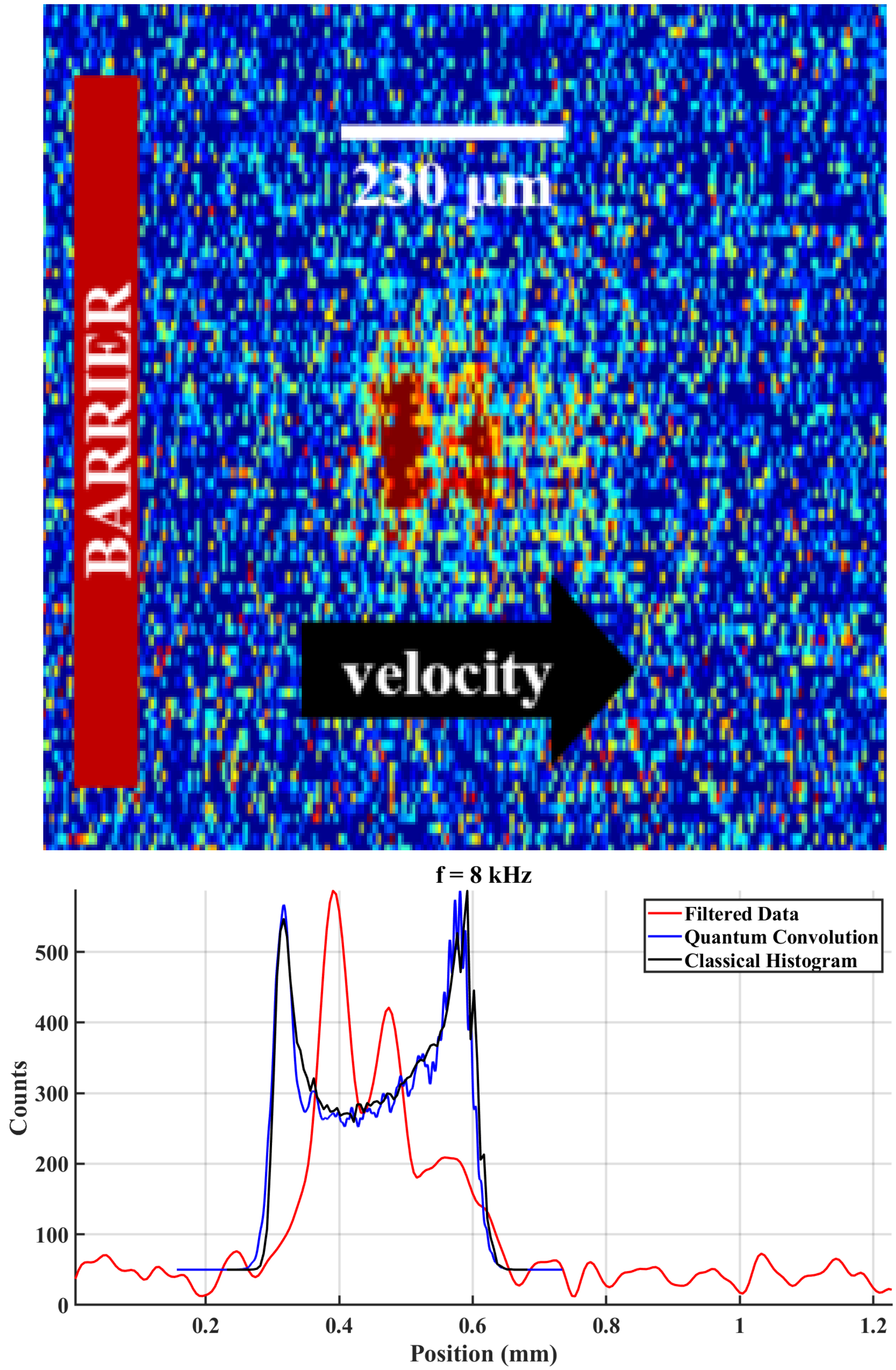

FIG. 7.13: Top: False color image of atoms exhibiting double-lobe structure produced by an oscillating barrier modulated at $f = 8$ kHz. Bottom: Corresponding data for image shown on top. The ROI sum is compared to classical and quantum theory for $f = 8$ kHz and a slower initial atomic velocity. Image taken 13.3 ms after interacting with the barrier. The quantum convolution blurs the sidebands leaving the envelope that resembles the classical theory.

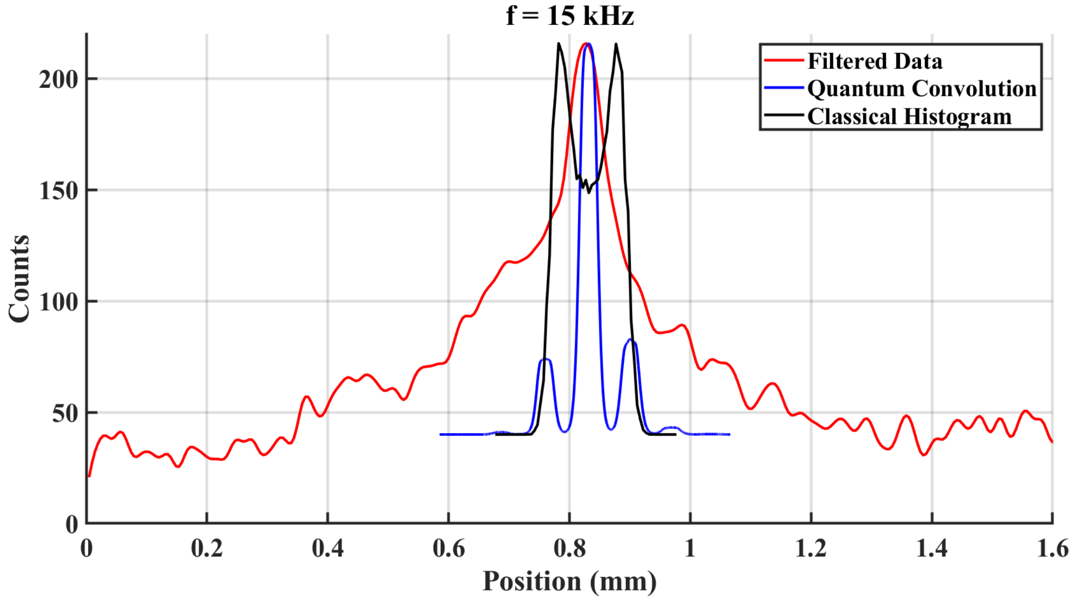

FIG. 7.14: ROI sum compared to classical and quantum theory for $f = 15$ kHz and a slower initial atomic velocity. Data collected with 51.3 ms of time-of-flight after interacting with the barrier. The data collected here is an average of 70 images and then filtered to remove noise, but not structure.

width, but differ in structure. The experimental data shows one peak, but is much wider than either theory. This indicates that the data more closely matches the quantum theory as it shows the presence of one tall peak, and it is conceivable that the much smaller sidebands were undetectable, or somehow smeared. On the other hand, a similar plot but with $f = 10$ kHz shown in figure 7.15 displays the opposite case. The quantum now shows a twin-horned distribution, while the classical is one single peak. The data shows two peaks, but the width of the data is much broader than either the quantum or classical predictions. Also, just as the experimental data was wider than predicted in figure 7.14, this plot shows a similar trend as the experimental data is also generally wider than predicted by the theory (see fig. 7.7 (bottom) and 7.9 (bottom)).

The 13 kHz (fig. 7.16) data suggests that sidebands may have been generated by the barrier. The data on this plot also emphasizes that the data is better de-

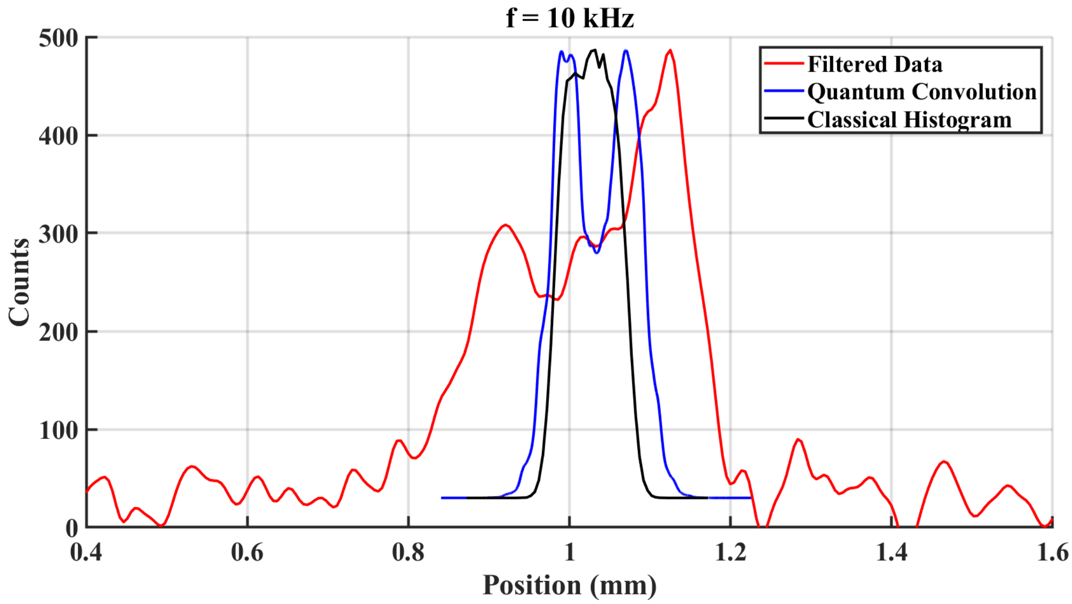

FIG. 7.15: ROI sum compared to classical and quantum theory for $f = 10$ kHz and a slower initial atomic velocity. Data collected with 21.3 ms of time-of-flight after interacting with the barrier. The quantum convolution blurs the sidebands leaving the quantum envelope.

scribed by the quantum distribution (based on overall structure, even while ignoring sidebands) than the classical distribution. Figure 7.14 shows this behavior somewhat at 15 kHz, but the 13 kHz data is more convincing. Overall, it would appear that the experimental data tends to qualitatively or coarsely resemble the quantum theory more than the classical theory, but there is not good absolute agreement between the data and quantum theory.

7.4 Phase Dependence

The sideband generation and the dichotomy of reflection and transmission are affected by the oscillation phase of the barrier relative to the initial position and velocity of the incoming atomic wave packet. A long packet will make the result less sensitive to the barrier phase due to the large number of barrier cycles with which the atoms interact. The velocity may also have an effect on phase dependence, as

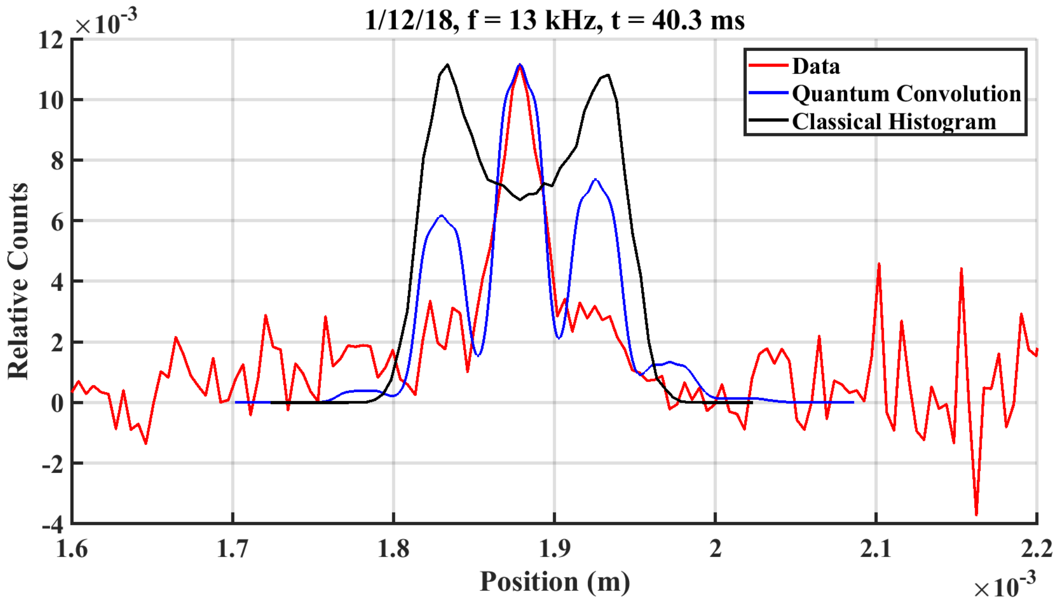

FIG. 7.16: ROI sum compared to classical and quantum theory for f=13 kHz and a slower initial atomic velocity. Data collected with 40.3 ms of time-of-flight after interacting with the barrier. The data collected here is an average of 4 images and is not filtered to remove noise.

it may help to control how long the atoms spend interacting with the barrier as well. However, in general it is the barrier frequency that has the largest influence in whether or not the resulting distributions are phase dependent. At very low frequencies the scattering becomes dependent on the phase. This is simply caused by the change in barrier energy while atoms are interacting with the barrier. However, the result changes depending on the energy of the barrier when the atoms interact, and whether the barrier energy is increasing or decreasing. Figure 7.17 shows the effect of barriers with different phases based on classical and quantum simulations. Different phases begin to have differing expansion rates beginning at $f = 6$ kHz, where it is barely noticable. The differences increase as the frequency decreases, and at $f = 1$ kHz there is a significant effect.

The trend is similar for the final velocity, although the differences seem to be greater, and begin at higher frequencies. Nonetheless, figure 7.17 shows the impact of different phases. The differences are present, but also not severe at or above 2 kHz. Just as we compared the classical and quantum theories in figures 7.7, 7.9, 7.8, and 7.10, it is useful to compare the results of both theories as the barrier phase is changed. These comparisons are shown in figure 7.17 for relatively low frequencies. The quantum data is displayed in the upper subplots. The middle subplot shows the classical data, and the bottom is the fractional differences between the classical and quantum results. The differences become larger at the lowest frequencies, at 1 kHz for example. However, 2 kHz shows better than 90% agreement between classical and quantum results.

According to theory, we do not anticipate the phase of the barrier oscillation to play a large role in the experiment for frequencies larger than 2 kHz. Low barrier frequencies are known to cause the final momentum wavefunction to be dependent on the modulation phase of the barrier. In order to assess which frequencies may be affecting the atoms, the axial position and cloud size was measured while varying the phase of the barrier. Figure 7.18 shows the size of the cloud as a function of barrier modulation phase. Cloud sizes were compared for 1, 5, and 8 kHz barrier frequencies and at the same times of flight. Notably, the $f = 1$ kHz data shows a difference in behavior as the phase is altered, while the $f = 5$ kHz and $f = 8$ kHz data is consistent with no phase-dependence. However, the behavior is apparently bimodal shown by the two distinctly different cloud sizes at 180 degrees. I cannot explain the bimodal behavior, but the overall data indicates that low frequencies like 1 kHz are capable of producing a different result after interacting with the modulated barrier, while the other frequencies are not. Figure 7.18 (bottom) shows the axial position of the cloud as a function of barrier modulation phase in a similar fashion as figure 7.18 (top). However, unlike figure 7.18 (top), this data shows similar behavior for all frequencies and phases observed. The dependence on barrier oscillation phase becomes apparent at low frequencies, like 1 kHz, as the cloud size changes as a

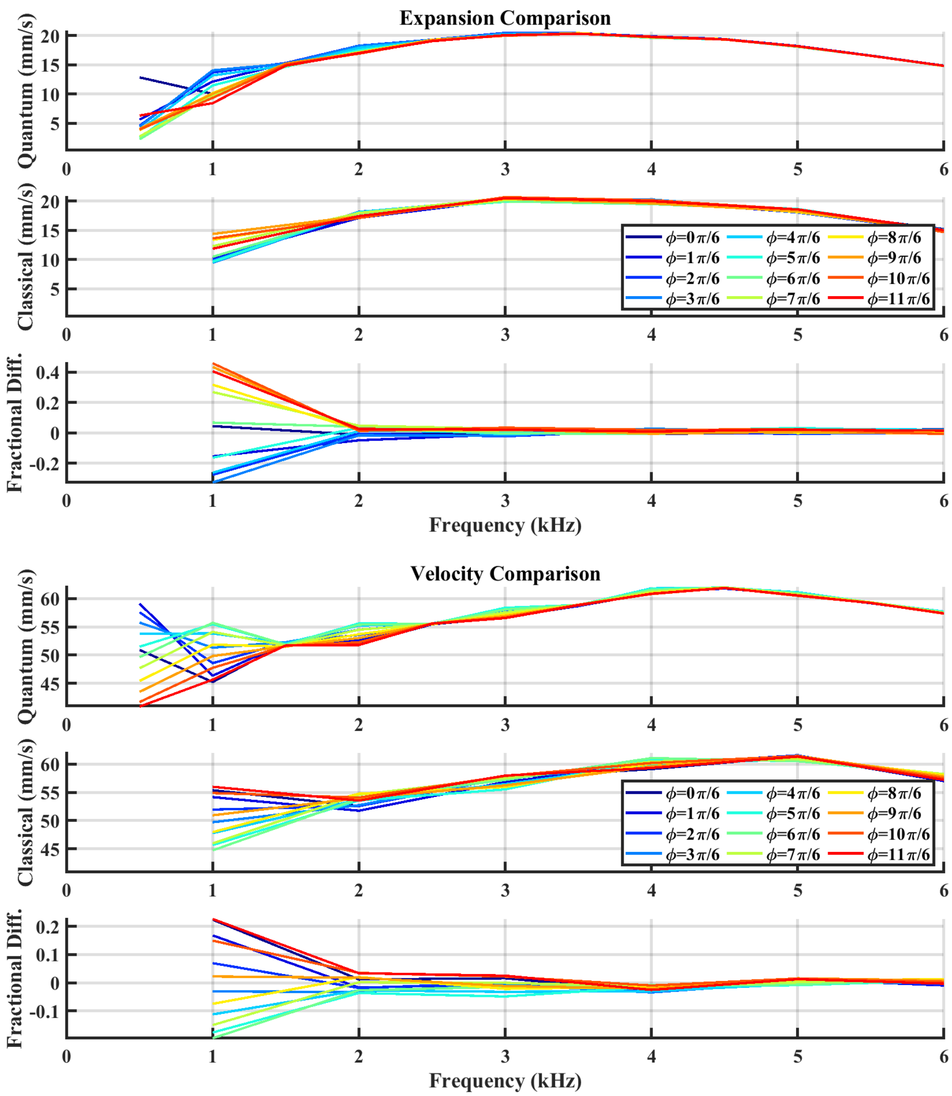

FIG. 7.17: Quantum and classical expansion rate (top) and velocity (bottom) comparison for different phases. The initial velocity is $v_i = 5.0$ cm/s.

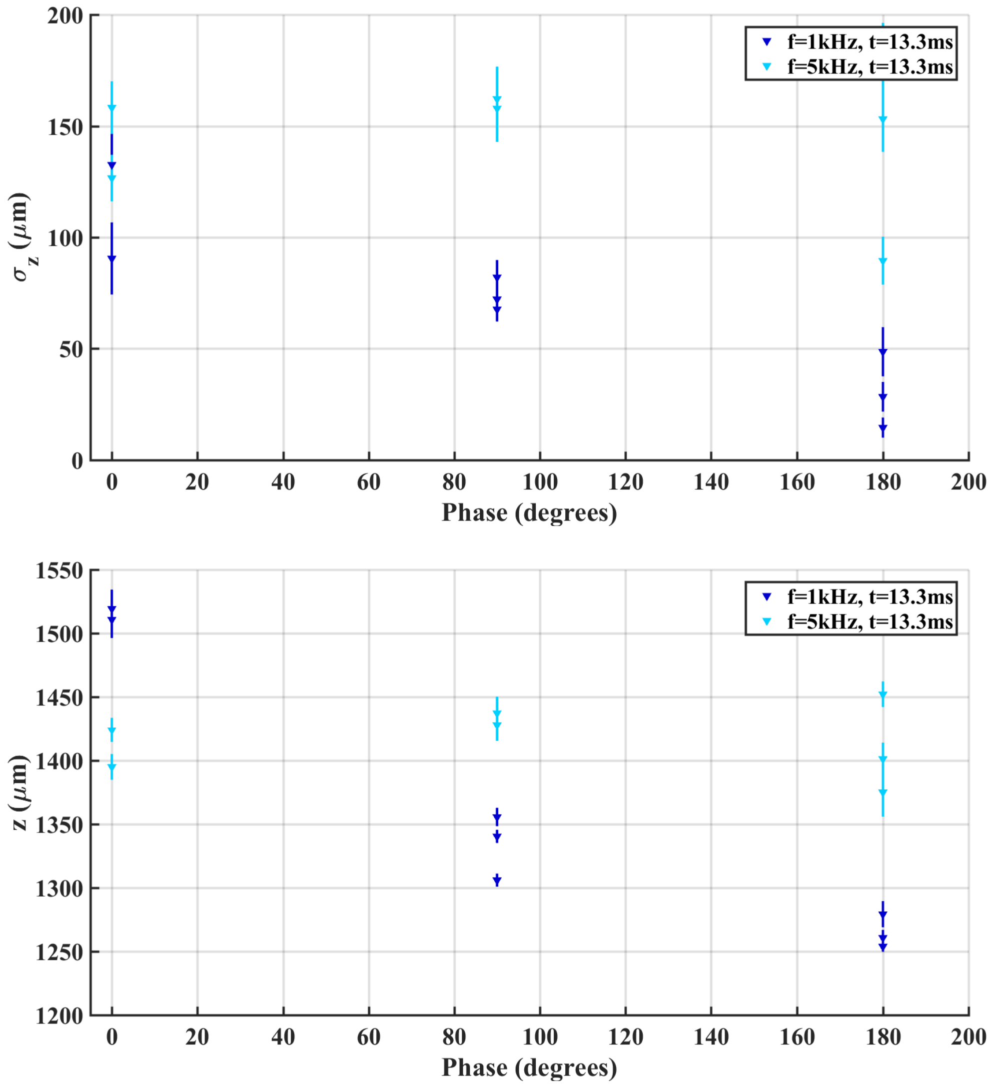

FIG. 7.18: Axial cloud size (top) and position (bottom) of atomic clouds encountering an oscillating barrier with different phases: 0, 90, and 180 degrees. Data for $f = 8$ kHz does not show any effect.

function of barrier phase while the time-of-flight is held constant. This dependence on phase disappears for frequencies greater than 2 kHz. The 5 kHz and 8 kHz data show similar cloud sizes at different barrier phases.

7.5 Transverse Behavior of Scattered Atoms

7.5.1 Transverse Focusing

We see focusing of the atoms in the transverse direction (with the focus occurring at some specific axial distance and time-of-flight). We speculate that this transverse focusing is due to the fact that the barrier beam is not sufficiently flat over the transverse width of the BEC. Figure 7.19 shows horizontal and vertical radial cloud sizes over time. The data indicates that interacting with the barrier causes atoms to focus in the horizontal direction and behave normally in the vertical direction. At this time, we do not have reason to believe that this effect influences sideband generation. The expansion that occurs after the atoms reach the focus (similar to a diverging optical beam) does not hurt our imaging quality as the absorption images are collected with the axial camera, with an imaging axis along the horizontal radial direction.[9]

7.5.2 Kapitsa-Dirac Effect

Our goal for this experiment was, in general, to observe a quantum mechanical effect that we intended to detect by resolving discrete atomic clouds. One can imagine our surprise when we initially observed discrete atomic clouds on a different axis where we did not expect to find them. We investigated this phenomena

[9] It is true that expansion along the imaging axis is detrimental, however extremely excessive expansion would have to occur to overcome the camera's depth of field, which is on the order of one millimeter.

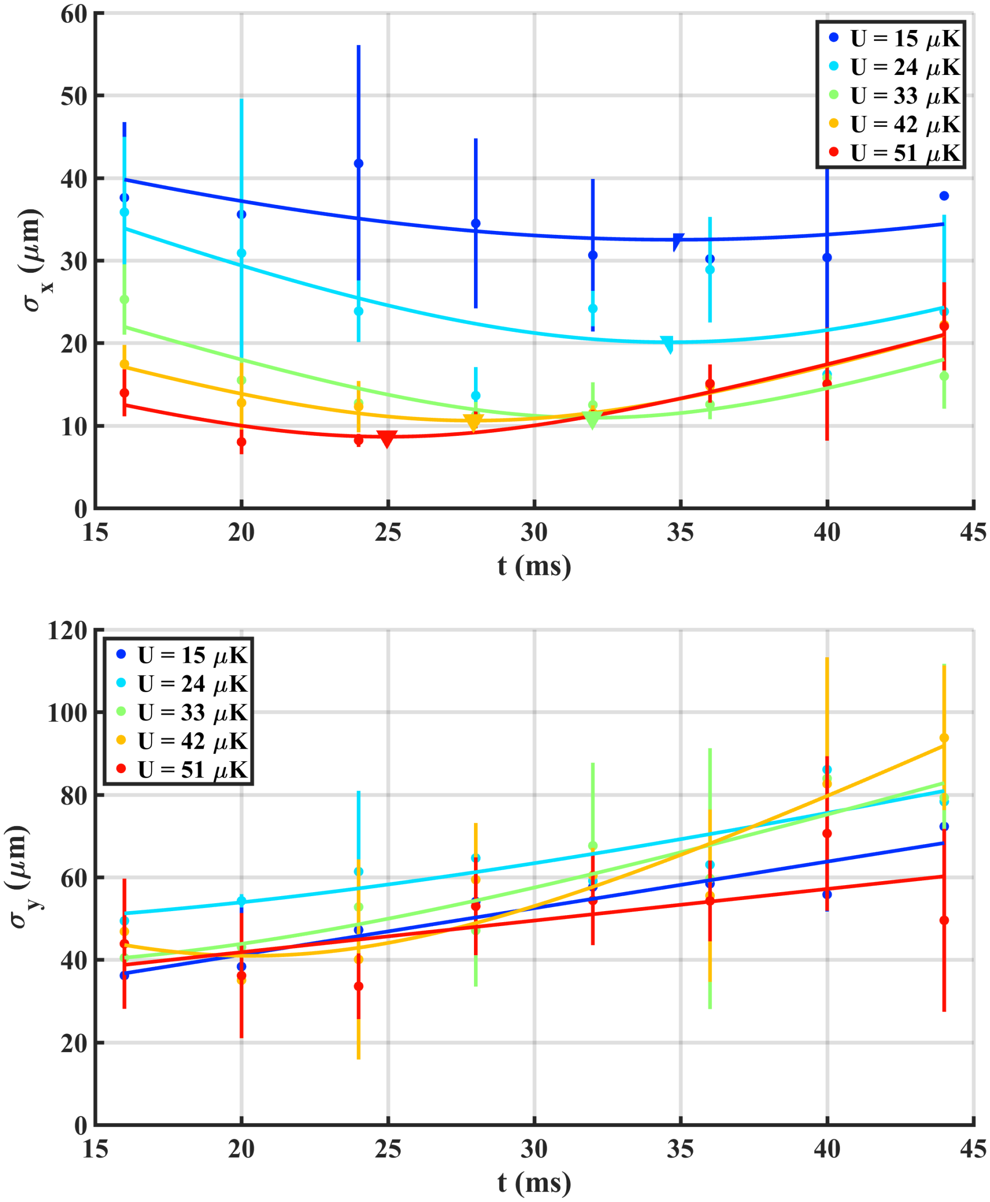

FIG. 7.19: Radial horizontal (top) and vertical (bottom) radial cloud sizes over time show that interacting with the barrier causes atoms to focus in the horizontal direction and behave normally in the vertical direction. Data was collected at multiple barrier energies, indicated by color. The downward facing triangle markers show the minimum cloud size, or focus, for the horizontal direction. This reveals a trend in which a taller barrier causes the atoms to focus more tightly, and at a location closer to the barrier. The atoms observed on the radial camera should have mostly, if not all, reflected off of the barrier. Data is fit to a function with the form: $\sigma = \sqrt{a^2 + (b(t-c))^2}$.

and believe it to be caused by the Kapitsa-Dirac effect [83]. Given the similarity of this quantum mechanical observation to the detection of Floquet sidebands that we intended to observe, we felt this result was worthy of discussion despite it not being the result we were looking for. Also, while we were characterizing this result and before reaching a conclusion, we were concerned that this effect (at the time, unknown) would have a detrimental effect on sideband generation.

The Kapitsa-Dirac effect is a quantum mechanical effect in which matter is diffracted by a standing wave of light. We believe we have observed this effect (figure 7.20)[10] on our radial camera which looks down the axis of propagation of the atoms. We observed that atoms interacting with either a static or oscillating beam had the potential to reflect from the barrier with multiple clouds separated in the radial direction. We believe that the barrier beam retro-reflecting off of the vacuum chamber can create a weak standing wave that diffracts the atoms. We know from experience that the retro-reflected beam requires very little power to generate a standing wave, as this has occurred previously with a nearly-collimated 1064 nm dipole trapping beam [21]. Adjusting the alignment of the barrier beam proved ineffective in mitigating the diffraction effects. Initially, re-alignment appeared to help somewhat, but later it did not when the diffracted peaks occurred shortly thereafter. This erased the initial conclusion that we were able to control the diffraction, and replaced with no or inconclusive evidence that our adjust had an effect on the beam.

7.6 Summary

I would like to conclude this chapter by assessing the success of the experiment/analysis. Unfortunately, we did not see optimal data. Our goal was to resolve

[10]These are not the sidebands you're looking for!

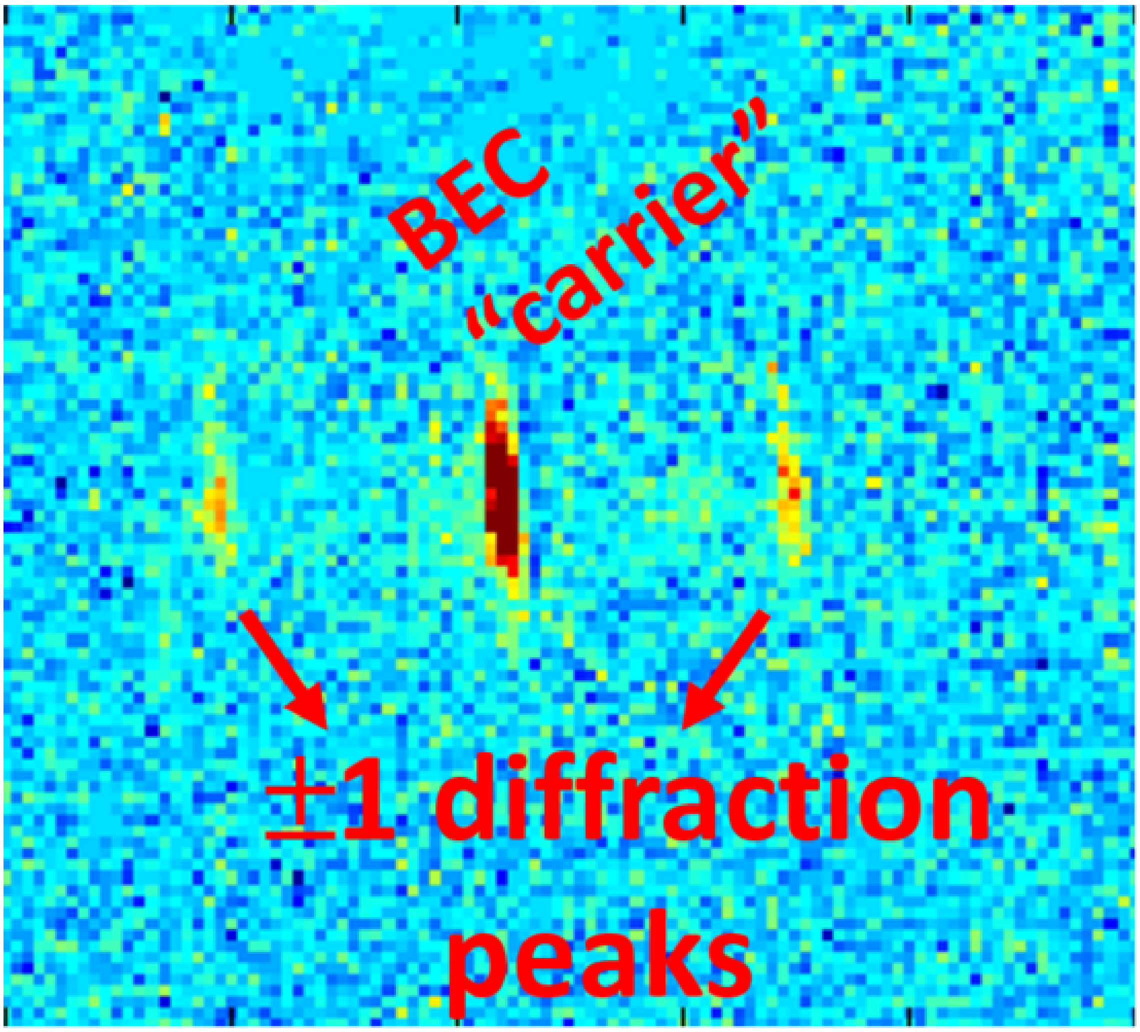

FIG. 7.20: Diffraction of a BEC by an accidental optical grating generated by an unwanted retro-reflection of the barrier beam.

discrete sidebands, and we have failed to do so. I believe that the data we have collected has helped to create a preliminary understanding of the system we are working with. The data does show a proof of principle in that the barrier is capable of acting as a kinetic energy shifter. We do not know if the quantum features we were looking for are unseen due to their absence, or our detection capabilities. However, we did encounter reproducibility issues with the barrier beam, and difficulty imaging atoms at long times of flight. The following list is a bullet point summary of the experimental results describing what was successfully accomplished and what did not work.

- Coarse agreement between theory and experiment.
- Experimental expansion rates are larger than theory predicts.
- Experiment can access the distinct sideband regime.
- At present, no clear evidence for sidebands.
- Often, density profiles do not match theory.
- Apparatus stability needs improvement.

The quantum simulation showed a small amount of transmitted atoms for frequencies that were 5 kHz or lower. Any transmitted atoms were excluded in the theoretical calculation of the expansion rate. Transmitted atoms were rarely detected during the experiment. However, the predicted transmission percentage is very small. Furthermore, when we have simultaneously observed atom clouds that have been transmitted and reflected, we noted that the transmitted cloud is larger in the vertical direction than the reflected cloud. This leads us to believe that the transmitted cloud is expanding faster in the vertical direction than the reflected cloud. A larger expansion rate and small atom number contribute to a very low optical depth that is likely responsible for these transmitted clouds having gone undetected.

CHAPTER 8

Conclusion

8.1 Summary of Results

In conclusion, this thesis presents measurements of the velocity distribution for a BEC scattered off an oscillating barrier in reflection mode. In support of these measurements, the thesis describes the both the theory for the scattering process, the design of the experiment, and the full apparatus required for implementing the measurement.

Importantly, the experiment successfully accessed a range of scattering behavior that encompassed both classical-like scattering and quantum scattering by varying the barrier oscillation frequency. While the experimental effort did not reveal the presence of scattering sidebands in the quantum regime, where they should have been present and observable, these measurements were somewhat better described by the quantum theory than the classical one. However, the experiment did observe a broadening of the scattered BEC's axial velocity distribution as a function of barrier frequency, which was coarsely consistent with that predicted by theory (both quantum and classical). However, the measured broadening of the distribution was consistently larger than the theoretical prediction: We do not have an explanation for this result, though part of the extra broadening may be due in part to the analysis method, on which more work is needed.

The experiment required a significant amount of instrument and technique development:

i) Levitation system: The Levitiathan current modulator was developed to provide a fast current control of a coil pair to levitate the atoms during the scattering process. In addition to the substantial amount of electronics work involved in designing and constructing the instrument, considerable time was devoted to integrating it into the main BEC appparatus and adjusting its settings so as to optimize the levitation. The Levitiathan can easily be used to convert most power supplies into a fast current source for controlling magnetic fields, so it can be used in many future applications.

ii) Push coil system: I made the coil to push the atoms during the first attempt at BEC scattering with Dr. Megan Ivory. However, the ability to send a brief high current pulse through it required the development of the Kraken current switch, which was constructed from discarded Levitiathan components and circuit boards. I learned how to use this push coil, including which direction the current should flow, and whether or not it can be combined with other fields.

iii) Barrier beam: While the overall barrier beam optical setup is conceptually similar to the one employed during the first BEC scattering attempt (with Dr. Megan Ivory), it was also completely re-engineered. Crucially, I devoted significant effort to measuring the waist of the focus to make sure that it was narrow enough, and so that this parameter could be reliably used for simulations of the scattering process. Notably, the use of a new asphere lens reduced the waist from 20 μm to 3.85 μm. On a separate note, the high-performance of these lenses suggests that they may be useful for developing a high-resolution BEC imaging system. The feedback scheme involving two voltage variable RF attenuators for controlling an AOM was developed to modulate the barrier sinusoidally. While the modulation was successful, it proved more difficult than expected, and ultimately did include some occasional phase jumps that were never solved (see discussion later in chapter).

iv) BEC apparatus polishing: Over the course of several years, the operation of the BEC apparatus was refined. Ultimately, various small improvements yielded an increase in the BEC atom number from $1 - 2 \times 10^4$ in 2014 to $2 - 4 \times 10^4$ in 2016.

v) Experiment design: The design of the experiment presented in this thesis went through multiple iterations before landing on the horizontal axial scattering scheme in free space used in the measurements. Initially, the role of atom-atom interactions in limiting the first scattering experiment was not appreciated until we encountered Kohn's theorem and ran some simulations (see figure 2.4). Once we settled on a free space version of the experiment, we initially focused on a method involving a BEC in vertical motion (to use gravity to accelerate the atoms before levitating them). Unfortunately, this method suffered from too broad an initial momentum distribution, though an attempt was made to reduce it with delta-kick cooling [76][77][78][79][80].

8.2 Why No Sidebands?

The main question that arises from the scattering measurements is "why were no sidebands observed?" At present, one cannot state from the current analysis whether the sidebands were just simply not there, or if they where somewhat suppressed (and the imaging signal-to-noise was insufficient to detect). Certainly, figure 7.16 at 13 kHz provides a tantalizing hint that sidebands may be lurking in the noise, or perhaps the pedestal of noise around the central peak is just noise (or even a diffraction artifact from the absorption imaging, though this is unlikely). A combined analysis with data taken at different times of flight may strengthen or weaken the argument for sidebands at this frequency.

Here we review some of the effects that may be responsible for suppressing the expected sidebands in some way(s):

Jitter: The BEC is released from the trap with some random velocity jitter primarily in the vertical direction, which over time becomes a position jitter (see figures 5.29 and 5.30). The horizontal jitter is sufficiently small that it is hard to see how it could be a problem. The vertical jitter could cause more trouble by resulting in the BEC hitting the barrier at a jittering (cycle-to-cycle) vertical location (thus making image averaging problematic). The impact of this vertical jitter should still be small since by design the barrier is relatively uniform in the vertical direction. However, we do see some increased vertical expansion after the BEC hits the barrier. This suggests that the barrier is not as uniform as we would like in the vertical direction.

Atom-atom interactions: The experiment is designed to minimize interactions by converting the BEC interaction energy into radial expansion kinetic energy, which occurs during the first few milliseconds after release from the trap. As indicated in chapter 2 (section 2.5.1 and fig. 2.4), we estimate that interactions should have little effect on the scattering process. However, when the BEC reflects off the barrier it is refocused in the horizontal direction. This refocusing is not intentional, but is due to the fact that the barrier is not uniform along the barrier beam propagation axis near the focus. The Kapitsa-Dirac effect that was observed is most clearly visible at this focus (see fig. 7.20). The BEC density at this focus necessarily increases, and so the interactions will increase, though it is unclear if they will be significant enough to impact the sidebands. However, I do not have evidence of change in the behavior of the BEC beyond the radial focusing (which is dependent on barrier energy, see fig. 7.19).

Optical lattice barrier beam: Our interpretation of the multiple diffraction peaks visible in fig. 7.20 is that they are the result of the BEC diffracting off an optical lattice in the barrier beam (i.e. Kapitsa-Dirac effect). Significant efforts were made to suppress these effects, but they were only unsuccessful, and the experimental parameter that made the effect come and go was never conclusively identified (at first, subtly changing beam alignment via vertical or focal adjustment seemed to help, but I am not convinced that the changes I saw in atomic structure were caused by my changes). We did not collect data while the Kapitsa-Dirac effect was present, but we could not monitor the effect simultaneously with collecting the main BEC scattering data. It is possible that a remnant of the optical lattice is present in the barrier beam, which would make the height of the barrier depend strongly on position. At its most basic, the experiment would be probing multiple barrier heights simultaneously. However, there could be some axial phase smearing occurring as well, so that the interference that produces the sidebands is not as pronounced, i.e. the sidebands become broader and less tall. Furthermore, a lattice in the barrier beam will also tend to funnel the atoms into the lattice sites somewhat leading to higher interactions. Estimating these effects requires 3D simulations of the barrier scattering process.

Imaging at an angle: While the axial imaging used for measuring the scattered axial profiles was setup with the absorption probe beam perpendicular to the axial propagation axis, it is possible that a small angle is present which would tend to increase the measured BEC position distribution. We think that this effect is relatively small and should not impair our ability to see the sidebands. However, if the Kapitsa-Dirac diffraction were present, then its effect is to move atoms in the horizontal transverse direction: in this case a small imaging angle could result in greater axial smear of position distribution, thus reducing the contrast on any sidebands.

Imaging signal-to-noise: One possibility is that the sidebands were present but were suppressed by one or more processes (see above). After all, experiments generally work less well than their design. It is possible that the sideband signal was lost somewhat in our imaging noise. However, we did average multiple images in an effort to better image any possible sidebands (see fig. 7.14 at 15 kHz), but none were apparent; this approach did show that a significant pedestal is present around the BEC carrier.

Barrier modulation phase jumps: While the feedback-based sinusoidal barrier modulation system worked fairly well, it did suffer from occasional phase jumps, i.e. the phase of the laser power sine wave would change abruptly. These jumps were infrequent, but their cause was never successfully identified. If such a phase jump occurred while the atoms were interacting with the barrier, then one would expect the interference that produces the sideband to degrade: the sideband would broaden and lower its amplitude, thus making it more difficult to observe. We do not think that this effect was significant enough to prevent us from observing sidebands, unless we were unlucky in when the phase jumps happened to occur.

Too much experimental variability: As explained in the next section, the experiment suffered from significant variability. The data was only taken on days when the barrier was first realigned and then calibrated. However, on at least one day the barrier showed transmission when it should not have (we did not take data that day), though no explanation was found. We cannot completely discount the possibility that the barrier (or some other quantity) may have drifted after its operation was verified, which may then have affected the search for sidebands.

8.3 Experimental Reproducibility

Unfortunately, the experiment did suffer from some irreproducible behavior that was never satisfactorily explained. This problem was managed by carefully re-aligning the apparatus and making calibrations (a time consuming process) when doing a data run. The BEC scattering data in chapter 7 was primarily taken over two days (Jan. 12, 2018 and Jan. 24, 2018), and we found the data on these two days was qualitatively consistent (see figures 7.7 and 7.8) and also showed some quantitative agreement. Here are the main difficulties encountered:

i) Vertical barrier wander: The barrier beam wanders vertically day-to-day by about 20 μm with a random direction. The cause was not identified at the time, but the solution was to start the day (after generating a BEC) by re-aligning the vertical barrier. Afterwards, the barrier height was either calibrated, or checked against an existing calibration. However, the alignment of the barrier beam was not tracked over the course of the data run. We did not have an explanation for the misalignment of the barrier beam (most of the optics alignment in the lab is relatively stable on a day-to-day basis) at the time. However, about half a year later (after the scattering BEC experiment was dismantled) the graduate students operating a laser dipole trap noticed a vertical periodic wander on the trap of about 20 μm with a roughly one hour period (larger excursions are possible as the lab warms up at the beginning of the day) associated with the lab's temperature. Notably, this behavior was not noticed on the same dipole trap prior to the BEC scattering experiment. The culprit appears to be the optics breadboard on which most of the barrier beam optics were held in place (and those of the dipole trap). It is possible that this vertical periodic wander existed during the BEC scattering data runs. However, the 20 μm wander is much smaller than the vertical waist of the barrier beam (795 μm), so the effect would likely be small.

ii) Optical lattice: We hypothesize that an optical lattice produced by a spurious reflection of the barrier beam (from a vacuum window) back on itself is producing the Kapitsa-Dirac diffraction of the BEC that sometimes occurs. The effect comes and goes. We have tested a number of experimental parameters, notably the barrier beam wavelength (small changes up to 2 nm), but have not found a reliable method to influence this effect. At some point, we thought that we were able to suppress the effect by modifying the barrier beam alignment, but eventually we saw signs of the effect again. It is possible that barrier beam wander (in particular the periodic wander identified a half year later, see paragraph above)) may be involved. We did not see the effect for the Jan. 12 and Jan. 24 data runs, though we were not in a position to observe the effect during most of the runs.

iii) Barrier modulation phase jumps: The sinusoidal modulation of the barrier height (i.e. laser power) occasionally has a phase jump in it, i.e. the phase resets itself randomly. These jumps are not that common, but their origin is unknown. While we do not think that these jumps had a significant impact on the measurements, ideally they should be eliminated if the experiment is re-attempted. My only comment on the occurrence of these jumps is they do not occur every time, and I do not remember seeing more than one of them during an oscillation sequence on the scope.

8.4 Outlook (And Potential Improvements)

There are a few improvements that could be made to overcome both technical and physical limitations towards resolving discrete sidebands. The sidebands are easier to resolve with a larger differential velocity, but simply opting to use frequencies and incident velocities that yield larger differential velocities does not guarantee the generation of sidebands. The oscillating barrier adds and subtracts kinetic energy to the atoms. So, by switching to a lighter atomic species the change in velocity will be larger for the same change in kinetic energy. Our apparatus is dual-species and equipped to cool rubidium and potassium. Switching to potassium has two immediate advantages: 1) it is a lighter element, and 2) it has an experimentally accessible Feshbach zero (^{39}K at 350 G) for canceling atom-atom interactions [84]. Potassium also has disadvantages. For example, it does not laser-cool as well as rubidium and requires sympathetic cooling to reach quantum degeneracy. Due to this problem, potassium might not yield as large a BEC as rubidium, which will make imaging more difficult. Potassium would also require a faster initial velocity to scale parameters used for rubidium. The barrier is currently produced by a tightly focused blue-detuned optical dipole laser beam. The source of this beam happens to be the laser typically used to laser-cool potassium at 767 nm, which is somewhat blue-detuned from rubidium's 780 nm D2 line. Therefore, a new laser would be required to produce a blue-detuned beam for potassium. However, it is possible that a red-detuned beam could also produce sidebands with an oscillating potential well. Unfortunately, at this time a laser cannot be used simultaneously as a barrier/well and for laser-cooling.

No matter which species is used for this experiment (or any other), it is best to have as large an atom number as possible to obtain the best imaging quality. To address this in the future, I believe the biggest limiting factor in producing a large rubidium BEC and most irreproducible element of the apparatus is currently the stability of the rubidium repumper laser. I believe fixing this problem would be the single biggest improvement in BEC production. This would help increase atom number and increase optical depth during imaging. If possible, adding a confining potential could also prevent unwanted expansion in the vertical direction that lowers optical depth. However, this may increase atom-atom interactions that distort sideband production. Another approach to imaging is to use non-destructive imaging techniques to observe the same atom cloud over a long period of time. This could potentially remove outliers caused by jitter or any other source of irreproducibility between apparatus cycles. This approach would also greatly reduce the time required to collect multiple data points. Unfortunately, this technique may require more atoms than our apparatus is currently capable of producing to be easily implemented. Fluorescence imaging could be used if the atoms are trapped by an axially oriented optical lattice after interacting with the barrier. In this scheme, different sidebands would be trapped in different lattice sites and a fluorescence probe beam could be applied for long times so that images benefit from many counts and high contrast.

The barrier modulation could also be improved so that it can respond faster and behave more like a sine wave. An Electro-Optic Modulator (EOM) could be used to do this as it has a faster response than our AOM's. Also, for the experiment to continue past single barrier scattering, we would require an additional barrier which will require twice the laser power available. We have access to a titanium sapphire laser, although it is not currently used for the barrier beam, and perhaps it might be the solution to providing more power. The barrier alignment has also been more delicate than we would prefer, but the only solution is to simply tweak the alignment prior to collecting data. This is not ideal as it has required us to collect as much data in one day as we can, for fear that the barrier will not yield the same effectiveness the following day. This could be solved by monitoring the barrier beam on a camera and using the information to control piezo-driven optical mounts, probably governed by a Field Programmable Gate Array (FPGA) for speed.[1]

We have made progress on this experiment. However, from an administrative standpoint I question whether or not this project should continue. Several times in the past I was complimented at conferences on how "neat" this experiment is, but I feel that it may lack practical application. In its current form (i.e. BEC in free space interacting with a modulated barrier [85]), the experiment does not have a clear application beyond testing basic physics (a laser barrier scheme was recently used to measure narrow atomic momentum distributions [85]). However,

[1] Experimentalists will likely laugh at this statement.

if the atoms are made to interact less (e.g. ^{39}K at 350 G), then the experiment can be conducted inside a trap (optical dipole trap or AC Zeeman trap (not yet demonstrated)) or trapping channel. The modulated barrier can then become a standard atomtronic element. It also becomes a building block for multi-barrier/well structures. Notably, one could try to make a non-ballistic atom pump using the successfully implemented electron/quantum pump from [24]. In fact, this specific pump might actually benefit from interactions and might be a means to deliver a specific number of atoms on demand. At this point the applications of atomtronics are unclear, but presumably if the atoms can be made to be coherent, then quantum computing/information and interferometry would be applications. Furthermore, the difficulty of this experiment may make implementing an application impractical. This experiment has also received no substantial funding while I was a student. By contrast, our lab's work with the AC Zeeman effect has proven itself superior in all of these aspects. It has produced more successful results, garnered funding, and is more practical. And so the question is, can the continuation of this experiment be justified, or is the opportunity cost too high? If choosing to proceed, one should carefully consider the time required to complete this. So far, two graduate students have attempted and failed to resolve discrete quantum mechanical sidebands.[2]

It is my optimistic ambition that this thesis proves useful to students who follow me. Bose-Einstein condensate theory will help students understand the theories of physics upon which the apparatus is governed. The apparatus chapter will hopefully provide a manual to guide students in the practical workings of the apparatus. Finally, the experimental setup, procedure, and results will be incredibly valuable should anyone choose to continue this project. Bose-Einstein condensates continue to be a useful medium in which to explore areas of many-body physics, fundamental

[2]When debating whether or not to continue collecting data, my adviser likened the timeline of this experiment to the United States winning the war in Afghanistan.

quantum mechanics, precision metrology, and quantum computing.

APPENDIX A

Additional Expansion Rate Plots

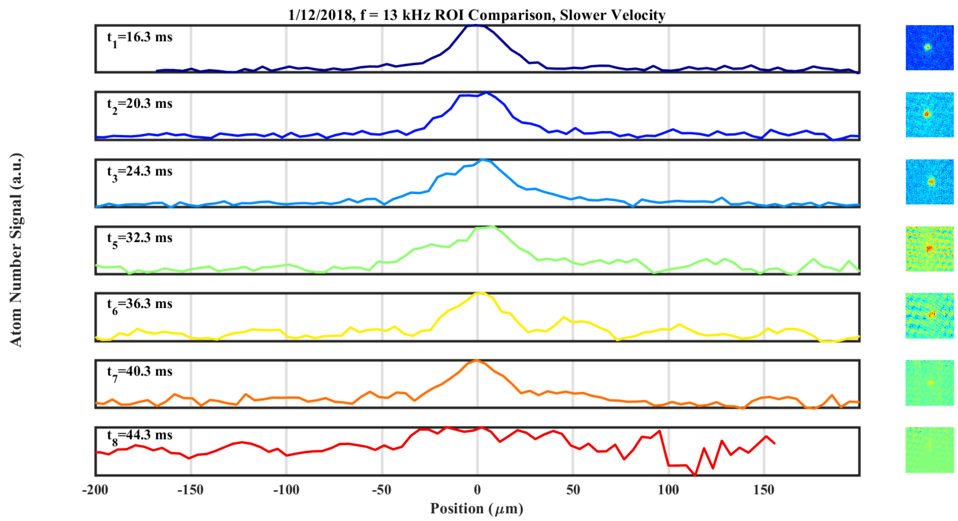

FIG. A.1: This plot shows the filtered ROI (Region of Interest) sum for multiple times of flight. The atom cloud clearly expands over time in the axial direction. The data shown was collected for the slower initial atomic velocity and a barrier modulation frequency of 13 kHz (preliminary data collected on 1/12/2018).

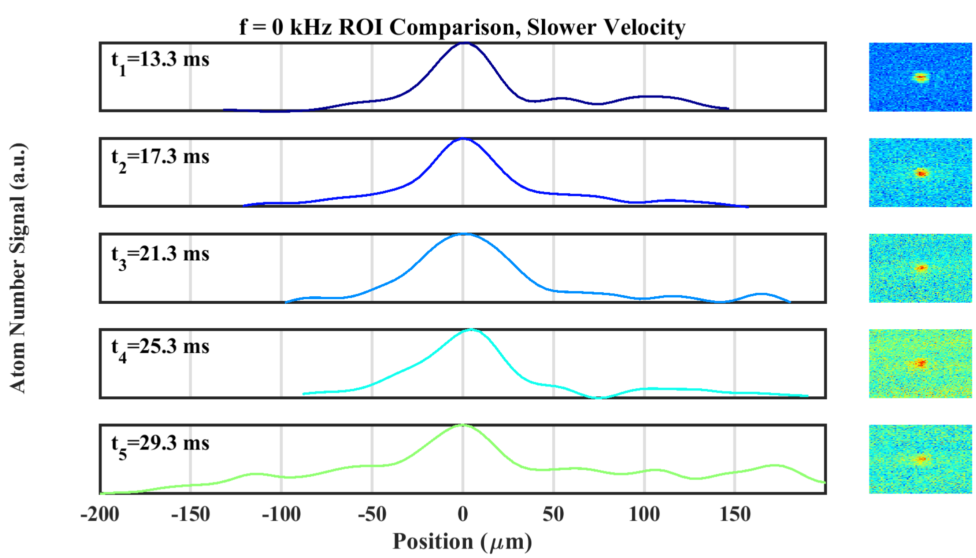

FIG. A.2: This plot shows the filtered ROI (Region of Interest) sum for multiple times of flight. The atom cloud clearly expands over time in the axial direction. The data shown was collected for the slower initial atomic velocity and a static barrier.

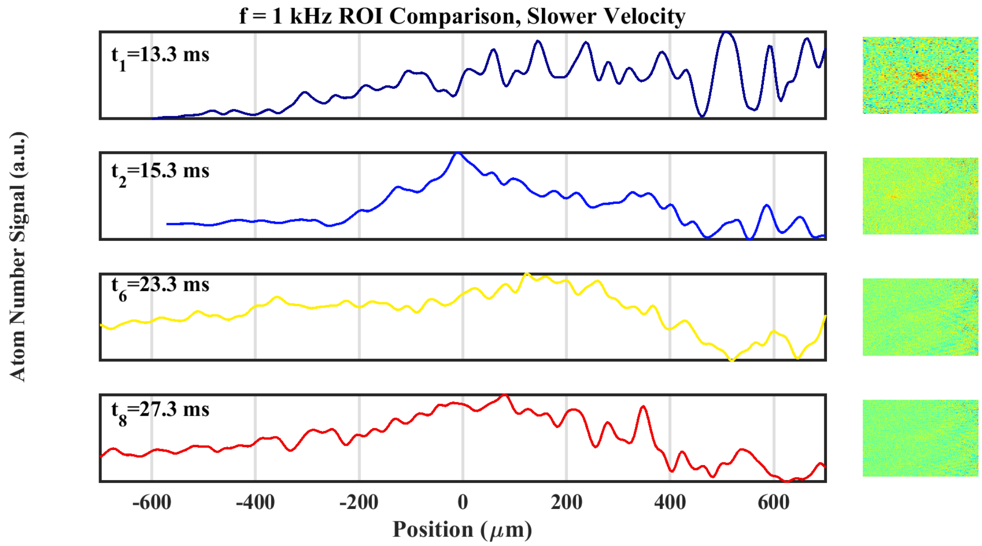

FIG. A.3: This plot shows the filtered ROI (Region of Interest) sum for multiple times of flight. The atom cloud clearly expands over time in the axial direction. The data shown was collected for the slower initial atomic velocity and a barrier modulation frequency of 1 kHz.

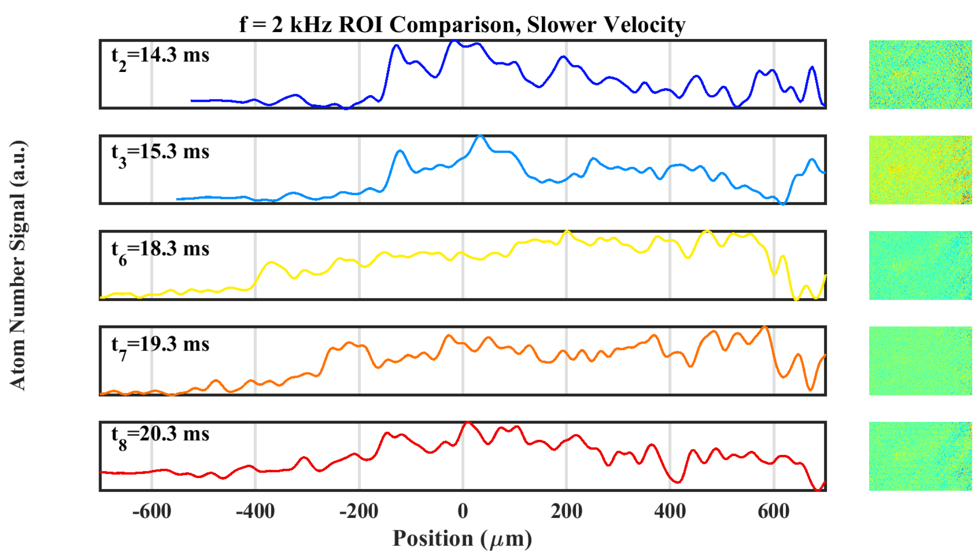

FIG. A.4: This plot shows the filtered ROI (Region of Interest) sum for multiple times of flight. The atom cloud clearly expands over time in the axial direction. The data shown was collected for the slower initial atomic velocity and a barrier modulation frequency of 2 kHz.

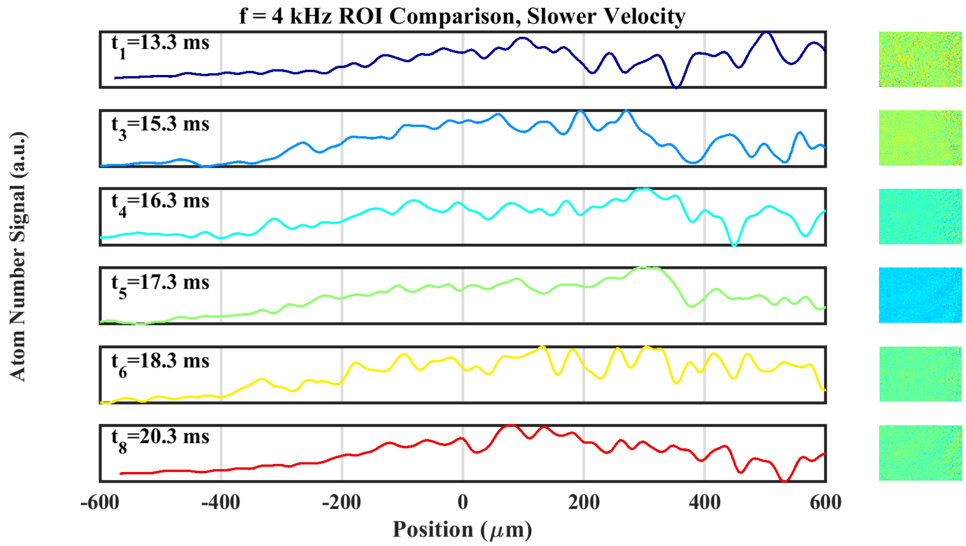

FIG. A.5: This plot shows the filtered ROI (Region of Interest) sum for multiple times of flight. The atom cloud clearly expands over time in the axial direction. The data shown was collected for the slower initial atomic velocity and a barrier modulation frequency of 4 kHz.

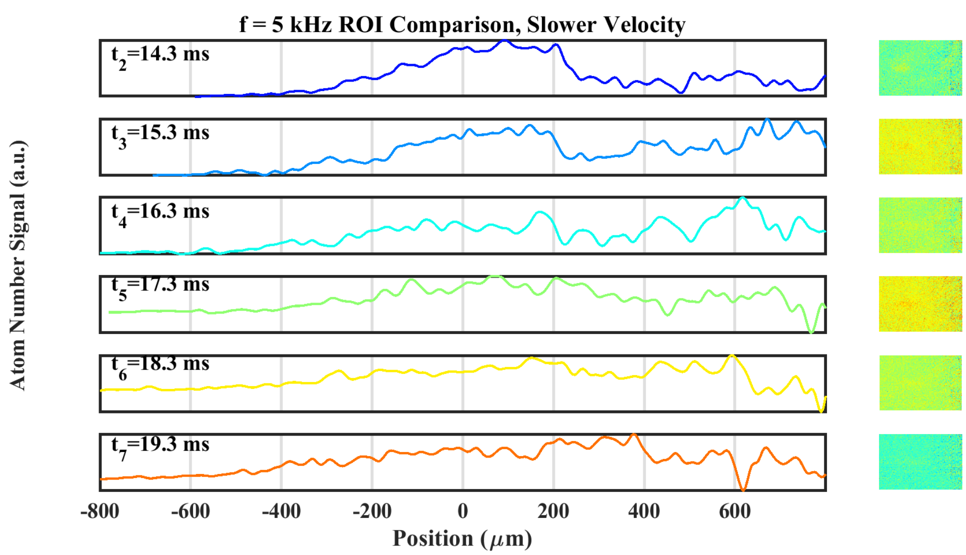

FIG. A.6: This plot shows the filtered ROI (Region of Interest) sum for multiple times of flight. The atom cloud clearly expands over time in the axial direction. The data shown was collected for the slower initial atomic velocity and a barrier modulation frequency of 5 kHz.

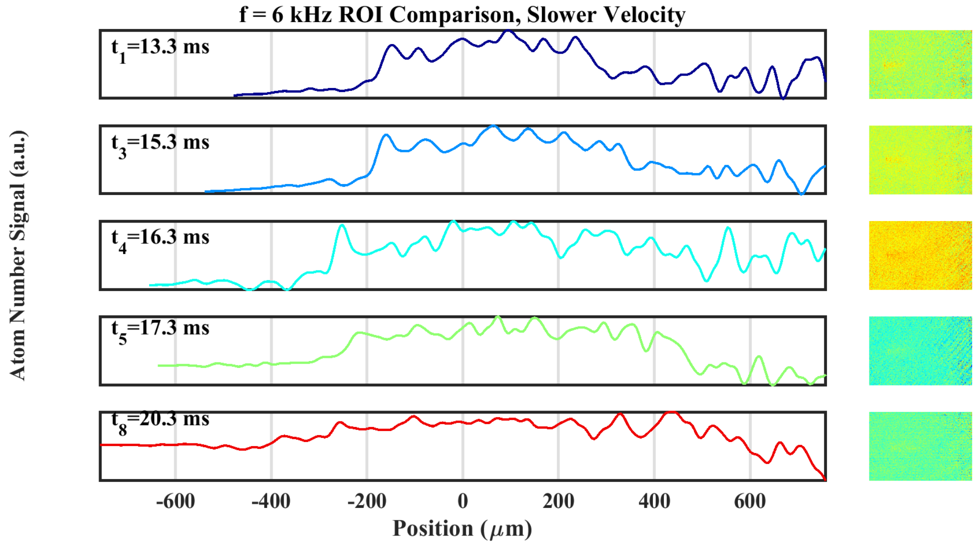

FIG. A.7: This plot shows the filtered ROI (Region of Interest) sum for multiple times of flight. The atom cloud clearly expands over time in the axial direction. The data shown was collected for the slower initial atomic velocity and a barrier modulation frequency of 6 kHz.

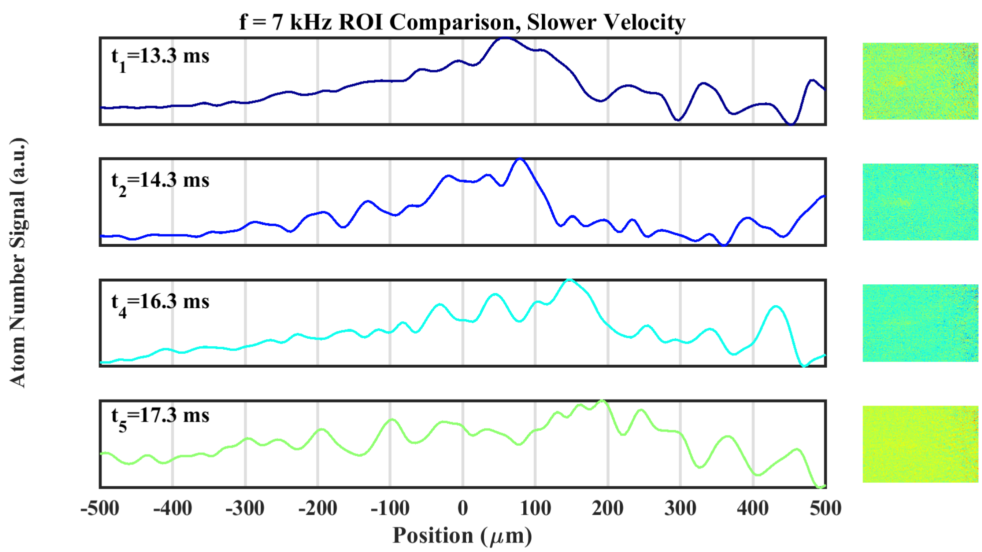

FIG. A.8: This plot shows the filtered ROI (Region of Interest) sum for multiple times of flight. The atom cloud clearly expands over time in the axial direction. The data shown was collected for the slower initial atomic velocity and a barrier modulation frequency of 7 kHz.

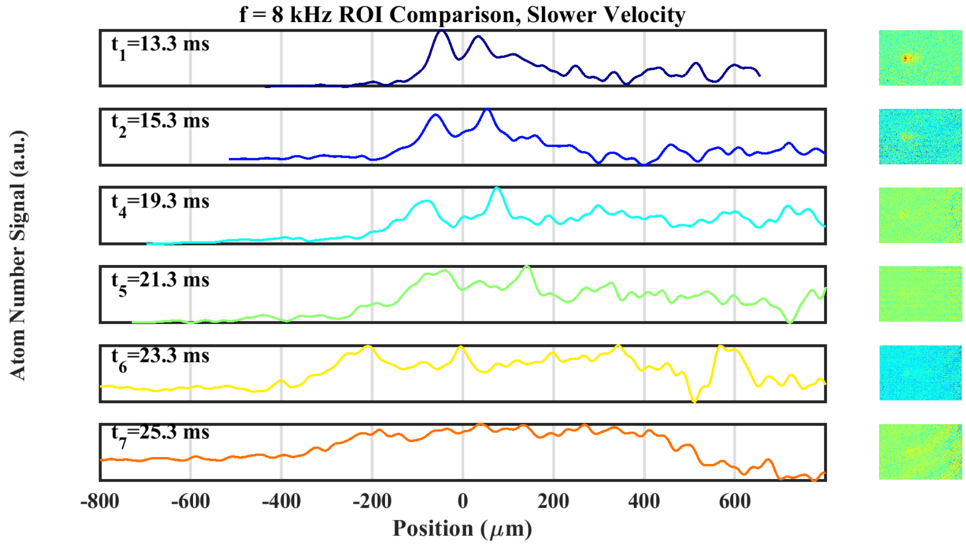

FIG. A.9: This plot shows the filtered ROI (Region of Interest) sum for multiple times of flight. The atom cloud clearly expands over time in the axial direction. The data shown was collected for the slower initial atomic velocity and a barrier modulation frequency of 8 kHz.

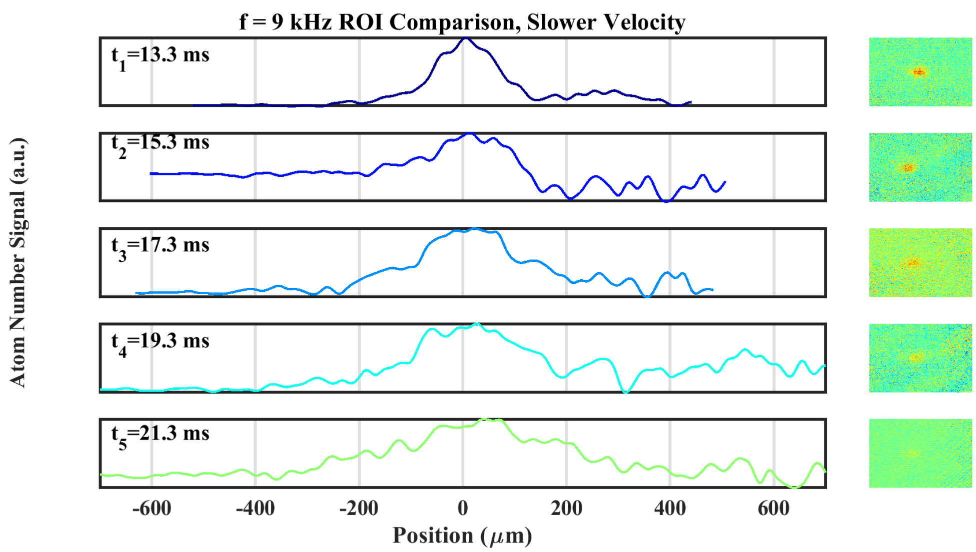

FIG. A.10: This plot shows the filtered ROI (Region of Interest) sum for multiple times of flight. The atom cloud clearly expands over time in the axial direction. The data shown was collected for the slower initial atomic velocity and a barrier modulation frequency of 9 kHz.

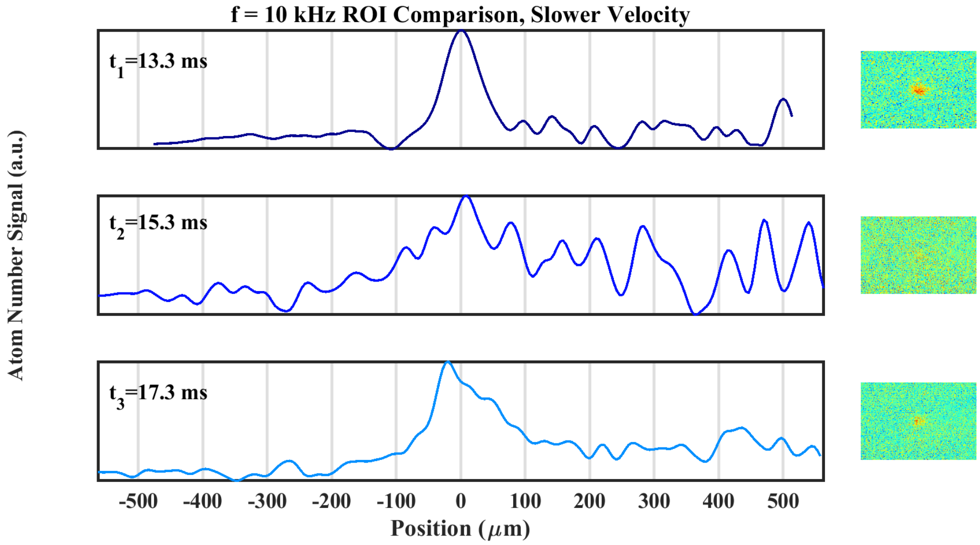

FIG. A.11: This plot shows the filtered ROI (Region of Interest) sum for multiple times of flight. The atom cloud clearly expands over time in the axial direction. The data shown was collected for the slower initial atomic velocity and a barrier modulation frequency of 10 kHz.

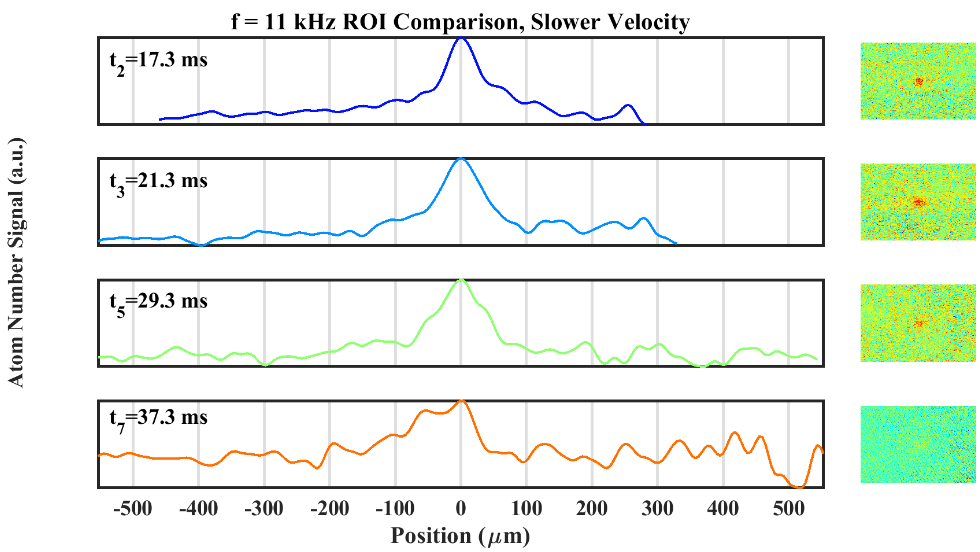

FIG. A.12: This plot shows the filtered ROI (Region of Interest) sum for multiple times of flight. The atom cloud clearly expands over time in the axial direction. The data shown was collected for the slower initial atomic velocity and a barrier modulation frequency of 11 kHz.

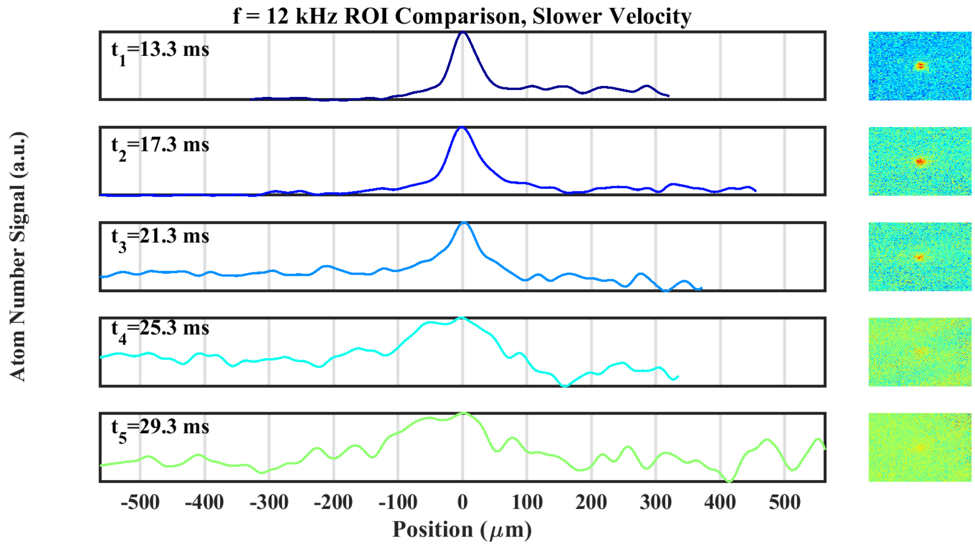

FIG. A.13: This plot shows the filtered ROI (Region of Interest) sum for multiple times of flight. The atom cloud clearly expands over time in the axial direction. The data shown was collected for the slower initial atomic velocity and a barrier modulation frequency of 12 kHz.

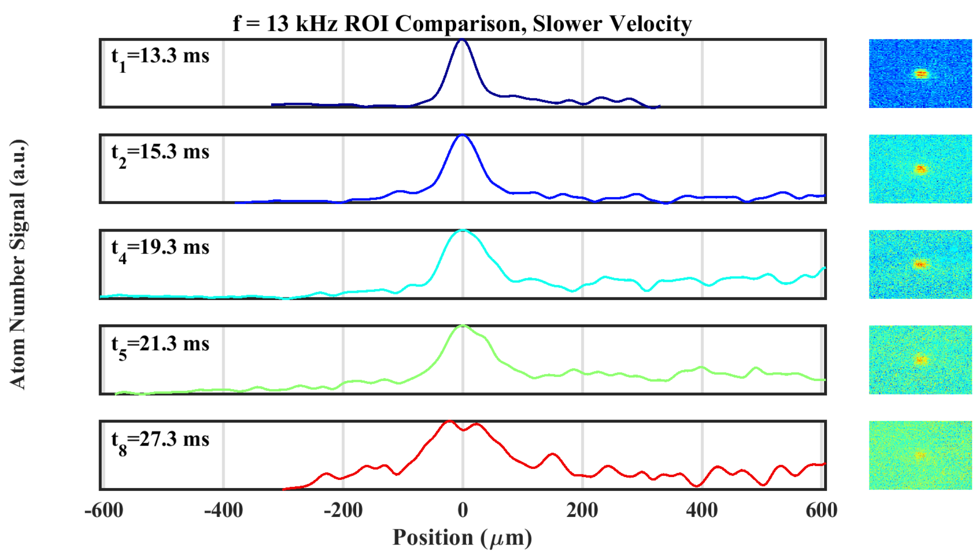

FIG. A.14: This plot shows the filtered ROI (Region of Interest) sum for multiple times of flight. The atom cloud clearly expands over time in the axial direction. The data shown was collected for the slower initial atomic velocity and a barrier modulation frequency of 13 kHz.

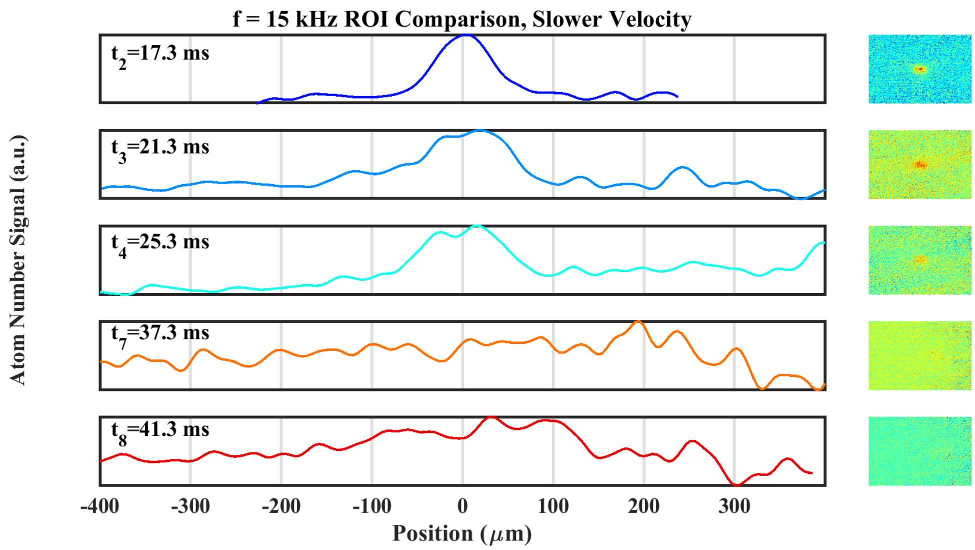

FIG. A.15: This plot shows the filtered ROI (Region of Interest) sum for multiple times of flight. The atom cloud clearly expands over time in the axial direction. The data shown was collected for the slower initial atomic velocity and a barrier modulation frequency of 15 kHz.

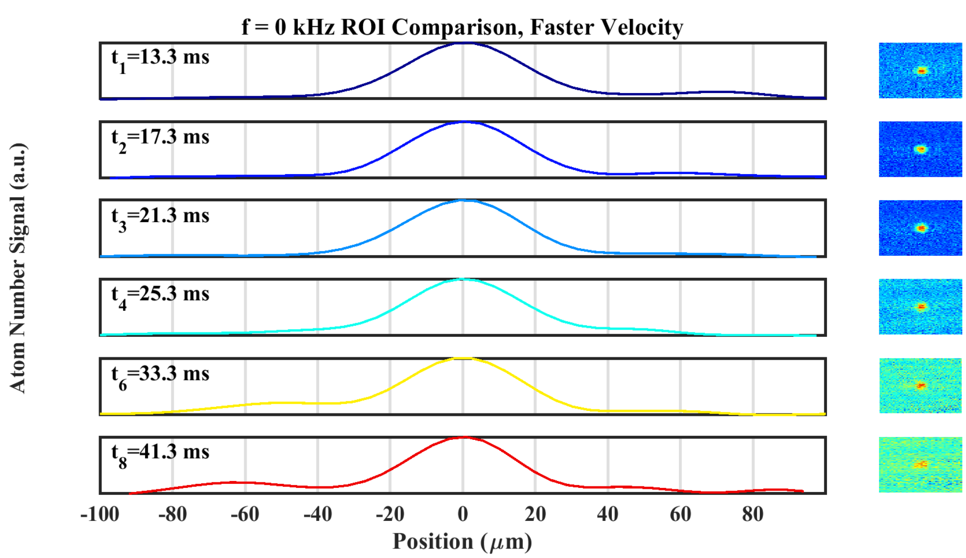

FIG. A.16: This plot shows the filtered ROI (Region of Interest) sum for multiple times of flight. The atom cloud clearly expands over time in the axial direction. The data shown was collected for the faster initial atomic velocity and a static barrier.

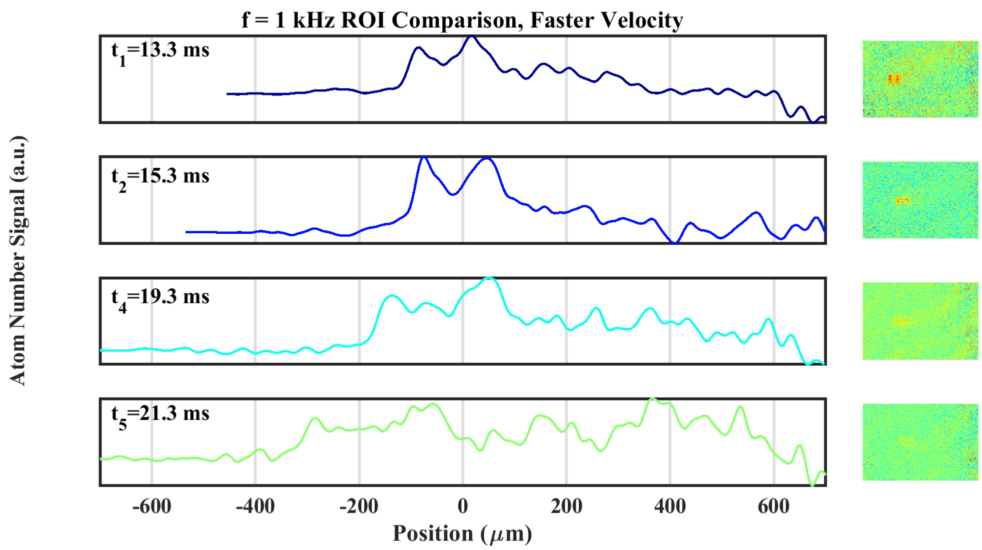

FIG. A.17: This plot shows the filtered ROI (Region of Interest) sum for multiple times of flight. The atom cloud clearly expands over time in the axial direction. The data shown was collected for the faster initial atomic velocity and a barrier modulation frequency of 1 kHz.

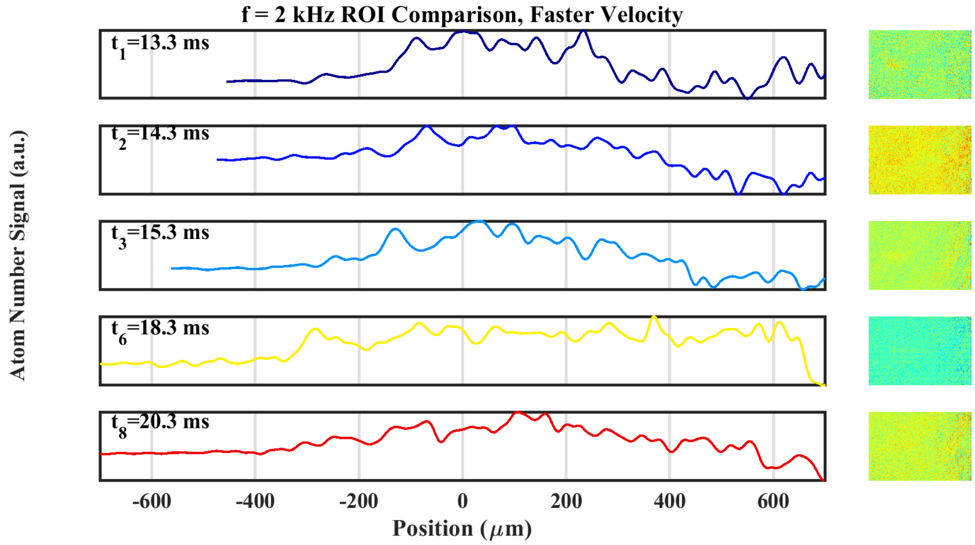

FIG. A.18: This plot shows the filtered ROI (Region of Interest) sum for multiple times of flight. The atom cloud clearly expands over time in the axial direction. The data shown was collected for the faster initial atomic velocity and a barrier modulation frequency of 2 kHz.

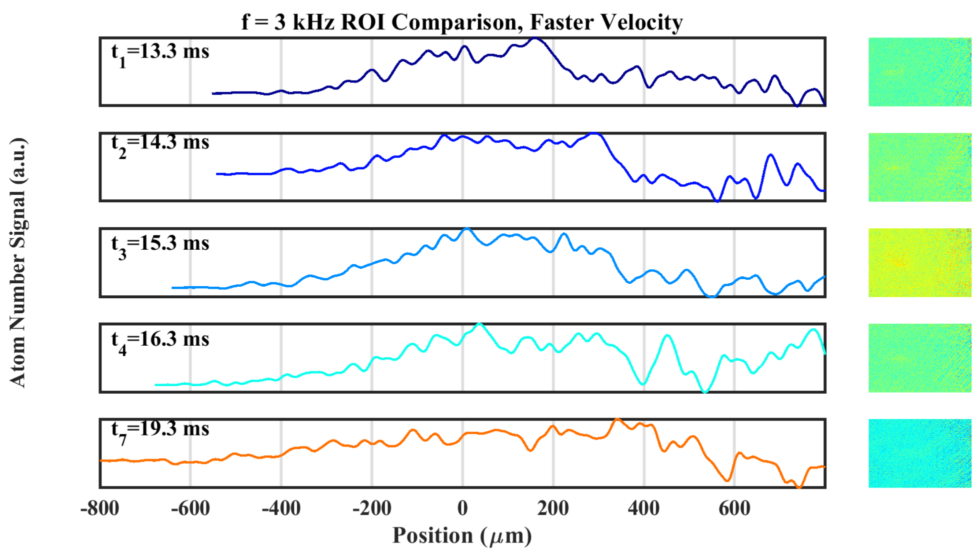

FIG. A.19: This plot shows the filtered ROI (Region of Interest) sum for multiple times of flight. The atom cloud clearly expands over time in the axial direction. The data shown was collected for the faster initial atomic velocity and a barrier modulation frequency of 3 kHz.

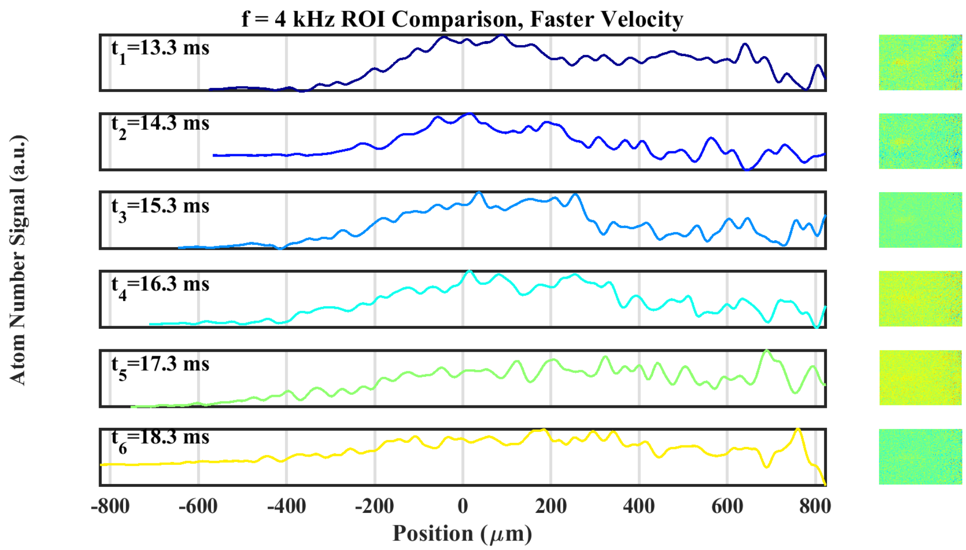

FIG. A.20: This plot shows the filtered ROI (Region of Interest) sum for multiple times of flight. The atom cloud clearly expands over time in the axial direction. The data shown was collected for the faster initial atomic velocity and a barrier modulation frequency of 4 kHz.

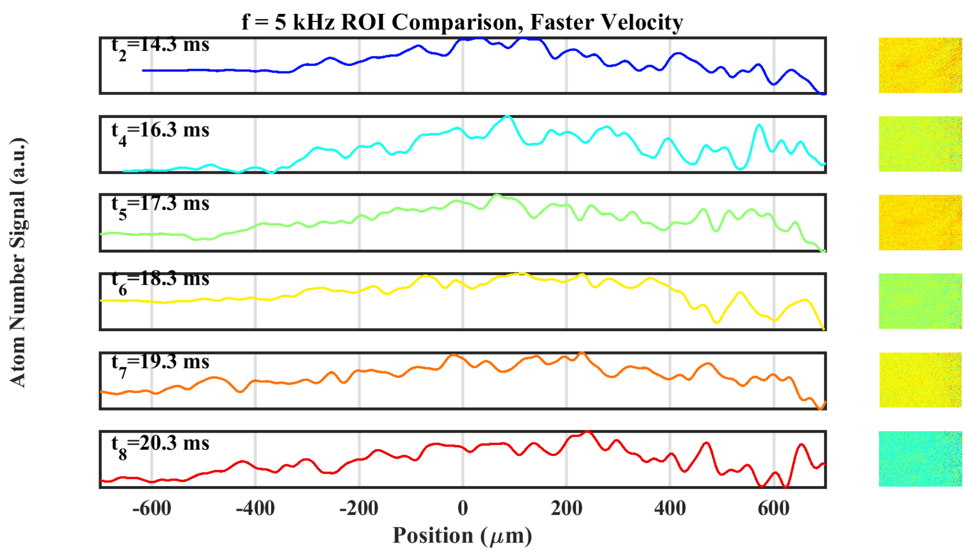

FIG. A.21: This plot shows the filtered ROI (Region of Interest) sum for multiple times of flight. The atom cloud clearly expands over time in the axial direction. The data shown was collected for the faster initial atomic velocity and a barrier modulation frequency of 5 kHz.

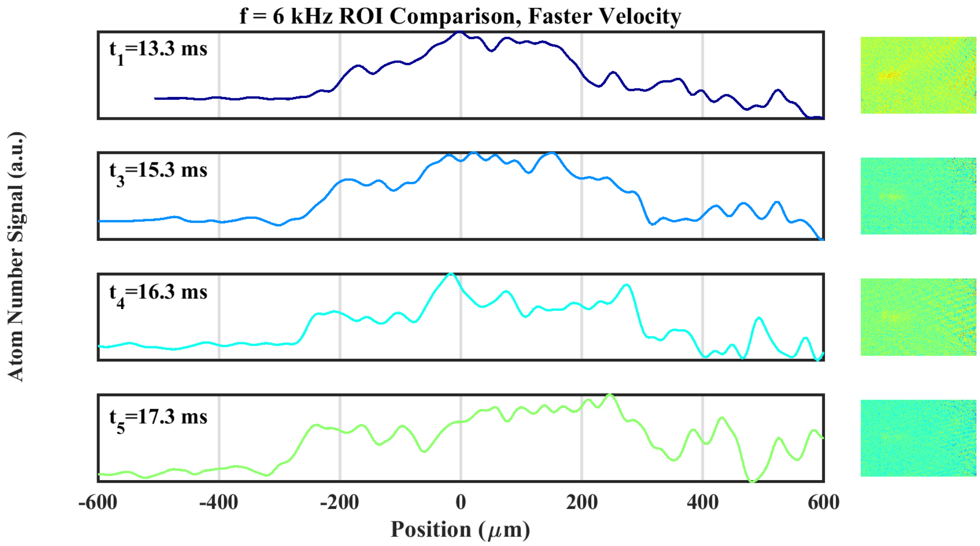

FIG. A.22: This plot shows the filtered ROI (Region of Interest) sum for multiple times of flight. The atom cloud clearly expands over time in the axial direction. The data shown was collected for the faster initial atomic velocity and a barrier modulation frequency of 6 kHz.

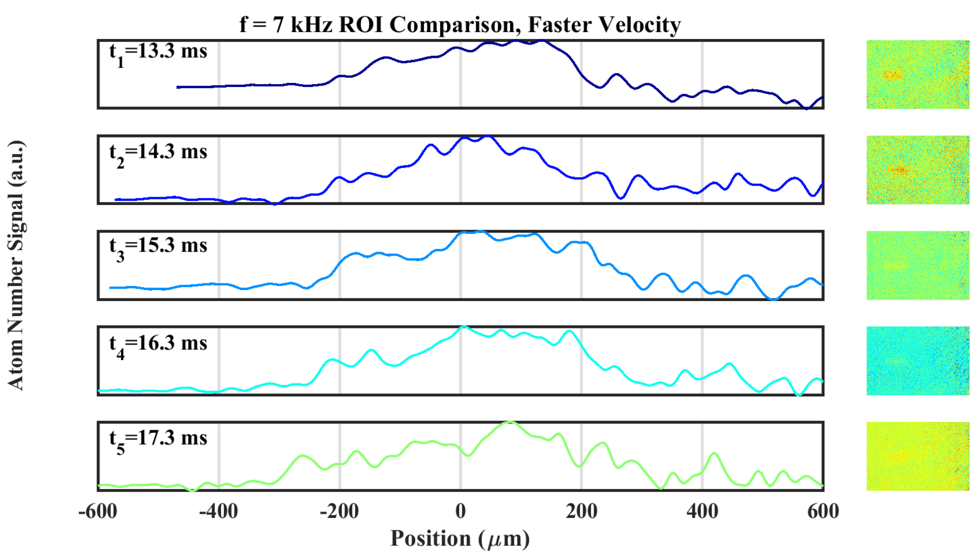

FIG. A.23: This plot shows the filtered ROI (Region of Interest) sum for multiple times of flight. The atom cloud clearly expands over time in the axial direction. The data shown was collected for the faster initial atomic velocity and a barrier modulation frequency of 7 kHz.

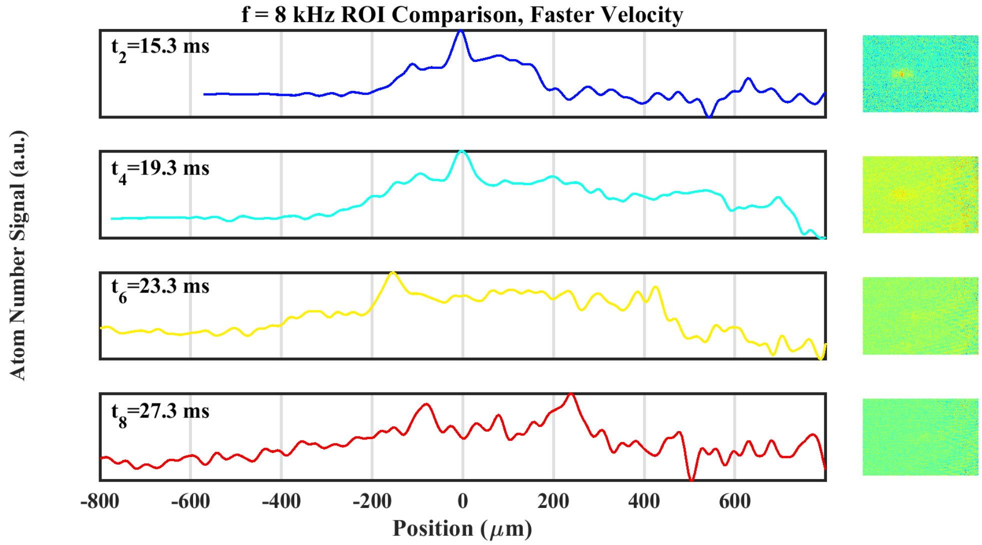

FIG. A.24: This plot shows the filtered ROI (Region of Interest) sum for multiple times of flight. The atom cloud clearly expands over time in the axial direction. The data shown was collected for the faster initial atomic velocity and a barrier modulation frequency of 8 kHz.

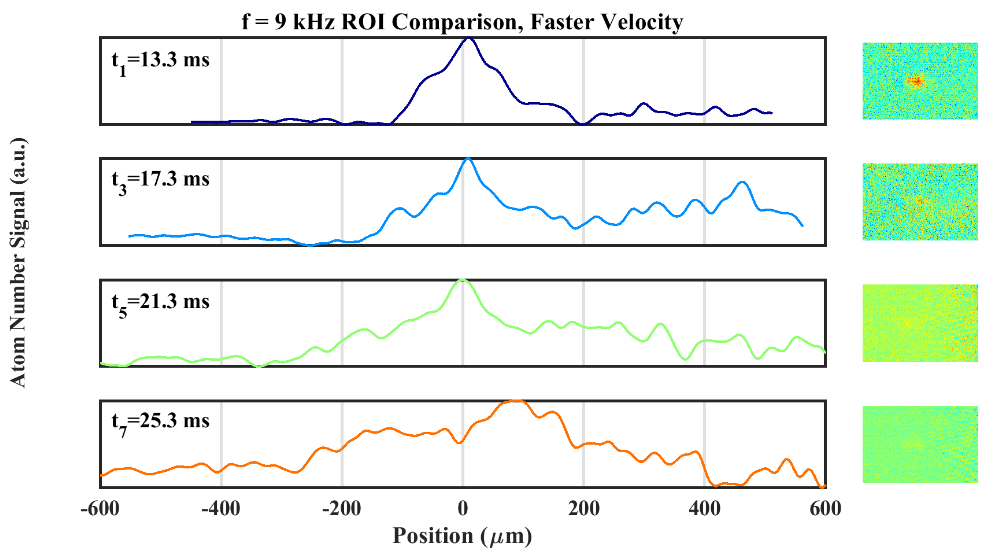

FIG. A.25: This plot shows the filtered ROI (Region of Interest) sum for multiple times of flight. The atom cloud clearly expands over time in the axial direction. The data shown was collected for the faster initial atomic velocity and a barrier modulation frequency of 9 kHz.

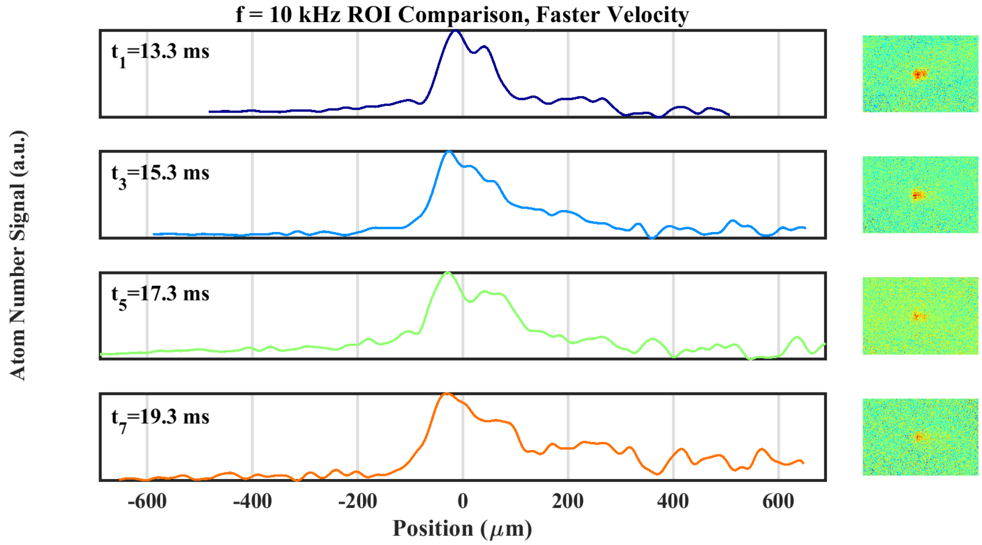

FIG. A.26: This plot shows the filtered ROI (Region of Interest) sum for multiple times of flight. The atom cloud clearly expands over time in the axial direction. The data shown was collected for the faster initial atomic velocity and a barrier modulation frequency of 10 kHz.

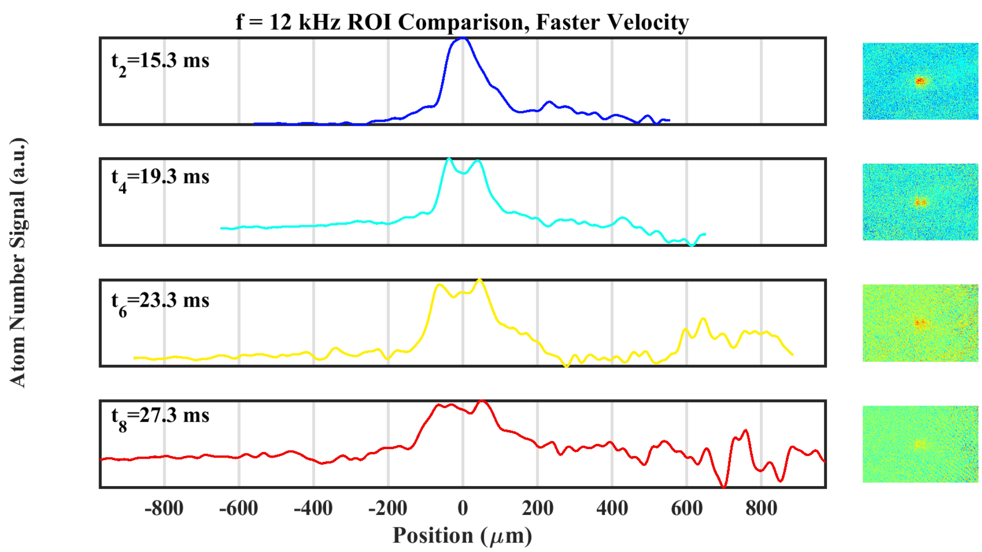

FIG. A.27: This plot shows the filtered ROI (Region of Interest) sum for multiple times of flight. The atom cloud clearly expands over time in the axial direction. The data shown was collected for the faster initial atomic velocity and a barrier modulation frequency of 12 kHz.

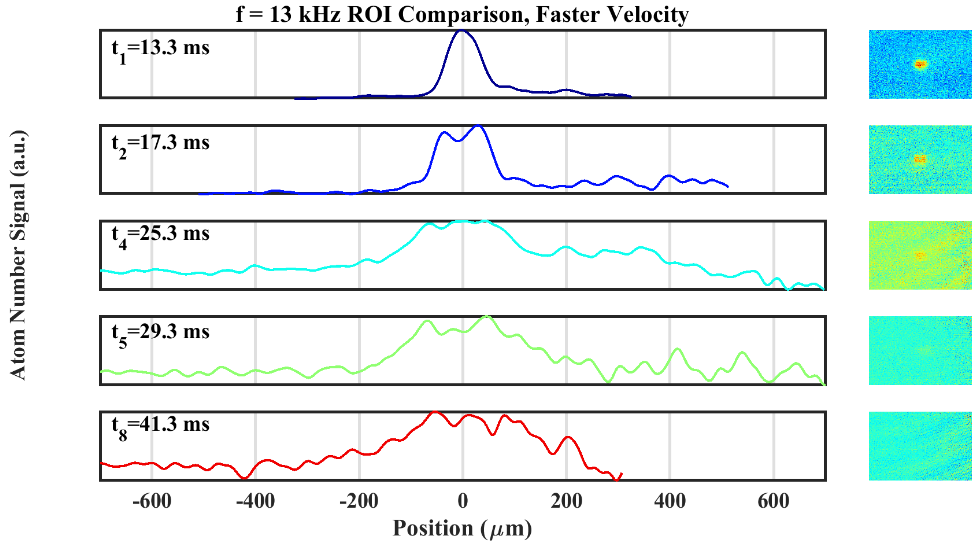

FIG. A.28: This plot shows the filtered ROI (Region of Interest) sum for multiple times of flight. The atom cloud clearly expands over time in the axial direction. The data shown was collected for the faster initial atomic velocity and a barrier modulation frequency of 13 kHz.

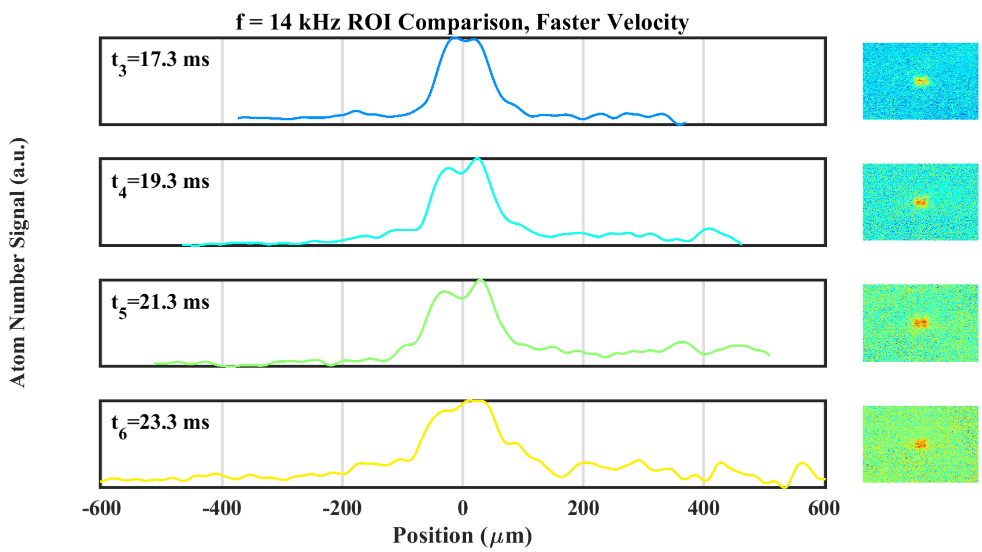

FIG. A.29: This plot shows the filtered ROI (Region of Interest) sum for multiple times of flight. The atom cloud clearly expands over time in the axial direction. The data shown was collected for the faster initial atomic velocity and a barrier modulation frequency of 14 kHz.

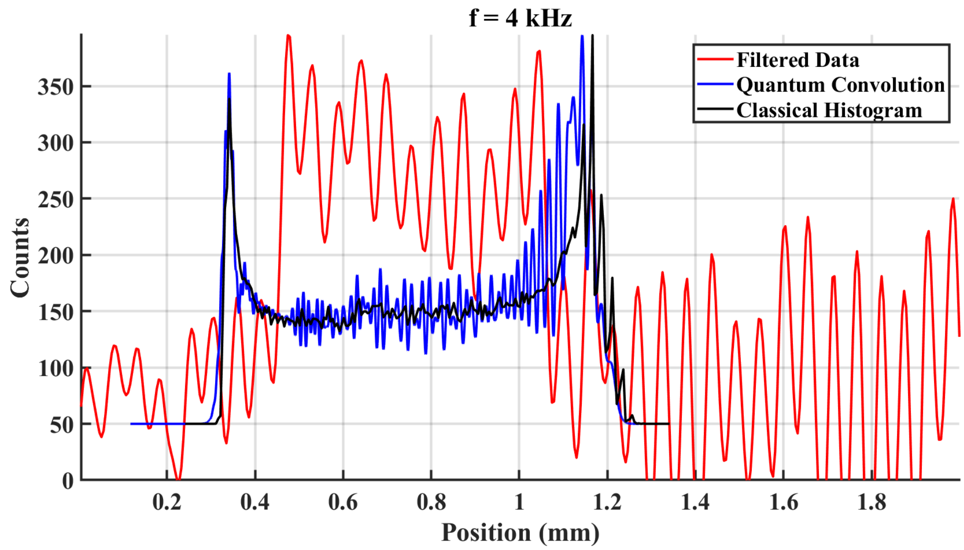

FIG. A.30: ROI sum compared to classical and quantum theory for $f = 4$ kHz and a slower initial atomic velocity.

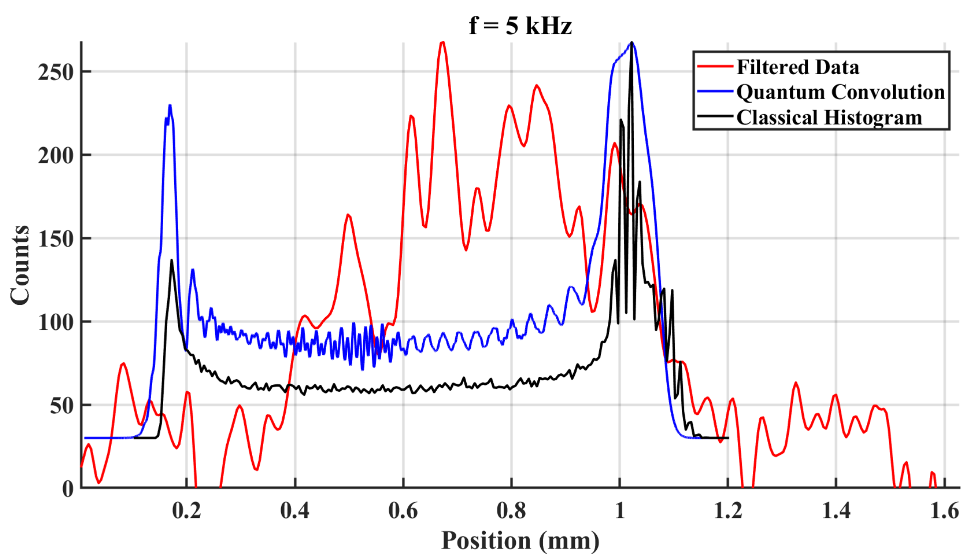

FIG. A.31: ROI sum compared to classical and quantum theory for $f = 5$ kHz and a slower initial atomic velocity.

APPENDIX B

Additional Overshoot Pulse Tuning Plots

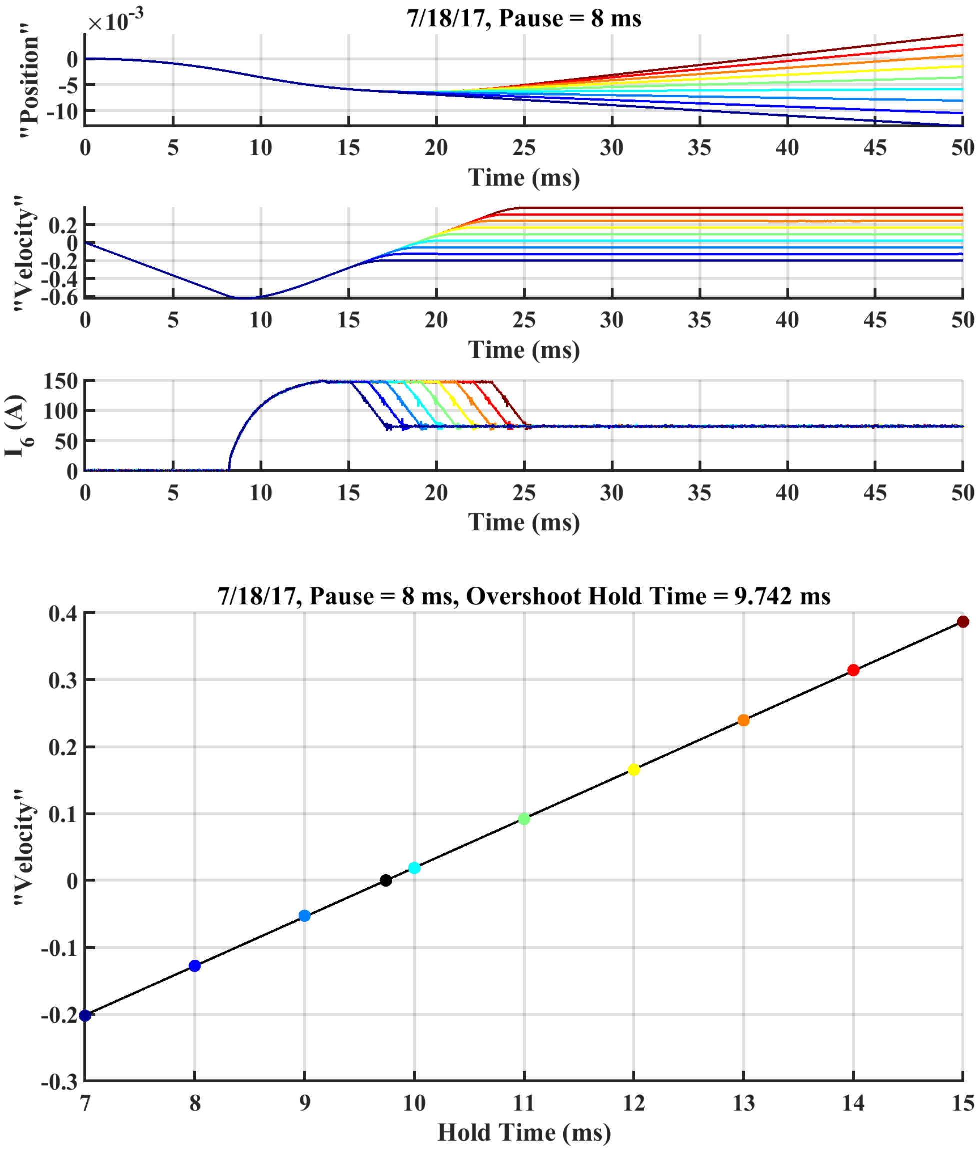

FIG. B.1: See section 5.4, figure 5.24 for explanation.

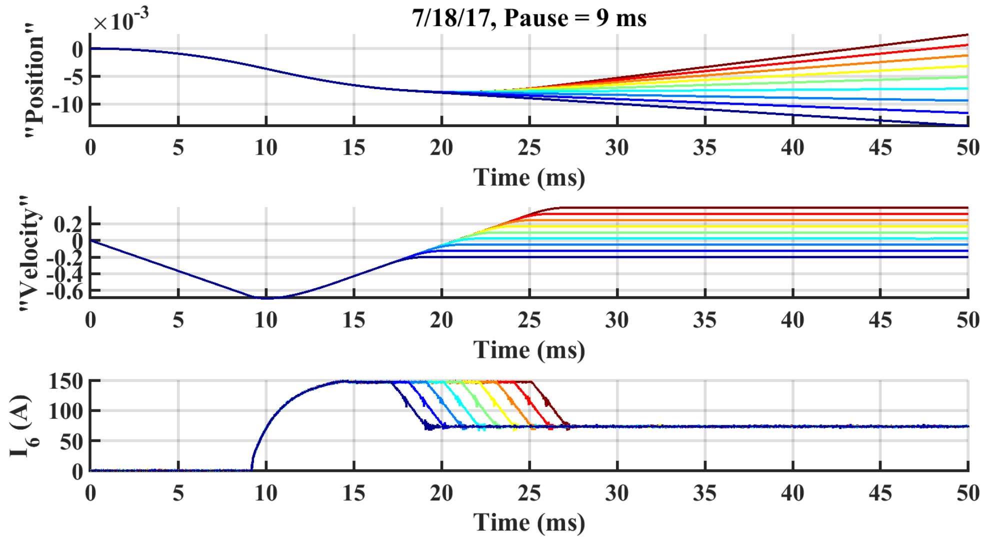

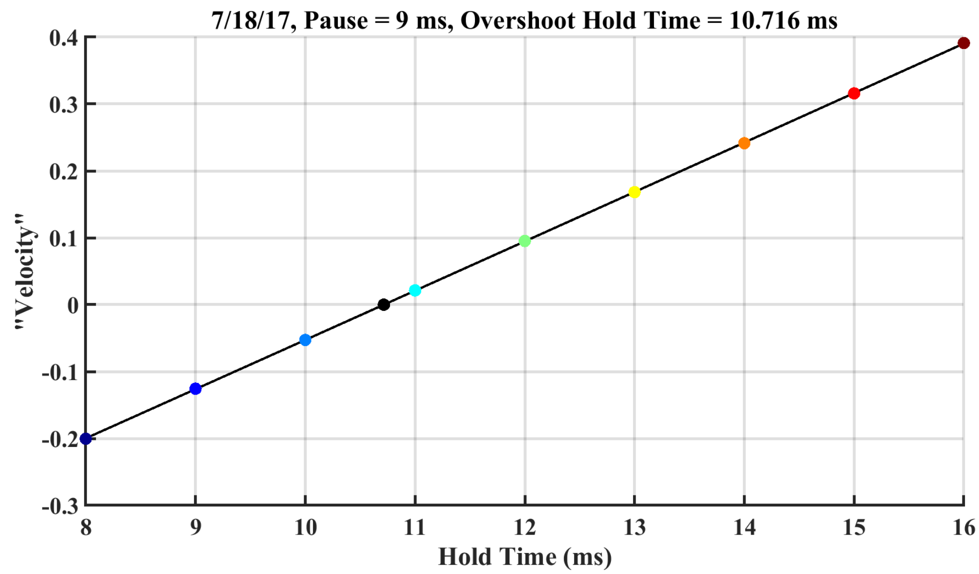

FIG. B.2: See section 5.4, figure 5.24 for explanation.

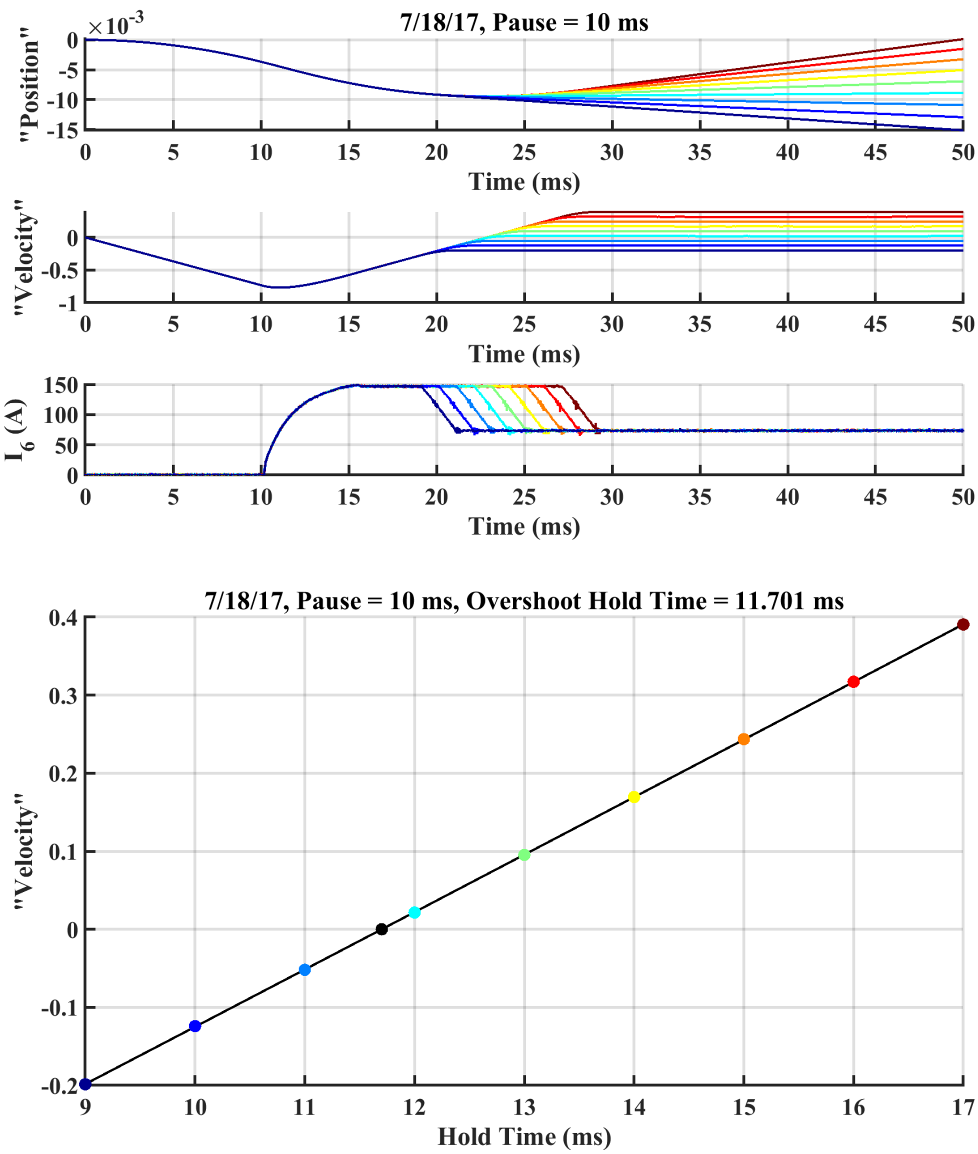

FIG. B.3: See section 5.4, figure 5.24 for explanation.

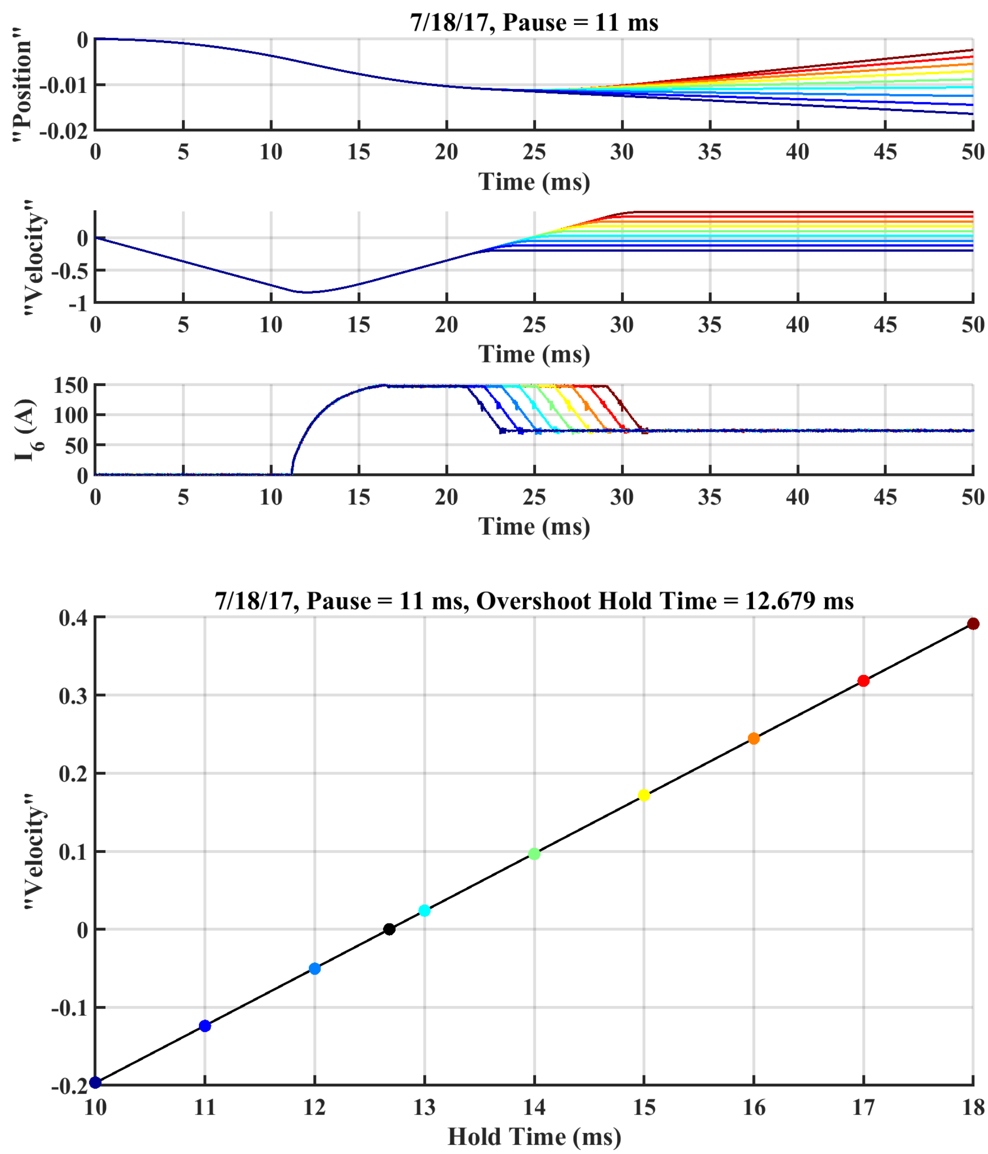

FIG. B.4: See section 5.4, figure 5.24 for explanation.

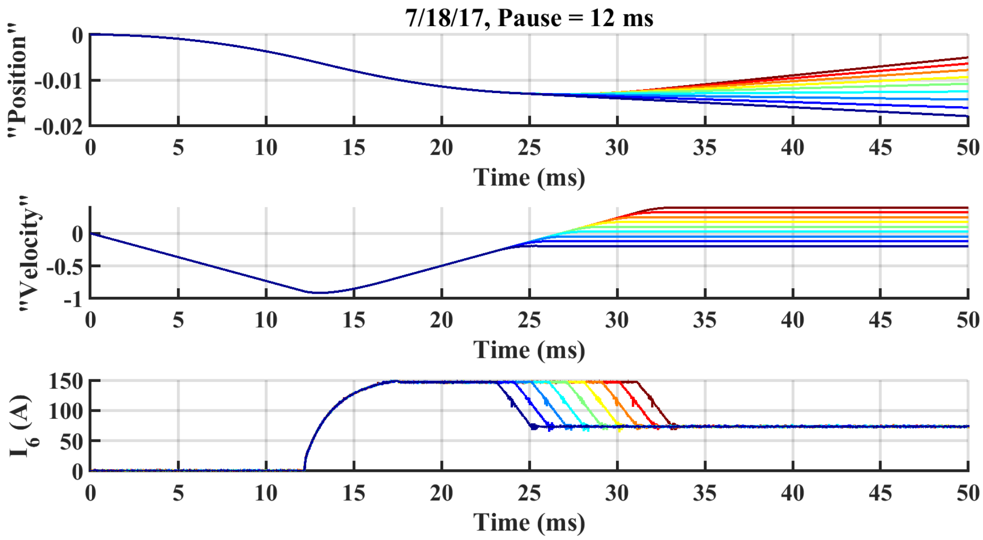

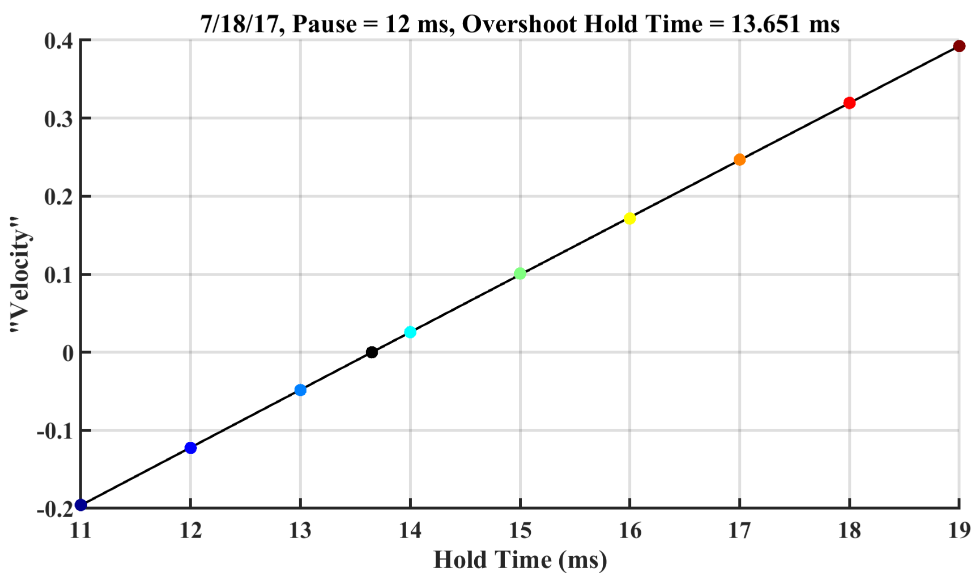

FIG. B.5: See section 5.4, figure 5.24 for explanation.

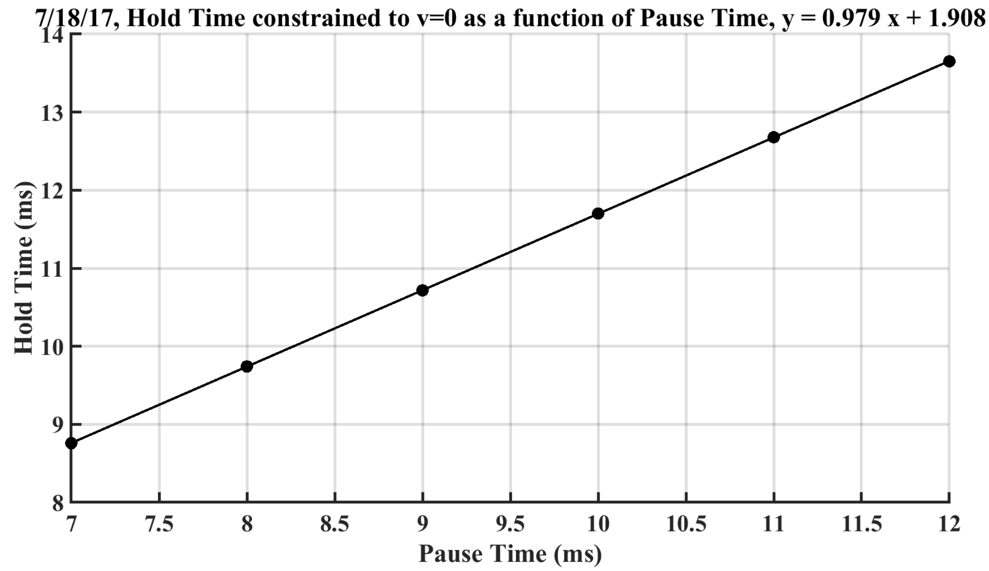

FIG. B.6: Hold time for optimal overshoot pulse for different pause times before turning on coil 6. Applicable to section 5.4.

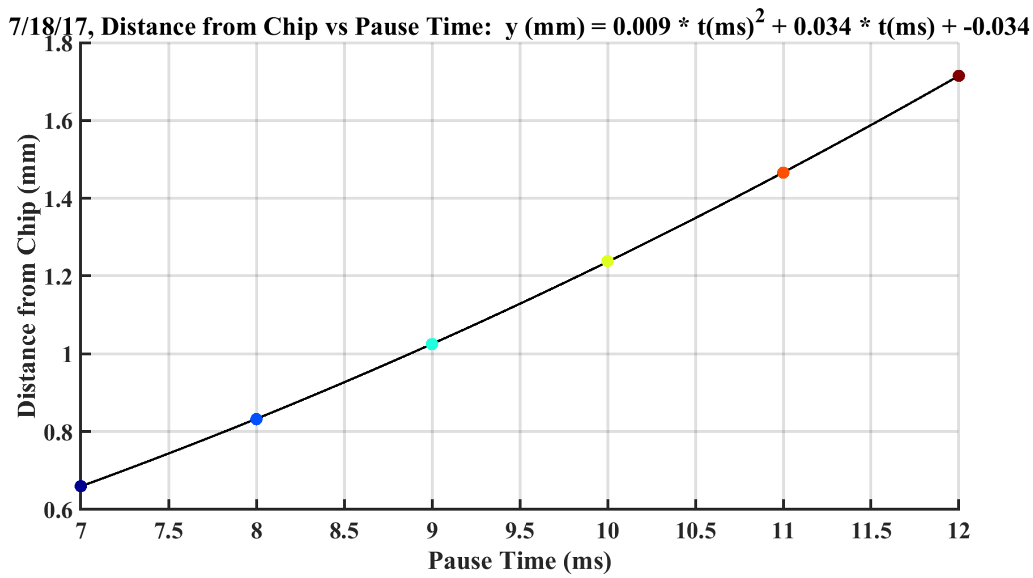

FIG. B.7: Based on the data from figure 5.25 (the colors of the points on this plot also correspond to those of figure 5.25), this curve shows the distance the atoms will fall before levitating as a function of the time waited before turning on coil 6. Applicable to section 5.4.

APPENDIX C

Push Coil Data

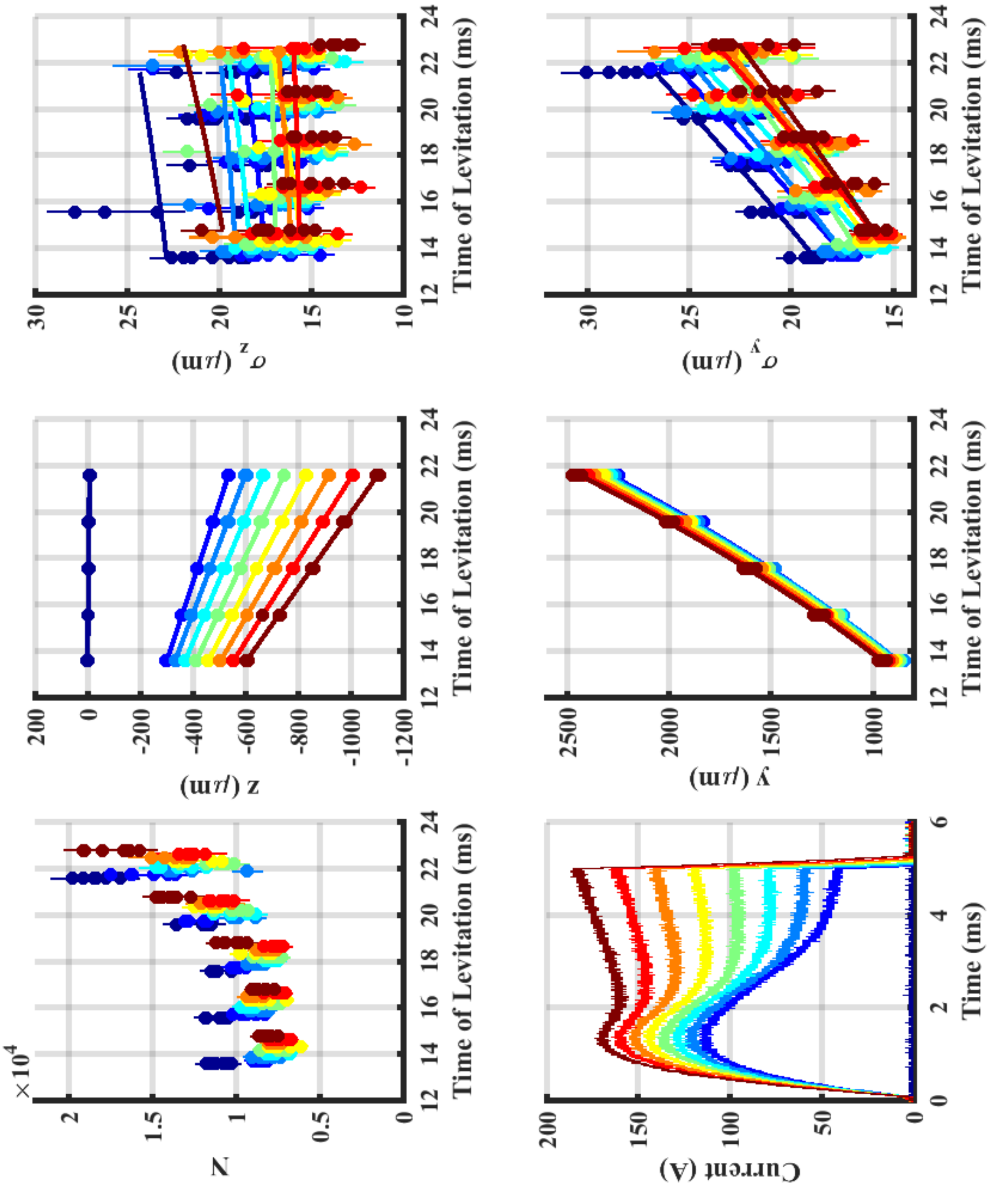

FIG. C.1: Various plots with different push coil currents from data collected with the axial camera.

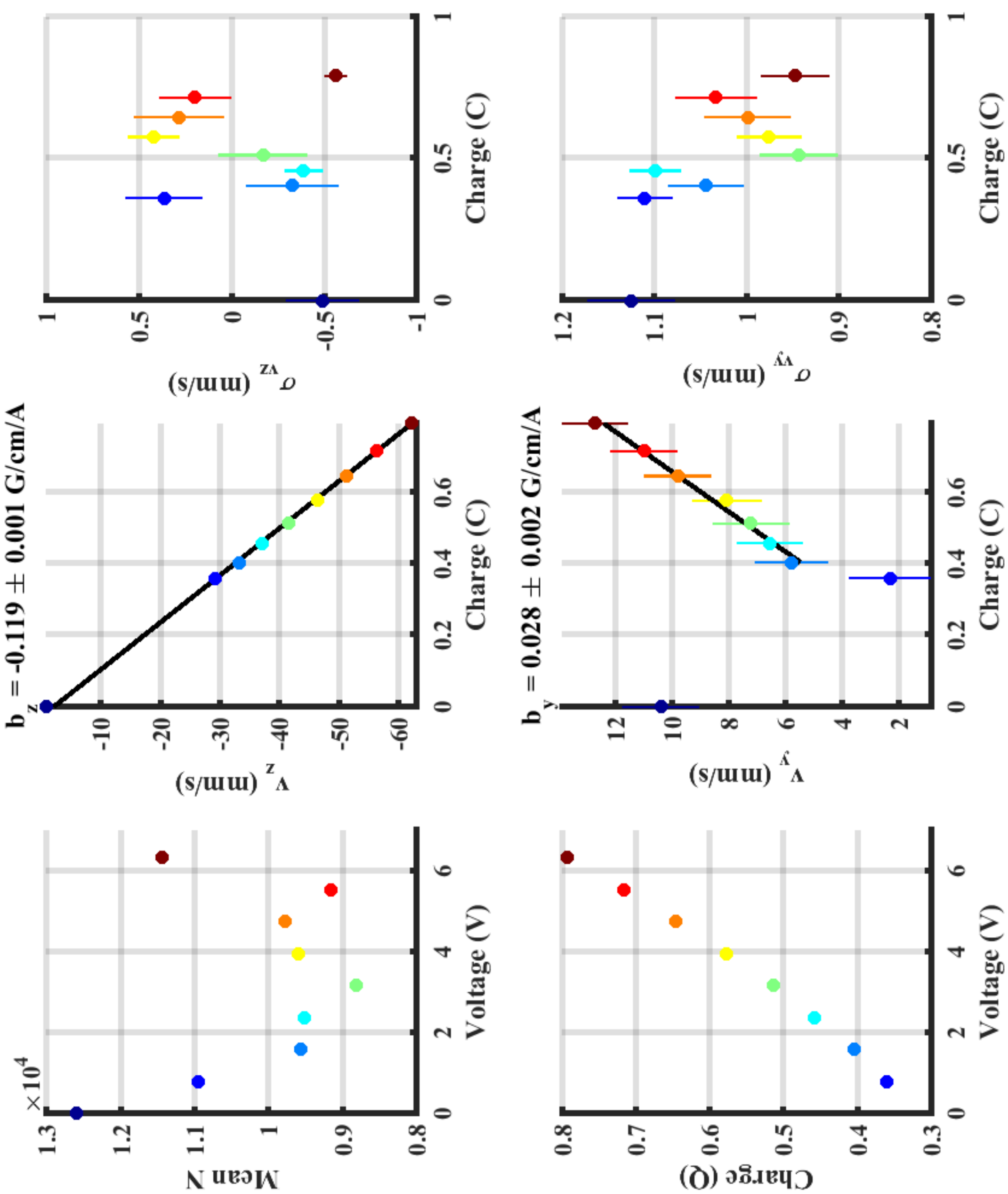

FIG. C.2: Various plots derived from fitting data in figure C.1.

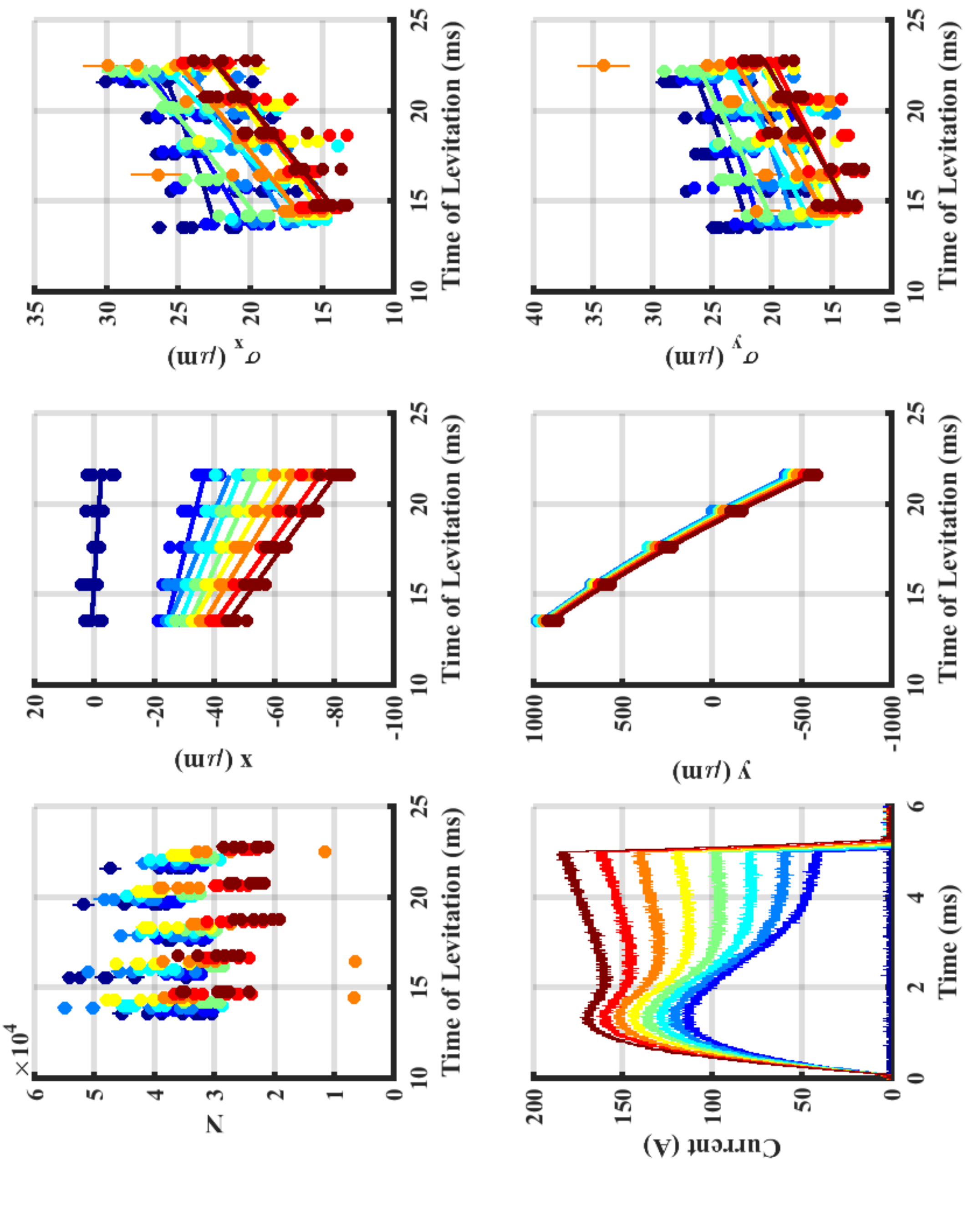

FIG. C.3: Various plots with different push coil currents from data collected with the radial camera.

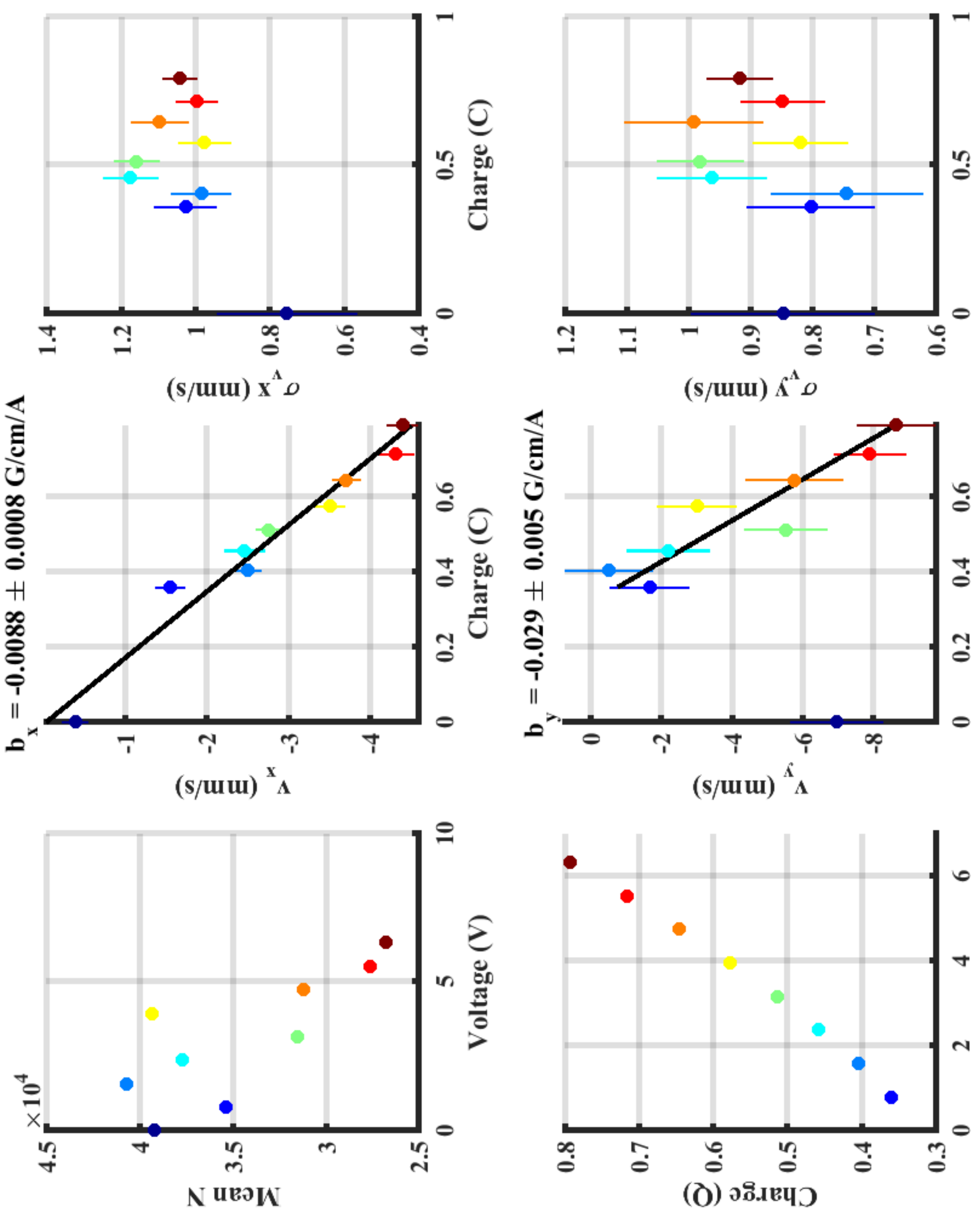

FIG. C.4: Various plots derived from fitting data in figure C.3.

APPENDIX D

ADwin Sequencer Panel

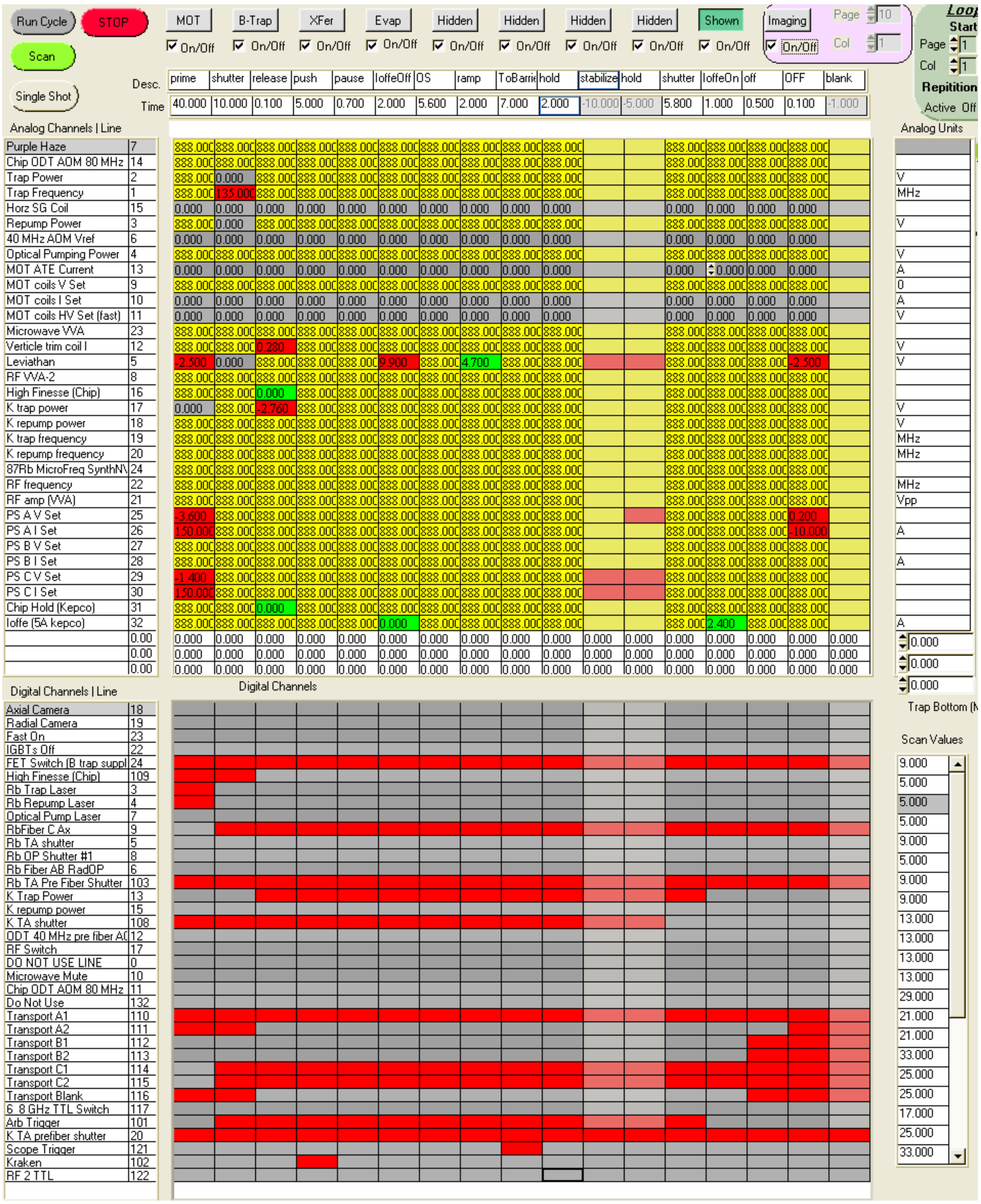

FIG. D.1: ADwin sequencer panel. The panel shown contains the timings and settings for the single barrier scattering experiment. The prior panels generate a BEC, and the last panel is used for imaging.

APPENDIX E

Unit Conversion

$$\ell_0 = \frac{\sigma_b}{\sigma'_b} \tag{E.1}$$

$$\omega_0 = \frac{\hbar}{m\ell_0^2} \tag{E.2}$$

$$\alpha = \alpha' \tag{E.3}$$

$$\omega = \omega_0 \omega' \tag{E.4}$$

$$p = \sqrt{m\hbar\omega_0}\, p' \tag{E.5}$$

$$U = \hbar\omega_0 U' \tag{E.6}$$

$$x = \ell_0 x' \tag{E.7}$$

$$t = \frac{1}{\omega_0} t' \tag{E.8}$$

$$v = \sqrt{\frac{\hbar\omega_0}{m}}\, v' \tag{E.9}$$

BIBLIOGRAPHY

[1] P. K. Tien and J. P. Gordon, "Multiphoton Process Observed in the Interaction of Microwave Fields with the Tunneling between Superconductor Films," Phys. Rev. **'19**, 647 (1963).

[2] M. Buttiker and R. Landauer, "Traversal Time for Tunneling," Phys. Rev. Lett. **49**, 1739 (1982).

[3] M. Gärttner, F. Lenz, C. Petri, F. K. Diakonos, and P. Schmelcher, "Quantum scattering in driven single- and double-barrier systems 1," Phys. Rev. E **81** (2010).

[4] A. Emmanouilidou and L. E. Reichl, "Floquet scattering and classical-quantum correspondence in strong time-periodic fields," Phys. Rev. A **65** (2002).

[5] A. Pimpale, S. Holloway, and R. J. Smith, "Tunnelling through moving barriers," J. Phys. A **24**, 3533 (1991).

[6] V. A. Fedirko and V. V. Vyurkov, "Tunnelling through Oscillating Barrier," Phys. Stat. Sol. **221**, 447 (2000).

[7] A.-P. Jauho, "Numerical simulations of resonant tunneling in the presence of inelastic processes," Phys. Rev. B **41**, 327 (1990).

[8] S. Rahav and P. W. Brouwer, "Semiclassical theory of a quantum pump," Phys. Rev. B **74** (2006).

[9] M. Henseler, T. Dittrich, and K. Richter, "Classical and quantum periodically driven scattering in one dimension," Phys. Rev. E **64** (2001).

[10] W. A. Lin and L. E. Ballentine, "Quantum Tunneling and Chaos in a Driven Anharmonic Oscillator," Phys. Rev. Lett. **65**, 2927 (1990).

[11] L. M. Pecora, H. Lee, D.-h. Wu, T. Antonsen, M.-j. Lee, and E. Ott, "Chaos regularization of quantum tunneling rates," Phys. Rev. E **065201**, 2 (2011).

[12] D. A. Steck, W. H. Oskay, and M. G. Raizen, "Observation of Chaos-Assisted Tunneling Between Islands of Stability," Science. **293**, 274 (2001).

[13] D. A. Steck, W. H. Oskay, and M. G. Raizen, "Fluctuations and Decoherence in Chaos-Assisted Tunneling," Phys. Rev. Lett. **88**, 120406 (2002).

[14] F. Grossmann, T. Dittrich, P. Jung, and P. Hanggi, "Coherent Destruction of Tunneling," Phys. Rev. Lett. **67**, 516 (1991).

[15] F. Wilczek, "Quantum Time Crystals," Phys. Rev. Lett. **109** (2012).

[16] D. V. Else, B. Bauer, and C. Nayak, "Floquet Time Crystals," Phys. Rev. Lett. **117** (2016).

[17] J. Zhang, P. W. Hess, A. Kyprianidis, P. Becker, A. Lee, J. Smith, G. Pagano, I. Potirniche, A. C. Potter, A. Vishwanath, et al., "Observation of a discrete time crystal," Nature **543**, 217 (2017), ISSN 0028-0836, URL `http://dx.doi.org/10.1038/nature21413`.

[18] J. Smits, L. Liao, H. T. C. Stoof, and P. V. D. Straten, "Observation of a Space-Time Crystal in a Superfluid Quantum Gas," Phys. Rev. Lett. **121** (2018), ISSN 1079-7114, URL `https://doi.org/10.1103/PhysRevLett.121.185301`.

[19] M. H. Anderson, J. R. Ensher, M. R. Matthews, C. E. Wieman, and E. A. Cornell, "Observation of Bose-Einstein Condensation in a Dilute Atomic Vapor," Science. **269**, 198 (1995).

[20] W. Ketterle, "Nobel lecture : When atoms behave as waves : Bose-Einstein condensation and the atom laser," Rev. Mod. Phys. **74**, 1131 (2002).

[21] M. K. Ivory, Ph.D. thesis, College of William and Mary (2016).

[22] M. K. Ivory, T. A. Byrd, A. J. Pyle, K. K. Das, K. A. Mitchell, S. Aubin, and J. B. Delos, "Ballistic atom pumps," Phys. Rev. A **90**, 023602 (2014), ISSN 1050-2947, `1510.02860`, URL `http://link.aps.org/doi/10.1103/PhysRevA.90.023602`.

[23] D. J. Thouless, "Quantization of Particle Transport," Phys. Rev. B - Condens. Matter Mater. Phys. **27**, 6083 (1983).

[24] B. Kaestner, V. Kashcheyevs, S. Amakawa, M. D. Blumenthal, L. Li, T. J. B. M. Janssen, G. Hein, K. Pierz, T. Weimann, U. Siegner, et al., "Single-parameter nonadiabatic quantized charge pumping," Phys. Rev. B - Condens. Matter Mater. Phys. **77**, 1 (2008), ISSN 10980121, `0707.0993`.

[25] M. Switkes, C. M. Marcus, K. Campman, and A. C. Gossard, "An Adiabatic Quantum Electron Pump," Science. **283**, 1905 (1999).

[26] P. W. Brouwer, "Rectification of displacement currents in an adiabatic electron pump," Phys. Rev. B **63** (2001).

[27] F. Giazotto, P. Spathis, S. Roddaro, S. Biswas, F. Taddei, M. Governale, and L. Sorba, "A Josephson Quantum Electron Pump," Nat. Phys. **7** (2011), `arXiv:1102.4207v1`.

[28] M. Lohse, C. Schweizer, O. Zilberberg, M. Aidelsburger, and I. Bloch, "A Thouless quantum pump with ultracold bosonic atoms in an optical superlattice," Nat. Phys. pp. 1–6 (2015).

[29] S. Nakajima, T. Tomita, S. Taie, T. Ichinose, H. Ozawa, L. Wang, M. Troyer, and Y. Takahashi, "Topological Thouless pumping of ultracold fermions," Nat. Phys. (2016).

[30] S. Chu, L. Hollberg, J. E. Bjorkholm, A. Cable, and A. Ashkin, "Three-Dimensional Viscous Confinement and Cooling of Atoms by Resonance Radiation Pressure," Phys. Rev. Lett. **55**, 48 (1985).

[31] D. Sesko, C. G. Fan, and C. E. Wieman, "Production of a cold atomic vapor using diode-laser cooling," JOSA B **5**, 1225 (1988).

[32] E. L. Raab, M. Prentiss, A. Cable, S. Chu, and D. E. Pritchard, "Trapping of Neutral Sodium Atoms with Radiation Pressure," Phys. Rev. Lett. **59**, 2631 (1987).

[33] P. D. Lett, R. N. Watts, C. I. Westbrook, W. D. Phillips, and P. L. Gould, "Observation of Atoms Laser Cooled below the Doppler Limit," Phys. Rev. Lett. **61**, 169 (1988).

[34] J. Dalibard and C. Cohen-Tannoudji, "Laser cooling below the Doppler limit by polarization gradients: simple theoretical models," JOSA B **6**, 2023 (1989).

[35] C. Chin, S. Chu, A. J. Kerman, and V. Vuletic, "Beyond Optical Molasses : 3D Raman Sideband Cooling of Atomic Cesium to High Phase-Space Density," Phys. Rev. Lett. **84**, 439 (2000).

[36] A. L. Migdall, J. V. Prodan, D. Phillips, T. H. Bergeman, and H. J. Metcalf, "First Observation of Magnetically Trapped Neutral Atoms," Phys. Rev. Lett. **54**, 2596 (1985).

[37] S. Chu, J. E. Bjorkholm, A. Ashkin, and A. Cable, "Experimental Observation of Optically Trapped Atoms," Phys. Rev. Lett. **57**, 314 (1986).

[38] K. B. Davis, M. O. Mewes, M. R. Andrews, N. J. van Druten, D. S. Durfee, D. M. Kurn, and W. Ketterle, "Bose-Einstein Condensation in a Gas of Sodium Atoms," Phys. Rev. Lett. **75**, 3969 (1995).

[39] C. C. Bradley, C. A. Sackett, J. J. Tollett, and R. G. Hulet, "Evidence of Bose-Einstein Condensation in an Atomic Gas with Attractive Interactions," Phys. Rev. Lett. **75**, 1687 (1995).

[40] B. Demarco and D. S. Jin, "Onset of Fermi Degeneracy in a Trapped Atomic Gas," Science. **285**, 1703 (1999).

[41] C. T. Fancher, A. J. Pyle, A. P. Rotunno, and S. Aubin, "Microwave AC Zeeman force for ultracold atoms," Phys. Rev. A **97** (2018).

[42] T. A. Byrd, M. K. Ivory, A. J. Pyle, S. Aubin, K. A. Mitchell, J. B. Delos, and K. K. Das, "Scattering by an oscillating barrier: Quantum, classical, and semiclassical comparison," Phys. Rev. A **86**, 13622 (2012), ISSN 1050-2947, `arXiv:1205.1484v1`, URL `http://link.aps.org/doi/10.1103/PhysRevA.86.013622`.

[43] M. K. Ivory, A. R. Ziltz, C. T. Fancher, A. J. Pyle, A. Sensharma, B. Chase, J. P. Field, A. Garcia, D. Jervis, and S. Aubin, "Atom chip apparatus for experiments with ultracold rubidium and potassium gases.," Rev. Sci. Instrum. **85**, 043102 (2014), ISSN 1089-7623, URL `http://www.ncbi.nlm.nih.gov/pubmed/24784588`.

[44] D. J. Tannor, *Introduction to Quantum Mechanics A Time-Dependent Perspective* (University Science Books, 2007), ISBN 978-1-891389-23-8.

[45] G. P. Agrawal, "Nonlinear Fiber Optics," (2001).

[46] K. Das and S. Aubin, "Quantum Pumping with Ultracold Atoms on Microchips: Fermions versus Bosons," Phys.\ Rev.\ Lett. **103**, 123007 (2009), ISSN 0031-9007, `arXiv:0912.3588v1`.

[47] M. Weidemuller and C. Zimmermann, *Cold Atoms and Molecules* (Wiley-VCH Verlag ambH, 2009).

[48] A. Einstein, "Sitzungsberichte der Preussischen Akademie der Wissenschaften Physikalisch-mathematische Klasse," Sitzungberichte der Preuss. Akad. der Wissenschaften Phys. Klasse p. 261 (1924).

[49] S. N. Bose, "Planck's Law and Light Quantum Hypothesis," Z. Phys. **26** (1924).

[50] D. G. Fried, T. C. Killian, L. Willmann, D. Landhuis, S. C. Moss, D. Kleppner, and T. J. Greytak, "Bose-Einstein Condensation of Atomic Hydrogen," Phys. Rev. Lett. **81**, 3811 (1998).

[51] C. Pethick and H. Smith, *BoseEinstein Condensation in Dilute Gases* (Cambridge University Press, 2002).

[52] W. Ketterle, D. S. Durfee, and D. Stamper-Kurn, in *1998 Enrico Fermi summer Sch. Bose-Einstein condesation Varenna, Italy* (1998).

[53] W. Kohn, "Cyclotron Resonance and de Haas-van Alphen Oscillations of an Interacting Electron Gas," Phys. Rev. **123**, 1242 (1961).

[54] A. T. Sommer, Ph.D. thesis, Massachusetts Institute of Technology (2013).

[55] J. F. Dobson, "Harmonic-Potential Theorem: Implications for Approximate Many-Body Theories," Phys. Rev. Lett. **73**, 2244 (1994).

[56] M. Pappa, P. C. Condylis, G. O. Konstantinidis, V. Bolpasi, A. Lazoudis, O. Morizot, D. Sahagun, M. Baker, and W. von Klitzing, "Ultra-sensitive atom imaging for matter-wave optics," New J. Phys. **13**, 115012 (2011), ISSN 1367-2630, URL `http://stacks.iop.org/1367-2630/13/i=11/a=115012`.

[57] C. T. Fancher, Ph.D. thesis, College of William and Mary (2017).

[58] A. R. Ziltz, Ph.D. thesis, College of William and Mary (2015).

[59] D. A. Steck, "Rubidium 87 D Line Data," (2003).

[60] E. Majorana, "Atomi orientati in campo magnetico variabile," Nuovo Cim. **9** (1932).

[61] J. Schwinger, "On nonadiabatic processes in inhomogenous fields," Phys. Rev. **51** (1937).

[62] R. Roy, A. Green, R. Bowler, and S. Gupta, "Rapid cooling to quantum degeneracy in dynamically shaped atom traps," Phys. Rev. A **93** (2016).

[63] A. L. Marchant, S. A. Hopkins, T. P. Wiles, and S. L. Cornish, "Bose-Einstein condensation of 85 Rb by direct evaporation in an optical dipole trap," Phys. Rev. A **85** (2012).

[64] J.-F. Clément, J.-P. Brantut, M. Robert-de Saint-Vincent, R. A. Nyman, A. Aspect, T. Bourdel, and P. Bouyer, "All-optical runaway evaporation to Bose-Einstein condensation," Phys. Rev. A **79**, 061406 (2009), ISSN 1050-2947, URL `http://link.aps.org/doi/10.1103/PhysRevA.79.061406`.

[65] M. D. Barrett, J. A. Sauer, and M. S. Chapman, "All-Optical Formation of an Atomic Bose-Einstein Condensate," Phys. Rev. Lett. **87**, 010404 (2001), ISSN 0031-9007, URL `http://link.aps.org/doi/10.1103/PhysRevLett.87.010404`.

[66] Y.-J. Lin, A. R. Perry, R. L. Compton, I. B. Spielman, and J. V. Porto, "Rapid production of 87Rb Bose-Einstein condensates in a combined magnetic and optical potential," Phys. Rev. A **79**, 063631 (2009), ISSN 1050-2947, URL `http://link.aps.org/doi/10.1103/PhysRevA.79.063631`.

[67] A. Szczepkowicz, L. Krzemien, A. Wojciechowski, K. Brzozowski, M. Kruger, M. Zawada, M. Witkowski, J. Zachorowski, and W. Gawlik, "Optimal geometry for efficient loading of an optical dipole trap," Phys. Rev. A **79** (2008), ISSN 1050-2947, `0809.1999v2`, URL `http://arxiv.org/abs/0809.1999`.

[68] D. Feldbaum, H. Wang, J. Weinstein, D. Vieira, and X. Zhao, “Trapping radioactive Rb82 in an optical dipole trap and evidence of spontaneous spin polarization,” Phys. Rev. A - At. Mol. Opt. Phys. **76**, 3 (2007), ISSN 10502947, `0708.3826`.

[69] D. Comparat, a. Fioretti, G. Stern, E. Dimova, B. L. Tolra, and P. Pillet, “Optimized production of large Bose-Einstein condensates,” Phys. Rev. A - At. Mol. Opt. Phys. **73**, 1 (2006), ISSN 10502947.

[70] C.-L. Hung, X. Zhang, N. Gemelke, and C. Chin, “Accelerating evaporative cooling of atoms into Bose-Einstein condensation in optical traps,” Phys. Rev. A **78**, 011604 (2008), ISSN 1050-2947, URL `http://link.aps.org/doi/10.1103/PhysRevA.78.011604`.

[71] M. J. Williams and C. Fertig, “Multipartite model of evaporative cooling in optical dipole traps,” Phys. Rev. A **91**, 1 (2015), ISSN 1050-2947, URL `http://link.aps.org/doi/10.1103/PhysRevA.91.023432`.

[72] D. L. Jenkin, D. J. McCarron, M. P. Köppinger, H. W. Cho, S. a. Hopkins, and S. L. Cornish, “Bose-Einstein condensation of 87Rb in a levitated crossed dipole trap,” Eur. Phys. J. D **65**, 11 (2011), ISSN 14346060, `1104.0495`.

[73] R. M. Price, Ph.D. thesis, University of Maryland (2015).

[74] A. R. Perry, Ph.D. thesis, University of Maryland (2015).

[75] D. L. Campbell, Ph.D. thesis, University of Maryland (2015).

[76] H. Ammann and N. Christensen, “Delta Kick Cooling : A New Method for Cooling Atoms,” Phys. Rev. Lett. **78** (1997).

[77] S. H. Myrskog, J. K. Fox, H. S. Moon, J. B. Kim, and A. M. Steinberg, “Modified delta-kick cooling” using magnetic field gradients,” Phys. Rev. A **61** (2000).

[78] T. Aoki, T. Kato, Y. Tanami, and H. Nakamatsu, “Delta-kick cooling using the Ioffe-Pritchard potential,” Phys. Rev. **73** (2006).

[79] T. Kovachy, J. M. Hogan, A. Sugarbaker, S. M. Dickerson, C. A. Donnelly, C. Overstreet, and M. A. Kasevich, “Matter Wave Lensing to Picokelvin Temperatures,” Phys. Rev. Lett. **114** (2015).

[80] A. Sugarbaker, Ph.D. thesis, Stanford University (2014).

[81] A. E. Siegman, “How to (Maybe) Measure Laser Beam Quality,” OSA Trends Opt. Photonics (Optical Soc. Am. **17** (1998).

[82] H. J. Metcalf and P. van der Straten, *Laser Cooling and Trapping* (Springer, 1999).

[83] P. L. Gould, G. A. Ruff, and D. E. Pritchard, "Diffraction of Atoms by Light: The Near-Resonant Kapitza-Dirac Effect," Phys. Rev. Lett. **56** (1986).

[84] G. Roati, M. Zaccanti, C. D. Errico, J. Catani, M. Modugno, A. Simoni, M. Inguscio, and G. Modugno, "39K Bose-Einstein Condensate with Tunable Interactions," Phys. Rev. Lett. **010403**, 1 (2007).

[85] R. Ramos, D. Spierings, S. Potnis, and A. M. Steinberg, "Atom-optics knife edge : Measuring narrow momentum distributions," Phys. Rev. A **023611**, 1 (2018).

VITA

Andrew James Pyle

Andrew James (AJ) Pyle was born on the 27th of February, 1989 in Lenhartsville, Pennsylvania. He attended Greenwich Elementary School, Kutztown Area Middle School and graduated from Kutztown Area High School in 2007. After high school, he entered Kutztown University of Pennsylvania. He graduated Summa Cum Laude in 2011 with a Bachelor of Science in Physics and a Bachelor of Science in Chemistry. AJ entered the College of William & Mary in the fall of 2011, and began work for Dr. Seth Aubin in the Ultracold Atoms Group to help develop the ultracold apparatus with which to study quantum pumping. He received a Master of Science in 2013. AJ married his beloved wife, Jillian on September 9, 2017. AJ began working for ACEnT Laboratories in Hampton, Virginia in July 2018, supporting the development of advanced aerospace propulsion and power systems for NASA and the USAF. AJ also works with Grey Gecko in Newport News, Virginia, developing corrosion detection devices under contract with Lockheed Martin, for the Department of Defense.